I. R. IRAN

ISSN: 2423-7167
e-ISSN: 1735-9244

International Journal of Engineering

Journal Homepage: www.ije.ir

MERC

TRANSACTIONS C: ASPECTS

Volume 35, Number 03, March 2022

Materials and Energy Research Center

In the Name of God

INTERNATIONAL JOURNAL OF ENGINEERING
Transactions A: Basics

International **J**ournal of **E**ngineering *Transactions A: Basics* (ISSN 1728-1431) (EISSN 1735-9244)
International **J**ournal of **E**ngineering *Transactions B: Applications* (ISSN 1728-144X) (EISSN 1735-9244)
International **J**ournal of **E**ngineering *Transactions C: Aspects* (ISSN 2423-7167) (EISSN 1735-9244)
Web Sites: www.ije.ir & www.ijeir.info E-mails: ije.editor8@gmail.com, Tel: (+9821) 88771578, Fax: (+9821) 88773352
Materials and Energy Research Center (MERC)

ISSN: 2423-7167, e-ISSN: 1735-9244

International Journal of Engineering, Volume 35, Number 03, March 2022

CONTENTS

Transactions C: Aspects

H. Hamidi; A. Moradi Abadi; S. A. Amin Mousavi	A New Method for Open Government using of Information Technology	493-501
M. Abbasghorbani	Prioritization of Transmission Network Components Based on their Failure Impact on Reliability of Composite Power Systems	502-509
N. Mirhosseini; R. Davarnejad; A. Hallajisani; E. Cano-europa; O. Tavakoli	Sugarcane Molasses as a Cost-effective Carbon Source on *Arthrospira maxima* Growth by Taguchi Technique	510-516
H. Benbouhenni	Amelioration Effectiveness of Torque and Rotor Flux Control Applied to the Asynchronous Generator for Dual-rotor Wind Turbine using Neural Third-order Sliding Mode Approaches	517-530
H. Noferesti; M. Gerami	Bolt Pre-tension Effect on Performance of Bolted Extended End-plate Moment Connections under Cyclic Loading	531-543
K. Bouaraour; N. Hebbir	Numerical Study of Twin Jets Interactions using Realizable Model	544-551
U. V. Saindane; S. Soni; J. V. Menghani	Friction and Wear Performance of Brake Pad and Optimization of Manufacturing Parameters using Grey Relational Analysis	552-559
V. D. Golakiya; M. K. Chudasama	Experimental Formability Study of Ti6Al4V Sheet Metal using Friction Stir Heat Assisted Single Point Incremental Forming Process	560-566
A. Abbasian; A. Ravangard; I. Hajian Nia; S. Mirzamohammadi	Investigation of Microstructure and Mechanical Properties of Newly Developed Advanced High Strength TRIP Steel	567-571
S. J. Niranjana; S. S. Kubsad; S. Manjunatha; Y. Nagaraj; I. Bhavi; B. M. Angadi; A. J. Chamkha; M. B. Vanarotti	Experimental Investigation and Numerical Simulation of Air Circulation in a Non-AC Bus Coach System	572-579
A. Khecho; S. A. Ghaffari; M. Behzadnasab; M. Rahmat	Role of Mixing Method and Solid Content on Printability of Alumina Inks for Stereolithography 3D Printing Process	580-586
M. A. Choupani; S. S. Tabatabaee Moradi; S. A. Tabatabaei Nejad	Study on Attapulgite as Drilling Fluid Clay Additive in Persian Gulf Seawater	587-595

ISSN: 2423-7167, e-ISSN: 1735-9244

International Journal of Engineering, Volume 35, Number 03, March 2022

A. Nikitasari; G. Priyotomo; A. Royani; S. Sundjono	Exploration of *Eucheuma* Seaweed Algae Extract as a Novel Green Corrosion Inhibitor for API 5L Carbon Steel in Hydrochlorid Acid Medium	596-603
F. Razmi; A. Rowhanimanesh; A. Dideban	An Optimal Boolean Approach for Computational Modeling of Gene Regulatory Networks from Temporal Gene Expression Profile	604-612

International Journal of Engineering

Journal Homepage: www.ije.ir

A New Method for Open Government using of Information Technology

H. Hamidi*[a], A. Moradi Abadi[b], S. A. Amin Mousavi[b]

[a] *Department of Information Technology, Faculty of Industrial Engineering, K. N. Toosi University of Technology, Tehran, Iran*
[b] *Science and Research Branch, Islamic Azad University, Tehran, Iran*

P A P E R I N F O

Paper history:
Received 27 September 2021
Received in revised form 10 November 2021
Accepted 16 November 2021

Keywords:
Information Technology
Open Government Pattern
Tax Affairs Organization
Stakeholders

A B S T R A C T

The purpose of this paper is to explore dimensions of open government in tax affairs organization of Iran country as a governmental organization. Three main factors of policy, culture, and technology were identified after investigating open government's plan in the United States of America, Austria, Mexico countries and the conducted interviews with experts in three fields of information technology, Executive, and legal. Four subfactors of internal directive, legal, strategic planning, and performance for policy and five subfactors of security, tools, open government program, data, and infrastructure for technology and six sub-factors of employees readiness, communicational channels, knowledge management, changes management, agency stakeholders, and participatory activities were considered for culture. A structured interview was conducted with three experts in legal, information technology and administrative fields for initial evaluation and finding new factors. The statistical population in this research was considered among Tax Affairs Organization of Iran country's employees. The mentioned pattern was evaluated based on partial least squares approach and confirmed at strong level after extracting information from the distributed questionnaires. Three factors of policy, technology and culture have effect on open government and between them culture has the main priority.

***doi**: 10.5829/ije.2022.35.03c.01*

1. INTRODUCTION

Open government is a pervasive movement to expand citizens' access to government affairs. Open government is of the relatively new achievements that have close relationship with information technology. Its principles have been based on democratic values. Citizens' right of access to government documents and measures for public supervision is of the open government goals. They can also extract their required information from this context. This means that citizens are able to receive more data and information about their need by using web electronic contexts [1]. The doctrine governing open government states that citizens should have the right to access government documents and inquiry for public supervision [2]. Alalwan et al. [3-5] consider the emergence of social media as a factor that has provided opportunity for people's engagement and interaction in open government work.

It has changed people's expectations about how government works. They also consider achievement of transparency, participation, and partnership as one of the goals of open government . Emergence of web is one of the significant developments in the Internet. Davis [6], Alharbi and Drew [7] consider it as the factor of opening data and sharing non-sensitive information about operations and services by governmental organizations and business. Benbasat and Barki [8] consider open data as an important source due to its potential to empower citizens, business, and conversion of government to public services delivery. Al-Shihi et al. [2] believe that the government should use the capacity availability of open government data with high quality as a main input source for industry despite harness of the economic value of open data assets and advantage related to business opportunities. Users despite data overlapping may confuse also overlapping data set and contradictory data set. Brasel and Gips [9] consider increase of

*Corresponding Author Institutional Email: *h_hamidi@kntu.ac.ir* (H. Hamidi)

Please cite this article as: H. Hamidi, A. Moradi Abadi, S. A. Amin Mousavi, A New Method for Open Government using of Information Technology, ***International Journal of Engineering, Transactions C: Aspects*** Vol. 35, No. 03, (2022) 493-501

transparency, stimulation of economic growth, improvement of government services and accountability, encouraging the reuse of information, improvement of public relations and attitude towards the government, and improvement of government data and processes as six incentives to open the data in the countries. Obstacles of participation including lack of incentive, abilities, business models and technical knowledge among users. Budiono et al. [10], Carlsson et al. [11], Chong [12], Chong et al. [13], Daraei and Hamidi [14] concern for privacy, confidentiality and responsibility, complexity of the activities required for identification, understanding and using the data can be mentioned as the obstacles of the expansion of open data

Chong et al. [15] totally consider employees and budget constraint, the likelihood of loss of income, and the uncertainty of its compliance with the Data Protection Act as the most problematic obstacle among 20 unique specified obstacles. The concern for coordination between security and openness has been stated as an important factor in other researches. However, competition between the principles of information management and balancing due to the required internal information has been sometimes reported as the important factor. Chong et al. [16] states open government project of organization as a public plan that its details show how the principles of transparency and open government statement are of the main mission of organization. This project in senior policy, legal and technology management fields in organization with the public experts and experts' view reflects open government in which specific measures' details should be carried out according to the schedule table. Alvanchi et al. [17], Lee and Kwak [18] consider "Open Government Implementation Model" as a model of public method to implement open government projects that includes some suggestions for step by step implementation of open government and includes some indices to measure the success of individual steps. Provision of a specific framework can be helpful for the next measures including implementation and operation of open government due to the development of e-government in Iran country and more provision of services electronically and online by governmental organizations and institutions in Iran, and due to the movement of developed countries toward creation and operation of open government in line with e-government, and since an specific study has not been conducted till now on implementing, designing and creating open government in governmental organizations which provide e-services, and there is not still an appropriate understanding in this regard.

The aim of conducting this research is to identify factors that have an effect on implementation of open government in the Tax affairs Organization of Iran country as governmental organization. Open government projects in different countries are firstly studies for this purpose. Then the research methodology is stated and afterwards the results of findings are analyzed. Finally the results of findings are analyzed, concluded, and summarized .

2. RESEARCH LITERATURE

Open government model in three countries, the United States of America, Austria and Mexico is addressed in this part .

2. 1. Open Government Framework of America Department of Interior (DOI) DOI has accepted integrated lifecycle management to access for planning and implementing business processes, which is of the primary goals of open government. Expansion of DOI government framework includes a process of comprehensive management within the life cycle total time of evaluation and planning program of primary stages in order to measure performance and processes of improvement. In addition, the framework includes the methods to identify, understand and address to the technology, policy, and cultural issues of DOI related to certain projects of open government (Open Government project of America):

Key technologies' areas: Security, infrastructure, tools, enterprise architecture, and current open government pilots and programs ;

Key policies' areas: Strategic planning, performance, legal, internal directives, acquisition and privacy;

Key culture areas: Employee readiness, communication channels, stakeholders, and existing and emerging public collaboration vehicles.

The framwork for Open Government project of America is illustrated in Figure 1.

2. 2. Open Government of Austria Country Open government is the comprehensive redesign of administrative policies and activities according to the principles of modern management and public governance. In terms of the above cases, open government focuses on transparency, participation and partnership. KDZ Implementation model is significantly based on "Lee & Kwak Implementation Model" [18].

Implementation Model, open government data is four steps :

Stage 1 – Increasing Data Transparency: Opens access to administrative data .

Stage 2 – Improving Open Participation: Opens government and administration for the ideas and knowledge of the public .

Stage 3 – Enhancing Open Collaboration: Improves Open Collaboration between administrative agencies, the government, citizens, the public, and the economy. Open participation allows the use of social media to connect

Figure 1. Open government framework of Department of Interior of America country

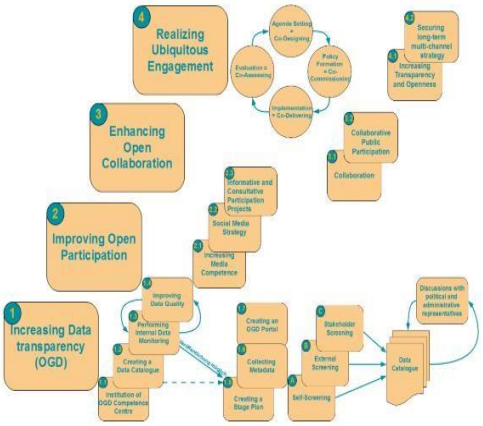

Figure 2. Open Government Implementation Model of Austria [18]

people and their ideas. Open Collaboration allows the achievement of specific outputs.

Stage 4 – Realizing Ubiquitous Engagement: Allows the engagement of the public through transparency, participation, and collaboration.

The Open Government Implementation Model of Austria is shown in Figure 2.

2. 3. Open Government of Mexico Country

Mexican government has applied several projects under the OGP by applying new technologies and innovation in order to increase transparency, empower citizens, fight against corruption, and harness new technologies to strengthen the government. One of these open government projects that called PbR-SED is seeking to strengthen transparency in budget. PbR-SED project is known as one of the measures that the Mexican government has committed to do it for "open government program for Mexico" since twentieth of September 2011. In addition to a series of operations in this method, the information on government funding, governmental investments (governmental bonds), transfers in and federal government, performance indices and assessments is published and updated.

The effect of a number of factors has been examined in this project, which include:

- Contextual factors
- Budget factors
- Information systems factors .
- Collaboration factors
- Knowledge factors
- Trust factors

2. 4. Identified Factors in Open Government

Open government of the government of America seems more comprehensive than other countries after evaluating open government model in the three mentioned countries. The proposed model includes three basic dimensions of policy, culture and technology. Each of these dimensions was then compared correspondingly with the factors and models of other countries and studies. The following table was obtained finally.

Table 1 summarized the identifying factors in open government project.

3. RESEARCH METHODOLOGY

The statistical population in this research was considered among Tax Affairs Organization of Iran country's employees given that open government has been composed of different dimensions and required comprehensive information and pervasive vision to the subject. Among the employees those who have comprehensive viewpoint in both policy and Information Technology fields were selected by purposive and judgmental sampling. 90 questionnaires were distributed in the population of 120 employees. 87 questionnaires were collected finally. Data collection tool was questionnaire and five-point Likert scale has been used. Finally, variance-based method with partial squares approach was used given that the sample size is limited, as well as data was not normal. SmartPLS and SPSS tools were used for this purpose. Three countries of United States of America, Austria and Mexico were selected for further review after reviewing open government project in different countries in order to determine an appropriate pattern for providing in tax affairs organization of Iran country. With regard to research literature, each of these three countries was following a different approach in the field of open government. Open Government Project of United States of America among them had more precise expression of the subject. It was selected as the base model for this purpose. A structured interview was

conducted with three experts in legal, information technology and administrative fields in the initial step for initial evaluation and the possibility of providing this project pattern. Accordingly, there was the possibility to provide the pattern. The following model was finally proposed based on United States of America Model due to the literature review and the conducted interviews . Figure 3 shows the Model stating the relationships between variables.

As it has been demonstrated in the above figure, three main factors of culture, policy and technology have an effect on open government based on this framework. Policy dimension itself is influenced by internal directive, strategic planning, legal and performance. Technology factor is also influenced by factors such as security, tools, open government program, data, and infrastructure. Cases such as employees' readiness,communicational channels, knowledge management, changes management, agency stakeholders, and participatory have an effect on cultural factors.

TABLE 1. summarizing the factors identified in open government

Main dimension	Factor	Index
Policy	Strategic planning [19]	Strategic planning, performance, legal, internal guidelines, business, and privacy
	Performance [20]	Political factors, including political support by senior officials, lawmakers and policymakers
	Rules [21]	• Rules and regulations of governmental investment ▪ Rules and regulations of civil services
	Implementation Strategy [22]	▪ The designers intent of the reform and the suggested path of this change from top to
	Power [23]	Centralization level of decision-makers in organization
	Leadership [24]	▪ Supporting a leader or team mechanisms, as well as guidance-oriented measures through policies and other delimitations
	Supervision [25, 26]	Steps and mechanisms for decision-making and monitoring decisions with regard to technology application, such as selection of teams or networks and other mechanisms of interaction between participants
Technology	Technology [27-36]	Security, infrastructures, tool, organizational architecture, and current leaders of open government and programs
	Information Technology [37-44]	dynamic information and user needs, information quality, usability, security issues, incompatibility of technology, complexity of technology, skills and technical experience, and newness of technology are of the concepts of information technology and data.
Technology	Information and Data [45-50]	▪ Protection of focused policies, procedures and recording data quality ▪ Administeration of list of data sources to assess data quality
Culture	Employees' readiness [51]	▪ Employees' readiness, communicational channels, beneficiaries, and the existing public relations and public partnerships
	Factors related to knowledge [42]	▪ Experience in the field of previous reform [professional experience] ▪ Sharing knowledge with members of other domains [group work] ▪ Formal education [education]
	Transparent responsibilities [48-50]	Explaining the tasks and responsibilities to build trust between participants who use the intended project.
	Incentives [42]	Applying various incentives and become known among the public
Culture	Professional experience [51]	Knowledge and expertise related to specific job to work, including professional history, occupational and operational experience, and aducation are considered among the most important issues
	Team work experience [51]	Acquired skills of team to work such as sharing previous knowledge and experience of the individuals who working in the team
	Social media [33]	▪ Development of social media strategy ▪ Increase of media ability
	Changes' management [21]	Efficient projects and change management issues such as transparent responsibilities, good comprehensive project and considering the risks, appropriate control and supervision, organizing resources properly and well-managed partnership between governmental and governmental-private organizations.

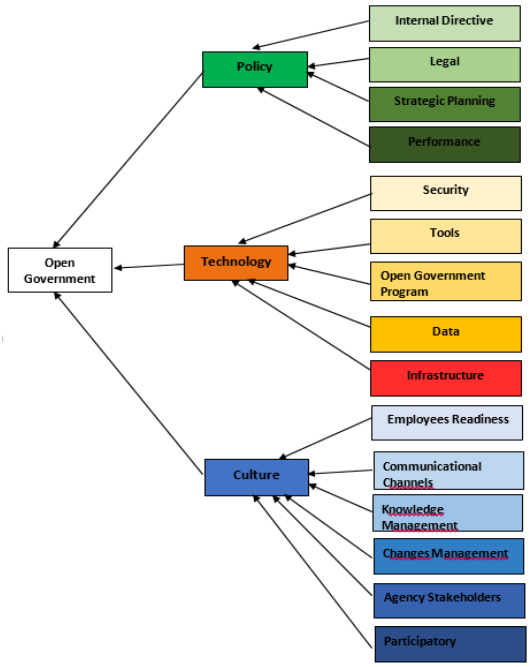

Figure 3. Model stating the relationships between variables

A primary questionnaire was prepared to evaluate the provided model. The questionnaire was evaluated by content validity ratio (CVR) index after evaluating it by the experts on the necessity. As a result, two questions were eliminated. Then the simplicity, clarity, and relevance of the questionnaire's questions were evaluated by content validity index (CVI) test. Eventually the modified questionnaire was distributed. The collected data was placed in KMO and Bartlett's

H1: Policy has an effect on open government. Policy itself has been composed of four parts of internal directive, strategic planning, and legal and performance.

H2: Technology has an effect on open government. Technology itself has been composed of five factors of security, infrastructure, open government program, data, and tools.

H3: Culture has an effect on open government. Culture itself includes six factors of employees' readiness, communicational channels, knowledge management, changes management, agency stakeholders, and participatory. Figure 4 shows the hypotheses.

4. DATA ANALYSIS

Variance-based methods were used given that the sample size is 87 and small, as well as data was not normal. Partial squares approach was used for this purpose. Findings analysis is conducted at two levels of measurement model and structural model. The relationship between the items and the variables is examined in the measurement model, while the relationship between variables is examined in the structural model. Since the legal variable has been intended of composite type, therefore, it has not been examined in tests such as reliability, validity, and divergent and convergent validity .

4. 1. Evaluation of Questionnaire Reliability

Three factors of Cronbach's Alpha, collective reliability, and composite reliability are examined to evaluate the questionnaire reliability. Acceptability criterion in Cronbach's Alpha test for this index, which will show the reliability of reflective measurement model is at least 0.7. Composite reliability index has greater priority compared to Cronbach's Alpha. This is because Cronbach's alpha assumes that observable variables of each measurement model have similar weights. But there is not composite reliability index of this assumption. Acceptable value for this index is between 0.7 and 0.95. In addition, collective reliability represents the generalizability level of the questionnaire's questions, and the acceptable value for it is higher than 0.5 .

Table 2 summarized the evaluation and reliability of questionaire applied in this work.

4. 2. Coefficient of Determination Index Test (R^2)

This test is the main criterion of evaluating endogenous latent variables in the confirmatory path model. It indicates how much the independent variables have been able to predict the behavior of dependent variable. Faqih, and Jaradat [24] described values of 0.67, 0.33, and 0.19 for endogenous latent variables, significant, moderate, and weak, respectively. But if endogenous latent variable is under the effect of a small number (one or two) of exogenous variables, average values of the coefficient of determination are also acceptable. Dwivedi et al. [23] have described values of 0.25, 0.5, and 0.75 for the endogenous variables in the structural path model, weak, moderate, and significant.

Table 3 list out R^2 for the coefficient of determination index.

As can be observed in the above table the value of coefficients of determination is higher than 0.67. So they are placed in significant (strong) group.

4. 3. Overall Fitting of Model's Test

This index is the square of the multiplication of two values of communality values' average and average of coefficients of path determination (R square) and is calculated by the following formula. Values of 0.01, 0.25 and 0.36 have been described weak, moderate and strong respectively. Equation (1): Overall fitting of model

$$\mathrm{GOF} = \sqrt{\overline{\text{communality}} * \overline{\text{R square}}} \quad (1)$$

GOF value in this research is 0.855 and since its value is higher than 0.36, it is described strong.

$$GOF = \sqrt{0.7316 * 0.99976} = 0.855$$

4. 3. Effect Size Index The index is introduced to determine the severity of the relationship between latent variables of the model of this criterion. The values of 0.35, 0.15and 0.02 have been described significant, moderate, and weak, respectively. In other words, this criterion can help to measure the amount of effect of an exogenous variable for an endogenous variable in structural equations modeling. It is calculated based on the following formula in which F2 reflects the effect of a variable on B.

Equation (2): Effect size index

$$F^2 = \frac{R^2_{included} - R^2_{excluded}}{1 - R^2_{excluded}} \quad (2)$$

Coefficient of determination of endogenous variable=$R^2_{included}$

Coefficient of determination of endogenous dimension variable from exogenous variable=$R^2_{excluded}$

The effect of culture, policy, and technology variables on open government was evaluated separately according to the above formula and the following results were obtained. The effect of size index is given in Table 4.

TABLE 2. Evaluation of questionnaire reliability

Variable	Cronbach's alpha	Composite reliability	Collective reliability
Changes' management	0.9075	0.9312	0.7305
Communicational channels	0.8051	0.8735	0.6347
Data	0.9314	0.9480	0.8749
Employees' readiness	0.8918	0.9204	0.6982
Performance	0.8319	0.8824	0.6033
Infrastructure	0.8932	0.9336	0.8234
Internal directive	0.9058	0.9409	0.8416
Knowledge management	0.8858	0.9292	0.8139
Open government program	0.9087	0.9360	0.7854
Participatory activity	0.8228	0.8942	0.7388
Security	0.8692	0.9014	0.6050
Stakeholders	0.8816	0.9274	0.8105
Strategic planning	0.7366	0.8480	0.6574
Tools	0.9322	0.9458	0.7142

TABLE 3. Coefficient of determination index (R^2)

Latent Variable	R^2
Culture	0.999972
Open government	0.999973
Policy	0.999970
Technology	0.999990

TABLE 4. Effect size index

Exogenous variable	*f*
Culture	0.999372881
Technology	0.999257446
Policy	0.99785527

5. CONCLUSION

Accordingly, we evaluate each of these factors in Tax affairs organization in this section.

Policy: The main dimension of policy itself divided into four parts of internal directive, strategic planning, performance, legal. In this regard, it seems that an appropriate context is provided for implementation of open government in terms of policy making in tax affairs organization of Iran country according to the taxpayers' exchange of information guideline, the subject of Article (120) of Fifth Development Plan Act, as well as Articles 169 and 169 frequent direct tax Act, which pave the way for exchange of information between governmental organizations and institutions, as well as people.

Technology: Main dimension of technology itself is divided into five parts of security, infrastructure, tool,

open government program, and data. Internal sectors' of Tax affairs organization in the domain of infrastructure are currently communicating with each other via Internet, as well as with foreign organizations through Internet or offline. Improvement of the quality of current infrastructure must be seriously considered, especially in the counties.

Culture: The main dimension of culture itself is divided into six parts that include participatory activities, Agency's Stakeholders, communicational channels, employees' readiness, changes' management, and knowledge management. In this part, participatory activities are done in various sectors, if necessary, such as formation of working group meetings or think tank. They would be canceled in the case of meeting the requirements or changing the works' priority and they are not permanently.

6. REFERENCES

1. Al-Louzi, B., Iss, B.J.J.o.C. and Computer, "Factors influencing customer acceptance of m-commerce services in jordan", ***Jordan. Journal of Communication and Computer***, Vol. 9, No. 1, (2011), 1424-1436.
2. Al-Shihi, H., Sharma, S.K., Sarrab, M.J.E. and Technologies, I., "Neural network approach to predict mobile learning acceptance", Vol. 23, No. 5, (2018), 1805-1824, doi: 10.1007/s10639-018-9691-9
3. Alalwan, A.A., Baabdullah, A.M., Rana, N.P., Tamilmani, K. and Dwivedi, Y.K.J.T.i.S., "Examining adoption of mobile internet in saudi arabia: Extending tam with perceived enjoyment, innovativeness and trust", Vol. 55, (2018), 100-110, doi: 10.1016/j.techsoc.2018.06.007
4. Alalwan, A.A., Dwivedi, Y.K. and Rana, N.P.J.I.J.o.I.M., "Factors influencing adoption of mobile banking by jordanian bank customers: Extending utaut2 with trust", ***International Journal of Information Management***, Vol. 37, No. 3, (2017), 99-110, doi: 10.1016/j.ijinfomgt.2017.01.002
5. Alalwan, A.A., Rana, N.P., Dwivedi, Y.K., Algharabat, R.J.T. and Informatics, "Social media in marketing: A review and analysis of the existing literature", ***Telematics and Informatics***, Vol. 34, No. 7, (2017), 1177-1190, doi: 10.1016/j.tele.2017.05.008
6. Davis, F.D.J.M.q., "Perceived usefulness, perceived ease of use, and user acceptance of information technology", ***MIS Quarterly: Management Information Systems***, (1989), 319-340, doi: 10.2307/249008
7. Alharbi, S. and Drew, S., "The role of self-efficacy in technology acceptance", in Proceedings of the Future Technologies Conference, Springer. (2018), 1142-1150.
8. Benbasat, I. and Barki, H.J.J.o.t.a.f.i.s., "Quo vadis tam?", ***Journal of the Association for Information Systems***, Vol. 8, No. 4, (2007), 7, doi: 10.17705/1jais.00126
9. Brasel, S.A. and Gips, J.J.J.o.C.P., "Tablets, touchscreens, and touchpads: How varying touch interfaces trigger psychological ownership and endowment", ***Journal of Consumer Psychology***, Vol. 24, No. 2, (2014), 226-233, doi: 10.1016/j.jcps.2013.10.003
10. Budiono, F., Lau, S. and Tibben, W.J., "Cloud computing adoption for e-commerce in developing countries: Contributing factors and its implication for indonesia", in PACIS. (2018), 90.
11. Carlsson, C., Carlsson, J., Hyvonen, K., Puhakainen, J. and Walden, P., "Adoption of mobile devices/services-searching for answers with the utaut", in Proceedings of the 39th annual Hawaii international conference on system sciences (HICSS'06), IEEE. Vol. 6, (2006), 132a-132a.
12. Chong, A.Y.-L.J.E.S.w.A., "Predicting m-commerce adoption determinants: A neural network approach", Vol. 40, No. 2, (2013), 523-530, doi: 10.1016/j.eswa.2012.07.068
13. Chong, A.Y.-L., Chan, F.T. and Ooi, K.-B.J.D.s.s., "Predicting consumer decisions to adopt mobile commerce: Cross country empirical examination between china and malaysia", Vol. 53, No. 1, (2012), 34-43, doi: 10.1016/j.dss.2011.12.001
14. Daraei, A. and Hamidi, H.J.I.j.o.p.h., "An efficient predictive model for myocardial infarction using cost-sensitive j48 model", ***Iranian Journal of Public Health***, Vol. 46, No. 5, (2017), 682.
15. Chong, A.Y.-L., Darmawan, N., Ooi, K.-B. and Lin, B.J.I.J.o.M.C., "Adoption of 3g services among malaysian consumers: An empirical analysis", ***International Journal of Mobile Communications,***, Vol. 8, No. 2, (2010), 129-149, doi: 10.1504/IJMC.2010.031444
16. Chong, J.-L., Chong, A.Y.-L., Ooi, K.-B. and Lin, B.J.I.J.o.M.C., "An empirical analysis of the adoption of m-learning in malaysia", ***International Journal of Mobile Communications,***, Vol. 9, No. 1, (2011), 1-18, doi: 10.1504/IJMC.2011.037952
17. Alvanchi, A., Didehvar, N., Jalilehvand, M., Adami, P. and Shahmir, S.J.I.J.o.E., "Semi-augmented reality, a novel approach to improve customer safety in the pre-sale process of under construction buildings", ***International Journal of Engineering, Transactions A: Basics***, Vol. 34, No. 10, (2021), doi: 10.5829/ije.2021.34.10a.01
18. Lee, G. and Kwak, Y.H., "Open government implementation model: A stage model for achieving increased public engagement", in Proceedings of the 12th Annual International Digital Government Research Conference: Digital Government Innovation in Challenging Times. (2011), 254-261.
19. Dai, H. and Palvia, P., "Factors affecting mobile commerce adoption: A cross-cultural study in china and the united states", (2008), doi: 10.1145/1644953.1644958
20. Hamidi, H. and Mohammadi, K.J.I.J.o.I.I.T., "Modeling fault tolerant and secure mobile agent execution in distributed systems", ***International Journal of Intelligent Information Technologies***, Vol. 2, No. 1, (2006), 21-36, doi: 10.4018/jiit.2006010102
21. Donga, G., Zindiye, S.J.B. and Journal, S.S., "Assessing the acceptance of mobile marketing among south african students", ***Business & Social Sciences Journal***, Vol. 3, No. 1, (2018), 46-57, doi:
22. Duarte, P. and Pinho, J.C.J.J.o.B.R., "A mixed methods utaut2-based approach to assess mobile health adoption", ***Journal of Business Research***, Vol. 102, (2019), 140-150, doi: 10.1016/j.jbusres.2019.05.022
23. Dwivedi, Y.K., Shareef, M.A., Simintiras, A.C., Lal, B. and Weerakkody, V.J.G.I.Q., "A generalised adoption model for services: A cross-country comparison of mobile health (m-health)", Vol. 33, No. 1, (2016), 174-187, doi: 10.1016/j.giq.2015.06.003
24. Faqih, K.M., Jaradat, M.-I.R.M.J.J.o.R. and Services, C., "Assessing the moderating effect of gender differences and individualism-collectivism at individual-level on the adoption of mobile commerce technology: Tam3 perspective", ***Journal of Retailing and Consumer Services***, Vol. 22, (2015), 37-52, doi: 10.1016/j.jretconser.2014.09.006
25. Gao, T.T., Rohm, A.J., Sultan, F. and Pagani, M.J.J.o.B.R., "Consumers un-tethered: A three-market empirical study of consumers' mobile marketing acceptance", ***Journal of Business***

Research, Vol. 66, No. 12, (2013), 2536-2544, doi: 10.1016/j.jbusres.2013.05.046

26. Guo, X., Zhao, Y., Jin, Y. and Zhang, N., "Two-sided adoption of mobile marketing platforms: Towards an integrated conceptual model", in 2010 Ninth International Conference on Mobile Business and 2010 Ninth Global Mobility Roundtable (ICMB-GMR), IEEE. (2010), 474-480.
27. Hamidi, H. and Kamankesh, A.J.I.J.o.I.T.S.R., "An approach to intelligent traffic management system using a multi-agent system", ***International Journal of Intelligent Transportation Systems Research***, Vol. 16, No. 2, (2018), 112-124, doi: 10.1007/s13177-017-0142-6
28. Herrero, Á. and San Martín, H.J.C.i.H.B., "Explaining the adoption of social networks sites for sharing user-generated content: A revision of the utaut2", Vol. 71, No., (2017), 209-217, doi: 10.1016/j.chb.2017.02.007
29. Hew, J.-J., Badaruddin, M.N.B.A., Moorthy, M.K.J.T. and Informatics, "Crafting a smartphone repurchase decision making process: Do brand attachment and gender matter?", ***Telematics and Informatics***, Vol. 34, No. 4, (2017), 34-56, doi: 10.1016/j.tele.2016.12.009
30. Hew, T.-S., Leong, L.-Y., Ooi, K.-B. and Chong, A.Y.-L.J.J.o.C.I.S., "Predicting drivers of mobile entertainment adoption: A two-stage sem-artificial-neural-network analysis", ***Journal of Computer Information Systems***, Vol. 56, No. 4, (2016), 352-370, doi: 10.1080/08874417.2016.1164497
31. Hirschman, E.C.J.J.o.c.r., "Innovativeness, novelty seeking, and consumer creativity", ***Journal of Consumer Research***, Vol. 7, No. 3, (1980), 283-295, doi: 10.1086/208816
32. Hsu, C.-I., Shih, M.-L., Huang, B.-W., Lin, B.-Y. and Lin, C.-N.J.E.S.w.A., "Predicting tourism loyalty using an integrated bayesian network mechanism", Vol. 36, No. 9, (2009), 11760-11763, doi: 10.1016/j.eswa.2009.04.010
33. Huang, L., Mou, J., See-To, E.W., Kim, J.J.J.o.R. and Services, C., "Consumer perceived value preferences for mobile marketing in china: A mixed method approach", ***Journal of Retailing and Consumer Services***, Vol. 48, (2019), 70-86, doi: 10.1016/j.jretconser.2019.02.007
34. Nilchi, A.N., Vafaei, A. and Hamidi, H., "Evaluation of security and fault tolerance in mobile agents", in 2008 5th IFIP International Conference on Wireless and Optical Communications Networks (WOCN'08), IEEE. (2008), 1-5.
35. S., B., B. L. and Mason, "An empirical study of innate consumer innovativeness, personal characteristics, and new-product adoption behavior", ***Journal of the Academy of Marketing Science***, , (2003), 61-73, doi: 10.1177/0092070302238602
36. Imtiaz, S.J.I.J.o.I.C.T. and Convergence, D., "The studies of unified theory of acceptance and use of technology (utaut) in m-commerce context", ***International Journal of Information Communication Technology and Digital Convergence***, Vol. 3, No. 1, (2018), 42-56, doi:
37. Torabi, A., Hamidi, H. and Safaie, N.J.I.J.o.E., "Effect of sensory experience on customer word-of-mouth intention, considering the roles of customer emotions, satisfaction, and loyalty", ***International Journal of Engineering, Transactions C: Aspects***, Vol. 34, No. 3, (2021), 682-699, doi: 10.5829/ije.2021.34.03c.13
38. Jaradat, M.-I.R.M., Faqih, K.M.J.I.J.o.B. and Management, "Investigating the moderating effects of gender and self-efficacy in the context of mobile payment adoption: A developing country perspective", ***International Journal of Business and Management,***, Vol. 9, No. 11, (2014), 147, doi: 10.5539/ijbm.v9n11p147
39. Kalinic, Z., Marinkovic, V.J.I.S. and Management, e.-B., "Determinants of users' intention to adopt m-commerce: An empirical analysis", Vol. 14, No. 2, (2016), 367-387, doi: 10.1007/s10257-015-0287-2
40. Bahrami, L., Safaie, N. and Hamidi, H., "Effect of motivation, opportunity and ability on human resources information security management considering the roles of attitudinal, behavioral and organizational factors. ", ***International Journal of Engineering, Transactions C: Aspects***, (2021), 2624-2635, doi: 10.5829/ije.2021.34.12c.07
41. Khalifa, M. and Shen, K.N.J.J.o.e.i.m., "Explaining the adoption of transactional b2c mobile commerce", ***Journal of Enterprise Information Management,***, (2008), doi: 10.1108/17410390810851372
42. Kim, C., Mirusmonov, M. and Lee, I.J.C.i.h.b., "An empirical examination of factors influencing the intention to use mobile payment", Vol. 26, No. 3, (2010), 310-322, doi: 10.1016/j.chb.2009.10.013
43. Kim, H.-W., Chan, H.C. and Gupta, S.J.D.s.s., "Value-based adoption of mobile internet: An empirical investigation", Vol. 43, No. 1, (2007), 111-126, doi: 10.1016/j.dss.2005.05.009
44. KIR, B. and Altinbaåžak Farã°NA, Ä., "How to increase the participation of customers to location-based mobile marketing: The case of an emerging country turkey", ***International Journal Of Management & Information Technology,***, (2016), 3001–3021, doi: 10.24297/ijmit.v11i5.4687
45. Ktoridou, D., Epaminonda, E. and Vrontis, D., "Technological and cultural aspects of the use of mobile marketing evidence from cyprus", in The 2007 International Conference on Next Generation Mobile Applications, Services and Technologies (NGMAST 2007), IEEE., (2007), 19-28.
46. Kwofie, M. and Adjei, J.K., "Understanding the factors influencing mobile commerce adoption by traders in developing countries: Evidence from ghana", in International Working Conference on Transfer and Diffusion of IT, Springer. (2019), 104-127.
47. Lallmahomed, M.Z., Lallmahomed, N., Lallmahomed, G.M.J.T. and Informatics, "Factors influencing the adoption of e-government services in mauritius", Vol. 34, No. 4, (2017), 57-72, doi: 10.1016/j.tele.2017.01.003
48. Lamarre, A., Galarneau, S. and Boeck, H.J.I.J.o.L.T.i.C., "Mobile marketing and consumer behaviour current research trend", Vol. 3, No. 1, (2012), 201, doi:
49. Leong, L.-Y., Ooi, K.-B., Chong, A.Y.-L. and Lin, B.J.I.J.o.M.C., "Influence of individual characteristics, perceived usefulness and ease of use on mobile entertainment adoption", ***Journal of Mobile Communications***, Vol. 9, No. 4, (2011), 359-382, doi: 10.1504/IJMC.2011.041141
50. Liébana-Cabanillas, F., Marinković, V. and Kalinić, Z.J.I.J.o.I.M., "A sem-neural network approach for predicting antecedents of m-commerce acceptance", Vol. 37, No. 2, (2017), 14-24, doi: 10.1016/j.ijinfomgt.2016.10.008
51. Liébana-Cabanillas, F., Marinkovic, V., de Luna, I.R., Kalinic, Z.J.T.F. and Change, S., "Predicting the determinants of mobile payment acceptance: A hybrid sem-neural network approach", Vol. 129, (2018), 117-130, doi: 10.1016/j.techfore.2017.12.015

Persian Abstract

چکیده

امنیت امروزه با توجه به تلاش دولت جمهوری اسلامی ایران در راستای توسعه دولت الکترونیک همچنین سیاست‌گذاری‌های صورت گرفته به‌منظور اشتراک‌گذاری، استفاده مجدد و نشر آزاد اطلاعات، به نظر می‌رسد بستر مناسبی برای بررسی دولت‌باز در کشور ایران فراهم‌شده است. در این پژوهش ابعاد دولت‌باز در سازمان امورمالیاتی کشور ایران به‌عنوان یک سازمان دولتی بررسی می‌شود. بدین منظور پس از بررسی طرح دولت‌باز در کشورهای ایالات‌متحده آمریکا، اتریش، مکزیک و مصاحبه‌های صورت گرفته با خبرگان در سه حوزه فناوری اطلاعات، اجرایی و حقوقی سه عامل اصلی سیاست، فرهنگ و تکنولوژی شناسایی شد که چهار عامل فرعی دستورالعمل داخلی، حقوقی، برنامه‌ریزی استراتژیک، اجرایی برای سیاست و پنج عامل فرعی اجرایی، امنیت، ابزار، برنامه دولت‌باز، داده، زیرساخت برای تکنولوژی و شش عامل فرعی آمادگی کارکنان، کانال‌های ارتباطی، مدیریت دانش، مدیریت تغییرات، ذینفعان سازمان و فعالیت‌های مشارکتی برای فرهنگ در نظر گرفته شد. درنهایت الگوی مذکور پس از استخراج اطلاعات پرسشنامه‌های توزیع‌شده، بر اساس رویکرد حداقل مربعات جزئی مورد ارزیابی قرار گرفت و در سطح قوی مورد تائید قرار گرفت.

International Journal of Engineering

Journal Homepage: www.ije.ir

Prioritization of Transmission Network Components Based on their Failure Impact on Reliability of Composite Power Systems

M. Abbasghorbani*

Electrical Engineering Department, Shomal University, Amol, Iran

PAPER INFO

Paper history:
Received 24 November 2020
Received in revised form 13 November 2021
Accepted 17 November 2021

Keywords:
Reliability Centered Maintenance
Reliability Evaluation
Monte Carlo Simulation

ABSTRACT

This paper proposes an efficient method to identify the importance of transmission network components from the network's reliability perspective. The proposed method is able to reveal the weak points of the network and can be employed as useful tool by power system planners to identify where investments should be made to increase the overall system reliability. The proposed approach has two main stages, including evaluation of the network contingency states and a sensitivity analysis which shows the link between reliability of each component and overall system reliability. Unlike the similar methods in this area and with the help of two reasonable simplifications, the proposed method can be employed to real transmission networks with acceptable computational burden. The proposed method is implemented on two test systems including the IEEE Reliability Test System (IEEE RTS) and the Roy Billinton Test System (RBTS). The obtained results demonstrate the efficiency of the proposed approach.

***doi**: 10.5829/ije.2022.35.03c.02*

NOMENCLATURE

$\boldsymbol{T}$	Line flow vector	L_i	Load at bus i
$\boldsymbol{T^{max}}$	Rating vector for lines	$IEAR_i$	Interrupted energy assessment rate at bus i ($/kWh)
$\boldsymbol{A}$	Matrix relating the line flows to the power injections at buses	NL	Number of load buses
$\boldsymbol{PG}$	Generation output	NLS	Number of load segments of the LDC
$\boldsymbol{PG^{max}}$	Upper limit for generation output	T_j	Time duration of each load segment of the LDC
$\boldsymbol{PG^{min}}$	Lower limit for generation output	$P(e_k)$	Available probability of set e_k
AP_i	Available power at load bus i	$Q(\bar{e}_k)$	Unavailable probability of set $\bar{e}_k$
ENS	Energy Not Served	$EENS$	Expected Energy Not Served

1. INTRODUCTION

Due to the deregulation of the power systems and emergence of the electricity markets, it is desirable to further improve reliability and availability of the power systems in order to increase the competitiveness of the electricity markets. In this regards, reliability and risk assessments are of great concern for the utilities and considerable researches have been conducted in this area in the past decades [1-5].

New deregulated environment also forces utilities to reduce overall costs. Maintenance costs are considered as a large part of the operation costs. However, reducing maintenance activities can lead to higher damages caused by an increased number of forced outages due to poor maintenance [6, 7]. Therefore, it would be a good solution to rank the network components based on their needs for maintenance and conduct the maintenance budget to those components that are critical for network.

In maintenance planning, network components can be ranked by condition and importance indices [8-10] .The condition index reflects the physical health of each component and can be determined by condition indicators such as type, age and operating history. On the other hand, importance index is associated with the risk imposed on the system due to the outage of each

*Corresponding Author Institutional Email: ghorbani@shomal.ac.ir
(M. Abbasghorbani)

Please cite this article as: M. Abbasghorbani, Prioritization of Transmission Network Components Based on their Failure Impact on the Reliability of Composite Power Systems, ***International Journal of Engineering, Transactions C: Aspects*** Vol. 35, No. 03, (2022) 502-509

component. This paper is focused on identifying the importance index of the transmission components which is related to their position in the network.

Although the determination of network critical component plays a very important role in the asset management methods, a limited number of researches have addressed this issue in the transmission network. Due to the mesh structure, complex configuration and great number of components in the transmission network, a method is needed capable of prioritizing the equipment within an acceptable time frame and with logical computations volume.

For instance, the components of common substations have been prioritized in literature [11] without considering the effect of transmission lines or generating units. Also, Hilber and Bertling [12] and Hilber et al. [13] proposed a number of indexes to rank the components of power distribution networks according to their outage costs. These approaches are suitable for distribution networks which have radial configurations and could not be applied to transmission networks.

Implementing the methods proposed by Dehghanian et al. [14] and Gharakheili e al. [15] require access to the experts with deep information about the system. Given that the transmission network is located in a large geographical area with a great number of components, it is challenging to find specialists who have accurate information about all the components and thus limits the possibility of using these methods. The effect of substations' components failure on the prioritization process of network equipment has been considered in a number of studies [10, 16-18] .However, in practice, implementing these methods for real networks with a large number of substations having different layouts will be a very complicated and time consuming task. Moreover, by literture review [10, 16-19] , the enumeration method has been used to investigate the possible network contingencies which in real networks can dramatically prolong the computation time and limit the application of these methods. For instance, Setreus et al. [17] investigated all first- and second-order contingencies. However, transmission networks are usually reliable to the outage of one or two components and major portion of expected energy not served belongs to the higher order contingencies. Moreover, using enumeration method to evaluate all of the higher order contingencies can be very time consuming in large transmission networks.

To cover the above challenges, this paper provides an effective way to determine the importance of transmission network components over a reasonable period of time. To reduce the computational burden, two assumptions have been considered in this paper. First of all, failure of substation components can be taken into account by increasing the unavailability of the lines or generating units, connected to the substation. Since, the substation components failure can lead to the loss of transmission lines or generating units. Hence, in general and according to consultation with the network repair and maintenance specialists, it can be deduced that those substation components located on more important transmission lines and generating units of the network, are of high prominence in the network. Therefore, only by determining the priority of the lines and generating units, one can perceive the importance of substation components with an acceptable approximation and it is not necessary to model all network substations with all the corresponding details. In the next step, the Monte-Carlo simulation method has been employed to investigate the probable network contingencies. In this method, the probable network contingencies are selected based on the failure probability in each network component. So, unlike the enumeration method, there is no need to check all possible events up to a specific order (for example, 3, 4 or more). Based on these two simplifications and in order to reveal the weak points of the network, the proposed approach could be applied in large networks.

The rest of the paper is organized as follows. The Monte-Carlo based method for evaluation of the reliability of the composite power system is briefly presented in section 2. Section 3 provides a detailed description of the proposed approach to determine the importance of network components. The numerical results obtained from simulations on two test systems IEEE RTS and RBTS and the discussions are presented in section 4. Finally, a conclusion is drawn in section 5.

2. COMPOSITE POWER SYSTEM RELIABILITY EVALUATION APPROACH

In the electric power systems, Monte-Carlo simulations are employed to estimate the reliability indices by simulating the actual process and random behavior of the system. The procedure and details of the composite system risk evaluation can be found in literture [1]. In this paper, in order to evaluate the risk of the composite power system, a computer routine has been developed in MATLAB based on a Monte Carlo-based approach. The developed approach is summarized in three steps, as expressed below.

2. 1. State Sampling In order to determine the state (failure or normal) of the network components, random numbers, uniformly distributed in [1], are generated and assigned to each component. Then, comparing the random number to the component's unavailability, the component is considered to be failed if the random number is less than the component's unavailability; otherwise it is assumed in normal state. This step is repeated for all components of the transmission network.

If there is any failed component, step 2 must be approached otherwise step 1 must be repeated.

2. 2. Contingency State Analysis Once system state is obtained, as can be seen in Equation (1) a linear programming optimal power flow is solved to reschedule the generating units, eliminate line overloading and avoid load shedding if possible or maximize the total load which can be met on each load bus.

In Equation (1), the priority for supplying loads in each contingency state is considered by their IEAR. Furthermore, loads are modelled using multi-step annual Load Duration Curves (LDC) [1].

$$\begin{aligned} &\max \sum_{i=1}^{NL} AP_i \times IEAR_i \\ &s.t. \\ &\quad \mathbf{T} = \mathbf{A} \times (\mathbf{PG} - \mathbf{AP}) \\ &\quad \mathbf{PG}^{\min} \le \mathbf{PG} \le \mathbf{PG}^{\max} \\ &\quad AP_i \le L_i \\ &\quad |\mathbf{T}| \le \mathbf{T}^{\max} \end{aligned} \tag{1}$$

The annual energy not served due to the contingency state k, can be obtained by Equation (2).

$$ENS_k = \sum_{i=1}^{NL} \sum_{j=1}^{NLS} (L_{ij} - AP_{ij}) \times T_j \tag{2}$$

where, i and j represent the index of load bus and load segment in the corresponding LDC, respectively.

2. 3. Quantification of EENS Assuming that the outages of the transmission components are independent, the occurrence probability of the contingency state k can be calculated using Equation (3) [20, 21].

$$Prob_k = P(e_k) \times Q(\bar{e}_k) \tag{3}$$

where, e_k and $\bar{e}_k$ are sets of elements of contingency state k which are in service and on outage, respectively.

The *EENS* due to the occurrence of the k^{th} contingency state is expressed by

$$EENS_k = Prob_k \times ENS_k \tag{4}$$

The total EENS for the composite power system can be obtained by aggregation of the EENS values of all contingency states.

3. IMPORTANCE INDEX OF NETWORK COMPONENTS

The importance of each network component is related to its position in the network structure. In order to determine the importance of each component, the following two stages were considered. Moreover, the flowchart of the proposed approach is illustrated in Figure 1.

3. 1. Contingency States Analysis In the first stage, the Monte-Carlo approach (based on the procedure described in section 2) is employed to select and analyze the contingency states of the network. The procedure is described by the following steps.

Step 1. Choose a state for the network by determining the state (normal or failure) of all components, according to the state sampling procedure presented in section 2.

Step 2. Regarding to the selected state, run the optimal power flow presented in Equation (1), and calculate the ENS for the selected contingency state using Equation (2).

Step 3. If the ENS for the selected state is not zero, save the state and go back step 1. Steps 1-3 are repeated for a predefined number of iterations.

3. 2. Sensitivity Analysis for Ranking the Network Components After performing the aforementioned three steps in section 3.1, a database is formed that contains the contingency states which result in load curtailment. In order to determine the importance index of the network components, the following basic idea is applied:

A component is of higher important if a specific increase in its failure rate results in higher increase in the overall expected energy not served, compared to another component. Based on this idea, the rank of each network component can be obtained based on the following steps.

Step 1. For each contingency state in the formed database, calculate the occurrence probability and EENS by Equations (3) and (4), respectively. Then, aggregate the EENS of the contingency states to obtain the overall EENS of the transmission network ($EENS_{Base}$).

Step 2. Increase the failure rate of the i^{th} component by a small value, e.g. ξ. Update the occurrence probability of the contingency states and recalculate the new EENS ($EENS_{New}$) of the composite power system similar to step 1.

Step 3. Calculate the importance index for the i^{th} component by subtracting the new EENS ($EENS_{New}$) of the transmission network from the $EENS_{Base}$ and dividing the result by ξ. Do steps 2 and 3 for all components of the network.

4. SIMULATION RESULTS AND DISCUSSION

In order to provide more insight into the presented approach and assessment of its performance, two test systems, namely RBTS and IEEE RTS were considered to perform simulations.

4. 1. Roy Billinton Test System (RBTS) The single line diagram of the RBTS is shown in Figure 2. It includes 9 lines and 11 generating units. The system peak load is 185 MW and the total capacity of the generating

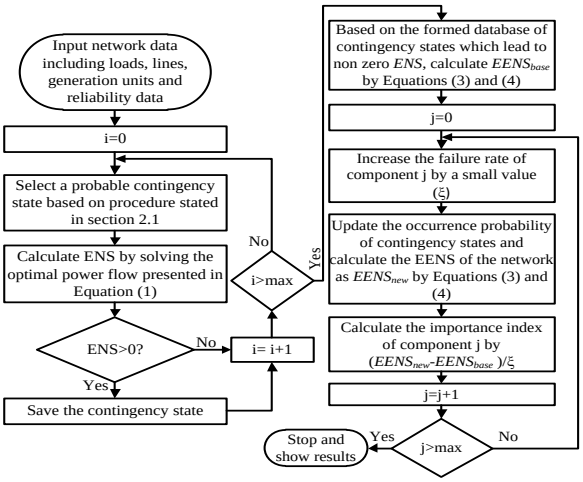

Figure 1. Flowchart of the proposed approach to determine the importance index of network components

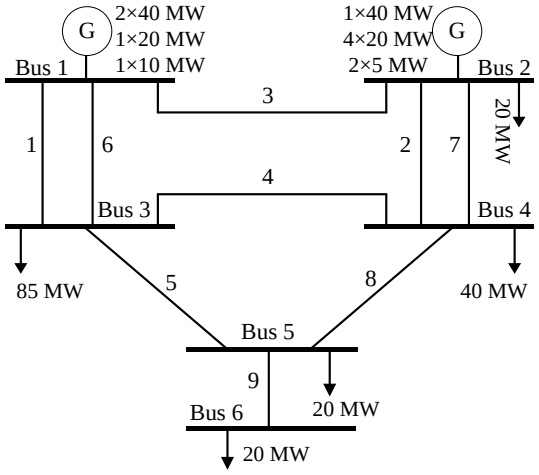

Figure 2. Single line diagram of the RBTS

units is 240 MW. The other network data such as failure and repair rate of each component as well as the generation units and transmission lines data are provided by Billinton et al. [22].

Contingency state analysis: Based on the presented approach in section 3, a contingency states analysis is performed in the RBTS. In this analysis the Monte-Carlo approach is repeated for 4000,000 iterations [23] to select and evaluate highly probable contingency states of the system and save those resulting in the load shedding.

It is worth noting that in both test systems, the priority order of the load buses for load curtailment was determined by the *IEAR*, which can be found in literature [23]. The loads on the load buses were modelled by nine-step LDC. The steps of the LDC and their time durations are presented in Table 1.

Using the state sampling method presented in section 2, 1103 distinct states were selected after 4000,000 iterations, among them there were 617 contingency states which led to the load curtailment. The overall EENS of the network was 148.8 MWh/year. The program was executed on a machine with Core i7 3.5 GHz CPU and 8 GB of RAM. The computation time was 2.748 mins.

Table 2 summarizes the contingency states which led to the load curtailment based on the number of failed components in each state. The contribution of each group of contingencies to the EENS of the system is also presented in Table 2. As can be seen in Table 2, there is a first-order contingency in the RBTS which has resulted in load shedding contributed to 70.54 percent of the EENS of the RBTS. The first-order contingency corresponds to the outage of line 9. Based on the presented results in Table 2, higher order contingency states have lower contribution to the EENS of the RBTS owing to their low occurrence probabilities.

TABLE 1. LDC data

LDC steps	Time duration (in hour of year)
1	19
0.95	96
0.9	314
0.85	656
0.8	1445
0.7	2027
0.6	1883
0.5	1977
0.4	319

The contingency states, leading to load shedding, have been also listed in Table 3 based on the type of the failed components. For instance, there are 17 contingency states which solely include failed transmission lines, constituting the major portion (72.35%) of the EENS in the RBTS. Hence it can be inferred that the major problem of the RBTS is related to the transmission lines.

TABLE 2. Contingency states grouping based on the number of failed components

No. of failed component	No. of contingency states	Contribution to the EENS of the system
1	1	70.54%
2	53	21.79%
3	367	7.14%
4	184	0.52%
5	12	0.002%

TABLE 3. Contingency grouping states based on the failed components

The failed components	No. of contingency states	Contribution to the EENS of the system
Line	17	72.35%
Generating unit	244	11.50%
Generating unit + Line	356	16.14%

The effect of each contingency state on the EENS is shown in Figure 3. As an example, 70.54 percent of the EENS is associated with the outage of line 9. As depicted in Figure 2, due to the radial configuration of the network, the outage of line 9 directly leads to the disconnection of the load bus 6. In the RBTS, outage of line 9 is much more important than the other contingency states. Therefore, for better illustration Figure 3 has two vertical axes. The left one belongs to outage of line 9 and the other contingency states is shown on the right vertical axis.

Ranking of the network components: The rank of the lines and generating units was determined based on the sensitivity analysis approach described in section 3. The importance index of the RBTS components is illustrated in Figure 4.

As shown in Figure 4, line 9 is the most important component in the RBTS. Similar to Figure 3, for better clarification, the importance index of line 9 is shown on a separate vertical axis (right one) and the importance index of the other components are shown on the left vertical axis. Followed by line 9, it can be seen in Figure 4 that generating units 11, 3 and 4 are more important than the other components. It must be noted that these units are the largest units in network, having the capacity of 40 MW. Generating units 3 and 4 are placed on bus 1 and generating unit 11 is mounted on bus 2.

4. 2. IEEE Reliability Test System (IEEE RTS)

The single line diagram of the IEEE RTS is illustrated in Figure 5. This test system is composed of 24 buses, 38 transmission lines and 32 generating units. The peak load in the system reaches 2850 MW while the total installed generating capacity amounts to 3405 MW. Detailed network data including reliability data for each component and the generation and transmission data can be obtained from literature [24].

Contingency state analysis*:* In this case study, the Monte-Carlo approach was repeated for 1,000,000 iterations [23] and highly probable contingency states of the system were selected and evaluated and those resulting in load shedding were saved. Utilizing the state sampling method described in section 2, after 1,000,000 iterations 37,697 distinct states were selected and among these states there were 16,683 contingency states which caused load curtailment. The overall EENS of the IEEE RTS was obtained as 2318.22 MWh/year. The computation time for this case study was 16.61 min.

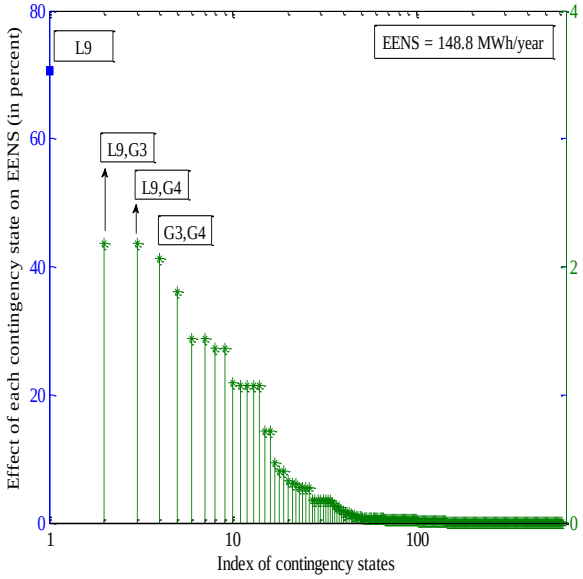

Figure 3. Impact of each contingency state on the EENS (in percent)

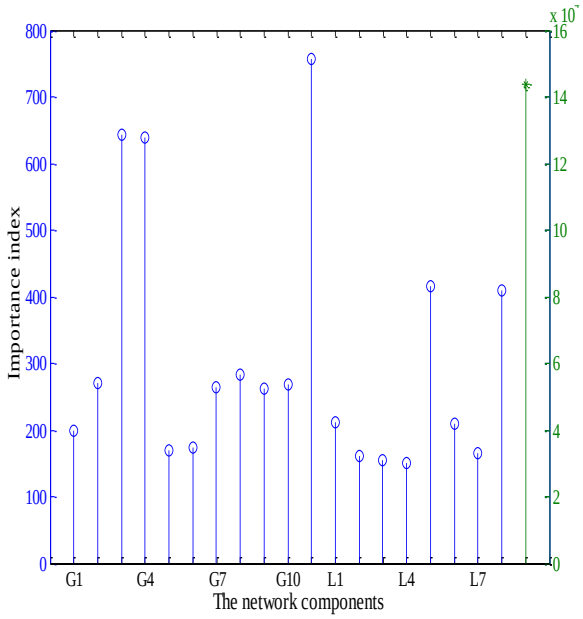

Figure 4. Importance index of lines and generating units in the RBTS

Table 4 summarizes the contingency states with the same number of failed components. The contribution of each group of the contingencies to the EENS of the system is also presented in this table. Based on the information given by Table 4, there is no first-order contingency which results in the load shedding. In other words, the RTS is reliable to the outage of one line or one generating unit. Moreover, the contribution of the second-order contingencies to the EENS is not considerable (6.18 percent). Therefore, as shown in Table 4, the major part

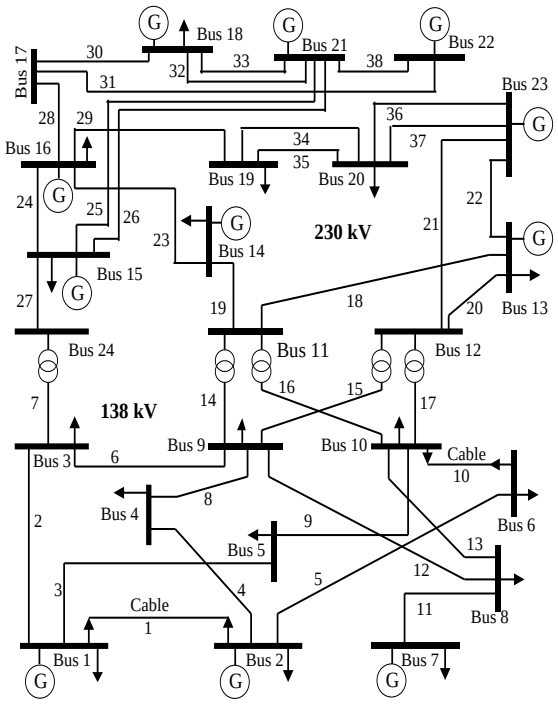

Figure 5. Single line diagram of the RTS

TABLE 4. Contingency states grouping based on the number of failed components

No. of failed component	No. of contingency states	Contribution to the EENS of the system
1	0	0%
2	13	6.18%
3	836	30.42%
4	6620	44.29%
5	6756	18.03%
6	2037	1.05%
7	361	0.03%
8	60	0.00%

of the EENS in the IEEE RTS is associated with the third- and fourth-order contingencies.

In order to provide more insight into efficiency of the proposed method, it's worth estimating the simulation time if the enumeration method was considered to evaluate the contingency states. As mentioned, in proposed method, it takes 16.61 min to simulate 37697 distinct states. While considering enumeration technique as alternative method leads to 974120 states (including one to four components in failure mode) which must be evaluated. Obviously, this will take a very long time. Moreover, this problem can be much more acute in real transmission networks with hundreds of lines and generating units.

The contingency states which resulted in load shedding are summarized in Table 5 based on the type of the failed component. For instance, there are 14,916 contingency states which solely include failed generating units, majorly contributing to the EENS of the IEEE RTS (99.68%). Furthermore, lines outages have negligible impact on the EENS of the network. Therefore, it can be concluded that the major problem of the IEEE RTS is associated to the generating units and the IEEE RTS is very reliable against transmission lines outages.

The information regarding impact of each contingency state on the EENS is depicted in Figure 6. For instance, more than seven percent of the EENS has been imposed due to simultaneous outages of the generating units 22, 23 and 32. Generating units 22, 23 and 32, located on buses 18, 21 and 23, respectively are the largest units in network, having the capacities of 400, 400 and 350 MW, respectively.

Ranking of the lines and generating units: The sensitivity analysis technique described in section 3 is used to rank the transmission lines and generating units. Based on the obtained results, importance indices of the IEEE RTS components are illustrated in Figure 7.

In the IEEE RTS, generating units are more important than transmission lines. Hence, for better illustration, in Figure 7 the importance indices of lines and generating units are shown on right and left vertical axis respectively. Based on this figure, generating units 22, 23

TABLE 5. Contingency states grouping based on the failed components

The failed components	No. of contingency states	Contribution to the EENS of the system
Line	2	0.00%
Generating unit	14916	99.68%
Generating unit + Line	1765	0.32%

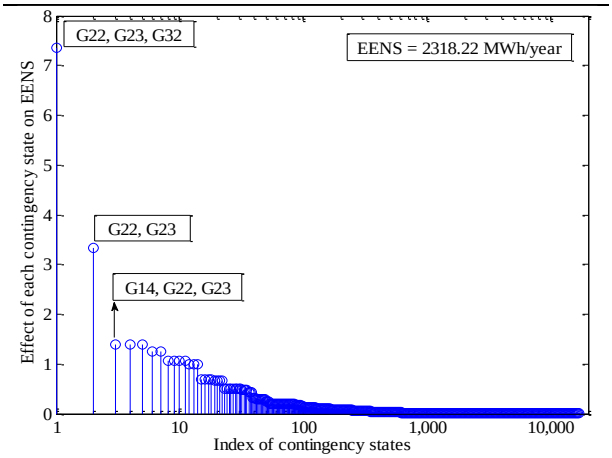

Figure 6. Impact of each contingency state on the EENS (in percent)

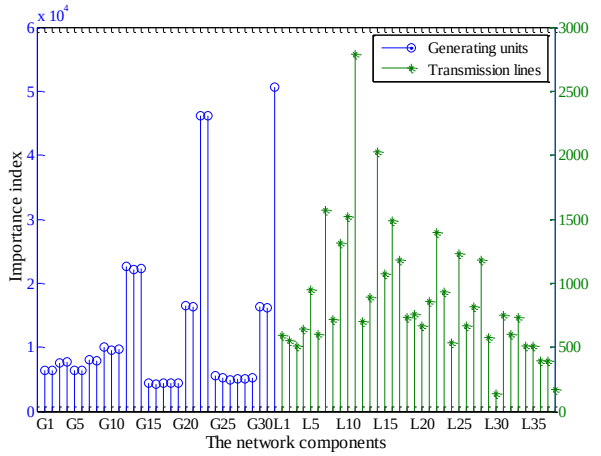

Figure 7. Importance index of lines and generating units in the RTS

and 32 are of higher importance from network perspective, comparing to the other components. As mentioned earlier, these units possess largest capacities within the network. Moreover, line 11 is the most important transmission line in the network. As can be seen in Figure 5, outage of line 11 results in isolation of bus 7. Hence, all the 300 MW generation capacity of bus 7 will be lost.

5. CONCLUSION

This paper proposed a probabilistic approach for ranking network components, based on their importance from the network perspective. The proposed approach is established based on the Monte-Carlo based techniques which are commonly employed for evaluating the reliability of the composite power systems. Hence, the proposed approach can be easily applied to the real transmission networks in a straightforward manner to identify the critical components within the system. The application of the proposed methodology was demonstrated through two case studies on IEEE RTS and the RBTS. Based on the findings in both case studies, the proposed approach can find the most influential components in the context of power system reliability. Moreover, the proposed method is able to reveal the weak points of the network and serve as a useful tool for the power system planners to identify where investments should be made to increase the overall system reliability.

6. REFERENCES

1. Li, W., "Risk assessment of power systems, models, methods and applications", (2005),
2. Valinejad, J., Oladi, Z., Barforoushi, T. and Parvania, M.J.I.J.o.E., "Stochastic unit commitment in the presence of demand response program under uncertainties", ***International Journal of Engineering Transactions B: Applications***, Vol. 30, No. 8, (2017), 1134-1143, doi: 10.5829/ije.2017.30.08b.04
3. Sedighi, A.R. and Hamidian, M.J.I.J.o.E., "A novel method for implementing of time-of-use to improve the performance of electric distribution systems: A case study", ***", International Journal of Engineering Transactions C: Aspects***, Vol. 30, No. 3, (2017), 357-365, doi: 10.5829/idosi.ije.2017.30.03c.05
4. Billinton, R., Fotuhi-Firuzabad, M. and Bertling ,L.J.I.T.o.P.S., "Bibliography on the application of probability methods in power system reliability evaluation 1996-1999", ***IEEE Transaction Power System***, Vol. 16, No. 4, (2001), 595-602, doi: 10.1109/MPER.2001.4311539
5. Basiri, M.H., Sharifi, M.R. and Ostadi, B.J.I.J.o.E., "Reliability and risk assessment of electric cable shovel at chadormalu iron ore mine in iran", ***International Journal of Engineering Transactions A: Basic***, Vol. 33, No. 1, (2020), 170-177, doi: 10.5829/ije.2020.33.01a.20
6. Babaeimorad, S., Fattahi, P. and Fazlollahtabar, H., "A joint optimization model for production scheduling and preventive maintenance interval", ***International Journal of Engineering Transactions B: Applications***, Vol. 34, No. 11, (2021), 2508-2516, doi: 10.5829/ije.2021.34.11b.13
7. Fu, J., Nunez, A. and Schutter, B.D., "A short-term preventive maintenance scheduling method for distribution networks with distributed generators and batteries", ***IEEE Transaction Power System***, Vol. 36, No. 3, (2021), 2516-2531, doi: 10.1109/59.76730
8. Balzer, G.J.C., "Selection of an optimal maintenance and replacement strategy of hv equipment by a risk assessment process",(2006), doi :
9. Chan, T., Liu, C.-C. and Choe, J.-W., "Implementation of reliability-centered maintenance for circuit breakers", in IEEE Power Engineering Society General Meeting, 2005, IEEE. (2005), 684-690.
10. Abbasghorbani, M., Mashhadi, H.R., Damchi, Y.J.I.G., Transmission and Distribution, "Reliability-centred maintenance for circuit breakers in transmission networks", ***IET Generation, Transmission and Distribution***, Vol. 8, No. 9, (2014), 1583-1590, doi: doi:10.1049/iet-gtd.2013.0530
11. Espiritu, J.F., Coit, D.W. and Prakash, U.J.E.P.S.R., "Component criticality importance measures for the power industry", ***Electric Power System Research***, Vol. 77, No. 5-6, (2007), 407-420, doi: 10.1016/j.epsr.2006.04.003
12. Hilber, P. and Bertling, L., "Component reliability importance indices for electrical networks", in 2007 International Power Engineering Conference (IPEC 2007), IEEE. (2007), 257-263.
13. Hilber, P., Miranda, V., Matos, M.A. and Bertling, L.J.I.T.o.P.S., "Multiobjective optimization applied to maintenance policy for electrical networks", ***IEEE Transaction Power System***, Vol. 22, No. 4, (2007), 1675-1682, doi: 10.1109/TPWRS.2007.908468
14. Dehghanian, P., Fotuhi-Firuzabad, M., Bagheri-Shouraki, S. and Kazemi, A.A.R.J.I.S.J., "Critical component identification in reliability centered asset management of power distribution systems via fuzzy ahp", ***IEEE Systems Journal***, Vol. 6, No. 4, (2011), 593-602, doi: 10.1109/JSYST.2011.2177134
15. Gharakheili, M.A., Fotuhi-Firuzabad, M. and Dehghanian, P.J.I.S.J., "A new multiattribute decision making support tool for identifying critical components in power transmission systems", ***IEEE Systems Journal***, Vol. 12, No. 1, (2015), 316-327, doi: 10.1109/JSYST.2015.2500262
16. Abbasghorbani, M., Mashhadi, H.R.J.I.G., Transmission and Distribution, "Circuit breakers maintenance planning for composite power systems", ***IET Generation, Transmission and Distribution***, Vol. 7, No. 10, (2013), 1135-1143, doi: 10.1049/iet-gtd.2012.0484

17. Setreus, J., Hilber, P., Arnborg, S. and Taylor, N.J.I.T.o.P.S., "Identifying critical components for transmission system reliability", ***IEEE Transaction Power System***, Vol. 27, No. 4, (2012), 2106-2115, doi: 10.1109/TPWRS.2012.2188144
18. Fattaheian-Dehkordi, S., Fotuhi-Firuzabad, M. and Ghorani, R.J.I.T.o.P.S., "Transmission system critical component identification considering full substations configuration and protection systems", ***IEEE Transaction Power System***, Vol. 33, No. 5, (2018), 5365-5373, doi: 10.1109/TPWRS.2018.2797895
19. Ghorani, R., Fotuhi-Firuzabad, M., Dehghanian, P., Li, W.J.I.G., Transmission and Distribution, "Identifying critical components for reliability centred maintenance management of deregulated power systems", ***IET Generation, Transmission and Distribution***, Vol. 9, No. 9, (2015), 828-837, doi: 10.1049/iet-gtd.2014.0361
20. Choi, J ,.Billinton, R., Futuhi-Firuzabed, M.J.I.P.-G., Transmission and Distribution, "Development of a nodal effective load model considering transmission system element unavailabilities", ***IEE Proceedings- Generation, Transmission and Distribution***, Vol. 152, No. 1, (2005), 79-89, doi: 10.1049/ip-gtd:20041132
21. Choi, J., Tran, T., Kwon, J., Thomas, R., Mount, T., Billinton, R.J.I.g., transmission and distribution, "Nodal probabilistic production cost simulation considering transmission system unavailabilty", ***IET Generation, Transmission and Distribution***, Vol. 2, No. 1, (2008), 32-42, doi: 10.1049/iet-gtd:20060393
22. Billinton, R., Kumar, S., Chowdhury, N., Chu, K., Debnath, K.,, Goel, L., Khan, E., Kos, P., Nourbakhsh, G. and , O.-A., J., , "A reliability test system for educational purpose", ***IEEE Transaction Power System***, Vol. 4, No. 3, (1989), 1238-1244, doi: 10.1109/59.76730
23. Yang, H., "Incorporating station related maintenance and aging outages in composite system reliability evaluation ,(2005)
24. IEEE APM Subcommittee, "The ieee reliability test system-1996", ***IEEE Transaction Power System,***, Vol. 14, No. 3, (1999), 1010-1020, doi: 10.1109/59.780914

Persian Abstract

چکیده

این مقاله یک روش کارآمد برای تعیین اهمیت هریک از تجهیزات شبکه انتقال ارائه می‌کند. روش پیشنهادی قادر به شناسایی نقاط ضعف شبکه قدرت می‌باشد و می‌تواند به عنوان ابزاری مفید در بخش برنامه‌ریزی شبکه مورد استفاده قرار گیرد. در واقع به کمک روش پیشنهادی این مقاله شرکت‌های برق منطقه‌ای قادر خواهند بود برای رسیدن به بهترین قابلیت اطمینان ممکن، منابع مالی محدود خود را به سمت تجهیزاتی سوق دهند که از اهمیت بیشتری برای شبکه برخوردار است. روش پیشنهادی از دو بخش اصلی تشکیل شده است. بخش اول شامل ارزیابی حوادث احتمالی شبکه است و در بخش دوم از آنالیز حساسیت برای تعیین ارتباط بین قابلیت اطمینان هر تجهیز با قابلیت اطمینان کل شبکه استفاده شده است. بر اساس دو ساده‌سازی صورت گرفته، روش پیشنهادی مقاله قادر به پیاده‌سازی در شبکه‌های واقعی است. عملکرد روش پیشنهادی بر روی دو شبکه انتقال نمونه RTS و RBTS مورد بررسی قرار گرفته است. نتایج بدست آمده کارایی روش پیشنهادی را تایید می‌کند.

International Journal of Engineering

Journal Homepage: www.ije.ir

Sugarcane Molasses as a Cost-effective Carbon Source on *Arthrospira maxima* Growth by Taguchi Technique

N. Mirhosseini[a], R. Davarnejad*[a], A. Hallajisani[b], E. Cano-europa[c], O. Tavakoli[d]

[a] *Department of Chemical Engineering, Faculty of Engineering, Arak University, Arak, Iran*
[b] *Biofuel Research Laboratory, Caspian Faculty of Engineering, College of Engineering, University of Tehran, Tehran, Iran*
[c] *Laboratorio de Metabolismo, Departamento de Fisiología, Escuela Nacional de CienciasBiológicas, InstitutoPolitecnico Nacional, Código Postal 07738 Ciudad de México, Mexico*
[d] *School of Chemical Engineering, College of Engineering, University of Tehran, Tehran, Iran*

PAPER INFO

Paper history:
Received 10 October 2021
Received in revised form 4 December 2021
Accepted 8 December 2021

Keywords:
Cost Effective
Growth
Microalgae
Statistical Analysis
Sugarcane Molasses

ABSTRACT

In this research, a new cost-effective carbon source of medium was provided in terms of high-efficiency growth from *Arthrospira maxima*. Sugarcane molasses was used in two different modes (alternative and additive) at four different concentrations (0, 0.5, 1.0 and 1.5 gL^{-1}) to determine the effect of new carbon source versus its standard carbon source of Zarrouk's medium ($NaHCO_3$). The experimental results were analyzed by Taguchi L8 method as a statistical technique. The highest biomass production obtained when sugarcane molasses was added as an alternative source, which was 5.31 times higher than the usual Zarrouk's media. Furthermore, final biomass concentration increased with increasing molasses concentration from 0 to 1.5 gL^{-1} in this group. At highest concentration, phycocyanin (at 0.11 and 0.12 gL^{-1}), allophycocyanin (at 0.13 and 0.12 gL^{-1}), carotenoids (at 2340 and 2535 mgL^{-1}), chlorophyll a (at 23.83 and 24.83 mgL^{-1}), and chlorophyll b (at 0.343 and 2.99 mgL^{-1}) obtained when molasses were added as an additive and alternative sources, respectively. Finally, the replacement of standard carbon sources of medium with sugarcane molasses had the potential possibility in order to reduce the production costs of *Arthrospira maxima* growth.

***doi**: 10.5829/ije.2022.35.03c.03*

NOMENCLATURE

A	Absorbance at different wavelength	DT	Doubling time
APC	Allophycocyanin	μ_{max}	Maximum specific growth rate
$C_{w.d}$	Concentration of *Arthrospira maxima* by dry-weight	P	Productivity
$C_{w.dt}$	Biomass concentration (gL^{-1}) at time $t_{cd.w}$ (days)	PC	Phycocyanin
$C_{w.d0}$	The initial biomass concentration (gL^{-1}) at the time t_0	R^2	Interpret R Squared
C_a	Chlorophyll a	t_0	Initial time by day
C_b	Chlorophyll b	$t_{cw.d}$	Selected time in the day
C_{x+c}	Carotenoid		

1. INTRODUCTION

Microalgae are a group of eukaryotic algae and prokaryotic cyanobacteria which do the photosynthesis [1]. Among the commercial species of microalgae, *Spirulina* is one of the most essential microalgae for a wide range of applications in various industries [2-5]. as a source of vitamins [6]. Recently, there is a massive demand of natural pigment extraction from *Spirulina* due to their non-toxic, non-allergic, and antimicrobial effects (FDA has banned the use of synthetic colorants) [7-9].

Furthermore, *Spirulina* contains the most important sources of pigments [10]. The phycocyanin and allophycocyanin have considerably been noticed world.

Biomass growth of microalgae depends on the environmental situations such as lighting [11], temperature [12] and pH [13]. Furthermore, aeration plays a significant role on the production of biomass by

*Corresponding Author's Email: r-davarnejad@araku.ac.ir (R. Davarnejad)

Please cite this article as: N. Mirhosseini, R. Davarnejad, A. Hallajisani, E. Cano-europa, O. Tavakoli, Sugarcane Molasses as a Cost-effective Carbon Source on *Arthrospira Maxima* Growth by Taguchi Technique, ***International Journal of Engineering, Transactions C: Aspects*** Vol. 35, No. 03, (2022) 510-516

increasing the dissolved oxygen content of culture [14]. In fact, light intensity can affect the biomass and pigments production [15-17]. Nutrient availability is one of the major promising strategies to change and control the microalgae growth and the production of pigments [18]. The essential nutrients are an organic or inorganic carbon source as well as nitrogen, and other micronutrient during the cultivation [19]. Nowadays, feasibility of *Spirulina* growth in several nutritional conditions has been encouraged to enhance biomass and pigment production [18]. Therefore, various media can be used for the growth of Spirulina like Zarrouk[20], modified Zarrouk [21], CFTRI & JPJM [22] and Bangladesh one [23]. However, there are different applications on algae such as wastewater treatment through their produced biomasses [24, 25] but, their nutrition should be an important issue.

Carbon source is one of the most cost-effective factors in the production of biomasses and pigments [26]. The replacement of basic carbon sources of media ($NaHCO_3$) with cost-effective materials such as glucose and molasses has previously been reported in the cultivation of Spirulina platensis [27-29]. Since, there were no published works on the impacts of sugarcane molasses on the cultivation of *Arthrospira maxima*, the current research was conduct on this area. Moreover, sugarcane molasses as an alternative and additive carbon source of Zarrouk's media was prepared at four different concentrations (0, 0.5, 1.0 and 1.5 gL^{-1}) in this research.

2. EXPERIMENTS

2. 1. Inoculums Preparation and Cultivation Method Axenic Arthrospira maxima CIB79 strain was obtained from National Polytechnic Institute (IPN), (Mexico City, Mexico), which was grown in a batch culture. The cultivation process using Zarrouk's media was carried out at laboratory temperature ranging from 28-32 °C under a white fluorescent with an illumination of 1350±100 lux light intensity. The treatments continuously aerated by adjusting a fixed aeration with an air pump [AC-9602 (RESUN, Mexico)] during 7 days of cultivation. Furthermore, the measurement of culture pH was daily carried out using a pH-meter (HANNA, pH21 pH/mV meter, US). Zarrouk's media with $NaHCO_3$ 16.8 gL^{-1}, $NaNO_3$ 2.5 gL^{-1}, K_2HPO_4 0.5 gL^{-1}, K_2SO_4 1.0 gL^{-1}, NaCl 1.0 gL^{-1}, $MgSO_4.7H_2O$ 0.2 gL^{-1}, EDTA-$Na_2.2H_2O$ 0.08 gL^{-1}, $CaCl_2.2H_2O$ 0.04 gL^{-1}, and $FeSO_4.2H_2O$ 0.01 gL^{-1}, micronutrient elements solution (H_3BO_3 2.86 gL^{-1}, $MnCl_2.4H_2O$ 1.81 gL^{-1}, $ZnSO_4.7H_2O$ 0.222 gL^{-1}, MoO_3 0.01 gL^{-1}, $CoCl_2.6H_2O$ 0.01 gL^{-1}, $CuSO_4.5H_2O$ 0.079 gL^{-1}) 1.00 mLL^{-1} was used as a cultivation media. All chemicals were purchased from Merck Company (Darmstadt, Germany). The media preparation was carried out according to the literature [30]. Treatments were performed in a 125 mL Erlenmeyer flask containing 25 mL of Arthrospira maxima inoculum with an initial biomass concentration of 1.08 gL^{-1}. During the process of growth, double-distilled water was daily added to keep the media in a constant level. The cultivation environment was prepared either with (additive) or without (alternative) basic carbon source of Zarrouk's media. Then, sugarcane molasses as a cheap by-pass product [at different concentrations (0.5, 1 and 1.5 gL^{-1})] were added into the media in the mixotrophic culture to determine the effect of new carbon source versus standard carbon source of Zarrouk's media. The biomass growth and pigment production were recorded during the cultivation. all experiments were repeated three times and the data reproducibility were carefully checked. The data collections were performed during 2019-2020 in September.

2. 2. Analysis and Pigments Measurement The biomass concentration ($C_{w.d}$, gL^{-1}) by dry-weight was daily recorded for each treatment by measuring optical density at wavelength of 674 nm using a spectrophotometer (Thermo Scientific, England) based on the validation curve. The maximum specific growth rate (μ_{max}, day^{-1}) and doubling time (DT, day) at the end of each run was calculated based on literature [31]:

$$\mu_{max} = \frac{\ln(C_{w.d_t}) - \ln(C_{w.d_0})}{t_{C_{w.d}} - t_0}, DT = \frac{0.693}{\mu} \quad (1)$$

Phycobiliproteins concentration was determined using repeated freezing-thawing cycles [18]. The concentrations of phycocyanin (PC) and allophycocyanin (APC) were measured using the following equations at wavelengths of 620 and 652 nm, respectively [32]:

$$PC\ (gL^{-1}) = \frac{A_{620} - 0.474\ A_{652}}{5.34}, APC\ (gL^{-1}) = \frac{A_{652} - 0.208\ A_{620}}{5.09} \quad (2)$$

The pellet collected from the previous step homogenized with 0.4 mL of acetone and chloroform solvent (7:3 v/v) and refrigerated for few days until no color could be seen in the pellet. Then, it was centrifuged at 13300 rpm for 5 min and then the green supernatant was collected. Its absorption was determined at wavelengths of 470, 645 and 662 nm by spectrophotometer. The total content of chlorophyll (C_a) and carotenoid ($C_{(X+C)}$) were calculated using the following equations [33]:

$$C_a = 11.24 \times A_{662} - 2.04 \times A_{645}, C_b = 20.13 \times A_{645} - 4.19 \times A_{662}\ (mgL^{-1}) \quad (3)$$

$$C_{(x+C)} = (1000 \times A_{470}) - (1.09C_a - 63.14C_b)/214\ (mgL^{-1}) \quad (4)$$

All pigments extraction processes were carried out under the dim light to protect them from degradation.

2. 3. Experimental Design The experiments were designed using Taguchi L8 method by Minitab software (2019). The parameters and their levels were tabulated in Table 1.

The experimental design represents eight treatments evaluated by Taguchi L8 approach (four two-level parameters) as shown in Tables 2. Evaluation of experimental data was based on signal-to-noise ratio (S/N ratio) and mean ratio.

All graphic designs and pigment calculations in this study were performed using the Graph Pad Prism 8 software.

3. RESULTS AND DISCUSSION

3. 1. Calibration Curve for Culture Media The maximum absorption wavelength (674 nm) was calculated by measuring the absorption spectra in the wavelengths from 300 to 800 nm, which was in good agreement with the literature [33]. The relationship between concentration of *Arthrospira maxima* by cell dry-weight ($C_{w.d}$) and corresponding absorbance results at 674 nm were estimated by the straight-line equation as follows:

$$A_{674} = 0.5800 \times (C_{w.d}) + 0.02010, (R^2 = 0.9971) \quad (5)$$

TABLE 1. Experimental parameters and their level

Parameters	Level No.	Value of each Level
Sugarcane molasses concentration	4	0, 0.5, 1.0, 1.5
Adding method of molasses	2	1 (additive carbon source), 2 (alternative carbon source)

TABLE 2. Orthogonal array of Taguchi L8 (4^1 2^1)

Treatments No.	Concentration	Adding method
1a	0	1
2	0.5	1
3	1	1
4	1.5	1
5	0	2
6	0.5	2
7	1	2
8	1.5	2

[a] treatment that was prepared in control culture media (Zarrouk's media). Number 1 represents molasses was added as an additive nitrogen source. Number 2 represents molasses was added as an alternative nitrogen source.

3. 2. Effect of Molasses Concentrations on Growth Parameters

3. 2. 1. Biomass Dried Weight Figure. 1 estimates healthy cells and illustrates $C_{w.d}$ affected by changes in the molasses concentration. The lag-phase of most cultures was 2 days. The highest cell concentration (4.49 gL^{-1}) was obtained at the maximum concentration of molasses (1.5 gL^{-1}) with bicarbonate-free media, which was almost 1.5 times higher than molasses-based media with bicarbonate (Fig. 1b). Furthermore, molasses concentration increment from 0.5 to 1.5 gL^{-1} led to a significant enhancement in the biomass accumulation. The result was in agreement with a similar work on Spirulina platensis [27]. Other results showed an increase of $C_{w.d}$ between 0.495 gL^{-1} and 0.609 gL^{-1} after 7 day of cultivation when culture media was supplemented by 0.1% and 1% v/v of sugarcane vinasse.

In additive-molasses group, treatment 4 had the highest molasses concentration and produced the highest $C_{w.d}$ although it was not high enough to be effective compared with the alternative group. In treatment 2 the cell growth was higher than that treatment 1 and also higher than that encountered by Andrade and Costa [34] during mixotrophic growth ($C_{w.d}$= 1.14 gL^{-1}) of *Spirulina platensis* with molasses (0.75 gL^{-1}) at the media light intensity (45.5 µmol $m^{-2}s^{-1}$) although they used *Spirulina platensis* microalgae for cultivation period of 11 days; while *Arthrospira maxima* microalgae during 7 days of cultivation was used in the current research [35]. Moreover, the $C_{w.d}$of the highest molasses concentration in both groups (additive and alternative) was higher than that of *Spirulina platensis* growth stimulated in media supplemented with glucose ($C_{w.d}$=2.52 gL^{-1}) during mixotrophic condition [36]. However, light and organic carbon source are the two most important factors on the growth rate of Arthrospira maxima in the mixotrophic condition; but, the light could not effectively penetrate in a high-concentrated media. It causes turbidity after 4 days. According to the literature, this phenomenon inhibited photosynthetic activity of Spirulina platensis[37]. On the other hand, the cultivation conditions such as light and organic carbon source in heterotrophic condition can inhibit growth process [38].

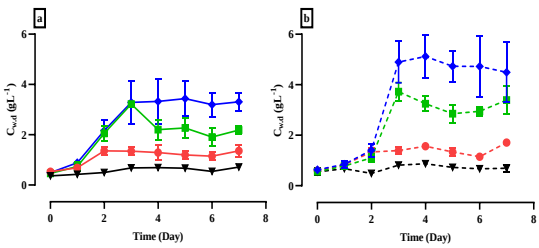

Figure 1. Change in biomass concentration during the period of day: additive (panel a) and alternative (panel b) molasses. (▼: 0 gL^{-1}, ●: 0.5 gL^{-1}, ■: 1 gL^{-1},♦: 1.5 gL^{-1})

3. 2. 2. Culture Media PH The pH was gradually increased in molasses additive-based media as bicarbonate dissolved in the media that releases CO_2 and OH^- (as data shown in Fig. 2). Then, the pH increased with respect to time during cultivation according to the following equations [39]:

$$NaHCO_3^- \rightarrow Na^+(micronutrientforgrowingalgae) + HCO_3^- \quad (6)$$

$$HCO_3^- \xrightarrow{\text{Carbonic anhydrase enzyme}} CO_2(carbonsource) + OH^-(alkaline) \quad (7)$$

In both molasses-based media, the pH decreased 2 days after inoculation and then increased due to the activity of bacteria in the media. Additional amounts of bacteria were contained in the media at high concentration of molasses. Based on Oswald principle, the organic compounds of wastewater were converted into CO_2 by oxidation bacteria in the media at the beginning of cultivation. Then, carbonate was formed by chemical reaction of CO_2 and water. Carbonate then was used by microalgae throughout photosynthetic process. OH^- ions were released and pH of the solution has increased [40]. Therefore, Arthrospira maxima utilized organic carbon such as molasses for producing CO_2 through respiration (the heterotrophic growth) while the growth should be photoautotrophic when Arthrospira maxima utilized light as an energy source and carbon dioxide as a carbon source during the photosynthetic process (pH media will remain high due to photoautotrophic growth). According to this research, the $C_{w.d}$ reached its maximum value when the pH value was in minimum (9.10±0.3). This result is properly justified by a similar work reported in literature [41].

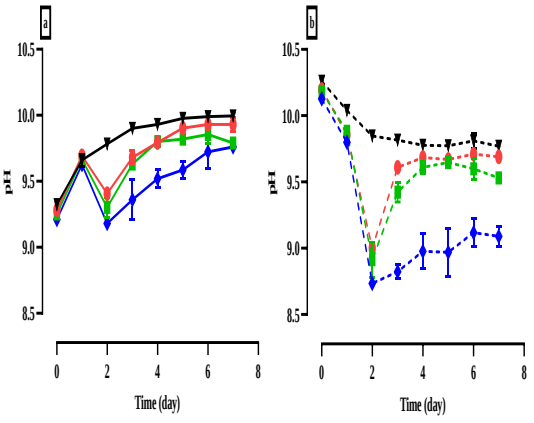

Figure 2. Changes in pH during the growth phase of *Arthrospira maxima*: additive (panel a) and alternative (panel b) molasses. (▼: 0 gL^{-1}, ●: 0.5 gL^{-1}, ■: 1 gL^{-1},♦: 1.5 gL^{-1})

3. 2. 3. Growth Parameters Figure. 3 shows the effect of various concentration ns of molasses-containing media on μ_{max} and DT at the end of each run (7 days). Moreover, μ_{max} and the minimum DT (0.3 day^{-1}, 2.3 day) occurred at concentration of 1.5 gL^{-1} in the media when molasses was added as an alternative carbon source. Furthermore, sum of the μ_{max} values of autotrophic and heterotrophic cultures corresponded to μ_{max} of the mixotrophic culture [36]. These results revealed that the lowest DT (2.55 day) is in fact at the highest μ_{max} (0.27) at concentration of 1.5 gL^{-1} when molasses is added as an additional carbon source. Moreover, μ_{max} decreased from 0.09 to 0.3 day^{-1} when the initial concentration increased from 0.05 to 1.5 gL^{-1}.

3. 3. Effect of Molasses Concentrations on the Pigments Production

3. 3. 1. Phycocyanin and Allophycocyanin Contents According to Figures 4(a) and 4(b), the value of PC increased with time and concentration of molasses increment. The formation of PC pigment in the highest concentration remained consistent in a high level after 4 days of cultivation. That is probably due to the turbidity of media after 4 days (rapid growth of biomass during the first few days of cultivation) [37]. Furthermore, Arthrospira maxima requires high light intensity to cover turbidity problem after 4 days of cultivation at high concentrations of carbon source. Changes in APC content in molasses-containing media as an additive and alternative are shown in Figures 4(c) and 4(d).

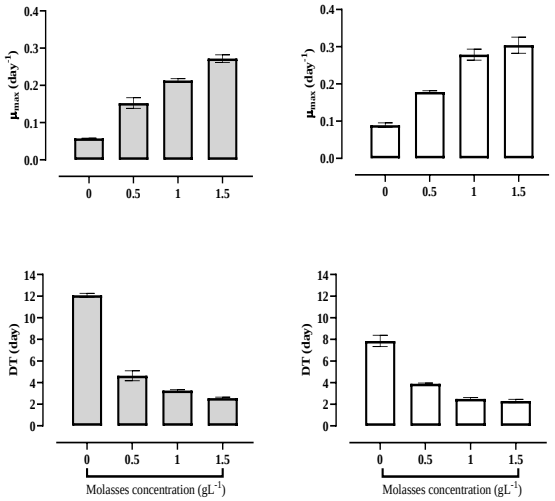

Figure 3. Effect of different concentrations of molasses-based media on μ_{max} specific growth rate (panel a & b) and doubling time (panel c & d) whereas molasses was added as an additive (gray box) and alternative (white box) carbon sources

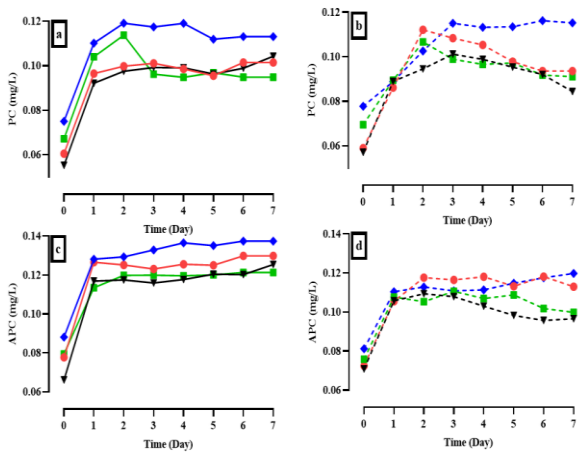

Figure 4. Changes in phycocyanin (panel a & b) and allophycocyanin (panel c & d) content in molasses-containing media. (▼: 0 gL^{-1}, ●: 0.5 gL^{-1}, ■: 1 gL^{-1},♦: 1.5 gL^{-1})

At the highest concentration, the APC and PC contents increased from 0.08 to 0.13 mgL^{-1} and from 0.07 to 0.12 mgL^{-1}, respectively. In photoautotrophic culture, PC and APC did not grow as fast as the mixotrophic culture while photoautotrophic culture cannot be satisfied by biomass growth in clash with the mixotrophic culture. On the other hand, the results showed that the mount of PC and APC slightly increased with time in the control treatment. Therefore, it was concluded that carbon source and its concentration as well as light intensity during the cultivation were the significant factors. Moreover, the amounts of PC and APC pigment in the carbon-free conditions were declining. Therefore, carbon source was a vital source for *Arthrospira maxima* growth.

3. 3. 2. Photosynthetic Content Table 3 shows the amount of photosynthetic pigments (C_a, C_b and $C_{(x+c)}$) for each treatment on the final day of cultivation. It was observed that molasses was not able to produce the highest content of photosynthesis pigment throughout the course of cultivation due to the lack of light penetration [42]. The C_a, C_b and $C_{(X+C)}$ of *Arthrospira maxima* were in maximum at maximum pH value [43]. According to the control treatment, the highest C_a, C_b and $C_{(X+C)}$ growth data were at 29.13, 10.25 and 2672 mgL^{-1}, respectively. This amount was similar to treatment 5 (without any carbon source). In addition, the amount of photosynthetic pigments decreased with an increase in molasses concentration in the both methods.

Furthermore, molasses concentration increment may disrupt microalgae breath and consequently reduce the pigment content. The current study shows a good efficiency compared with the control treatment in terms of C_a. It almost was 2.5 times higher than that of the *Spirulina platensis* growth in additive molasses-based Zarrouk's media [27].

TABLE 3. Estimation of photosynthetic pigments in Arthrospira maxima

Treatment No	Molasses addition method	C_a(mgL^{-1})	C_b(mgL^{-1})	$C_{(X+C)}$ (mgL^{-1})
1[a]	Additive	29.13	10.25	2672
2		27.23	2.89	2542
3		26.58	1.89	2582
4		23.83	0.343	2340
5	Alternative	28.59	10.34	2620
6		28.05	3.44	2553
7		24.43	2.17	2540
8		24.83	2.99	2535

[a] *treatment that was prepared in control culture media (Zarrouk's media)*

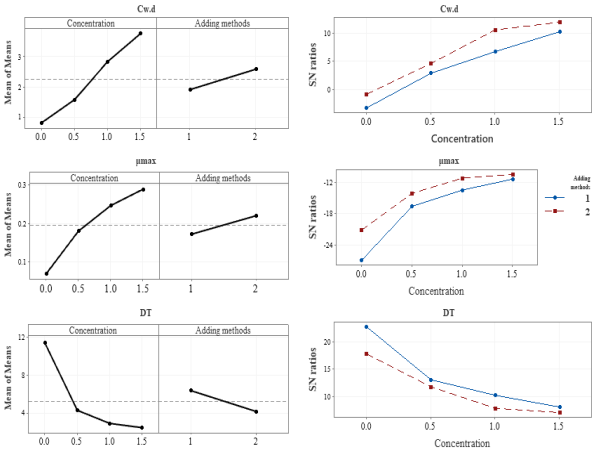

Figure 5. Mean graph (vertical diagram on the left side) and S/N ratio graph (diagram on the right side) corresponding to biomass concentration (gL^{-1}), specific growth rate and doubling time.

3. 3. 3. Experimental Analysis and Design Figure. 5 shows Mean and S/N ratio graph corresponding to the growth parameters.

The maximum value of S/N ratio plot of $C_{w.d}$ and μ_{max} described the optimum level for a particular parameter. On the other hand, smaller S/N ratio was the best factor for the DT. Furthermore, molasses as an alternative carbon source (adding methods 2) at a concentration of 1.5 $gL^{-1}$was chosen as the best parameter.

4. CONCLUSIONS

Arthrospira maxima cultivation requires the best carbon source instead of bicarbonate source of Zarrouk's media as well as sufficient concentration for the enhanced

biomass growth. $C_{w.d}$and μ_{max} amounts almost increased with an increase in the molasses concentration from 0.5 to 1.5 gL^{-1} during the cultivation. However, adding molasses as an additive and alternative carbon source should be useful but, molasses consumption (as an additive carbon source) did not show an excellent output on $C_{w.d}$in comparison with the alternative sources. Moreover, the availability of organic carbon source in media and sufficient light during the first few days of cultivation increased the penetration of light and carbon-fixation route into the media. The formation of PC pigment simultaneously decreased or consistently remained high throughout most part of the cultivation period. Its reason is due to the effect of restricted light dispersion (biomass accumulation). Furthermore, the intensity of light could increase after the first few days of cultivation in order to avoid the growth rate inhibition.

5. REFERENCES

1. Urtubia, H.O., Betanzo, L.B. and Vásquez, M.J.A.O.f.I.B., "Microalgae and cyanobacteria as green molecular factories: Tools and perspectives", ***Intech Publisher***, (2016), 1-27, doi: 10.5772/63006
2. Molino, A., Iovine, A., Casella, P., Mehariya, S., Chianese, S., Cerbone, A., Rimauro, J., Musmarra, D.J.I.j.o.e.r. and health, p., "Microalgae characterization for consolidated and new application in human food, animal feed and nutraceuticals", ***International Journal of Environmental Research and Public Health***, Vol. 15, No. 11, (2018), 2436, doi: 10.3390/ijerph15112436
3. Gupta, S. and Bux, F., "Application of microalgae in wastewater treatment, Springer, (2019).
4. Umana, U.S., Ebong, M.S., Godwin, E.O.J.J.o.H., Earth, and Future, "Biomass production from oil palm and its value chain", ***Journal of Human, Earth and Future***, Vol. 1, No. 1, (2020), 30-38, doi: 10.28991/HEF-2020-01-01-04
5. Shao, W., Ebaid, R., El-Sheekh, M., Abomohra, A. and Eladel, H.J.G.y.A., "Pharmaceutical applications and consequent environmental impacts of spirulina (arthrospira): An overview", ***Grasas y Aceites***, Vol. 70, No. 1, (2019), e292-e292, doi: 10.3989/gya.0690181
6. Sotiroudis, T.G. and Sotiroudis, G.T.J.J.o.t.S.C.S., "Health aspects of spirulina (arthrospira) microalga food supplement", ***Journal of the Serbian Chemical Society***, Vol. 78, No. 3, (2013), 395-405, doi: 10.2298/JSC121020152S
7. Sen, T., Barrow, C.J. and Deshmukh, S.K.J.F.i.n., "Microbial pigments in the food industry—challenges and the way forward", ***Frontiers in Nutrition***, Vol. 6, (2019), 7, doi: 10.3389/fnut.2019.00007
8. Ariede, M.B., Candido, T.M., Jacome, A.L.M., Velasco, M.V.R., de Carvalho, J.C.M. and Baby, A.R.J.A.r., "Cosmetic attributes of algae-a review", ***Algal Research***, Vol. 25, (2017), 483-487, doi: 10.1016/j.algal.2017.05.019
9. Singh, S., Dwivedi, V., Sanyal, D. and Dasgupta, S.J.A.P., "Therapeutic and nutritional potential of spirulina in combating covid-19 infection", ***AIJR Preprints***, (2020), doi: 10.21467/preprints.49
10. Park, W.S., Kim, H.-J., Li, M., Lim, D.H., Kim, J., Kwak, S.-S., Kang, C.-M., Ferruzzi, M.G. and Ahn, M.-J.J.M., "Two classes of pigments, carotenoids and c-phycocyanin, in spirulina powder and their antioxidant activities", ***Molecules***, Vol. 23, No. 8, (2018), 2065, doi: 10.3390/molecules23082065
11. Carvalho, J.C.M., Francisco, F.R., Almeida, K.A., Sato, S. and Converti, A.J.J.o.P., "Cultivation of arthrospira (spirulina) platensis (cyanophyceae) by fed-batch addition of ammonium chloride at exponentially increasing feeding rates 1", ***Journal of Phycology***, Vol. 40, No. 3, (2004), 589-597, doi: 10.1111/j.1529-8817.2004.03167.x
12. Vonshak, A. and Tomaselli, L., Arthrospira (spirulina): Systematics and ecophysioiogy, in The ecology of cyanobacteria. 2000, Springer.505-522.
13. Ogbonda, K.H., R.E. Aminigo and G.O. Abu, "Influence of temperature and ph on biomass production and protein biosynthesis in a putative spirulina sp", ***Bioresource Technology***, Vol. 98, (2007), 2207-2211., doi: 10.1016/j.biortech.2006.08.028
14. Cooke, G.D., Welch, E.B., Peterson, S. and Nichols, S.A., "Restoration and management of lakes and reservoirs, CRC press, (2016).
15. Danesi, E.D.G., Rangel-Yagui, C.O., Sato, S. and Carvalho, J.C.M.d.J.B.j.o.m., "Growth and content of spirulina platensis biomass chlorophyll cultivated at different values of light intensity and temperature using different nitrogen sources", ***Brazilian Journal of Microbiology***, Vol. 42, No. 1, (2011), 362-373, doi: 10.1590/S1517-83822011000100046
16. Kumar, M., Kulshreshtha, J. and Singh, G.P.J.B.J.o.M., "Growth and biopigment accumulation of cyanobacterium spirulina platensis at different light intensities and temperature", ***Brazilian Journal of Microbiology***, Vol. 42, (2011), 1128-1135, doi: 10.1590/S1517-83822011000300034
17. Torzillo, G., Vonshak, A.J.B. and Bioenergy, "Effect of light and temperature on the photosynthetic activity of the cyanobacterium spirulina platensis", ***Biomass and Bioenergy***, Vol. 6, No. 5, (1994), 399-403, doi: 10.1016/0961-9534(94)00076-6
18. Mirhosseini, N., Davarnejad, R., Hallajisani, A., Cano-Europa, E., Tavakoli, O., Franco-Colín, M. and Blas-Valdivia, V.J.I.J.o.F.S., "Cultivations of arthrospira maxima (spirulina) using ammonium sulfate and sodium nitrate as an alternative nitrogen sources", ***Iranian Journal of Fisheries Sciences***, Vol. 20, No. 2, (2021), 475-489.
19. Grobbelaar, J.U.J.H.o.m.c.b. and phycology, a., "Algal nutrition: Mineral nutrition", (2004), 97-115.
20. Raoof, B., Kaushik, B., Prasanna, R.J.B. and bioenergy, "Formulation of a low-cost medium for mass production of spirulina", ***Biomass and Bioenergy***, Vol. 30, No. 6, (2006), 537-542.
21. Rajasekaran, C., C.P.M. Ajeesh, S. Balaji, M. Shalini, R. Siva, R. Das, D.P. Fulzele and T. Kalaivani, "Effect of modified zarrouk's media on growth of different spirulina strains", ***Walailak Journal of Science and Technology***, Vol. 13, No. 67-75., doi: 10.1016/j.biombioe.2005.09.006
22. Salunke, K., Magar, S., Joshi, R. and Wadikar, M.J.B.d., "Comparative study on the growth of spirulina platensis on different culture media", ***Bioscience Discovery***, Vol. 7, No. 1, (2016), 90-92.
23. Khatun, R., Noor, P., Akhter, N., Jahan, M., Hossain, M., Munshi, J.J.B.J.o.S. and Research, I., "Spirulina culture in bangladesh xi: Selection of a culture medium, suitable for culturing a local strain of spirulina", ***Bangladesh Journal of Scientific and Industrial Research***, Vol. 41, No. 3, (2006), 227-234, doi: 10.3329/bjsir.v41i3.293
24. Hadiyanto, H., Soetrisnanto, D. and Christwardhana, M.J.I.J.o.E.-T.C.A., "Phytoremediation of palm oil mill effluent using pistia stratiotes plant and algae spirulina sp for biomass production", ***International Journal of Engineering Transactions C: Aspects***,

Vol. 27, No. 12, (2014), 1809-1814, doi: 10.5829/idosi.ije.2014.27.12c.02

25. Sharifzadeh, M. and HosseinAlizadeh, R.J.I.J.o.E., "Artificial neural network approach for modeling of mercury adsorption from aqueous solution by sargassum bevanom algae (research note)", ***International Journal of Engineering Transactions B: Applications***, Vol. 28, No. 8, (2015), 1124-1133, doi: 10.5829/idosi.ije.2015.28.08b.03
26. Soletto, D., Binaghi, L., Lodi, A., Carvalho, J. and Converti, A.J.A., "Batch and fed-batch cultivations of spirulina platensis using ammonium sulphate and urea as nitrogen sources", ***Aquaculture***, Vol. 243, No. 1-4, (2005), 217-224, doi: 10.1016/j.aquaculture.2004.10.005
27. R. Dineshkumar, P. Umamageswari, P. Jayasingam and P. Sampathkumar, "Enhance the growth of spirulina platensis using molasses as organic additives", ***World Journal of Pharmaceutical Research***, Vol. 4, (2015), 1057-1066.
28. Ogbonna, I.O., Ogbonna, J.C.J.E. and Engineering, P., "Effects of carbon source on growth characteristics and lipid accumulation by microalga dictyosphaerium sp. With potential for biodiesel production", ***Energy and Power Engineering***, Vol. 10, No. 2, (2018), 29-42, doi: 10.4236/epe.2018.102003
29. Sipaúba-Tavares, L., Tedesque, M. and Scardoeli-Truzzi, B.J.B.J.o.B., "Evaluation of the effects of sugarcane molasses as a carbon source for ankistrodesmus gracilis and haematococcus pluvialis (chlorophyceae)", ***Brazilian Journal of Biology***, Vol. 80, (2019), 594-600, doi: 10.1590/1519-6984.216820
30. Rodríguez-Sánchez, R., Ortiz-Butrón, R., Blas-Valdivia, V., Hernández-García, A. and Cano-Europa, E.J.F.c., "Phycobiliproteins or c-phycocyanin of arthrospira (spirulina) maxima protect against hgcl2-caused oxidative stress and renal damage", ***Food Chemistry***, Vol. 135, No. 4, (2012), 2359-2365, doi: 10.1016/j.foodchem.2012.07.063
31. Göksan, T., Zekeriyaoğlu, A. and Ak, İ.J.T.j.o.b., "The growth of spirulina platensis in different culture systems under greenhouse condition", ***Journal of Biology***, Vol. 31, No. 1, (2007), 47-52.
32. Benett, A.J.J.C.B., "Complementary chromatic adaptation ina filamentous blue-green alga", ***Journal of Cell Biology***, Vol. 58, (1973), 419-435, doi: 10.1083/jcb.58.2.419
33. Pumilia, G., Cichon, M.J., Cooperstone, J.L., Giuffrida, D., Dugo, G. and Schwartz, S.J.J.F.R.I., "Changes in chlorophylls, chlorophyll degradation products and lutein in pistachio kernels (pistacia vera l.) during roasting", Vol. 65, (2014), 193-198, doi: 10.1016/j.foodres.2014.05.047
34. dos Santos, R.R., O.d.Q.F. Araújo, J.L. de Medeiros and R.M. Chaloub, "Cultivation of spirulina maxima in media supplemented with sugarcane vinasse", ***Bioresource Technology***, (2016), doi: 10.1016/j.biortech.2015.12.077
35. Souza, M.d.R.A.Z.d. and Costa, J.A.V., "Mixotrophic cultivation of microalga spirulina platensis using molasses as organic substrate", (2007), doi: 10.1016/j.aquaculture.2006.11.021
36. Marquez, F.J., Sasaki, K., Kakizono, T., Nishio, N., Nagai, S.J.J.o.F. and Bioengineering, "Growth characteristics of spirulina platensis in mixotrophic and heterotrophic conditions", ***Journal of Fermentation and Bioengineering***, Vol. 76, No. 5, (1993), 408-410, doi: 10.1016/0922-338X(93)90034-6
37. Cheunbarn, S. and Peerapornpisal, Y.J.I.J.A.B., "Cultivation of spirulina platensis using anaerobically swine wastewater treatment effluent", ***Interanational Journal of Agricultural Biology***, Vol. 12, No. 4, (2010), 586-590.
38. Zhang, X.W., Y.M. Zhang and F. Chen, "Application of mathematical models to the determination optimal glucose concentration and light intensity for mixotrophic culture of spirulina platensis", ***Process Biochemistry***, Vol. 34, (1999), 477-481, doi: 10.1016/S0032-9592(98)00114-9
39. Jaiswal, P., Prasanna, R. and Kashyap, A.K.J.J.o.p.p., "Modulation of carbonic anhydrase activity in two nitrogen fixing cyanobacteria, nostoc calcicola and anabaena sp", ***Journal of Plant Physiology***, Vol. 162, No. 10, (2005), 1087-1094, doi: 10.1016/j.jplph.2005.03.006
40. Oswald, W.J. and Gotaas, H.B.J.T.o.t.A.S.o.C.E., "Photosynthesis in sewage treatment", Vol. 122, No. 1, (1957), 73-97.
41. Pandey, J., Tiwari, A. and Mishra, R.J.J.A.B.U., "Evaluation of biomass production of spirulina maxima on different reported media", ***Journal of Algal Biomass Utln***, Vol. 1, No. 3, (2010), 70-81.
42. Ogbonna, J.C. and Tanaka, H.J.B.t., "Cyclic autotrophic/heterotrophic cultivation of photosynthetic cells: A method of achieving continuous cell growth under light/dark cycles", ***Bioresource Technology***, Vol. 65, No. 1-2, (1998), 65-72, doi: 10.1016/S0960-8524(98)00018-2
43. Kim, S.-K., Ravichandran, Y.D., Khan, S.B., Kim, Y.T.J.B. and Engineering, B., "Prospective of the cosmeceuticals derived from marine organisms", ***Biotechnol Bioprocess Engineering***, Vol. 13, No. 5, (2008), 511-523.

Persian Abstract

چکیده

در این تحقیق، از منبع کربن مقرون به صرفه جدیدی با راندمان تولید بالا *Arthrospira maxima* استفاده شد. از ملاس نیشکر در دو حالت (جایگزین و افزودنی) و چهار غلظت مختلف (0، 0/5، 1 و 1/5 گرم در لیتر) برای تعیین تأثیر منبع کربن جدید در برابر منبع کربن استاندارد محیط زاروک استفاده شد. نتایج تجربی با استفاده از روش تاگوچیL8 به عنوان یک تکنیک آماری مورد تجزیه و تحلیل قرار گرفت. بیشترین تولید زیست توده زمانی حاصل شد که ملاس نیشکر به عنوان منبع جایگزین اضافه شد که تقریبا 5/31 برابر بیشتر از محیط استاندارد زاروک بود. علاوه بر این، غلظت زیست توده نهایی با افزایش غلظت ملاس از 0 تا 1/5 گرم در لیتر در این گروه افزایشیافت. در بالاترین غلظت ملاس، فیکوسیانین (در 0/11 و 0/12 گرم در لیتر)، آلوفیکوسیانین (در 0/13 و 0/12 گرم در لیتر)، کاروتنوئیدها (در 2340 و 2535 میلی گرم در لیتر)، کلروفیلa (در 23/83 و 24 میلیگرم در لیتر)، و کلروفیلb (در 0/343 و 2/99 میلی‌گرم در لیتر) به‌ترتیب زمانیکه ملاس بعنوان منبع افزودنی و جایگزین اضافه شد، به‌دست می‌آید. در نهایت، جایگزینی منبع کربن استاندارد محیط کشت زاروک با ملاس نیشکر امکان بالقوه ای را برای کاهش هزینه های تولید دارد.

International Journal of Engineering

Journal Homepage: www.ije.ir

Amelioration Effectiveness of Torque and Rotor Flux Control Applied to the Asynchronous Generator for Dual-rotor Wind Turbine using Neural Third-order Sliding Mode Approaches

H. Benbouhenni*

Department of Electrical & Electronics Engineering, Faculty of Engineering and Architecture, Nisantasi University, Istanbul, Turkey

P A P E R I N F O

Paper history:
Received 16 February 2021
Received in revised form 30 October 2021
Accepted 25 November 2021

Keywords:
Asynchronous Generator
Dual-Rotor Wind Turbine
Neural Third-order Sliding Mode
Direct Torque Control
Traditional Proportional-integral

A B S T R A C T

In this paper, a neural third-order sliding mode-direct torque control (NTOSM-DTC) for an asynchronous generator (AG) based dual-rotor wind turbine (DRWT) is proposed. The classical DTC strategy with traditional proportional-integral (PI) controllers has been widely applied to induction machines in recent years due to the high characteristics that it provides in comparison with the classical DTC switching technique. Meanwhile, it has a major drawback that are the significant current, rotor flux and torque ripples generated by the traditional PI controllers. To overcome these drawbacks, the improvement of this control technique by removing these controllers is designed in this paper. The proposed intelligenet nonlinear control technique is based on replacing the classical PI controllers with neural TOSM controllers which will have the same inputs as these controllers. The simulation was performed in Matlab software, and the results obtained make it possible to evaluate the characteristics of the proposed intelligenet nonlinear control technique over the traditional one.

***doi**: 10.5829/ije.2022.35.03c.04*

1. INTRODUCTION

In recent years, the demand for electric power has been increasing. This is due to an increase in number of engines used in our daily lives, as well as the abandonment of traditional energy sources such as petroleum. The latter has become a threat to human life. Conventional energies (fossil fuels and natural gas) are among the causes of global warming. This made several governments across the world search for other clean and economically inexpensive sources of energy. Among these solutions, we find solar energy, wind energy, the potential energy of water, these energies are inexpensive, and renewable energies. Moreover, it is clean and easily exploitable energies [1].

Wind energy is among the most widely used renewable energies in the field of electric power generation. This is because of the simplicity of use, clean energy, inexpensive and gives a significant value of electrical energy [2]. This method is based on placing the turbines on shafts against the wind. The rotation of the turbine leads to the rotation of the generator and thus the generation of electric power. Several generators can be used in wind energy, such as the asynchronous generator [3] and the synchronous generator [4]. However, the asynchronous generator is the most widely used in the field of electric power generation using wind energy, especially in the case of variable wind speed. This is due to the advantages and characteristics of the asynchronous generator such as ease of control, efficiency, durability, and low cost [5].

As is known, there are several ways to control electrical machines (generators), such as direct torque control (DTC) [6], filed-oriented control (FOC) [7], direct power control (DPC) [8], backstepping control [9], synergetic control [10], nonlinear control [11-13], etc. However, the direct torque control strategy is the most prevalent and widely used method for controlling

*Corresponding Author Institutional Email: habib.benbouenni@nisantasi.edu.tr (H. Benbouhenni)

Please cite this article as: H. Benbouhenni, Amelioration Effectiveness of Torque and Rotor Flux Control Applied to the Asynchronous Generator (AG) for Dual-rotor Wind Turbine Using Neural Third-order Sliding Mode Approaches, ***International Journal of Engineering, Transactions C: Aspects*** Vol. 35, No. 03, (2022) 517-530

electrical machines such as induction motor and synchronous motor, and this is because of the advantages and characteristics that it has compared to other methods. The direct torque control strategy is an easy algorithmic method, can be implemented easily, low cost, and gives very satisfactory results compared to other methods. This method relies on the use of hysteresis comparators and a lookup table to control the torque and flux of the electric machine. This method has been used to control several electrical machines such as the asynchronous motor [14], synchronous motor [15], multi-phase induction motor [16], synchronous generator [17], multi-phase synchronous motor [18], and asynchronous generator [19].

In the field of electric power generation from wind, this method is used to control the asynchronous generator, due to the simplicity of the algorithm and the dynamic response. In this case, the torque and flux of the asynchronous generator are controlled. Controlling these two amounts leads to controlling the current and the output active power generated by the generator (AG).

Despite the advantages of this method, it has several disadvantages like any other method. Among the disadvantages of the direct torque control method are ripples at the level of current, torque, and rotor flux. Plus, the direct torque control method gives a large total harmonic distortion (THD) ratio [20].

As it is known, these defects affect the yield and life span of the electric generator. The fluctuations in torque affect the quality of the current and the effective power [21].

There are several studies and scientific research conducted on the method of direct torque control in order to reduce the ripples of torque and current resulting from the asynchronous generator using several methods such as nonlinear methods (sliding mode control and super twisting algorithm), artificial intelligence (fuzzy logic, genetic algorithm, neural network, etc) and a combination of artificial intelligence and nonlinear methods (neuro-sliding mode control, fuzzy-super twisting algorithm, etc) in order to obtain a more robust method and thus, obtaining very satisfactory results. Fuzzy DTC control was proposed by Ayrira et al. [22] to control the asynchronous generator-based wind turbine. The proposed DTC strategy is more robust compared to the traditional DTC technique. On the other hand, the fuzzy DTC control reduces more the THD value of stator current and active power ripple compared to the traditional DTC technique.

A new method is proposed by Benbouhenni [23], based on the use of both space vector modulation (SVM) and proportional-integral (PI) controller. This is in order to reduce the fluctuations in both current and torque. This method is based on replacing lookup table and hysteresis comparators with SVM technique and PI controllers, respectively. The proposed method is more robust and can be easily accomplished. The simulation results showed the effectiveness of the proposed method in reducing torque ripples and THD value compared to the classical method. PI controller and neural networks are combined to improve the performance and effectiveness of direct torque control [24]. The results showed the effectiveness of the proposed method in improving the quality of the current produced by the asynchronous generator compared to the classical method.

Chattering is defined as the disadvantages of the traditional sliding mode approach at very high frequencies which creates noises in the system. A higher-order sliding mode approach is suitable for the elimination of this chattering phenomenon which was explained by Kelkouland Boumediene [25]. Many strategies like super twisting algorithm, terminal synergetic control, second-order continuous sliding mode, third-order sliding mode control, and fast terminal sliding mode approach are available in the works. These strategies are used to improve the characteristics of an asynchronous generator [26-28]. On use, the settling time and chattering are eliminated or minimized which was presented in the traditional sliding mode approach. These nonlinear methods have been relied upon in some works in order to improve the effectiveness of the direct torque control method in order to obtain a high quality in the current produced by the asynchronous generator. A second-order continuous sliding mode approach was used by Boudjema et al. [29] to improve the DTC method for an asynchronous generator-based wind turbine. The results showed the effectiveness of the DTC method with a second-order continuous sliding mode approach in reducing torque and current ripples compared to the classical DTC method with PI controllers. It also shows the effectiveness of the proposed nonlinear DTC method. Boudjema et al. [29] discussed about the value of THD of stator current, as we find out that the proposed nonlinear DTC method gave a much lower value than the classical DTC method. Another nonlinear technique was proposed by Benbouhenni and Bizon [30] to improve the performances of the DTC control technique of the asynchronous generator-based dual-rotor wind turbine (DRWT) system. This new nonlinear technique is based on a third-order sliding mode controller. However, the proposed DTC with third-order sliding mode is simple to control, easy to implement, robust algorithm, and reduces the THD value of stator current and power ripple compared to the DTC strategy with PI controllers. Fractional-order second-order continuous sliding mode approach was proposed to improve the characterisitics of DTC control with a modified SVM technique to control the asynchronous generator-based wind turbine [31]. The proposed nonlinear DTC control is more robust than classical DTC with a modified SVM technique. On the other hand, the DTC strategy with fractional-order second-order sliding mode approach reduces the ripples

in the torque, current, and rotor flux compared to the DTC strategy with the traditional second-order sliding mode approach. A new method for DTC control has been proposed based on the modified super twisting algorithm [32]. This new DTC method is a modification of the DTC-PI method, where PI controllers are replaced by modified super twisting algorithms.

In this work, a new nonlinear method is proposed in order to improve the efficiency and performance of the DTC control method, and thus improve the quality of the current and the active power generated by the asynchronous generator-based dual-rotor wind turbine system.

In addition, in this work, a new intelligent high-order sliding mode approach was proposed to improve the performance of the DTC control technique. this proposed high-order sliding mode approach is named the neural third-order sliding mode (NTOSM) strategy. This proposed intelligent nonlinear controller is a more robust, simple algorithm and easy to implement. The objective is to reduce the ripples in the current, rotor flux, and torque of asynchronous generator-based dual-rotor wind turbine systems. The principle of the schematic and the disadvantages or advantages of DTC with neural TSOM controllers are proposed.

The parameters used to observe the characteristics of the proposed intelligent nonlinear DTC control strategy are the THD value of stator current, rotor flux ripple, torque ripple, steady-state error, robustness, response time, and current ripple.

Summarizing, the novelty and main findings of this work are as follows:

- A new neural TOSM strategy based on the DTC technique is proposed to reduce the THD value of stator current;
- Neural TOSM controllers minimize the tracking error for torque and rotor flux towards the references of AG-based DRWT systems.
- The DTC-NTOSM technique with modified SVM technique minimizes ripples of torque, rotor flux, and stator current of AG-based DRWT systems.

Thus, the structure of the work is as follows. In section 2 dual-rotor wind turbine system models are presented. In section 3 the model of the AG is presented using Park transformations. In section 4 the proposed neural TOSM controller is presented. Section 5 includes the DTC control technique with designed neural TOSM controllers. Section 6 presents and discusses the results of the present research.

2. DUAL-ROTOR WIND TURBINE

Dual-rotor wind turbine is a new technology that has emerged in recent years to generate electricity from wind power. Studies on it have shown how effective this new technology is compared to classic turbines. This new technology is detailed in literature [33, 34]. This new technology offers more pneumatic torque than a single-rotor turbine. The dual-rotor wind turbine is not affected by the wind currents generated by the wind farm like this classic turbine, which in the future will be widely spread. Among the disadvantages of this technology is that it contains a larger number of mechanical components and is difficult to control compared to the classic turbine. But it offers a greater return compared to the rest of the existing technologies to this day.

The total aerodynamic torque of DRWT is the auxiliary rotor (AR) torque add to the main rotor (MR) torque as shown by the following equation [35]:

$$T_{DRWT} = T_{MR} + T_{AR} \quad (1)$$

with:

$$T_{AR} = \frac{1}{2\,\lambda_{AR}^{3}} . A . \rho . \pi . R_{AR}^{5} . C_{p} . w_{AR}^{2} \quad (2)$$

$$T_{MR} = \frac{1}{2\,\lambda_{MR}^{3}} . A . \rho . \pi . R_{AR}^{5} . C_{p} . w_{MR}^{2} \quad (3)$$

where, λ_{AR}, λ_{MR}: the tip speed ration of the main and auxiliary turbines, R_{MR}, R_{AR} : Blade radius of the auxiliary and main rotors, ρ : the air density and w_{AR}, w_{MR} the mechanical speed of the auxiliary and main rotors.

The tip speed ratios of the AR is given :

$$\lambda_{AR} = \frac{w_{AR} . R_{AR}}{V_{1}} \quad (4)$$

The tip speed ratios of the MR is given :

$$\lambda_{MR} = \frac{w_{MR} . R_{MR}}{V_{MR}} \quad (5)$$

where, V_{MR} is the speed of the unified wind on main rotor and V_1 is the wind speed on an auxiliary rotor.

The wind speed on the main turbine is given by Yahdou et al. [36]:

$$V_{x} = V_{1}(1 - \frac{1 - \sqrt{(1 - C_{T})}}{2}(1 + \frac{2 . x}{\sqrt{1 + 4 . x^{2}}})) \quad (6)$$

with Vx : is the velocity of the disturbed wind between rotors at point x and C_T the trust coefficient, which is taken to be 0.9; x: the non-dimensional distance from the auxiliary rotor disk. So, with respect to x=15, the value of the Vx close to the main rotor is computable (rotors are located 15 meters apart from each other) [37].

The power coefficient C_P equation is approximated using a non-linear function according to following expression [10].

$$C_{P} = (0.5 - 0.167)(\beta - 2)\sin\left[\frac{\pi(\lambda + 0.1)}{18.5 - 0.3(\beta - 2)}\right] - 0.0018(\lambda - 3)(\beta - 2) \quad (7)$$

3. THE AG MODEL

The Park model of the AG is largely used. The equations of fluxes and voltages for the AG rotor and stator in the Park reference frame are given as follows [38, 39]:

$$\begin{cases} V_{ds} = R_s I_{ds} + \dfrac{d}{dt}\psi_{ds} - \omega_s \psi_{qs} \\ V_{qs} = R_s I_{qs} + \dfrac{d}{dt}\psi_{qs} + \omega_s \psi_{ds} \\ V_{dr} = R_r I_{dr} + \dfrac{d}{dt}\psi_{dr} - \omega_r \psi_{qr} \\ V_{qr} = R_r I_{qr} + \dfrac{d}{dt}\psi_{qr} + \omega_r \psi_{dr} \end{cases} \quad (8)$$

$$\begin{cases} \psi_{ds} = L_s I_{ds} + M I_{dr} \\ \psi_{qs} = L_s I_{qs} + M I_{qr} \\ \psi_{dr} = L_r I_{dr} + M I_{ds} \\ \psi_{qr} = L_r I_{qr} + M I_{qs} \end{cases} \quad (9)$$

The electrical model of the AG is completed by the following mechanical equation:

$$T_{em} = T_r + J \cdot \frac{d\Omega}{dt} + f \cdot \Omega \quad (10)$$

The torque (T_{em}) can be written as follows:

$$T_{em} = \frac{3}{2} p \frac{M}{L_s} (\psi_{qs} I_{dr} - \psi_{ds} I_{qr}) \quad (11)$$

4. NEURAL THIRD-ORDER SLIDING MODE CONTROLLER

In this part, it is explained how to implement this new method (neural TOSM) and its advantages. This new method is a modification of the TOSM technique published by Benbouhenni and Bizon [30].

4. 1. Design of the TOSM Controller There are many nonlinear controllers proposed to control the flux/torque of AC machines in the literature. Among all the strategies proposed for the high-order sliding mode approach, the super twisting controller is an exception, which requires only information on the sliding surface [11]. The third-order sliding mode approach is an effective technique for uncertain systems and it overcomes the main disadvantages of the classical sliding mode approach described. TOSM is a non-linear controller and is an alternative to linear and nonlinear techniques. This method was first proposed in order to improve the performance and efficiency of the direct power control (DPC) of asynchronous generator-based DRWT system [40] and then applied to DTC control of an asynchronous generator-based DRWT system. However, this technique is based on the super twisting algorithm. The control input of the TOSM controller comprises of three inputs as Equation (12).

$$u(t) = u_1 + u_2 + u_3 \quad (12)$$

With :

$$u_1(t) = \lambda_1 \sqrt{|S|} \times sign\,(S) \quad (13)$$

$$u_2(t) = \lambda_2 \times \int sign\,(S) \times dt \quad (14)$$

$$u_3(t) = \lambda_3 \times sign\,(S) \quad (15)$$

The control input of the TOSM controller is obtained as Equation (16).

$$u(t) = \lambda_1 \sqrt{|S|}.sign(S) + \lambda_2 \int sign(S)dt + \lambda_3 sign(S) \quad (16)$$

where, λ1, λ2 and λ3 are tuning constants of the TOSM controller.

Figure 1 shows block diagram representation of TOSM controller. Through this figure, the TOSM controller is a simple algorithm and easy to implement.

The stability condition is given by the following relation:

$$S\dot{S} < 0 \quad (17)$$

4. 2. Design of the Neural TOSM Controller Neural TOSM controller is a new nonlinear technique, where this proposed technique is a simple algorithm, easy to implement, and more robust. This proposed new nonlinear technique based on a combined neural algorithm and TOSM controller in order to obtain a robust controller. This new nonlinear method (neural TOSM) is a modification of the TOSM method, where *sign(U)* of the TOSM controller is compensated by neural networks. Figure 2 shows the proposed neural TOSM controller. Through this figure, the proposed neural TOSM controller is a simple algorithm and easy to implement.

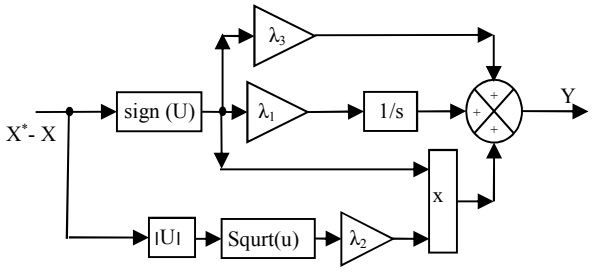

Figure 1. Structure of the TOSM controller

In the proposed neural TOSM controller, feedforward neural network controllers were used to the replace the *sign(U)* functions.

This proposed controller is used in this paper for reducing a stator current, torque, and rotor flux ripples in an AG-based DRWT system using the DTC technique which the inverter was controlled by the modified SVM strategy.

5. DTC CONTROL WITH NEURAL TOSM CONTROLLERS

5. 1. DTC-TOSM Strategy The DTC-TOSM principle is to control the torque and the rotor flux of the AG-based DRWT systems. The rotor flux is controlled utilizing the direct axis voltage V_{dr}, while the torque is controlled utilizing the quadrature axis voltage V_{qr} [41].

As is known, flux and torque ripples which represent the big problems of the classical DTC control with PI controllers can be very hurtful for the AG-DRWT because of the use of the hysteresis comparators and switching table or PI controllers [30]. The major idea was to replace the PI controllers with TOSM controllers and at the same time to conserve the major characteristics of the whole system.

The DTC-TSOM technique, which is proposed to control the torque and rotor flux of the AG-DRWT system is shown in Figure 3.

The magnitude of rotor flux, which can be estimated by the following experssions [23]:

$$\begin{cases} Q_{r\alpha} = \int_0^t (V_{r\alpha} - R_r I_{r\alpha})dt \\ Q_{r\beta} = \int_0^t (V_{r\beta} - R_r I_{r\beta})dt \end{cases} \quad (18)$$

The rotor flux amplitude is given below:

$$Q_r = \sqrt{Q_{r\alpha}^2 + Q_{r\beta}^2} \quad (19)$$

with:

$$\left|\overline{Q_r}\right| = \frac{\left|\overline{V_r}\right|}{w_r} \quad (20)$$

The rotor flux angle is calculated by Equation (21):

$$\theta_r = arctg\left(\frac{Q_{r\beta}}{Q_{r\alpha}}\right) \quad (21)$$

The electromagnetic torque, which can be estimated by Equation (22):

$$T_{em} = -\frac{3}{2} p \cdot (Q_{r\alpha} I_{r\beta} - Q_{r\beta} I_{r\alpha}) \quad (22)$$

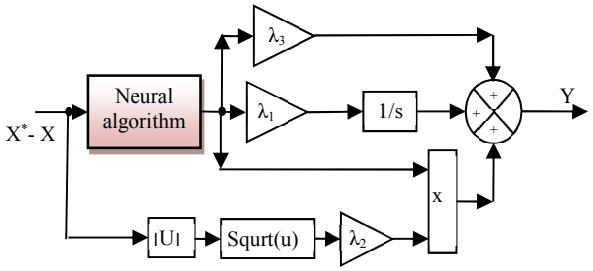

Figure 2. Structure of the command law of the proposed neural TOSM controller

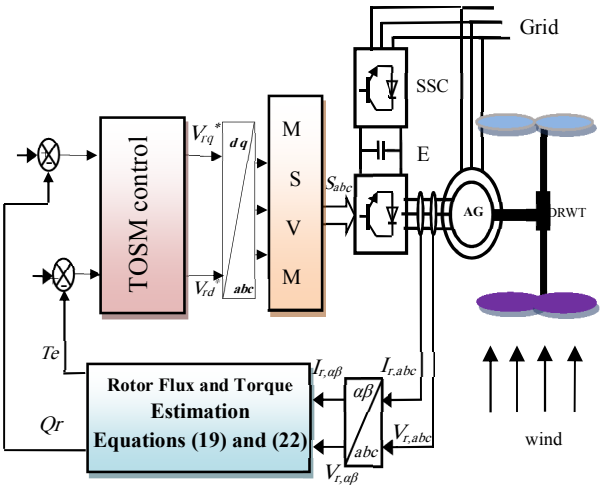

Figure 3. Bloc diagram of the AG with DTC-TOSM

The errors of the electromagnetic torque and rotor flux are shown in Equations (23) and (24).

$$S_{Tem} = T_{em}^* - T_{em} \quad (23)$$

$$S_{Qr} = Q_r^* - Q_r \quad (24)$$

where the surfaces are the flux magnitude error $S_{\varphi r} = \varphi_r^* - \varphi_r$ and the electromagnetic torque error $S_{Tem} = T_{em}^* - T_{em}$.

The sliding surfaces shown in Equations (23) and (24) are used as input to the TOSM control law. Torque and rotor flux TOSM controllers are used to influence respectively on the two rotor voltage components as in Equations (25) and (26).

$$V_{dr}^* = \lambda_1 \sqrt{|S_{Qr}|}.sign(S_{Qr}) + \lambda_2 \int sign(S_{Qr})dt + \lambda_3 sign(S_{Qr}) \quad (25)$$

$$V_{qr}^* = \lambda_1 \sqrt{|S_{Tem}|}.sign(S_{Tem}) + \lambda_2 \int sign(S_{Tem})dt + \lambda_3 sign(S_{Tem}) \quad (26)$$

The controller structure for the TOSM controller for the torque and rotor flux of the DTC control strategy is presented in Figures 4 and 5, respectively.

The DTC-TOSM control technique is proposed by Benbouhenni and Bizon [30] to obtain a minimum rotor

flux and torque ripples and to minimize the chattering phenomenon. The DTC-TOSM strategy improves the performances of the asynchronous generator compared to DTC with PI controllers.

5. 2. DTC-NTOSM Control strategy The DTC control with neural TSOM controllers, which is proposed to control the torque and rotor flux of the AG-DRWT system is shown in Figure 6. This proposed strategy is more simple, easy to implement. This proposed strategy is robust compared to traditional DTC and DTC-TOSM techniques.

The DTC-NTOSM method is a modification of the DTC-TOSM method, where the proposed NTOSM method is used instead of the TOSM controller. The newly proposed method is based on a combination of the TOSM controller and feedforward neural networks in order to improve the characteristics and advantages of the DTC method of the AG-DRWT system.

The controller structure for the neural TOSM algorithms for the torque and rotor flux of the DTC control strategy of the AG-DRWT system is presented in Figures 7 and 8, respectively.

In order to make the feedforward neural networks, we used the Levenberg-marquardt backpropagation algorithm. This algorithm is a simple algorithm. However, the feedforward neural networks structure consists of three layers: hidden layer, output layer, and input layer. The characteristics of the feedforward neural networks used to improve the TOSM controller are summarized in Table 1.

The feedforward neural network training of torque is shown in Figure 9. Figure 10 shows the training plot of

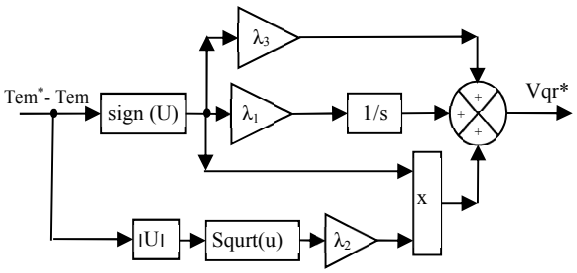

Figure 4. Structure of the TOSM torque controller

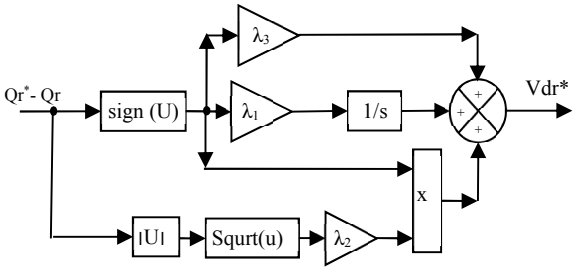

Figure 5. Structure of the TOSM flux controller

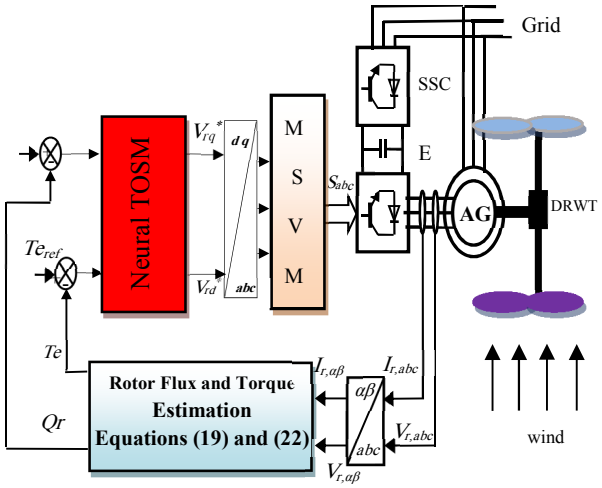

Figure 6. Bloc diagram of the AG with DTC-NTOSM

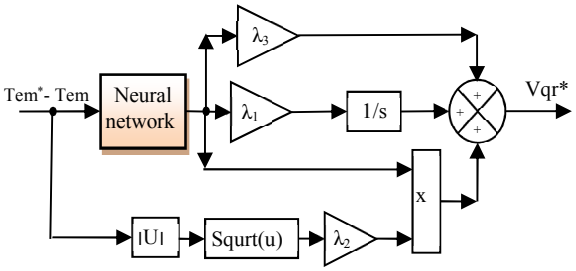

Figure 7. Proposed neural TOSM torque controller

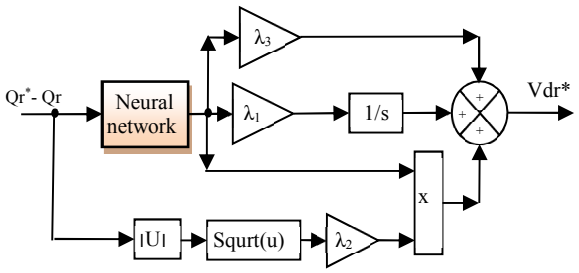

Figure 8. Proposed neural TOSM flux controller

the feedforward neural networks for torque and rotor flux. From this figure, the best training performance is $3.6315e^{-006}$ at epoch 29 for torque and $3.4867e^{-008}$ at epoch 3 for rotor flux. The error plot of feedforward neural networks is shown in Figure 11. Through this figure, we find that the targeting field is [-0.5 0.5] and the training value is R=0.99997, and the output is given by (output = 1*Target+$2.6e^{-005}$) for torque and for rotor flux the training value is R=0.99912, and the output is given by (output = 1*Target+$3.3e^{-006}$). On the other hand, Gradiant, Mu, and Validation Checks are shown in Figure 12 and they represent the properties of the feedforward neural networks of torque. From this figure, the best Gradiant, Mu, and validation checks are $7.1107e^{-006}$, 0.08, and 0 at epoch 29, respectively.

TABLE 1. Parameters of the feedforward neural networks

4	Values
Performances	Mean Squard Error (mse)
Training	Levenberg-Marquardt algorithm (trainlm)
TrainParam.show	50
TrainParam.Lr	0.05
Neurons of output layer	1
TrainParam.goal	0
TrainParam.mu	0.8
Neurons of input layer	1
Coeff of acceleration of convergence(mc)	0.9
Derivative	Default (default deriv)
Neurons of hidden layer	12
Number of hidden layer	1
Functions of activation	Tensing, Purling, trainlm
Number of output layer	1
TrainParam.eposh	200
Number of input layer	1

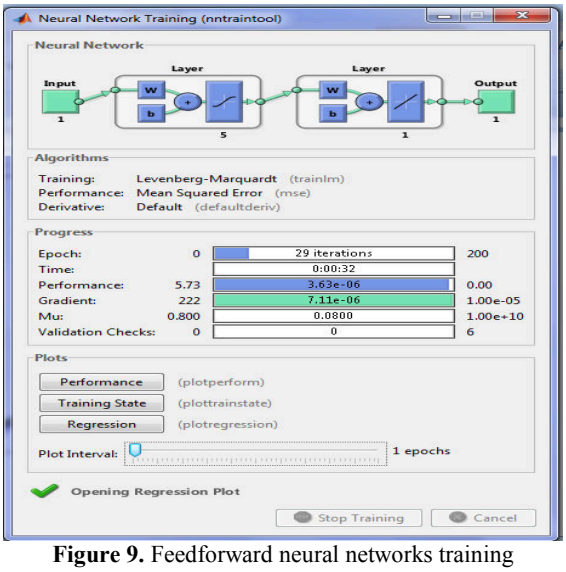

Figure 9. Feedforward neural networks training

6. ANALYSIS AND SIMULATION RESULTS

The designed control techniques are simulated and compared regarding stator current harmonics distortion, rotor flux ripple, reference tracking, torque ripples, and robustness against AG parameter variations.

The simulations are carried out with a 1.5 MW AG attached to a 398 V/50 Hz grid, by using the simulation numerique. The generator parameters used in this work

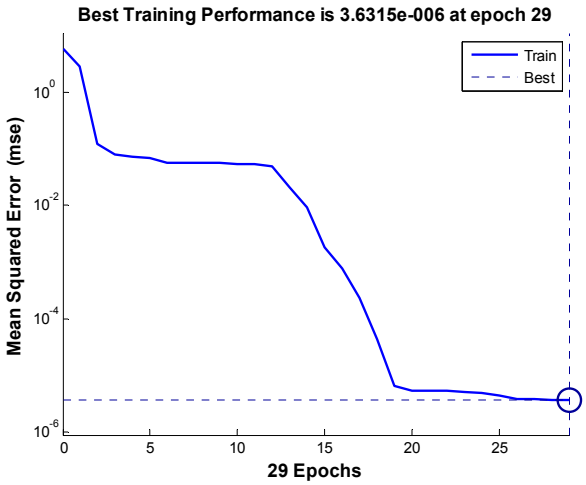

(a) Torque

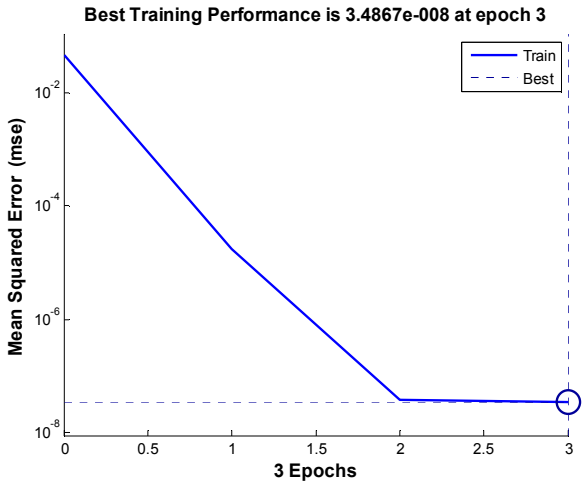

(b) Rotor flux

Figure 10. Training plot

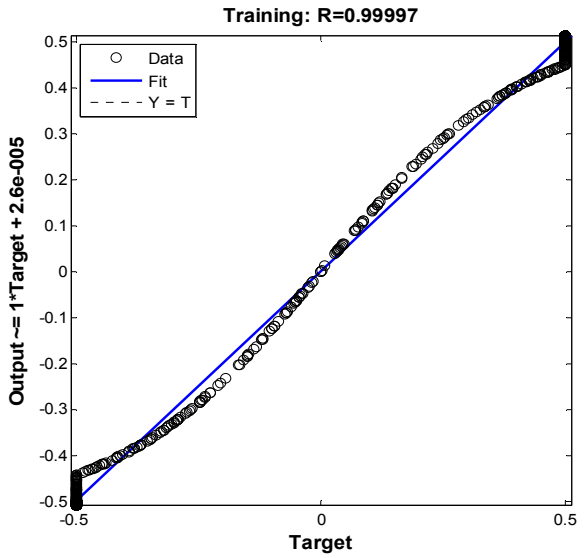

(a) Torque

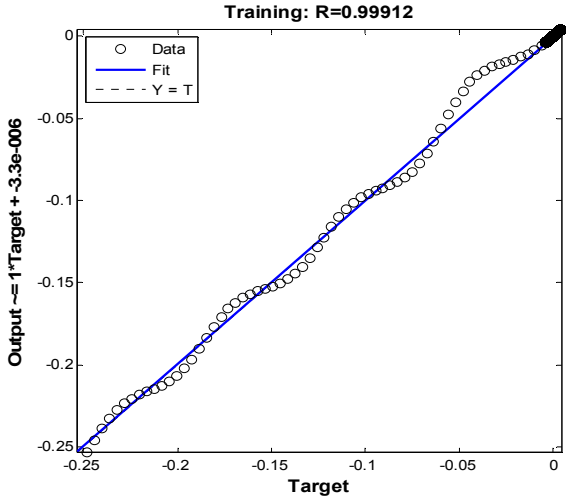

(b) Rotor flux

Figure 11. Error plot

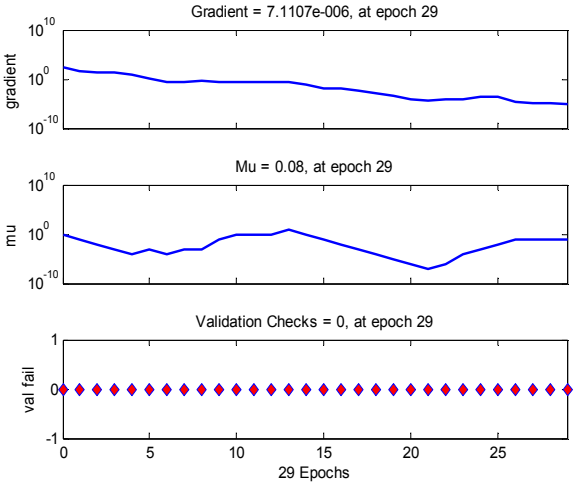

Figure 12. Characteristics of the feedforward neural network for torque

are the same as the generator parameters used in the literature [29-32]. The two nonlinear DTC strategies; DTC-TOSM and DTC-NTOSM are simulated and compared in terms of torque ripple, reference tracking, current ripple, THD value of current, and rotor flux ripple.

A. First test: This test represents the reference tracking test. This test aims to study the behavior of the proposed strategies of nonlinear DTC control by taking the generated speed as constant and equal to the nominal value. As well as knowing which DTC method provides the best results and minimizes electromagnetic torque and rotor flux ripples together. The results obtained are shown in Figures 13 to 20. As it's shown in Figures 15-16, for the two nonlinear DTC strategies, the rotor flux, and torque track almost perfectly their reference values.

Figure 17 shows the stator current of both nonlinear DTC control techniques. It, therefore, confirms that the amplitudes of the currents depend on the state of the drive system and the value of the load rotor flux and torque.

Figures 13 and 14 show the THD value of stator current of the AG-based DRWT system for both nonlinear DTC control strategies. It can be clearly observed through these figures that the THD value is reduced for the DTC-NTOSM (THD = 0.32%) when compared to the DTC-TOSM (THD = 0.50%).

The zoom in the torque, rotor flux, and stator current is shown in Figures 18, 19 and 20, respectively. It can be seen that the DTC-NTOSM control strategy reduced the ripples in torque, rotor flux, and stator current compared to the DTC-TOSM control technique. Based on the results above, it can be said that the proposed DTC-NTOSM control strategy has proven its efficiency in reducing ripples and chattering phenomena in addition to keep the same advantages of the DTC-TOSM control strategy.

The results of this test are summarized in Table 2. Through this table, it can be said that the proposed DTC-

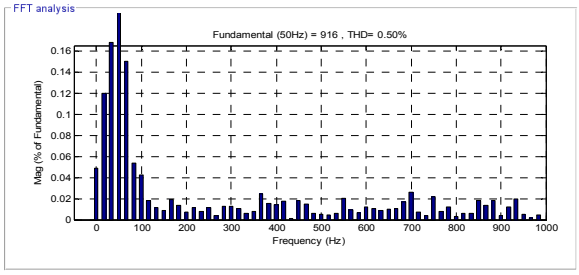

Figure 13. THD (DTC-TOSM)

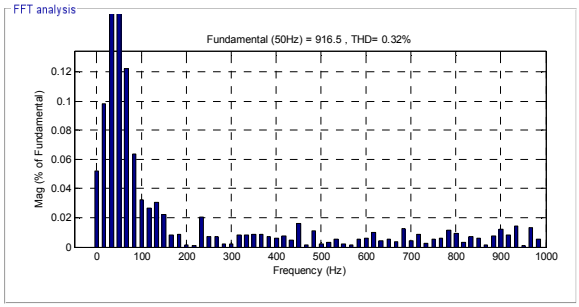

Figure 14. THD (DTC-NTOSM)

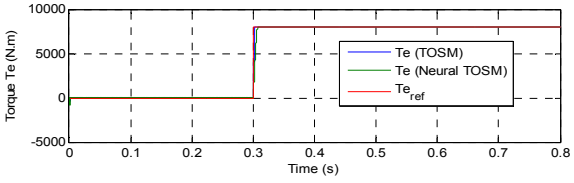

Figure 15. Torque

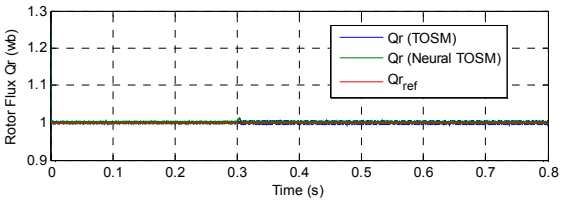

Figure 16. Rotor flux

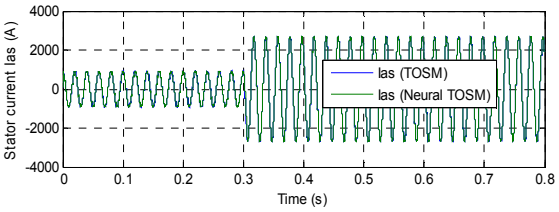

Figure 17. Stator current

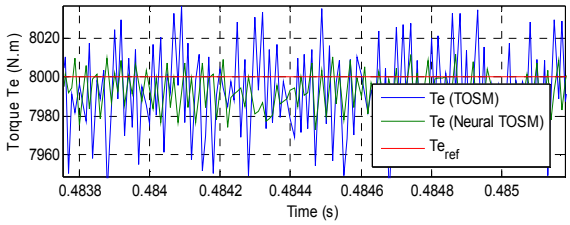

Figure 18. Zoom (torque)

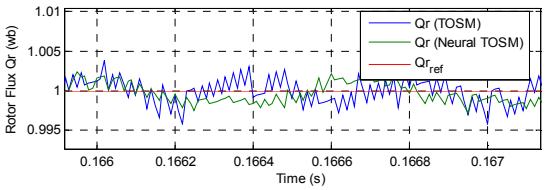

Figure 19. Zoom (rotor flux)

NTOSM control method is better than the DTC-TOSM control strategy in terms of reducing current, torque and rotor flux ripples. Also, in terms of dynamic response. On the other hand, the proposed DTC-NTOSM control method minimized the ripples of current, torque, and rotor flux by about 75%, 70 and 62.50%, respectively, compared to the DTC-TOSM control strategy.

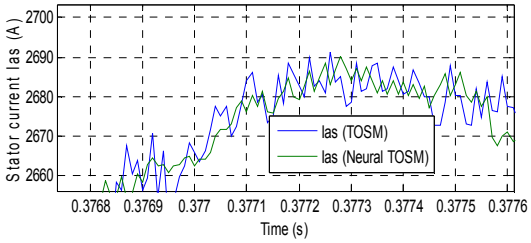

Figure 20. Zoom (current)

TABLE 2. Compare the results obtained from the proposed method with the classical method

Criteria	Strategies	
	DTC-TOSM	**DTC-NTOSM**
Dynamic response (s)	Medium	Fast
Settling time (ms)	High	Medium
Overshoot (%)	Remarkable ≈ 3%	Neglected near ≈ 1%
Torque and flux tracking	Good	Excellent
Sensitivity to parameter change	Medium	Low
Rise Time (s)	Medium	Low
THD (%)	0.50	0.32
Simplicity of converter and filter design	Simple	Simple
Torque: ripple (N.m)	Around 100	Around 30
Simplicity of calculations	Simple	Simple
Rotor flux: ripple (wb)	Around 0.008	Around 0.003
Improvement of transient performance	Good	Excellent
Stator current: ripple (A)	Around 20	Around 5
Quality of stator current	Good	Excellent

The proposed DTC-NTOSM control strategy reduced the THD value of current by about 36% compared to the DTC-TOSM control strategy.

B. Second test: The principal objective of this test is to examine the influence of an asychronous generator parameters variation on the rotor flux, stator current, and torque and behavior for the proposed intelligent nonlinear DTC control strategy. The simulation results are shown in Figures 21 to 28. These figures show that the torque and rotor flux follows the references with high accuracy for all the proposed methods (see Figures 23 and 24). However, the stator current remains sinusoidal (see Figure 25) and is related to the system and the reference value of the torque and rotor flux. On the other hand, we notice by looking at Figures 26 to 28 that the proposed intelligent nonlinear DTC-NTOSM control method significantly reduced the ripples of stator current, torque, and rotor flux compared to the DTC-TOSM control strategy.

Figures 21 to 22 show the THD value of stator current for two proposed DTC control strategies. It can be clearly observed that the THD value is reduced for the proposed intelligent nonlinear DTC-NTOSM control method (0.32%) when compared to the DTC-TOSM control

strategy (0.55%). This result is attractive for dual-rotor wind turbine applications to guarantee the quality and stability of the generated power when the generator parameters are changing. Thus, it can be said that the proposed intelligent nonlinear DTC-NTOSM control method provided better performance than the DTC-TOSM control strategy, and this is what we observed through two tests, as well as the THD ratio and the value of torque and rotor flux ripples (see Table 3).

Table 3 summarizes the results obtained. Through this table, the proposed intelligent nonlinear DTC-NTOSM control method minimized the ripples in the stator current, torque, and rotor flux by about 66.66%, 61.11%, and 60%, respectively compared to the DTC-TOSM control strategy. On the other hand, the proposed DTC-NTOSM control strategy reduced the THD value by about 41.81% compared to the DTC-TOSM control strategy.

On the other hand, this proposed intelligent nonlinear DTC-NTOSM control strategy minimized the THD value of stator current compared to other strategies (see Table 4).

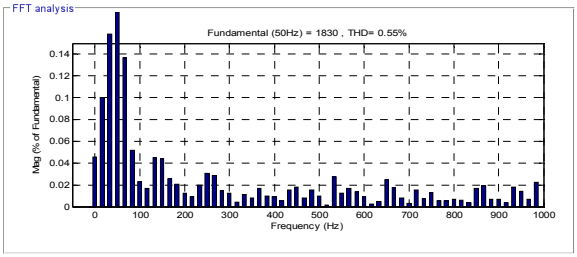

Figure 21. THD (DTC-TOSM)

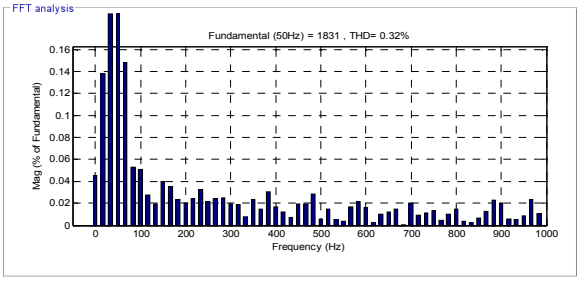

Figure 22. THD (DTC-NTOSM)

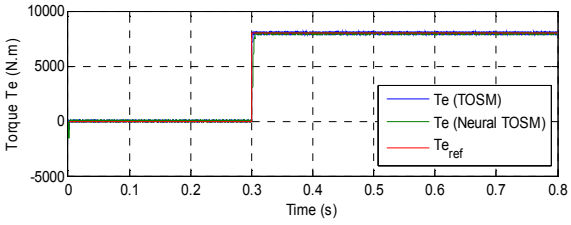

Figure 23. Torque

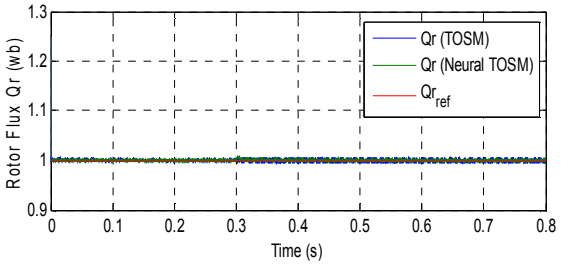

Figure 24. Rotor flux

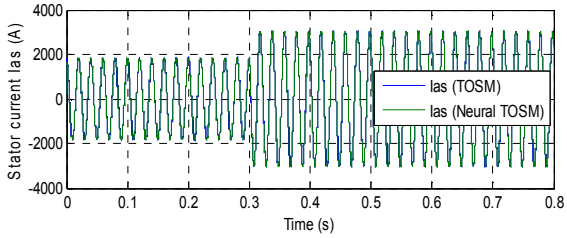

Figure 25. Stator current

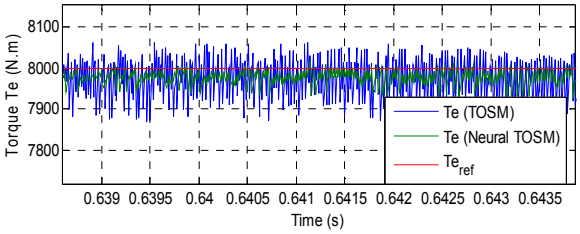

Figure 26. Zoom (torque)

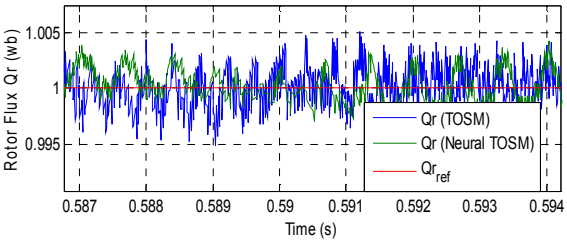

Figure 27. Zoom (rotor flux)

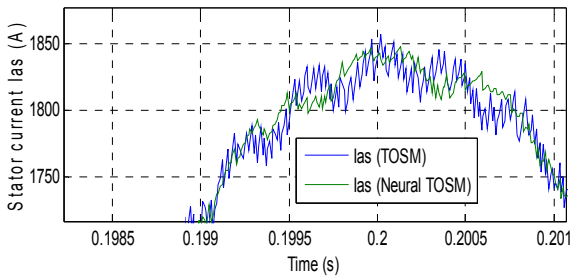

Figure 28. Zoom (current)

TABLE 3. Comparative ripples obtained from the DTC-TOSM with the proposed DTC-NTOSM strategy

	DTC-TOSM	Proposed DTC-NTSOM technique	Ratios
THD (%) of current	0.55	0.32	41.81 %
Rotor flux ripple (wb)	Around 0.01	Around 0.004	60 %
Stator current ripple (A)	Around 60	Around 20	66.66 %
Torque ripple (N.m)	Around 180	Around 70	61.11 %

TABLE 4. Compare the THD value obtained from the proposed method with values for several published methods

Techniques	THD (%)	Reference
DPC control with STA controller	1.66	Ref. [42]
DPC	4.88	Ref. [43]
VF-DPC	4.19	
Fuzzy SMC control	3.05	Ref. [44]
DPC-IP	0.43	Ref. [45]
PI controller	0.77	Ref. [46]
STA-SOSMC controller	0.28	
DPC control with intelligent metaheuristics	4.05	Ref. [47]
Intelligent super twisting sliding mode controller	0.52	Ref. [48]
DTC-SOCSMC	0.98	Ref. [29]
FOC	3.70	Ref. [7]
ISMC	9.71	Ref. [12]
MRSMC	3.14	
Direct FOC with synergetic sliding mode controller	0.50	Ref. [33]
DTC method	7.54	Ref. [49]
DTC method with genetic algorithm	4.80	
Traditional DTC strategy	6.70	Ref. [22]
Fuzzy DTC technique	2.04	
FOC with Type 2 fuzzy logic controller (FOC-T2FLC)	1.14	Ref. [50]
FOC with neuro-fuzzy controller (FOC-NFC)	0.78	
Two-level DTC method	9.87	Ref. [51]
Three-level DTC method	1.52	
Fuzzy 12 sector DTC control	1.74	Ref.[52]
DTC-NTOSM	0.32	Designed technique

where, DPC is the direct power control, VFDPC is the virtual flux direct power control, FOC is the field-oriented control, MRSMC is the multi-resonant-based sliding mode controller and SOCSM is the second-order continuous sliding mode

7. CONCLUSION

This work presents the simulation results of the rotor flux and electromagnetic torque neural third-order sliding mode control technique of a AG-based dual rotor wind turbine, using the modified SVM technique. With results obtained from the numerical simulation, it is clear that for the same operation condition, the proposed nonlinear DTC control with neural TOSM controllers had high effectiveness and performance than the DTC control using TOSM controllers and that is clear in the THD value of stator current which the use of the neural TOSM controller, it is minimized of harmonics more than the TOSM controller.

So, summarizing, the main findings of this research are as follows:

- Minimizes the rotor flux, current and torque ripples.
- Simple nonlinear DTC control was proposed.
- Minimization of the total harmonic distortion of stator current by 36%.
- A new intelligent nonlinear controller was presented and confirmed with numerical simulation.

The work can be extended with neuro-fuzzy-TOSM controllers (NFTOSM) to obtain minimum torque ripple, zero settling time, minimum flux ripple, robust control, and zero steady-state error. DPC-based neural TOSM controllers can also be taken up as an extension of this work.

8. REFERENCES

1. Mohan Kumar, P., Sivalingam, K., Lim, T.-C., Ramakrishna, S. and Wei, H.J.C.T., "Strategies for enhancing the low wind speed performance of h-darrieus wind turbine—part 1", ***Clean Technology***, Vol. 1, No. 1, (2019), 185-204, doi: 10.3390/cleantechnol1010013
2. AlGhamdi, S., Hamdan, I., Youssef, M.M. and Noureldeen, O.J.M., "Development and application of fuzzy proportional-integral control scheme in pitch angle compensation loop for wind turbines", ***Machines***, Vol. 9, No. 7, (2021), 135, doi: 10.3390/machines9070135
3. Alhato, M.M., Ibrahim, M.N., Rezk, H. and Bouallègue, S.J.M., "An enhanced dc-link voltage response for wind-driven doubly fed induction generator using adaptive fuzzy extended state observer and sliding mode control", ***Mathematics***, Vol. 9, No. 9, (2021), 963, doi: 10.3390/math9090963
4. Zhang, Z., Zhao, Y., Qiao, W. and Qu, L.J.I.T.o.I.A., "A discrete-time direct torque control for direct-drive pmsg-based wind energy conversion systems", ***IEEE Transactions on Industry Applications***, Vol. 51, No. 4, (2015), 3504-3514, doi: 10.1109/TIA.2015.2413760
5. Cortajarena Echeverria, J.A., Barambones Caramazana, O., Alkorta Egiguren, P. and Cortajarena Alcorta, J., "Grid frequency and amplitude control using dfig wind turbines in a smart grid", ***Mathematics***, (2021), doi: 10.3390/math9020143
6. Iacchetti, M.F., Marques, G.D. and Perini, R.J.I.T.o.P.E., "Torque ripple reduction in a dfig-dc system by resonant current controllers", ***IEEE Transactions on Power Electronics***, Vol. 30, No. 8, (2014), 4244-4254, doi: 10.1109/TPEL.2014.2360211
7. Amrane, F., Chaiba, A., Babes, B.E. and Mekhilef, S.J.R.R.S.T.-E.E.E., "Design and implementation of high performance field oriented control for grid-connected doubly fed induction generator via hysteresis rotor current controller", ***Revue Roumaine Sciences Techniques Electrotechnique Et Energetique***, Vol. 61, No. 4, (2016), 319-324.
8. Alhato, M.M., Bouallègue, S. and Rezk, H.J.M., "Modeling and performance improvement of direct power control of doubly-fed induction generator based wind turbine through second-order sliding mode control approach", ***Mathematics***, Vol. 8, No. 11, (2020), 1-31, doi: 10.3390/math8112012
9. Djeriri, Y.J.I.J.o.E. and Engineering, E., "Lyapunov-based robust power controllers for a doubly fed induction generator", ***IJEEE***, Vol. 16, No. 4, (2020), 551-558.
10. Benbouhenni, H. and Bizon, N.J.E., "Terminal synergetic control for direct active and reactive powers in asynchronous generator-based dual-rotor wind power systems", ***Electronics***, Vol. 10, No. 16, (2021), 1880, doi: 10.3390/electronics10161880
11. Boudjema, Z., Hemici, B. And Yahdou, A.J.J.O.E.E., "Second order sliding mode control of a dual-rotor wind turbine system by employing a matrix converter", ***Journal of Electrical Engineering***, Vol. 16, No. 3, (2016), 11-11.
12. Quan, Y., Hang, L., He, Y. and Zhang, Y.J.A.S., "Multi-resonant-based sliding mode control of dfig-based wind system under unbalanced and harmonic network conditions", ***Applied Sciences***, Vol. 9, No. 6, (2019), 1124, doi: 10.3390/app9061124
13. Ullah, N., Sami, I., Chowdhury, M.S., Techato, K. and Alkhammash, H.I.J.I.A., "Artificial intelligence integrated fractional order control of doubly fed induction generator-based wind energy system", ***IEEE Access***, Vol. 9, (2020), 5734-5748, doi: 10.1109/ACCESS.2020.3048420
14. Benbouhenni, H.J.I.J.o.E. and Engineering, E., "Seven-level direct torque control of induction motor based on artificial neural networks with regulation speed using fuzzy pi controller", ***Iranian Journal of Electrical and Electronic Engineering***, Vol. 14, No. 1, (2018), 85-94.
15. Nasr, A., Gu, C., Bozhko, S. and Gerada, C.J.E., "Performance enhancement of direct torque-controlled permanent magnet synchronous motor with a flexible switching table", ***Energies***, Vol. 13, No. 8, (2020), 1907, doi: 10.3390/en13081907
16. Heidari, H., Rassõlkin, A., Vaimann, T., Kallaste, A., Taheri, A., Holakooie, M.H. and Belahcen, A.J.E., "A novel vector control strategy for a six-phase induction motor with low torque ripples and harmonic currents", ***Energies***, Vol. 12, No. 6, (2019), 1102, doi: 10.3390/en12061102
17. Boussekra, F. and Makouf, A., "Sensorless speed control of ipmsm using sliding mode observer based on active flux concept", ***Modelling, Measurement and Control A,***, Vol. 93, (2020), 1-4, doi: 10.18280/mmc_a.931-401
18. Mehedi, F., Yahdou, A., Djilali, A.B. and Benbouhenni, H.J.J.E.d.S.A., "Direct torque fuzzy controlled drive for multi-phase ipmsm based on svm technique", ***Journal Européen des Systèmes Automatisés***, Vol. 53, No. 2, (2020), 259-266, doi: 10.18280/jesa.530213
19. Mondal, S., Kastha, D.J.I.J.o.E. and Electronics, S.T.i.P., "Input reactive power controller with a novel active damping strategy for a matrix converter fed direct torque controlled dfig for wind power generation", ***IEEE Journal of Emerging and Selected Topics in Power Electronics***, Vol. 8, No. 4, (2019), 3700-3711, doi: 10.1109/JESTPE.2019.2938012

20. Kebbati, Y., "Modular approach for an asic integration of electrical drive controls", ***International Journal of Engineering, Transactions B: Applications***, (2011).
21. Benbouhenni, H. and Boudjema, Z., "Two-level dtc based on ann controller of dfig using 7-level hysteresis command to reduce flux ripple comparing with traditional command", in 2018 International Conference on Applied Smart Systems (ICASS), IEEE. (2018), 1-8.
22. Ayrir, W., Ourahou, M., El Hassouni, B., Haddi, A.J.M. and Simulation, C.i., "Direct torque control improvement of a variable speed dfig based on a fuzzy inference system", ***Mathematics and Computers in Simulation***, Vol. 167, (2020), 308-324, doi: 10.1016/j.matcom.2018.05.014
23. Benbouhenni, H.J.I.J.o.S.G., "Stator current and rotor flux ripples reduction of dtc dfig drive using fstsmc algorithm", ***International Journal of Smart Grid***, Vol. 3, No. 4, (2019), 226-234, doi:
24. Benbouhenni, H.J.M.J.o.E.M., "Torque ripple reduction of dtc dfig drive using neural pi regulators", ***Majlesi Journal of Energy Management,***, Vol. 8, No. 2, (2019), 21-26.
25. Kelkoul, B. and Boumediene, A.J.E., "Stability analysis and study between classical sliding mode control (smc) and super twisting algorithm (sta) for doubly fed induction generator (dfig) under wind turbine", ***Energy***, Vol. 214, (2021), 118871, doi: 10.1016/j.energy.2020.118871
26. Shah, A.P. and Mehta, A.J., "Direct power control of grid-connected dfig using variable gain super-twisting sliding mode controller for wind energy optimization", in IECON 2017-43rd Annual Conference of the IEEE Industrial Electronics Society, IEEE. (2017), 2448-2454.
27. Azimi, A., Bakhtiari-Nejad, F. and Zhu, W.J.J.o.t.F.I., "Fractional-order control with second-order sliding mode algorithm and disturbance estimation for vibration suppression of marine riser", ***Journal of the Franklin Institute***, Vol. 358, No. 13, (2021), 6545-6565, doi: 10.1016/j.jfranklin.2021.06.022
28. Shah, A.P. and Mehta, A.J., "Direct power control of dfig using super-twisting algorithm based on second-order sliding mode control", in 2016 14th International Workshop on Variable Structure Systems (VSS), IEEE. (2016), 136-141.
29. Boudjema, Z., Taleb, R., Djeriri, Y., Yahdou, A.J.T.J.o.E.E. and Sciences, C., "A novel direct torque control using second order continuous sliding mode of a doubly fed induction generator for a wind energy conversion system", ***Turkish Journal of Electrical Engineering & Computer Sciences***, Vol. 25, No. 2, (2017), 965-975.
30. Benbouhenni, H. and Bizon, N.J.M., "Improved rotor flux and torque control based on the third-order sliding mode scheme applied to the asynchronous generator for the single-rotor wind turbine", ***Mathematics***, Vol. 9, No. 18, (2021), 2297, doi: 10.3390/math9182297
31. Almakki, A.N.J., Jbarah, A.A.N., Mazalov, A., Andrey, M.J.M.T.S. and Technologies, "Improved dfig dftc by using a fractional-order super twisting algorithms in wind power application", ***Transportation Systems and Technology***, Vol. 7, No. 3, (2021), 131-149, doi: 10.17816/transsyst202173131-149
32. Almakki, A.N.J. and Mazalov, A.A., "Improving the efficiency of direct flux and torque control technology for doubly-fed induction generator with a robust control using modified super-twisting algorithms", ***Vestnik Gosudarstvennogo universiteta morskogo i rechnogo flota imeni admirala S. O. Ma-karova,***, Vol. 13, No. 4, (2021), 586–603,, doi: 10.21821/2309-5180-2021-13-4-586-603.
33. Benbouhenni, H. and Bizon, N.J.E., "A synergetic sliding mode controller applied to direct field-oriented control of induction generator-based variable speed dual-rotor wind turbines", ***Energies***, Vol. 14, No. 15, (2021), 4437, doi: 10.3390/en14154437
34. Benbouhenni, H. and Bizon, N.J.E., "Third-order sliding mode applied to the direct field-oriented control of the asynchronous generator for variable-speed contra-rotating wind turbine generation systems", ***Energies***, Vol. 14, No. 18, (2021), 5877, doi: 10.3390/en14185877
35. Benbouhenni, H. and Bizon, N.J.M., "Advanced direct vector control method for optimizing the operation of a double-powered induction generator-based dual-rotor wind turbine system", ***Mathematics***, Vol. 9, No. 19, (2021), 2403, doi: 10.3390/math9192403
36. Yahdou, A., Hemici, B., Boudjema, Z.J.T.M.J.o.M. and Control, "Sliding mode control of dual rotor wind turbine system", ***The Mediterranean Journal of Measurement and Control***, Vol. 11, No. 2, (2015), 412-419.
37. Yahdou, A., Djilali, A.B., Boudjema, Z. and Mehedi, F.J.J.E.d.S.A., "Improved vector control of a counter-rotating wind turbine system using adaptive backstepping sliding mode", ***Journal Européen des Systèmes Automatisés***, Vol. 53, No. 5, (2020), 645-651.
38. Solat, A., Ranjbar, A. and Mozafari, B.J.I.J.o.E., "Coordinated control of doubley fed induction generator virtual inertia and power system oscillation damping using fuzzy logic", ***International Journal of Engineering, Transactions A: Basics***, Vol. 32, No. 4, (2019), 536-547, doi: 10.5829/ije.2019.32.04a.11
39. Douadi, T., Harbouche, Y., Abdessemed, R. and Bakhti, I.J.I.J.o.E., "Improvement performances of active and reactive power control applied to dfig for variable speed wind turbine using sliding mode control and foc", ***International Journal of Engineering, Transactions A: Basics,***, Vol. 31, No. 10, (2018), 1689-1697, doi: 10.5829/ije.2018.31.10a.11
40. Benbouhenni, H., "Direct active and reactive powers command with third-order sliding mode theory for dfig-based dual-rotor wind power systems", ***International Journal of Natural and Engineering Sciences***, Vol. 15, No. 1, (2021), 17-34.
41. Mazaheri Body, K. and Vaez Zadeh, S.J.I.J.o.E., "On line determination of optimal hysteresis band amplitudes in direct torque control of induction motor drives", ***International Journal of Engineering, Transactions A: Basics***, Vol. 15, No. 4, (2002), 329-338.
42. Yaichi, I., Semmah, A., Wira, P. and Djeriri, Y., "Super-twisting sliding mode control of a doubly-fed induction generator based on the svm strategy", ***Periodica Polytechnica Electrical Engineering and Computer Science***, Vol. 63, No. 3, (2019), 178-190.
43. Yusoff, N.A.M., Razali, A.M., Karim, K.A., Sutikno, T., Jidin, A.J.I.J.o.P.E. and Systems, D., "A concept of virtual-flux direct power control of three-phase ac-dc converter", ***International Journal of Power Electronics and Drive System***, Vol. 8, No. 4, (2017), 1776, doi: 10.11591/ijpeds.v8i4.pp1776-1784
44. Boudjema, Z., Meroufel, A., Djerriri, Y. and Bounadja, E., " Fuzzy sliding mode control of a doubly fed induction generator for energy conversion", ***Carpathian Journal of Electronic and Computer Engineering,***, Vol. 6, No. 2, (2013), 7-14.
45. Fayssal, A., Bruno, F. and Azeddine, "C. Experimental investigation of efficient and simple wind-turbine based on dfig-direct power control using lcl-filter for stand-alone mode", ***ISA Transactions***, (2021), 1-34, doi: 10.1016/j.isatra.2021.07.008
46. Mazen Alhato, M., Bouallègue, S. and Rezk, H., "Modeling and performance improvement of direct power control of doubly-fed induction generator based wind turbine through second-order sliding mode control approach," ***Mathematics***, Vol. 8, (2020), doi: 10.3390/math8112012

47. Alhato, M.M., Bouallègue, S.J.M. and Applications, C., "Direct power control optimization for doubly fed induction generator based wind turbine systems", ***Mathematical and Computational Applications***, Vol. 24, No. 3, (2019), 77, doi: 10.3390/mca24030077.

48. Benbouhenni, H.J.J.o.E.E., Electronics, Control and Science, C., "Intelligent super twisting high order sliding mode controller of dual-rotor wind power systems with direct attack based on doubly-fed induction generators", ***Journal of Electrical Engineering, Electronics, Control and Computer Science***, Vol. 7, No. 4, (2021), 1-8.

49. Mahfoud, S., Derouich, A., EL Ouanjli, N., EL Mahfoud, M. and Taoussi, M.J.S., "A new strategy-based pid controller optimized by genetic algorithm for dtc of the doubly fed induction motor", ***Systems***, Vol. 9, No. 2, (2021), 37, doi: 10.3390/systems9020037

50. Amrane, F. and Chaiba, A., "A novel direct power control for grid-connected doubly fed induction generator based on hybrid arti ficial intelligent c ontrol with space vector mo dulation", ***Revue Roumaine Sciences Techniques Electrotechnique Et Energetique***, (2018).

51. El Ouanjli, N., Derouich, A., El Ghzizal, A., Taoussi, M., El Mourabit, Y., Mezioui, K., Bossoufi, B.J.P. and Systems, C.o.M.P., "Direct torque control of doubly fed induction motor using three-level npc inverter", ***Protection and Control of Modern Power Systems***, Vol. 4, No. 1, (2019), 1-9, doi: 10.1186/s41601-019-0131-7

52. Younes, S., Salah, T., Sofia, L.B., Seddik, B., Nasim, U., Ahmad, A.A. and Ali, N.A., "Advanced fuzzy 12 dtc control of doubly fed induction generator for optimal power extraction in wind turbine system under random wind conditions," Vol. 13, (2021), 1-23, doi: 10.3390/su132111593

Persian Abstract

چکیده

در این مقاله، یک کنترل گشتاور مستقیم حالت لغزشی مرتبه سوم عصبی (NTOSM-DTC) برای یک ژنراتور ناهمزمان (AG) مبتنی بر توربین بادی دو روتور (DRWT) پیشنهاد شده‌است. استراتژی DTC کلاسیک با کنترل‌کننده‌های سنتی انتگرال متناسب (PI) به دلیل ویژگی‌های بالایی که در مقایسه با تکنیک سوئیچینگ DTC کلاسیک ارائه می‌دهد، در سال‌های اخیر به طور گسترده در ماشین‌های القایی اعمال شده است. در همین حال، یک اشکال عمده دارد که جریان قابل توجه، شار روتور و موج‌های گشتاور تولید شده توسط کنترل‌کننده‌های PI سنتی است. برای غلبه بر این اشکالات، بهبود این تکنیک کنترل با حذف این کنترلرها در این مقاله طراحی شده است. روش کنترل غیرخطی هوشمند پیشنهادی مبتنی بر جایگزینی کنترل‌کننده‌های PI کلاسیک با کنترل‌کننده‌های TOSM عصبی است که ورودی‌های مشابه این کنترل‌کننده‌ها را خواهند داشت. شبیه‌سازی در نرم‌افزار Matlab انجام شد و نتایج به‌دست‌آمده امکان ارزیابی ویژگی‌های تکنیک کنترل غیرخطی هوشمند پیشنهادی را نسبت به روش سنتی ممکن می‌سازد.

International Journal of Engineering

Journal Homepage: www.ije.ir

Bolt Pre-tension Effect on Performance of Bolted Extended End-plate Moment Connections under Cyclic Loading

H. Noferesti, M. Gerami*

Faculty of Civil Engineering, Semnan University, Semnan, Iran

P A P E R I N F O

Paper history:
Received 23 October 2021
Received in revised form 01 December 2021
Accepted 02 December 2021

Keywords:
Prequalified Connections
End Plate Connection
Abaqus Software

A B S T R A C T

The most important structural part of steel structures is the connections of the building frame. Tests conducted by the American Steel Institute have led to the introduction of prequalified connections, which is a good reference for designing connections in steel structures. In this paper, four bolted stiffened and unstiffened extended end-plate connections have been studied by numerical analysis with ABAQUS software. In this study, to examine the effect of bolt pre-tension rarely studied, a coefficient of pre-tension force, introduced based on the Iranian Steel Structures Design Regulations as well as the US Steel Design Regulations, has been considered. These connections have been modeled cyclically and in a displacement control manner. The cyclic behavior of the connections, dissipated energy, the resisting moment as well as the stress and strain distribution in the connection have been investigated. According to the results, by creating a pre-tension force in the bolts, the resisting moment of the connection would increase. The rate of growth of this resistance in the unstiffened connections was greater than that of the stiffened connections. The maximum increase in resistance was about 27% for the unstiffened connection and about 25% for the stiffened connection. The dissipated energy for the connections also increased with the increment of bolt pre-tension. The energy dissipation incremental rate was enhanced to a maximum of about 31% for the unstiffened connection and up to a maximum of about 24% for the stiffened connection.

***doi**: 10.5829/ije.2022.35.03c.05*

NOMENCLATURE

M	Moment resistance of a joint	K_1	$K_i - K_p$
Mp	Plastic moment capacity	n	Shape parameter
K_i	Initial stiffness	M_0	Reference moment
K_p	Strain-hardening stiffness	φ	Rotation of a joint
C	Empirically coefficient from test data	θ	Rotation of a joint

1. INTRODUCTION

In recent years, the implementation of high-rise steel structures with special steel moment frame systems using prequalified bolted connections has increased significantly. Among these, the main connections utilized are bolted extended end-plate moment connections with and without stiffeners, as well as bolt flange connections due to the high ductility of these connections; considering the limitations mentioned in Regulation AISC-358 [1], they are accepted as prequalified connections.

The bolted extended end-plate moment connections are one of the oldest beam-to-column moment connections, which can only be used with cruciform, box, and I-shaped column sections. Many researchers have examined the behavior of the bolted extended end-plate moment connections.

In 1990, Murray [2] introduced the process of designing four bolted stiffened and unstiffened extended end-plate, and eight bolted stiffened extended end-plate moment connections. Astaneh-Asl [3] explored two 4-bolted unstiffened and stiffened extended end-plate

*Corresponding Author Institutional Email: mgerami@semnan.ac.ir
(M. Gerami)

Please cite this article as: H. Noferesti, M. Gerami, Bolt Pre-tension Effect on Performance of Bolted Extended End-plate Moment Connections under Cyclic Loading, ***International Journal of Engineering, Transactions C: Aspects*** Vol. 35, No. 03, (2022) 531-543

specimens subjected to a cyclic test in 1999. In the first specimen, the ductility of the connection, which eventually led to the buckling of the beam flange, was investigated. In the second specimen, he used I-shaped shim plates between the endplate and the flange of the column. According to his results, the use of a shim plate could improve the performance of the connection.

In 1995, Jaspart and Maquoi [4] inspected the effect of bolt pre-tension on bolted connections. In their research, they proposed equations to estimate the stiffness and strength of the connection. Bahaari and Sherbourne [5] presented an analytical formulation to represent the moment-rotation relationship of extended end plate connections in 1997. A multiple–regression analysis procedure has been used to derive the parameters in terms of the connection description.

In 1998, Faella et al. [6] evaluated the effect of bolt pre-tension on the behavior of bolted connection with T-joint under axial loading by an experimental study. In 2000, Adey et al. [7] evaluated the parameters of beam dimensions, bolt arrangement, endplate thickness, and endplate stiffeners in the potential of energy dissipation of the bolted end-plate connection through testing on 15 connection specimens under cyclic loading. They found that the energy dissipated capacity diminished with increasing beam dimensions, while end-plate stiffeners led to higher energy dissipation. In 2003, Sumner [8] experimentally investigated the behavior of 4 bolted unstiffened extended end-plate and 8 bolted stiffened extended end-plate connections. They observed that the 4 bolted unstiffened extended end-plate connection and the 8 bolted stiffened extended end-plate connection can be used for seismic resistance in steel moment frames. Diaz et al. [9] presented a review on the modeling of joint behavior in steel frames in 2011. Various methods of modeling the rotational behavior of joints, consist of experimental testing, empirical models, analytical models, mechanical models and numerical models reviewed and compared together. Comparing the various methods, experimental and numerical models are more accurate.

In 2011, Gerami et al. [10] indicated that the cyclic behavior of bolted connections, including the bolted extended end-plate moment connections and the T-joint, would depend on the horizontal and vertical arrangement of the connection bolts. They found that by changing the arrangement of the bolts, the probability of rupture in the T-joint would increase compared to the connection with the endplate. Accordingly, they suggested the use of bolted extended end-plate moment connections in situations where the probability of a constructional defect in the execution of structures increases. In 2017, Morrison et al. [11] investigated the effect of end-plate stiffener removal and different bolt arrangement on the 8 bolted stiffened extended end-plate connection. They concluded that removing the end-plate stiffener would be economically viable, despite the need for higher thickness for the endplate.

In 2018, Guo et al. [12] used the static loading test, examined the effect of the strength of high-strength bolt materials and different bolt arrangements on the load bearing capacity as well as deformation of the bolted connection with the cover plate. Elsewhere, having studied parameters such as shear force, bolt diameter, endplate thickness, and the use of end-plate stiffener. In 2019, Elsabbgh et al. [13] evaluated the behavior of bolted un-stiffened extended end-plate moment connection under cyclic and monotonic loading. They observed that shear force had a significant effect on the connection stiffness. Lyu et al. [14] experimentally and numerically explored the effect of bolt pre-tension on the load bearing capacity of bolted connections with cover plate in 2021. They indicated that the effect of bolt pre-tension on the final tear-out failure mode was negligible. On the other hand, out-plane confinement would limit the piling-up of plate material in front of the bolt, which would reduce the related bearing resistance.

Recently, the construction of high-rise buildings has increased significantly worldwide. Studies also show that the bolted extended end-plate moment connections can be used in high-rise steel structures as a part of the lateral seismic resistance system of the moment frame. On the other hand, the implementation of such structures demands considerable time, due to administrative and financial issues and problems. Thus, due to the relatively long time of construction, it is important to consider the loads during construction and control the stability of the structure for different stages of construction.

In a complete structure, all connection bolts are fully pre-tensioned in the prequalified moment connections, and the structure will have acceptable seismic performance. However, during the construction of steel structures, the executive groups of steel structures usually fabricate some story of the structure and tighten the connection bolts, which is called the snug-tightened bolt in this paper. As the construction of the structure is completed, the lower stories, in which the connection bolts are snug-tightened, will be pre-tensioned at least to the level of preloading based on design codes, which in this paper is called the pre-tensioned bolt, so the connections are completed, while some of the upper stories have snug-tightened bolts. This process will continue until the construction of the structure is completed. Accordingly, it is demonstrated that the stiffness of the bolted connections changes during construction and the structural properties vary over time. Hence, to cover the gap between the design regulations, which mainly focus on the design of the structure in a full execution state, it is necessary to examine the seismic behavior of the bolted extended end-plate moment connections in both snug-tightened and pre-tensioned bolt with the effects during the construction of high-rise

structures while also considering the looseness and tightness of the connection bolts until the construction is completed.

A few studies have dealt with the effect of bolt pre-tension on the behavior of bolted extended end-plate moment connections. Considering the significant construction period of high-rise steel structures and their stability depends on bolt pre-tension effect on the behavior of bolted end plate moment connections, this paper has inspected the effect of different levels of bolt pre-tension on the behavior of bolted extended end-plate moment connections.

2. ANALYTICAL FORMULATION

Analytical models use the basic concepts of structural analysis: equilibrium, compatibility and material constitutive relations, to obtain the mathematical formulation leading to computing the rotational stiffness and moment resistance of a joint due to its geometric and mechanical properties.

In 1986, Yee and Melchers [15] proposed a mathematical model that could predict the moment-rotation relationships of bolted extended end plate connections, using the connection dimensions. The model represents a physically based approach to predict the moment-rotation curves, taking into account the possible failure modes and the deformation characteristics of the connection elements. The mathematical formulation to predict the M-θ relationship is given by Equation (1):

$$M = M_p \left\{1 - \exp\left[\frac{-(K_i - K_p + C\theta)\theta}{M_p}\right]\right\} + K_p\theta \quad (1)$$

To use the expression in Equation (1), the parameters M_p, K_i and K_p must be predicted analytically, where are plastic moment capacity, initial stiffness and strain-hardening stiffness, respectively. The value of C is empirically determined from test data. Bahaari and Sherbourne [5] introduced Equation (2) to account for moment-rotation behavior of bolted extended end plate connections based on the stiffener properties of the connection elements in 1997:

$$M = \frac{K_1\phi}{\left(1 + \left|\frac{K_1\phi}{M_0}\right|^n\right)^{(1+n)}} + K_p\phi \quad (2)$$

Where K_1=K_i –K_p; K_i and K_p represent the initial and strain hardening stiffness of the connection, respectively; M_0 is referred to as reference moment; and n is the shape parameter of the M- ϕ curve.

Since the analytical formulations have limitations to account for the local effects on rotational behavior of joints, numerical modeling and experimental testing are proposed to predict the moment-rotation performance of joints with sufficient accuracy [9].

3. FINITE ELEMENT MODELLING

Since the numerical simulation could be account for the important local effects that are difficult to measure with sufficient accuracy, e.g. prying and contact forces between the bolt and the connection component, is used to assess the rotational behavior of bolted extended plate connections. In this paper, the ABAQUS finite element program was used to numerically model the bolted extended end-plate moment connection. To verify the results of the program, one of the experimental bolted connections, studied by Saberi et al. [16], was numerically modeled. Experimental and numerical results will be compared to investigate the verification of numerical results of bolted connections, modeled using ABAQUS.

3. 1. Verification The connection test model was used as an experimental study conducted by Saberi et al. [16] called (EP-R) for verification. The specimen represents a corner connection according to the substructure proposed in FEMA350 [17]. Table 1 reports the geometric specifications of the connection. Test setup and boundary conditions are very important for cyclic loading tests of connections extra page charges are settled. The other opportunity is for an author to reduce the size of the manuscript before final submission. Reduction after processing is not possible.

The test setup and boundary conditions are displayed in Figure 1. As it can be seen, the column is in the horizontal situation and the beam is in a vertical position in this setup. Two pinned supports are used to connect the column to the rigid floor of the laboratory. According to FEMA350 [17], the standard SAC loading is applied by two one-way 50 ton hydraulic jacks to beam tip until specimen failure. To prevent lateral buckling, out-of-plane displacement of beam is constrained using lateral support installed in the load applying point. Strain gauges are placed on beam flange and web, column web, endplate and bolts. Mechanical material properties of various parts of the connection are mentioned in Table 2.

TABLE 1. Geometric specifications of connection components [16]

member	Specification
beam	IPB140
column	IPB200
Number of bolts (material category)	8(A490)
bolt diameter (mm)	M20
Endplate thickness (mm)	25

TABLE 2. Mechanical properties of the used materials [16]

Used part	Materials	Yield Stress (Mpa)	Ultimate stress (Mpa)
Beam, column, end plate	ST37	245	372
bolt	A490	-	1048

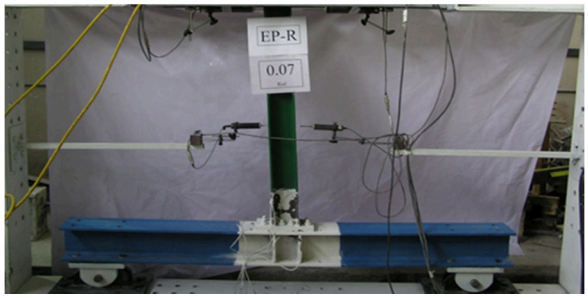

Figure 1. Test setup [16]

In numerical modeling, the dimensions and geometry of the beam, column, and other connection components have been considered similar to the test specimen. As the end plate and beam would be connected through fully penetration groove weld, these two parts were continuously modeled in the finite element model. The connection was subjected to cyclic loading based on SAC loading protocol according to FEMA350 [17] using a two one-way 50 ton hydraulic jack to beam tip until specimen failure, as shown in Figure 2.

3. 2. Comparison of Numerical and Experimental Results

At the end of loading, the formation of the plastic hinge occurred on the flange of the beam at a distance of 7cm from the end plate (Figure 3). On the other hand, as shown in Figure 4, after applying a cyclic load to the numerical model as in the experimental, the plastic hinge has been formed at 7cm away from the endplate.

Figure 5 also reveals the hysteretic moment at the column centerline versus total rotation obtained from the numerical study. The moment capacity in the bolted extended end-plate moment connection at 0.07 rad is 108.3 KN.m for the test specimen and 113.5 KN.m for the numerical model. Comparison of the results of the numerical and experimental study indicates a difference of 4.8%. Thus, the results of the numerical and experimental study are acceptable.

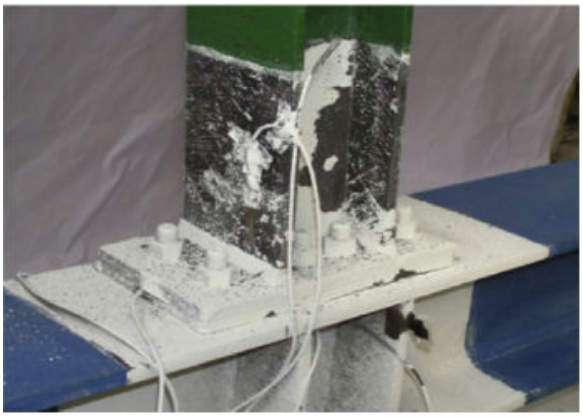

Figure 3. Beam flange deformation at the end of the loading [16]

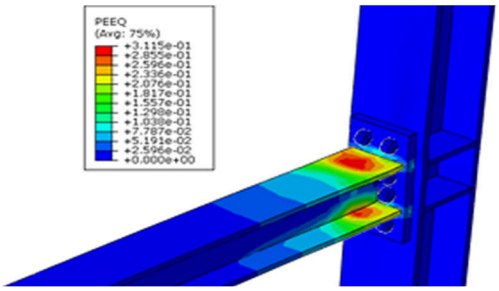

Figure 4. Formation of plastic hinge in beam flange in numerical modeling at the end of loading

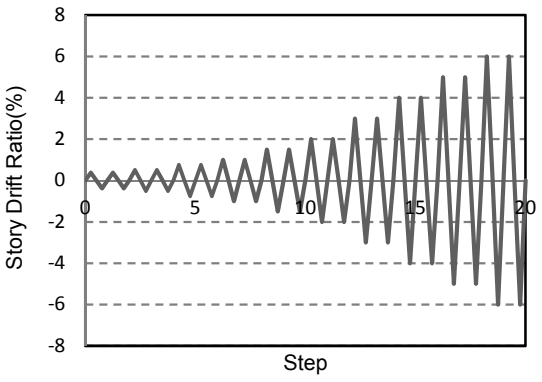

Figure 2. FEMA/SAC2000 loading protocol in accordance of FEMA350 [17]

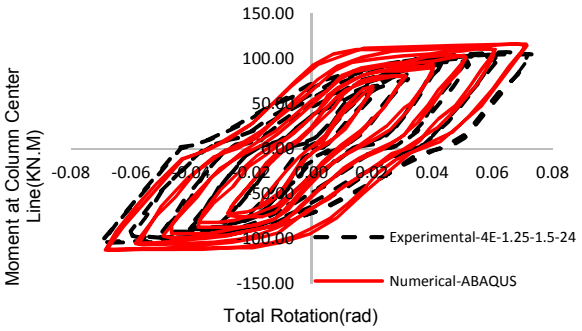

Figure 5. The hysteretic moment at column centerline versus total rotation

4. NUMERICAL STUDY OF THE EFFECT OF BOLT-PRETENSION ON CONNECTION BEHAVIOR

After verification of the numerical model in the ABAQUS program, this section studies the effect of bolt pre-tension on the prequalified connection behavior of the bolted endplate. To numerically examine the effect of pre-tension on the connection behavior, instead of modeling the entire frame, the connection can be separated from the inflection points, where the moment is zero; by placing pinned supports to resist the shear on these points, the substructure will be modeled and analyzed. The substructure represents a beam-to-column connection on the corner of the structure. Figure 6 shows the substructure schematically. The specimen studied in this research has been modeled accordingly. In the numerical study, the length of the beam and column has been considered 3 m. The geometric characteristics of the connection components have been outlined in Table 3. The cyclic loading based on SAC protocol has been applied to the specimen following FEMA350 [17]. Table 3 lists the steel and bolt material properties, which is the criterion for defining the material properties in numerical modeling.

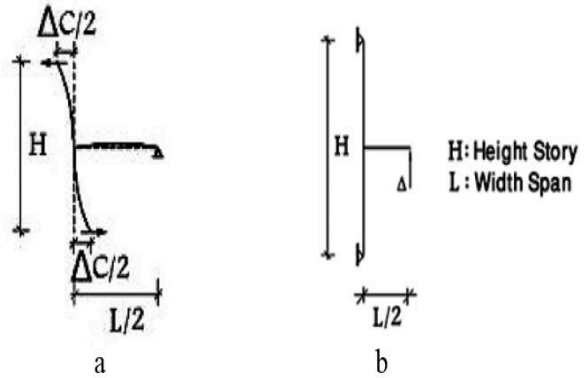

Figure 6. Flexural frame under lateral load: a) external connection isolated from inflection points, b) substructure used in numerical studies of specimens [17]

TABLE 3. Mechanical properties of the used materials [16]

Material	Part	Strain	Stress (Mpa)
ST37	Beam, column, endplate	0.001143	240
		0.02	240
		0.18	360
		0.2	370
		0.35	370
A490	bolt	0.00386	794
		0.0135	1035
		0.0309	1035
		0.2	1048

Figure 7 illustrates the characteristics of the connection components, including beams, columns, bolts, doubler plate, and connection plates, along with the connection geometric parameters reported in Table 4. Figure 8 presents the connection meshing in the program.

To inspect the effect of bolt pre-tension on the cyclic behavior of the bolted extended end-plate moment connections, two types of bolted stiffened and unstiffened extended end-plate moment connections have been studied. Table 5 presents the different levels of pre-tension bolt loads examined. Parameter α in the table indicates the pre-tension coefficient of the bolt relative to the bolt pre-tension following the Iranian national Design Code of Steel Structures [18]. In the model, where α is considered equal to one, the bolt pre-tension of the code is applied to the bolts. In numerical modeling, specimen meshing is done with a 3D stress model and in a structural form. This element uses reduced integration where a node is used at each edge intersection. The use of reduced integration leads to enhanced analysis speed and accuracy. On the other hand, to be able to observe the interaction in the contact surfaces of the connection, the contact element has been used tangentially with a coefficient of friction of 0.3 while the vertical interaction has been used as Hard Contact. This interaction prevents the nodes of the elements from collapsing at the point of contact. Cyclic displacement has been applied as a loading protocol at the end of the beam. This loading is in the form of control displacement. To provide the conditions for lateral restraint of the beam, the connection has been restricted at three points of the beam against lateral displacement. This constraint has been applied by restraining the out-of-plane displacement. Loading has been conducted in two steps. In the first step, pre-tensioning of the bolts has been done and then at the end of the beam, the displacement is applied as a cyclic load. The tie constraint has been utilized to connect the continuous plates, the column flange, and the web to each other. In this way, the nodes of both elements are connected and the relative displacement between them is constrained. This can be represented by welded plates to each other. There are two supports at the top and bottom of the connection. Using the MPC constraint, the top and bottom of the column are connected to a reference point.This point is represented as the restrained plane. The displacement and rotation of these reference points are then constrained. The near areas of connection have meshed finer. Since there is considerable stress concentration in these areas, the elements have been chosen smaller. Larger elements have been selected in the column as there is no expectation of large deformations.

5. DISCUSSION OF RESULTS

After applying the cyclic loading to all the specimens in Table 5, the M-θ hysteresis curves have been presented

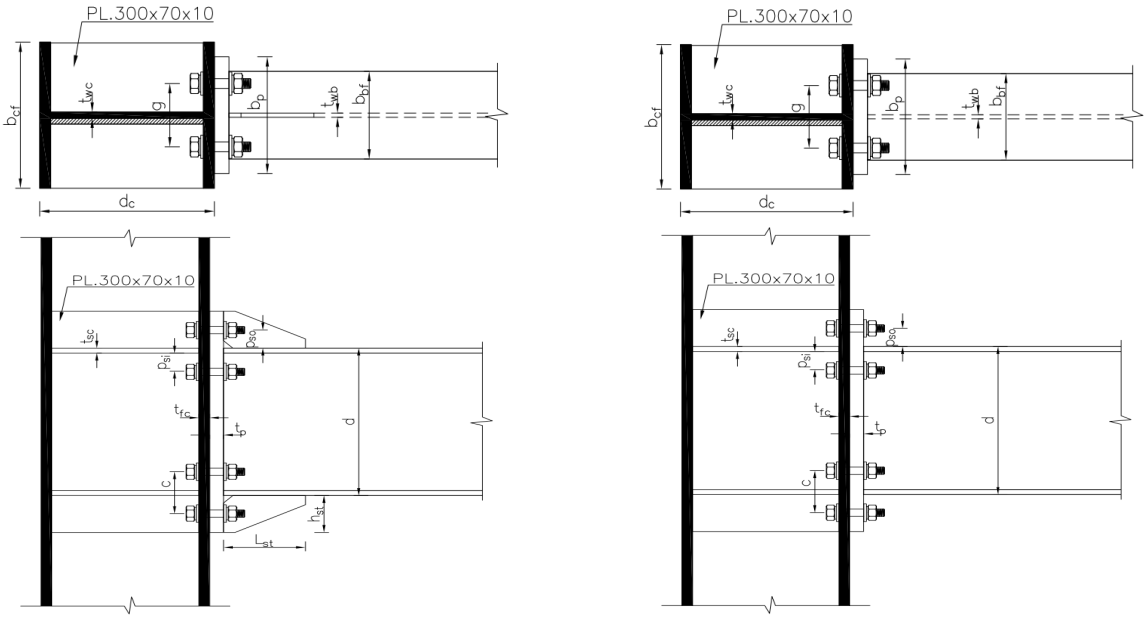

4 Bolted stiffened extended end-plate connection 4 Bolted unstiffened extended end-plate connection

Figure 7. Geometries of the bolted extended end-plate moment connections

TABLE 4. Connection Parameters

Connection type	Beam				Column				Bolt arrangement						End-plate stiffener	
	d	bbf	tfb	twb	dc	bcf	tfc	twc	pfi	pfo	pSi	pso	c	g	Lst	hst
Unstiffened connection	400	180	18.5	8.6	360	300	22.5	12.5	50	50	50	50	113.5	130	-	-
Stiffened connection	400	180	18.5	8.6	360	300	22.5	12.5	50	50	50	50	113.5	130	175	100

TABLE 5. Specimens with various levels of bolt pre-tension

Type of connection	Specimen No.	Specimen name	Type of bolt	$(\alpha * 0.55F_u)$[1]
BUEEP[2]	1	EP-00	A490	0
	2	EP-06	A490	0.6
	3	EP-10	A490	1.0
	4	EP-16	A490	1.6
	5	EP-18	A490	1.8
BSEEP[3]	6	SEP-00	A490	0
	7	SEP-06	A490	0.6
	8	SEP-10	A490	1.0
	9	SEP -16	A490	1.6
	10	SEP -18	A490	1.8

[1] $0.55F_u$ is the bolt pretension level based on Iranian Steel Code

[2] Bolted Un-Stiffened Extended End-Plate

[3] Bolted Stiffened Extended End-Plate

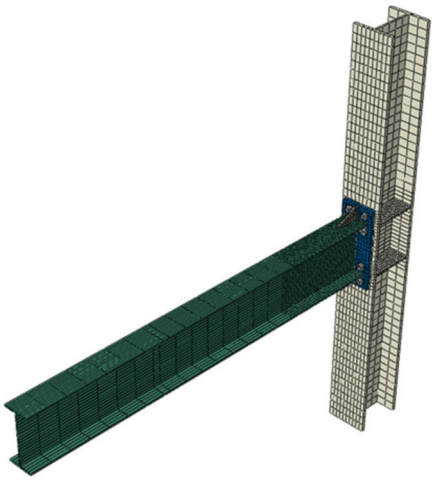

Figure 8. Connection mesh in finite element program

for all specimens related to the 4 Bolted unstiffened extended end-plate moment connection in Figure 9. Figure 10 also shows the hysteresis curves for the 4 bolted stiffened extended end-plate moment connections.

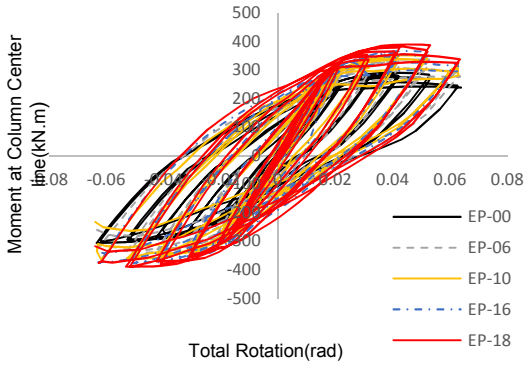

Figure 9. Hysteresis moment curve for different levels of α in BUEEP connection

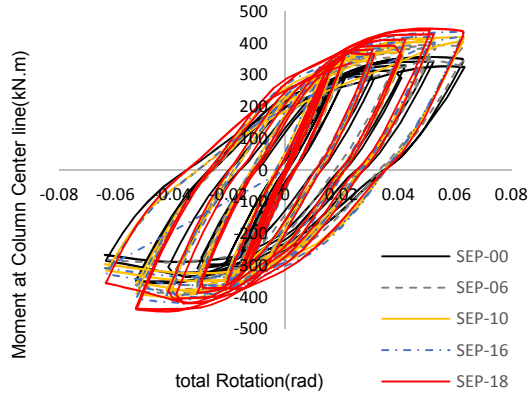

Figure 10. Hysteresis moment curve for different levels of α in BSEEP connection

As displayed in Figures 9 and 10, in the specimens EP-00 and SEP-00, α is 0 and represents the state without pre-tension, called a snug-tightened bolt. The hysteresis moment curve of the snug-tightened specimen has less moment resistance than the specimens with pre-tensioned bolts. The hysteresis curves are stable and have good energy absorption as well as dissipation. An important observation in the hysteresis curves of the snug-tightened specimens is that after the maximum resistance a softening behavior is observed in the specimen. This effect may be due to the local buckling of the beam flange under compression, which will be shown in this research. It can be obtained that the Lack of prying and contact force between bolts, end plate and column flange in snug-tightened specimens leads to more flexibility of the joint. Compared to snug-tightened, in pre-tensioned specimens, the prying and contact force increases due to pre-tensioning which leads to improve maximum moment resistance and more rigidity of the joint. The maximum resistance values of each specimen have been provided in Table 6.

It can be seen in both types of connections, increasing the bolt pre-tension would augment the resistance moment of the connection. It seems that in the unstiffened connection, increasing the bolt pre-tension has had a greater effect on enhancing the resistance. The amount of growth in resistance in the pre-tensioned bolt and for the case where the value of α = 1.8 is about 27% for the unstiffened connection and about 25% for the stiffened connection. Also, the increase in resistance in the unstiffened connection in the pre-tensioned bolt specimens, where α = 1.0, is about 19% and for the stiffened connection is about 17%. Figure 11 indicates the values in Table 6 for the unstiffened connection and Figure 12 for the stiffened connection.

TABLE 6. Maximum moment resistance

Group	Specimen	α	M_{max}(kN.m)	$\frac{M_{max}-M_{ref}}{M_{ref}}$ (%)
BUEEP	EP-00(Ref)	0	306.75	-
	EP-06	0.6	342.04	11.50
	EP-10	1.0	364.63	18.87
	EP-16	1.6	380.80	24.14
	EP-18	1.8	389.65	27.02
BSEEP	SEP-00(Ref)	0	356.89	-
	SEP -P-06	0.6	397.14	11.28
	SEP -P-10	1.0	419.03	17.41
	SEP -P-16	1.6	435.72	22.09
	SEP -P-18	1.8	445.99	24.97

As outlined in Figures 11 and 12, the ascending trend of flexural strength is almost linear. It can also be seen that the difference between the moment resistance for the specimens with α = 1.8 and α =1.6 in both BUEEP and BSEEP connections is less than for other specimens. Accordingly, increasing the bolt pre-tension beyond the value mentioned in the national code of steel structures will lead to increase in a bit amount of moment resistance.

Figures 13 and 14 reveal the envelope curve resulting from the hysteresis curve. Based on the envelope curves, it is observed that the initial stiffness of the snug-tightened specimens is less than the stiffness of the pre-tensioned specimens. This can be due to the enhanced stiffness of the connection and low rotation of the endplate than the column. Also, the resistance of pre-tensioned specimens is higher than that of the snug-tightened. In the specimens without stiffeners after a maximum resistance, softening occurred, which can be due to the local buckling of the flange and plastic strains distribution in the beam flange.

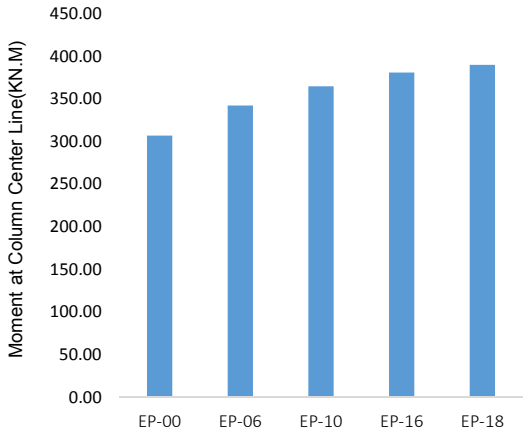

Figure 11. Resisting moment values– BUEEP

Figure 12. Resisting moment values - BSEEP

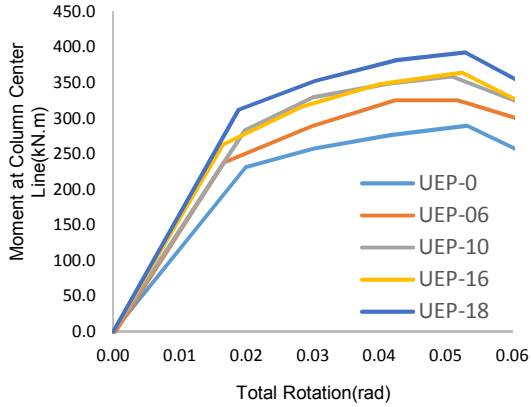

Figure 13. Moment versus total rotation hysteresis envelope of the specimens-BUEEP

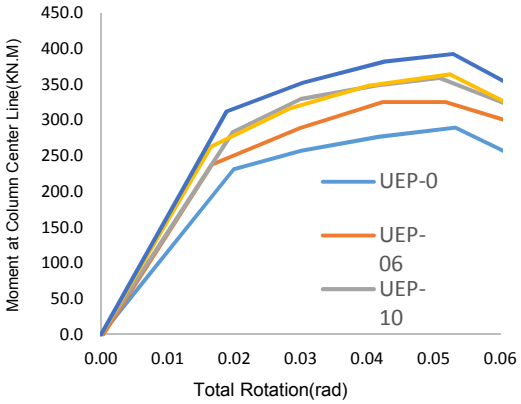

Figure 14. Moment versus total rotation hysteresis envelope of the specimens-BSEEP

Figures 15 to 17 demonstrate the yielded area for BUEEP connections. As can be seen, local buckling is evident in the flange at the end of the cyclic loading. The plastic hinge has occurred near the connection and there is no significant stress in the column. The local buckling of the beam flange, as well as the formation of the plastic hinge near the column, indicate that the cyclic behavior of the column is suitable for seismic loads. In both types of connections, the stress distribution is almost the same formation, but different plastic strains and yield areas can be observed. Figures 18 to 20 reveal the yield areas in the stiffened connection. As can be seen, for the snug-tightened connection, the yielding is more severe as compared to pre-tension. Also, in the pre-tensioned specimen with α = 1.0, a significant amount of beam flange and web near the connection has been yielded. In the pre-tensioned connection with α = 1.8, yield distribution in the beam flange and web decreased but was more severe. As a result, it can be expected that the dissipated energy would also be larger in these connections. In the stiffened connections, the plastic hinge has been formed in the near part of the end-plate stiffener.

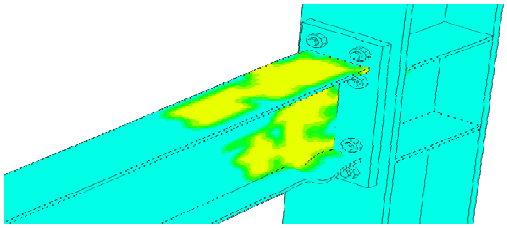

Figure 15. Yielding distribution of material - EP-00

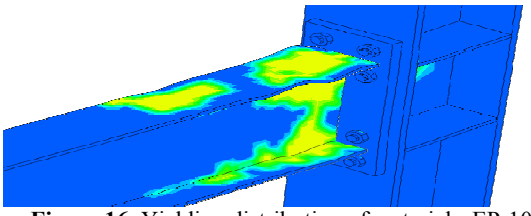

Figure 16. Yielding distribution of material - EP-10

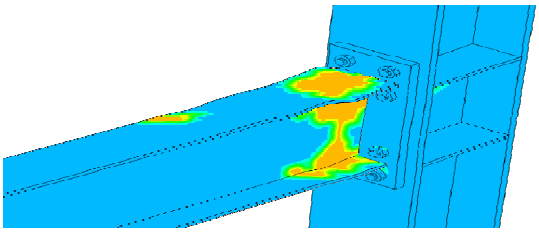

Figure 17. Yielding distribution of material - EP-10

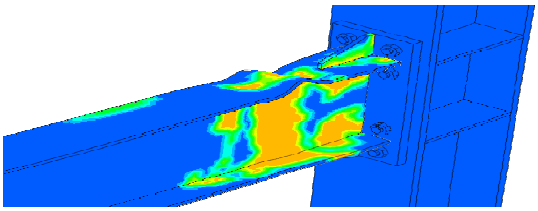

Figure 18. Yielding distribution of material - EP-00

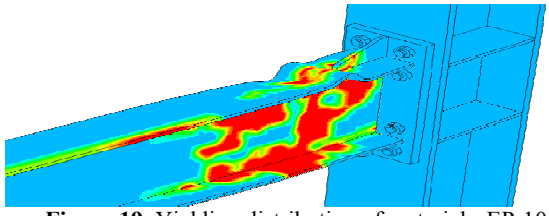

Figure 19. Yielding distribution of material - EP-10

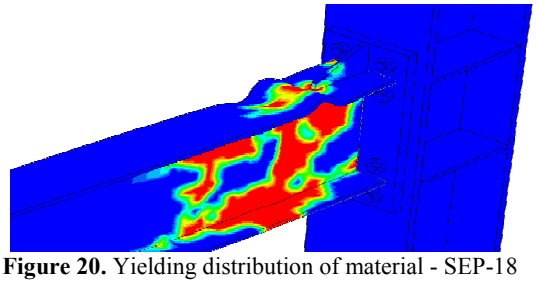

Figure 20. Yielding distribution of material - SEP-18

Major local deformations and buckling in the beam flange occurred after the end-plate stiffener. Also, the yielding areas in the specimen with pre-tension are larger than those of snug-tightened specimen.

Figure 21 shows the energy dissipation curve for the unstiffened specimens and Figure 22 indicates the energy dissipation curves for the stiffened connections. As can be seen in the connections with pre-tension, the energy dissipation has increased. This may be due to the enhanced connection resisting moment and more plastic distribution of deformation, leading to more ductility. Accordingly, more areas are yielded in these connections. Table 7 reports the maximum energy dissipated in different specimens as well as the increase in energy dissipated compared to the snug-tightened.

In Table 7, the energy dissipation of bolted connections with snug-tightened bolts called reference specimen, has been mentioned as E_{ref}. According to Table 7, it can be seen that the energy dissipation has grown with enhancement of α in both types of connections. This is due to more yielding deformation of materials in the specimens with enhanced alpha, resulting in greater ductility and energy dissipation. On the other hand, it is indicated that energy dissipation of pre-tensioned connections to E_{ref} for the unstiffened connection with α = 0.6 is about 18%, for α = 1.0 about 24%, for α = 1.6 about 29%, and for α = 1.8 about 31%.

It is also about 13% for the stiffened connection with α = 0.6, about 16% for α = 1.0, about 21% for α = 1.6,

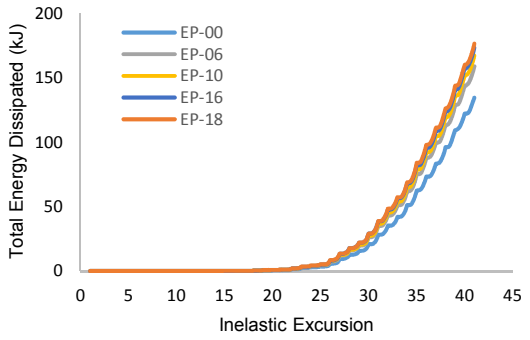

Figure 21. Total energy dissipated –BUEEP connections

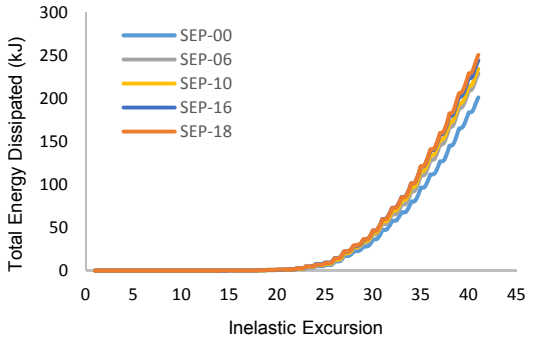

Figure 22. Total energy dissipated –BSEEP connections

and about 24% for α = 1.8. it can be found that enhancement of bolt pre-tension beyond that of proposed by the national design code has not significantly affected the energy dissipation enhancement. This suggests that if the bolt pre-tension is provided in accordance with the design code, the expected energy dissipation is fulfilled.

Energy dissipation for different levels of bolt pre-tension (α) at both end-plate connections with and without stiffeners have been exhibited in Figures 23 and 24.

Bolt stress variation during cyclic loading is a key parameter to be investigated. Figure 25 indicates the bolt axial stress variations with load steps for the BUEEP connections. It can be found that for snug-tightened specimens, the axial stress bolt is initially zero and then grows with load step enhancement during the loading up to cycle 17, where the stress after unloading reaches zero. However, after this cycle, some residual stress will occur. Regarding α = 1.0, the bolt stress, called pre-tension stress, starts from about 550 MPa and diminishes slightly with an increment of load steps. At the end of the load

TABLE 7. Total Energy Dissipation

Group	Specimen	α	E (kJ)	$\frac{E-E_{ref}}{E_{ref}}$ (%)
BUEEP	EP-00(Ref)	0	134.62	-
	EP-06	0.6	159.09	18.18
	EP-10	1.0	167.47	24.41
	EP-16	1.6	173.61	28.97
	EP-18	1.8	176.70	31.26
BSEEP	SEP-P-00(Ref)	0	201.09	-
	SEP -P-06	0.6	228.68	13.72
	SEP -P-10	1.0	234.06	16.40
	SEP -P-16	1.6	244.03	21.35
	SEP -P-18	1.8	250.20	24.42

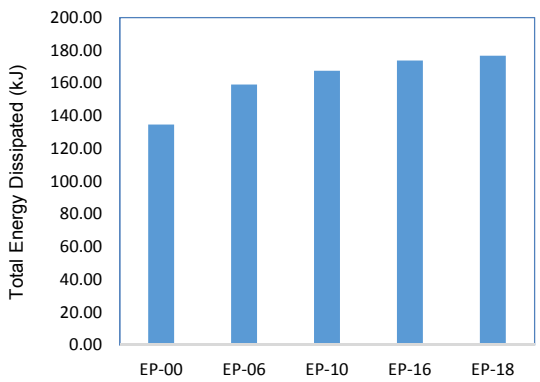

Figure 23. Maximum energy dissipation - BUEEP

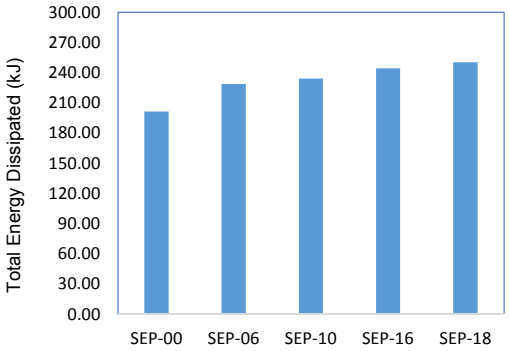

Figure 24. Maximum energy dissipation - BSEEP

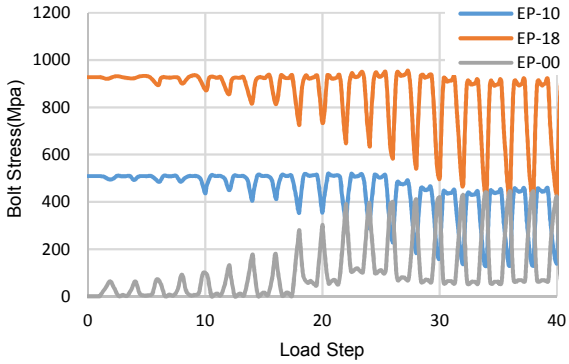

Figure 25. The stress created inside the bolts due to cyclic loading

cycle, the stress dropped to about 175 MPa. Concerning α = 1.8, the bolt pre-tension stress is about 925 MPa and fall with increase of the load cycle. For the last state, the bolt stress would decrease to 411 MPa. It seems that reduction of bolt stress is due to reciprocating of cyclic loading, especially in the higher cycles, as well as the bolts loosening.

The end-plate gap and deformation, which indicates the distance of the endplate and side of the column in which will be provided during cyclic loading, is also studied. Figure 26 illustrates the path of the endplate where the gap was studied along. Figure 27 shows the gap and deformation along the endplate of BUEEP connections and Figure 28 reveals it for BSEEP connections.

In the BUEEP connection, when the upper bolts are subjected to tension, the end-plate gap profile is almost similar for all cases including snug-tightened and pre-tensioned bolted connections, though the amount of end-plate gap will change along. The end-plate deformation will result in the maximum amount of gap for snug-tightened (EP-00) specimen by about 6 mm, while the minimum amount is about 4.5 mm for in EP-18. The end-plate gap distribution is slightly different when the bottom bolts are subjected to tension. In this case, more length of the endplate will be affected and deformed. This

may be due to the local buckling of the beam flange under compression, which affects the deformation of the endplate. As displayed in Figure 28, the end-plate gap profile in the BSEEP connection is almost linear along with the plate. This indicates that there is not much deformation in the endplate. This can be due to the end-plate stiffener causing more rigid endplate in BSEEP connections as compared to BUEEP connections. As shown in Figure 28, the amount of end-plate gap in the snug-tightened specimen is significantly greater than that in pre-tension specimens. Comparing Figures 27 and 28, it can be found that in BUEEP connections and for the EP-10 and EP-18 specimens, the end-plate gap is about 9% and 20% less than that for EP-00 specimens,

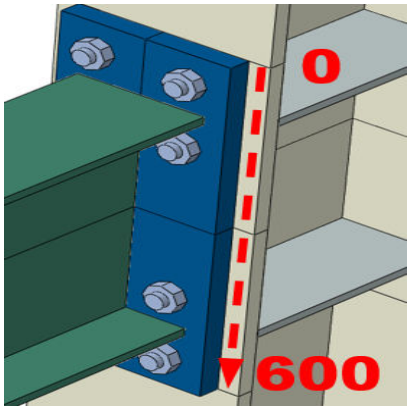

Figure 26. The path along the endplate, the gap studied

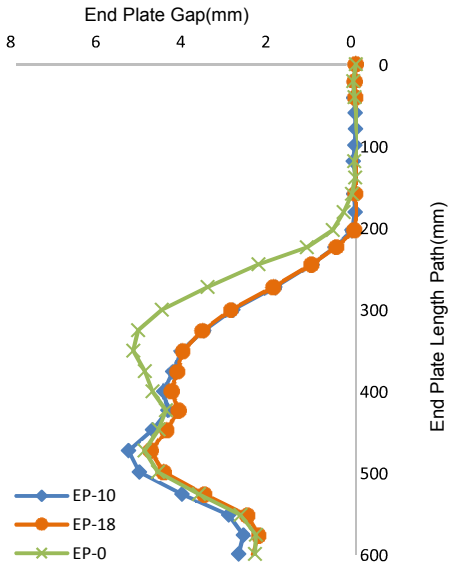

Bottom bolts under maximum tension at the end of cyclic load

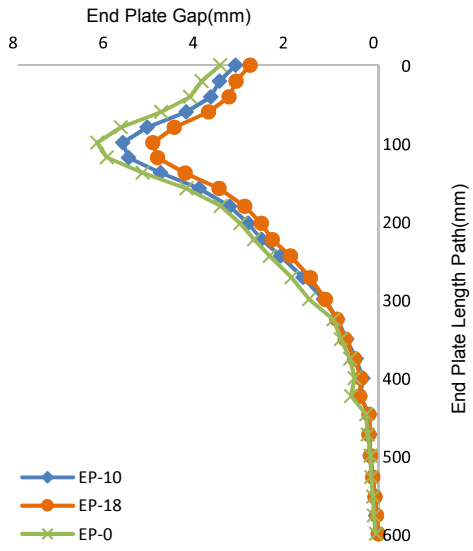

Upper bolts under maximum tension at the end of cyclic load

Figure 27. End-plate deformation of BUEEP

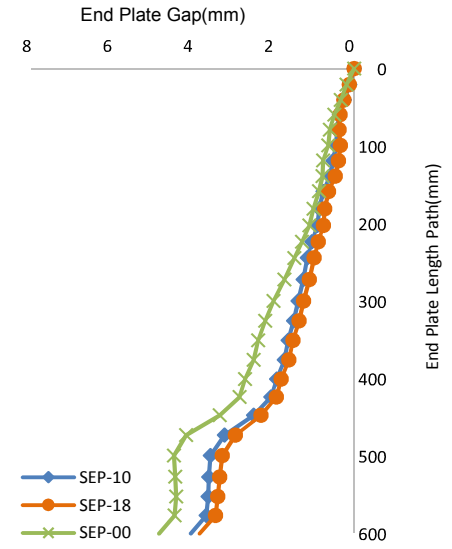

Bottom bolts under maximum tension at the end of cyclic load

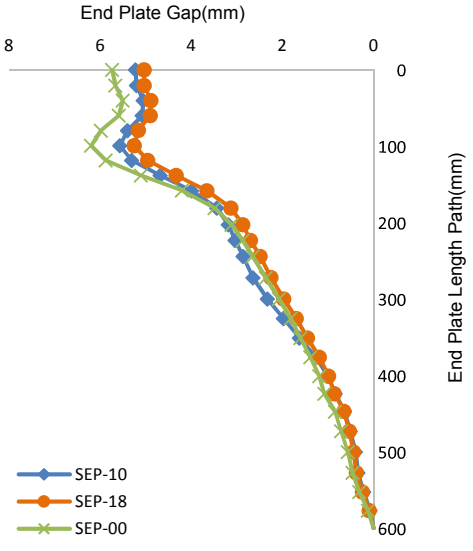

Upper bolts under maximum tension at the end of cyclic load

Figure 28. End-plate deformation of BSEEP

respectively. However, in BSEEP connections and for the SEP-10 and SEP-18 specimens, the end-plate gap has been reduced by 10 and 15%, respectively, compared with the SEP-00 specimen. Generally, the end-plate deformation and gap study in BUEEP and BSEEP connections suggest that in the snug-tightened specimen, the prying action has had a greater effect, leading to a larger amount of end-plate gap than in the pre-tensioned specimens.

6. CONCLUSION

This study dealt with sensitivity analysis of bolt pre-tension effect on bolted extended end-plate moment connection under cyclic loading for BUEEP and BSEEP connections. α was considered as a coefficient of bolt pre-tension to the bolt pre-tension mentioned in the national Design Code of Steel Structures. The hysteresis, total dissipated energy, maximum moment resistance and stress as well as strain distribution at the connections were studied. The results could be summarized as follows:

a. In BUEEP and BSEEP connections, as the bolt pre-tension increased, so did the connection moment resistance. Increased moment resistance in BUEEP connections including EP-18 and EP-10 specimens, compared with EP-00 specimen, was about 27% and 19%, respectively. However, in BSEEP connection including SEP-18 and SEP-10 specimens, the increase of moment resistance compared with SEP-00 specimen was about 25% and 17%, respectively. Thus, it can be deduced that by increasing the bolt pre-tension by 80% beyond the national Design Code of Steel Structures, the moment resistance of the BUEEP and BSEEP connections would only be increased by about 8%. This suggests that if the bolt pre-tension is provided according to the design codes, the cyclic performance of the connection would be sufficiently improved.

b. The increase in dissipated energy for unstiffened connections, including EP-06, EP-10, EP-16, and EP-18 was about 18%, 24%, 29% and 31% respectively. For stiffened connections including SEP-06, SEP-10, SEP-16, and SEP-18, the increased dissipated energy was also about 13%, 16%, 21%, and 24%, respectively. Thus, the bolt pre-tension following the design code, which is equivalent to $\alpha = 1.0$, was associated with an increase in dissipated energy by about 24% compared with the specimens, with α more than 1, which will not significantly increase the dissipated energy.

c. The strain and yielding distribution of connections indicated that inter-story drift was about 6% under cyclic loading and plastic deformations occurred on the beam flange. On the other hand, the column and panel zone would be elastic.

d. In hysteresis moment of specimens with snug-tightened bolt, softening occurred after the maximum resistance, which is due to inelastic deformation and buckling of the beam flange. However, this effect was less pronounced in pre-tensioned bolt connections.

e. In pre-tensioned bolted connections, the bolt pre-tension diminished with increasing load cycles, while the bolt load increased in snug-tightened bolted connections. This may be due to the effect of heightening the cyclic load on the loosening of the bolts.

f. The end-plate deformation and gap were studied. It was observed that in the BSEEP connections, the end-plate stiffener led to linear growth of the gap along with the plate, where the amount of deformation would be insignificant. However, due to the lower stiffness of the endplate in BUEEP connections, a significant amount of gap and deformation would occur along with the plate compared with BSEEP connections. On the other hand, in pre-tensioned bolted connections, an increase of bolt pre-tension would lead to reduced end-plate gap compared with the snug-tightened bolted connections and performance of connection was improved.

g. Studies of various mentioned parameters indicated the bolt pre-tension in accordance with design code ($\alpha=1.0$) will lead to a desirable performance of bolted connections under cyclic loading. In other words, the local study of bolt pre-tension effect shows the importance of pre-tension level in seismic behavior of steel moment resistance frames with bolted extended end plate moment connections, which must be pre-tensioned more than minimum mentioned in regulations.

7. REFERENCES

1. "Prequalified connections for special and intermediate steel moment frames for seismic applications", *A*merican Institute of Steel Construction, (2016).
2. Murray, T.J.E.e.p.c., American institute of steel construction, "Aisc design guide series 4", American Institute of Steel Construction, , (1990).
3. Astaneh-Asl, A., "Seismic design of bolted steel moment-resisting frames", Structural Steel Educational Council, Technical Information and Product Service(Steel Tips), , (1995).
4. Jaspart, J.-P. and Maquoi, R., "Effect of bolt preloading on joint behaviour", in Proceedings of the First European Conference on Steel Structures., (1995), 219-226.
5. Bahaari, M.R. and Sherbourne, A.N.J.J.o.S.E., "Finite element prediction of end plate bolted connection behavior. Ii: Analytic formulation", Vol. 123, No. 2, (1997), 165-175, doi: 10.1061/(ASCE)0733-9445(1997)123:2(165)
6. Faella, C., Piluso, V. and Rizzano, G.J.J.o.S.E., "Experimental analysis of bolted connections: Snug versus preloaded bolts", ***Journal of Structural Engineering***, Vol. 124, No. 7, (1998), 765-774, doi: 10.1061/(ASCE)0733-9445(1998)124:7(765)
7. Adey, B., Grondin, G. and Cheng, J.J.J.C.J.o.C.E., "Cyclic loading of end plate moment connections", ***Canadian Journal of***

Civil Engineering, Vol. 27, No. 4, (2000), 683-701, doi: 10.1139/l99-080

8. Sumner III, E.A., "Unified design of extended end-plate moment connections subject to cyclic loading, Virginia Polytechnic Institute and State University, (2003).
9. Díaz, C., Martí, P., Victoria, M. and Querin, O.M.J.J.o.c.s.r., "Review on the modelling of joint behaviour in steel frames", ***Journal of Constructional Steel Research***, Vol. 67, No. 5, (2011), 741-758, doi: 10.1016/j.jcsr.2010.12.014
10. Gerami, M., Saberi, H., Saberi, V. and Daryan, A.S.J.J.o.C.S.R., "Cyclic behavior of bolted connections with different arrangement of bolts", ***Journal of Constructional Steel Research,***, Vol. 67, No. 4, (2011), 690-705, doi: 10.1016/j.jcsr.2010.11.011
11. Morrison, M., Quayyum, S. and Hassan, T.J.E.S., "Performance enhancement of eight bolt extended end-plate moment connections under simulated seismic loading", ***Engineering Structures***, Vol. 151, (2017), 444-458, doi: 10.1016/j.engstruct.2017.08.040
12. Guo, H., Xiao, F., Liu, Y. and Liang, G.J.J.o.C.S.R., "Experimental and numerical study on the mechanical behavior of q460d high-strength steel bolted connections", ***Journal of Constructional Steel Research***, Vol. 151, (2018), 108-121, doi: 10.1016/j.jcsr.2018.09.012
13. Elsabbgh, A., Sharaf, T., Nagy, S. and Elghandour, M., "Behaviour of extended end plate bolted connections subjected to monotonic and cyclic loads", ***Journal of Constructional Steel Research***, Vol. 190, (2019), 142-159, doi: 10.1016/j.engstruct.2019.04.016
14. Lyu, Y.-F., Li, G.-Q., Wang, Y.-B., Li, H. and Wang, Y.-Z.J.E.S., "Effect of bolt pre-tension on the bearing behavior of high strength steel connections", ***Engineering Structures,***, Vol. 241, (2021), 112491, doi: 10.1016/j.engstruct.2021.112491
15. Yee, Y.L. and Melchers, R.E.J.J.o.S.E., "Moment-rotation curves for bolted connections", ***Journal of Structural Engineering***, Vol. 112, No. 3, (1986), 615-635, doi: org/10.1061/(ASCE)0733-9445
16. Saberi, V., Gerami, M. and Kheyroddin, A.J.E.S., "Seismic rehabilitation of bolted end plate connections using post-tensioned tendons", ***Engineering Structures***, Vol. 129, (2016), 18-30, doi: 10.1016/j.engstruct.2016.08.037
17. "Recommended seismic design criteria for new steel moment frame buildings", Federal Emergency Management Agency, California Universities for Research in Earthquake Engineering, (2000).
18. Iranian National Code of Design and Construction of Steel Structures, , No. 4, (2013).

Persian Abstract

چکیده

در سازه‌های فولادی مهم‌ترین قسمت سازه‌ای اتصالات قاب ساختمانی می‌باشد. آزمایشات انجام شده توسط موسسه فولاد آمریکا منجر به ارائه اتصالات پیش پذیرفته شده است که مرجع مناسبی برای طراحی واحد اتصالات در سازه‌های فولادی می‌باشد. در این مقاله، اتصالات با ورق انتهایی ٤ پیچی با و بدون سخت‌کننده به صورت تحلیل عددی با نرم‌افزار آباکوس مورد مطالعه قرار گرفته‌اند. در این تحقیق، به منظور بررسی میزان تاثیر پیش‌تنیدگی که به ندرت بررسی گردیده، ضریبی از نیروی پیش‌تنیدگی معرفی شده توسط آئین‌نامه طراحی سازه‌های فولادی ایران و همچنین آئین‌نامه طراحی فولاد آمریکا، در نظر گرفته شده است. این اتصالات به صورت چرخه‌ای و جابجایی کنترل مدل‌سازی شده‌اند. رفتار چرخه‌ای اتصالات، انرژی مستهلک شده، لنگر مقاوم و همچنین توزیع تنش و کرنش در اتصال مورد بررسی قرار می‌گیرد. بر اساس نتایج، با ایجاد نیروی پیش‌تنیدگی در پیچ‌ها، مقدار لنگر مقاوم اتصال افزایش می‌یابد. میزان افزایش این مقاومت در اتصالات بدون سخت‌کننده بیش‌تر از اتصالات با سخت‌کننده می‌باشد. مقدار افزایش مقاومت حداکثر برای اتصال بدون سخت‌کننده حدود ۲۷ درصد و برای اتصال با سخت‌کننده حدود ۲۵ درصد است. همچنین انرژی مستلهک شده برای اتصالات با افزایش نیروی پیش‌تنیدگی افزایش می‌یابد. مقدار افزایش انرژی مستهلک شده برای اتصال بدون سخت‌کننده حداکثر حدود ۳۱ درصد و برای اتصال با سخت‌کننده حداکثر تا حدود ٢٤ درصد افزایش می‌یابد.

International Journal of Engineering

Journal Homepage: www.ije.ir

Numerical Study of Twin Jets Interactions using Realizable Model

K. Bouaraour*[a], N. Hebbir[b]

[a] *Laboratory of Materials, Energetic Systems Technology and Environment, University of Ghardaia, Ghardaia, Algeria*
[b] *University of Larbi ben M'hidi, Oum Elbouaghi, Algeria*

PAPER INFO

Paper history:
Received 11 August 2021
Received in revised form 27 November 2021
Accepted 13 December 2021

Keywords:
Nozzles
Turbulent Flow
Merging Point
Combined Point

ABSTRACT

In the present study, we numerically investigated the twin turbulent jets characteristics and turbulent quantities when a solid object is placed between the two nozzles. The two jets are assumed to be isothermal, incompressible and fully developed. Turbulence is modeled by the k-ε Realizable model. The set of Reynolds averaged Navier Stokes equations are solved iteratively by the Fluent software. The numerical model is validated with the experimental results available in the literature. For many Reynolds numbers, it was found that velocities and its gradients decay along the longitudinal direction. The placement of a solid object between the twin jet affects the flow structure behind nozzles due to the curvature effect of the solid object. The converging region is disappeared and the combined points axial position increases with Reynolds number. The evolution is almost linearly with an increase in Reynolds number. The effect of turbulence intensity at the exit of the nozzle is also examined. For a fixed Reynolds number, the axial combined position increases almost linearly with turbulence intensity.

***doi**: 10.5829/ije.2022.35.03c.06*

NOMENCLATURE

S	Distance betweeen nozzles centrline (m)	*U, V*	Mean velocity in the horizontal and vertical directions respectively (m/s)
K	Turbulent kinetic energy (m^2/s^2)	U_i	Mean velocity in the x_i direction (m/s)
x, y	Horizontal and vertical coordinates (m)	**Greek Symbols**	
ℓ	Turbulent length (m)	ρ	Density (kg/m^3)
g	Gravity(m/s^2)	μ	Dynamic viscosity (kg/m.s)
d	Distance between nozzles (m)	ε	Dissipation rate of K (m^2/s^3)
P	Pressure (Pa)	ν	Kinematic viscosity (m^2/s)
Re	Reynolds number	**Subscripts**	
P_K	Turbulent generating source in K equation ($kg/m.s^3$)	0	Related to the outlet of nozzles
u_i	Turbulent fluctuation in x_i the direction (m/s)	t	turbulent

1. INTRODUCTION

Two jets interactions have many practical engineering applications as in the injection systems, burners, mixing and drying processes. Behind the nozzles, interaction between the two jets passes throw many steps until it merge to a single flow. Tanaka [1, 2] has found that flow field of twin jets interaction is characterized by three distinct zones: The converging zone, the merging zone and the combined zone. The converging zone is located between nozzle exit and the point where the inner shear layers of the jets merge. The location where the velocity at the symmetry plane reaches its maximum is called the combined point and denotes that the merging region ends and the combined region begins [3, 4]. The combined zone is downstream of the combined point where the two jets begin to resemble a self-similar single jet. The schematic of the flow field is given by Figure 1 [5]. When Reynolds number is greater than 2000, jets become turbulent as experimentally indicated by Kwon and Seo [6]. Inorder to increase the mixing and combustion efficiencies, Ali et al. [7] have investigated numerically

*Corresponding Author Institutional Email: bouaraourk@yahoo.fr
(B Kamel)

Please cite this article as: K. Bouaraour, N. Hebbir, Numerical Study of Twin Jets Interactions using Realizable Model, ***International Journal of Engineering, Transactions C: Aspects*** Vol. 35, No. 03, (2022) 544-551

the flame holding capability of a supersonic combustor by varying the distance of injector position. Results show that for moderate distance of injector position, large and elongated upstream recirculation can evolve which might be activated as a good flame holder.

Three different numerical models were used to investigate the interaction of twin plane parallel jets [5]. Results showed that position of merging and combined points are strongly affected by the velocity ratio and nozzles spacing. Correlations between the merge and combined points position are also made.

Many experimental and numerical studies focused on the interference region between the twin jets, by varying velocity ratio of the two jets [8], or by varying some geometrical parameters, such as nozzles spacing (S/d) [9-11]. Also, effect of different parameters on the flow structure is studied by Abdel-rahman [12], particularly initial and boundary conditions. Pandey and Kumar [13] studied the effects of pressure ratio and Mach numbers on the flow field along with the flow and lateral directions were examined. The main finding results was that the width of the twin jets spreads linearly downstream and grows with nozzles spacing and the merging length of the two jets can be increased either by reducing nozzles spacing or increasing Mach number. More recently, a numerical study focused on the characteristics of self-oscillating twin jets using the Reynolds Stress Turbulence Model [14]. Many nozzles spacing are used with a fixed Reynolds number (Re = 27000).

Numerical results show that for nozzle spacings of up to four, the two jets merge downstream and oscillate as an equivalent single jet, but for higher nozzle spacing, the two jets do not merge but oscillate separately. Nozzle shape is also examined, but it does not significantly affect the jet decay. In addition, twin oscillating jets produce higher spread and turbulence intensity over a wider area, which may be beneficial for cooling of hot devices in industrial applications.

In order to investigate the spatial evolution of a dual-plane jet flow and to contribute to a better understanding of the dual-plane jet flow, DNS was performed by Hao et al. [15]. For a fixed nozzle spacing, the combination of transport, convection, production, pressure, and viscous dissipation is well explained in the different flow regions. It is demonstrated that even in the highly intermittent region, the characteristics of small-scale motions are already close to the fully developed flow.

CFD software was used to solve a three-dimensional flow situation [16].The studied configuration is formed by nine impinging jets in a square array used to cool a plate maintained at constant heat flux. Numerical code has been executed using three k-ε models and the SST k-ω model. Numerical results show that this last has been noticed to be in maximum agreement with the experimental results, and the local heat transfer coefficient has been declining with the rise in separation distance.

In spite of numerous experimental and numerical investigations of turbulent jet flows, few studies focused on the investigation of flow characteristics when an obstacle is placed between the two jets, because of the difficulty of accurately predicting the interaction of the flow structures.

The aim of this study is to investigate numerically the effect of surface curvature when placing different solids bodies between the two parallel jets. The Fluent software was used to solve the governing dynamic equations, due to its efficiency to provide reasonable solutions in many earlier studies [17-20]. Turbulent velocities and turbulent fields were examined and compared with the configuration without obstacle.

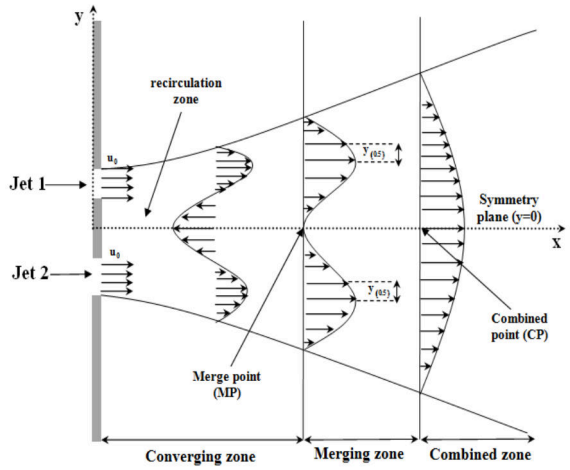

Figure 1. Schematic diagram of dual jet

2. GEOMETRICAL CONFIGURATION

The studied geometrical configurations are shown in Figure 2. We consider two parallel turbulent jets where the distance between nozzles centerline is **S** and nozzles width is **d,** where **S/d=6**. Dimensions adopted in the transverse and longitudinal directions are respectively **100d** and **200d**. Configurations are respectively denoted by A and B. The Configuration B is characterized by the placement of a a half-circle object between nozzles compared to the configuration A.

The working fluid is air, which is assumed to be incompressible and with constant thermo-physical properties. Reynolds numbers based on the inlet velocity and the nozzle width varied from 2000 to 8000. Turbulence intensity distribution at the nozzles exit section is uniform and takes different values (1, 3 and 6%).

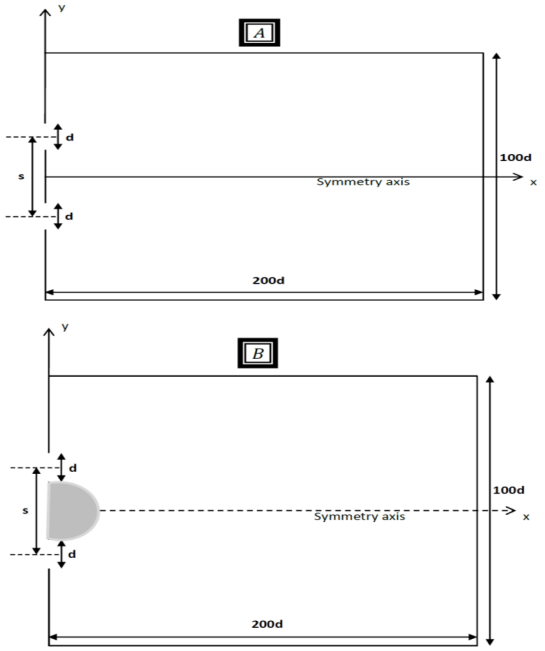

Figure 2. Geometrical configurations

3. GOVERNING EQUATIONS AND BOUNDARY CONDITIONS

The governing equations for turbulent flow are described mathematically by the Reynolds averaged Navier-Stokes equations (RANS). The flow is assumed to be steady, two dimensional, and fully developed at the exit of the nozzles. Turbulence intensity at the exit of the nozzles varies from 1 to 6%. The RANS equations can be written as follows:

$$\frac{\partial U_i}{\partial X_i} = 0 \tag{1}$$

$$\frac{\partial (U_i U_j)}{\partial X_j} = -\frac{1}{\rho}\frac{\partial P}{\partial X_i} + \frac{\partial}{\partial X_j}\left[\nu \frac{\partial U_i}{\partial X_j} - \overline{u_i u_j}\right] \tag{2}$$

Where turbulence stress is approximated as:

$$\overline{u_i u_j} = \frac{2}{3}\delta_{ij}K - \nu_t\left(\frac{\partial U_i}{\partial X_j} + \frac{\partial U_j}{\partial X_i}\right) \tag{3}$$

The Kronecker delta is given by δ_{ij} =1 if (i=j) and δ_{ij} =0 if (i ≠ j), and the turbulence viscosity is defined as:

$$\nu_t = C_\mu \frac{K^2}{\varepsilon} \tag{4}$$

Turbulence is modeled with the Realizable model [21] based on the k-ε model derived from the stationary Reynolds average Navier-Stokes equations. The Realizable model is an eddy-viscosity model similar to the standard k-ε model, which perform better results than the standard k-ε model when flow separation and recirculation occur. The concept of realizability introduced by Lumley signifies that the model must respect asymptotic situations. For exemple K and ε must never be negative. This model seems well adapted to circular jets, boundary layers with strong adverse pressure gradients, flows with strong curvature and vortex flows.

$$\frac{\partial (\rho U_i K)}{\partial X_i} = \frac{\partial}{\partial X_i}\left(\mu + \frac{\mu_t}{\sigma_K}\frac{\partial K}{\partial X_i}\right) + P_K - \rho\varepsilon \tag{5}$$

$$\frac{\partial (\rho U_i \varepsilon)}{\partial X_i} = \frac{\partial}{\partial X_i}\left(\mu + \frac{\mu_t}{\sigma_\varepsilon}\frac{\partial \varepsilon}{\partial X_i}\right) + C_{\varepsilon 1}\frac{\varepsilon}{K}P_K - \rho C_{\varepsilon 2}\frac{\varepsilon^2}{K+\sqrt{\nu\varepsilon}} \tag{6}$$

The analytical derivation results in a model with constants that are different from those employed in the standard k- ε model, where P_k is the sheer production of turbulence kinetic energy.

$$C_\mu = \frac{1}{A_0 + A_s U^* \frac{K}{\varepsilon}} \tag{7}$$

$$A_s = \sqrt{6}cos\emptyset \tag{8}$$

with:

$$\emptyset = \frac{1}{3}cos^{-1}(\sqrt{6}W) \tag{9}$$

$$W = S_{ij}S_{jk}S_{ki}/\tilde{S} \tag{10}$$

And the strain tensor is defined as:

$$S_{ij} = \frac{1}{2}\left(\frac{\partial U_i}{\partial X_j} + \frac{\partial U_j}{\partial X_i}\right) \tag{11}$$

$$\tilde{S} = \sqrt{S_{ij}S_{ji}} \tag{12}$$

$$U^* = \sqrt{S_{ij}S_{jk} + \tilde{\Omega}_{ij}\tilde{\Omega}_{ij}} \tag{13}$$

$$\tilde{\Omega}_{ij} = \Omega_{ij} - 2\epsilon_{ij}\omega_k \tag{14}$$

$$\Omega_{ij} = \overline{\Omega_{ij}} - \epsilon_{ij}\omega_k \tag{15}$$

Where ω_k is the angular velocity and $\overline{\Omega_{ij}}$ is the rotation coefficient tensor. The constants of this model are presented in Table 1.

TABLE 1. Constants of the Realizable k-ε model

A_0	$C_{\square 1}$	$C_{\square 2}$	σ_k	σ_ε
4.04	1.42	1.68	1	1.2

The boundary conditions for the considered problem can be expressed as:

- The velocity at the exit of the nozzles is: $U=U_0$ and $V_0=0$.
- Turbulent kinetic energy and its dissipation rate at the exit of the nozzles are respectively: $K_0=1.5(U_0I_0)^2$ and $\varepsilon_0=K_0^{1.5}/\ell$. ℓ: is a turbulent length scale (ℓ=d/10 m) and I_0 is the inlet turbulent intensity.
- At the gap of the outlet, gradients of all variables in the y- direction are set to zero.
- The velocity boundary conditions were fixed to zero over the solid walls.
- Symmetry condition is applied on the horizontal axis between nozzles.

4. NUMERICAL METHODS

The governing equations are discretized using finite volumes schemes and the solver is the commercial CFD code FLUENT 6.3.26. The velocity components are calculated at a staggered grid while the scalar variables are calculated at the main grid (not staggered). For coupling of mass and momentum equations, SIMPLEC algorithm is used [22]. The discretization of pressure is based on the PRESTO! scheme. The Green-Gauss cell based scheme is used for gradient discretization. Second-order upwind central differencing is used for flow terms, while first order upwind central differencing is used for turbulent kinetic energy and turbulent dissipation rate. The convergence criterion was taken 10^{-4} for the normalized residual of each equation. We have used relaxation factors of 0.7 for velocities, 0.8 for turbulent quantities and 0.3 for the pressure.

5. VALIDATION AND GRID INDEPENDENCE

To validate the mathematical model and numerical methods, it has been tested with the experimental results reported by Anderson and Spall [23]. The configuration of Anderson and Spall is like the configuration **A** with a nozzles spacing (S/d =9). Dimensions along the transverse and longitudinal directions are 100d and 150d, respectively. The Reynolds number was set at 6000 and the turbulent intensity at the outlet of the nozzles was 3.6%. Numerical simulations are obtained with non-uniform meshes of different grid sizes: 450 × 168, 480 × 252 and 600 × 336 (see Figure 3). The deviation between the two last meshes was less than 1.23% for the maximum vertical velocity and less than 2% for the maximum turbulent kinetic energy.

The maximum turbulent viscosity deviation reaches 0.95%, so mesh 3 was adopted (see Table 2).

Our numerical results show a good agreement with the experimental data, as indicated in Figure 4.

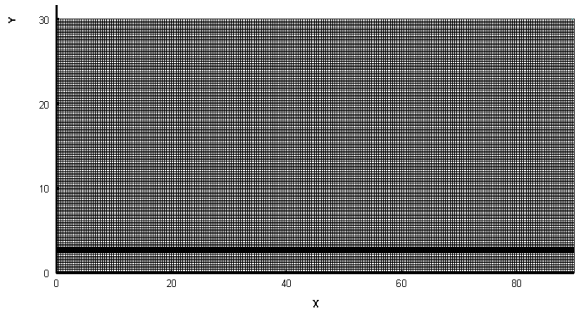

Figure 3. Computational grid structure

TABLE 2. Deviation between meshes

	Mesh1	Mesh 2	Mesh 3
V_{max} (m/s)	1.51	1.615	1.63
K_{max} (m²/s)	24.28	27.73	28.27
$\nu_{t\ max}$ (m²/s³)	1.789	1.772	1.789

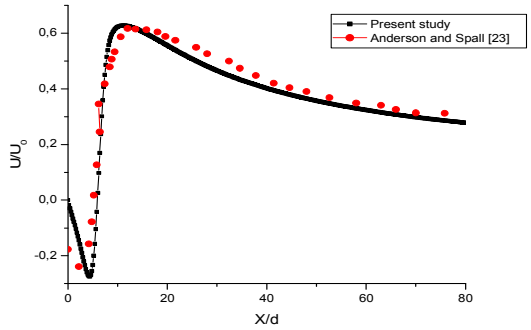

Figure 4. Axial mean velocity distribution along the symmetry axis for S/d=9

6. RESULTS AND DISCUSSION

We Considered two plan jets (S/d=6), where the Reynolds number was varied from 2000 to 8000. Turbulence intensity at the inlet of nozzles was varied from 1 to 6%. Figure 5 shows the evolution of the axial mean velocity on the symmetry axis (y=0) for different Reynolds numbers. The merging point is determined by the stagnation point, where the mean velocity is zero in the symmetry axis.

6. 1. Configuration A The mean axial velocity distribution at the symmetry axis is indicated in Figure 5. Since the velocity ratio is one (the same exit velocity for the two nozzles), the axial location of merge and combined points always occurs in the symmetry axis (y=0) as mentioned by Lin and Sheu [24], and by Anderson and Spall [23].

For a fixed Reynolds number, a very slight effect has been detected on the velocity profiles only for high Reynolds numbers, as indicated in Figure 6.

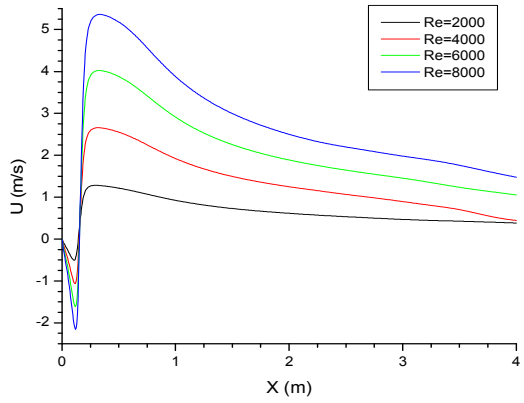

Figure 5. Axial mean velocity distribution along the symmetry axis for I_0=1%

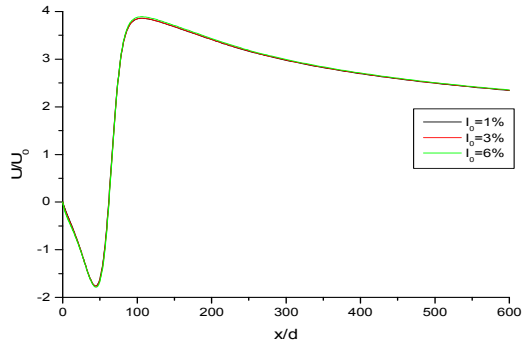

(a)

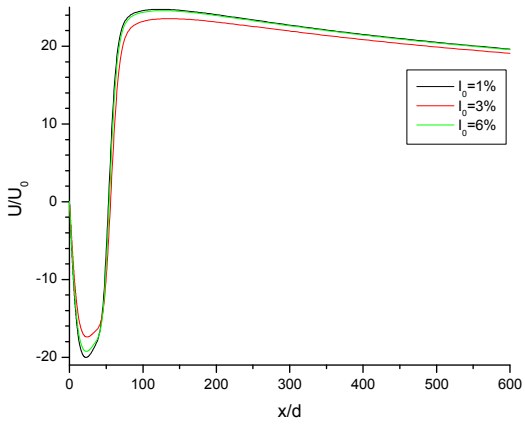

(b)

Figure 6. Intensity effect along the symmetry axis for:(a) Re=2000,(b) Re=8000

6. 2. Configuration B For the chosen Reynolds numbers, the figure below shows the evolution of the axial velocity at the symmetry axis for different turbulence intensities.

From Figure 7, we can see that velocity profiles maintain their self-similarity behaviour. We can also see that the combined point axial position increases with Reynolds number. The locations of combined points are illustrated in Table 3.

We have varied the intensity of the turbulence at the exit of the nozzles from 1 to 6%. For a fixed Reynolds number (Re=2000), no significant effect is observed on

I_0=1 %

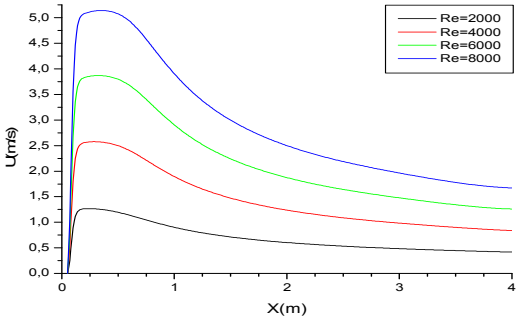

I_0=3%

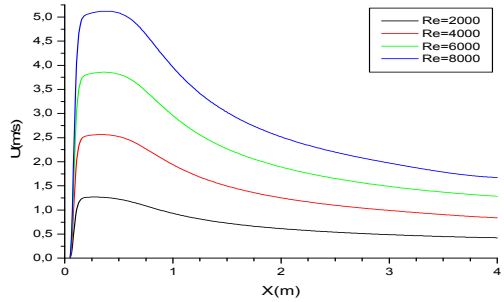

I_0=6%

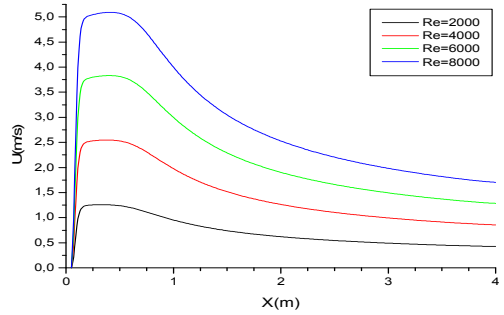

Figure 7. Axial mean velocity distribution along the symmetry axis

the mean axial velocity as indicated in Figure 8. The same behaviour is observed for the other Reynolds numbers.

It's noted that for a fixed spacing, combined point position is affected by turbulence intensity at the exit of nozzles. Combined point axial location increases almost linearly with turbulence intensity.

For a given turbulence intensity (3%), the x-velocity contours are given in Figure 9 for different Reynolds numbers. At the nozzle exit, high velocities lead to entrainment of fluid in the shear layers of the jets. Entrainment rates in the region between the two jets are high, which results in a region of very low pressure between the jets.

The velocities and its gradients decay along x-axis. Due to the effect of entrainment in the shear layer, the velocity between two jets increases with x-axis.

The Figure 10 demonstrates the vectors of mean velocity for Re=8000 and for I_0=1%. It is observed that the width of twin jets increased further downstream. The region from nozzle outlets to the merge point is the merge region, which is characterized by reverse flow in this region.

From merge point inner shear layers of the jets begin to merge and are characterized as velocity is zero. The merge point is also characterized by high pressure

TABLE 3. Locations of combined points for different Reynolds numbers

	X_{CP}(m) for I_0=1%	X_{CP}(m) for I_0=3%	X_{CP}(m) for I_0=6%
Re=2000	0.23	0.27	0.335
Re=4000	0.285	0.33	0.38
Re=6000	0.325	0.36	0.40
Re=8000	0.35	0.38	0.41

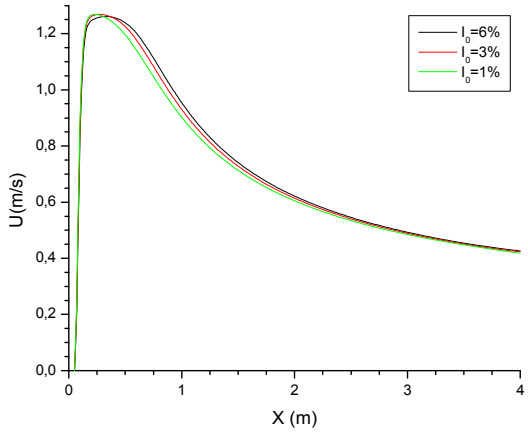

Figure 8. Axial mean velocity distribution along the symmetry axis for Re=2000.

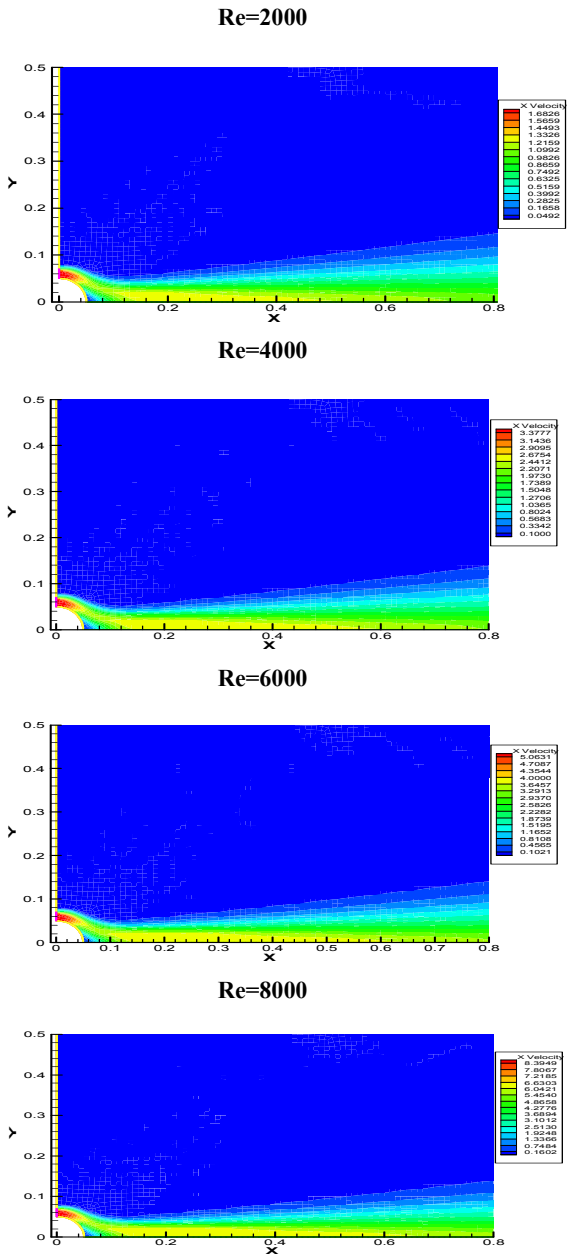

Figure 9. Axial velocity contours for configuration B

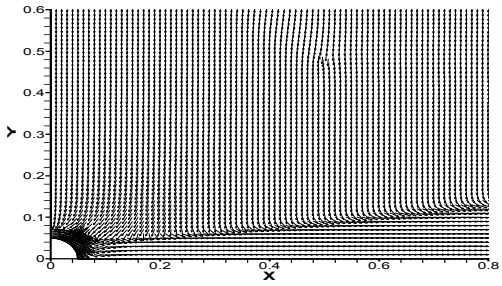

Figure 10. Vectors of mean velocity for Re=8000 and I_0=1%.

7. CONCLUSION

In this study, we have investigated numerically the effect of placing a solid object between nozzles in twin turbulent jets. The Realizable based k-ε model is used to describe turbulence, and the commercial Fluent 6.3.26 code is used for the resolution of the transport equations. The numerical model is validated with the experimental data available in the literature. Two different configurations have been tested:

The configuration **A,** which is characterised by the presence of two similar nozzles, where the nozzles width is **d** and the nozzles centerlines is **S (S/d=6)**. The configuration **B** differs from the first configuration by the placement of a solid object between nozzles. The Reynolds number at the exit of nozzles varies between Re=2000 and Re=8000. The flow structure for configuration B, is strongly affected behind nozzles compared to the configuration A. Due to the curvature effect of the solid object, the converging region is disappeared and the combined points axial position is strongly affected. The evolution is almost linearly with the increase of the Reynolds number. Combined points axial positions increases with Reynolds number and velocities and their gradients decay along the longitudinal direction. The effect of the turbulence intensity at the exit of the nozzle is examined. Three values are tested: I_0=1%, I_0=3 and I_0=6%. For a fixed Reynolds number, the axial combined position increases almost linearly with turbulence intensity.

8. REFERENCES

1. Tanaka, E.J.B.o.J., "The interference of two-dimensional parallel jets: 1st report, experiments on dual jet", ***Bulletin JSME***, Vol. 13, No. 56, (1970), 272-280, doi: 10.1299/jsme1958.13.272
2. Tanaka, E.J.B.o.J., "2nd report, experiments on the combined flow of dual jet", ***Bulletin JSME***, Vol. 17, (1974), 920-927, doi: 10.1299/jsme1958.17.920
3. Fairuzov, Y.V. and Arvizu, H.J.J.H.T., "Numerical solution for transient conjugate two-phase heat transfer with heat generation in the pipe wall", ***Journal of Heat Transfer***, Vol. 124, No. 6, (2002), 1213-1218, doi: 10.1115/1.1470170
4. Tenchine, D. and Moro, J.P., "Experimental and numerical study of coaxial jets", Vol. 3, (1997), 1381–1387, doi: 10.1080/18811248.1998.9733851
5. Mohammadi, M., Samadi, S. and Najafpour Darzi, G.J.I.J.o.E., "Production of single cell protein from sugarcane bagasse by saccharomyces cerevisiae in tray bioreactor", ***International journal of engineering, Transactions A: Basics***, Vol. 29, No. 8, (2016), 1029-1036, doi: 10.5829/idosi.ije.2016.29.10a.13
6. Kwon, S.J. and Seo, I.W.J.E.i.f., "Reynolds number effects on the behavior of a non-buoyant round jet", ***Experiments in Fluids***, Vol. 38, No. 6, (2005), 801-812, doi: 10.1007/s00348-005-0976-6
7. Ali, M., Ahmed, S. and SADR, A.A., "A numerical study on mixing of transverse injection in supersonic combustor", ***International journal of engineering, Transactions A: Basics***, (2004).
8. Elbanna, H. and Sabbagh, J.J.A.j., "Interaction of two nonequal plane parallel jets", ***AIAA Journal***, Vol. 25, No. 1, (1987), 12-13, doi: 10.2514/3.9571
9. Nasr, A. and Lai, J.J.E.i.f., "Two parallel plane jets: Mean flow and effects of acoustic excitation", ***Experiments in Fluids***, Vol. 22, No. 3, (1997), 251-260, doi: 10.1007/s003480050044
10. Elbanna, H., Gahin, S. and Rashed, M.J.A.j., "Investigation of two plane parallel jets", ***AIAA Journal***, Vol. 21, No. 7, (1983), 986-991, doi: 10.2514/3.8187
11. Elbanna, H., Sabbagh, J. and Rashed, M.J.A.j., "Interception of two equal turbulent jets", ***AIAA Journal***, Vol. 23, No. 7, (1985), 985-986, doi: 10.2514/3.9027
12. Abdel-Rahman, A.J.W.t.o.F.M., "A review of effects of initial and boundary conditions on turbulent jets", ***WSEAS Transactions on Fluid Mechanics***, Vol. 4, No. 5, (2010), 257-275, doi:
13. Pandey, K., Kumar, V.J.I.J.o.E.S. and Development, "Cfd analysis of twin jet flow at mach 1.74 with fluent software", ***International Journal of Environmental Science and Development***, Vol. 1, No. 3, (2010), 423-428, doi: 10.7763/IJESD.2010.V1.81
14. Mosavati, M., Balachandar, R. and Barron, R.J.P.o.F., "Characteristics of self-oscillating twin jets", ***Physics of Fluids 33***, Vol. 33, No. 3, (2021), 035129, doi: 10.1063/5.0033869
15. Hao, K., Tian, A., Zhou, Y.J.I.J.o.H. and Flow, F., "Characteristics of small-scale motions in a dual-plane jet flow", ***International Journal of Heat and Fluid Flow***, Vol. 91, (2021), 108851, doi: 10.1016/j.ijheatfluidflow.2021.108851
16. Singh, P., Grover, N.K., Agarwal, V., Sharma, S., Singh, J., Sadeghzadeh, M. and Issakhov, A.J.M.P.i.E., "Computational fluid dynamics analysis of impingement heat transfer in an inline array of multiple jets", ***Mathematical Problems in Engineering***, Vol. 2021, (2021), doi: 10.1155/2021/6668942
17. Pandey, K., Kumar, V.J.I.J.o.C.E. and Applications, "Cfd analysis of four jet flow at mach 1.74 with fluent software", ***International Journal of chemical engineering and applications***, Vol. 1, No. 4, (2010), 302, doi: 10.7763/IJCEA.2010.V1.53
18. Zheng, X., Jian, X., Wei, J. and Wenzheng, D.J.I.J.o.A.E., "Numerical and experimental investigation of near-field mixing in parallel dual round jets", ***International Journal of Aerospace Engineering***, Vol. 2016, (2016), doi: 10.1155/2016/7935101
19. Boussoufi, M., Sabeur-Bendehina, A., El Ganaoui, M., Morsli, S. and Ouadha, A.J.E.P., "Numerical simulation of the flow field analysis in the mixing twin jets", ***Energy Procedia***, Vol. 139, (2017), 161-166, doi: 10.1016/ j.egypro.2017.1.190
20. Jafarmadar, S.J.I.J.o.E., "The effects of pressure difference in nozzle's two phase flow on the quality of exhaust mixture", ***International Journal of Engineering-Transactions B: Applications***, Vol. 26, No. 5, (2013), 553-562, doi: 10.5829/idosi.ije.2013.26.05b.12
21. Shih, T.-H.J.C. and Fluids, "J. A new _< k-ε> eddy-viscosity model for high reynolds number turbulent flows-model development and validation", ***Computers and Fluids***, Vol. 24, (1995), 227, doi: 10.1016/0045-7930(94)00032-T
22. Baliga, B. and Patankar, S.J.N.H.T., "A new finite-element formulation for convection-diffusion problems", Vol. 3, No. 4, (1980), 393-409,
23. Anderson, E.A. and Spall, R.E.J.J.F.E., "Experimental and numerical investigation of two-dimensional parallel jets", ***Journal of Fluids Engineering***, Vol. 123, No. 2, (2001), 401-406, doi: 10.1115/1.1363701
24. Lin, Y. and Sheu, M.J.A.j., "Interaction of parallel turbulent plane jets", ***AIAA Journal***, Vol. 29, No. 9, (1991), 1372-1373, doi: 10.2514/3.10749

Persian Abstract

چکیده

در مطالعه حاضر، ما ویژگی‌های جت‌های آشفته دوقلو و مقادیر آشفته را زمانی که یک جسم جامد بین دو نازل قرار می‌گیرد، بررسی کردیم. فرض می شود که دو جت همدما، تراکم ناپذیر و کاملاً توسعه یافته هستند. آشفتگی با مدل Realizable k-ε مدل‌سازی می‌شود. مجموعه معادلات میانگین ناویر استوکس رینولدز به صورت تکراری توسط نرم افزار فلوئنت حل می شود. مدل عددی با نتایج تجربی موجود در ادبیات تایید شده است. برای بسیاری از اعداد رینولدز، مشخص شد که سرعت ها و گرادیان های آن در امتداد جهت طولی کاهش می یابند. قرار گرفتن یک جسم جامد بین جت دوقلو بر ساختار جریان در پشت نازل ها به دلیل اثر انحنای جسم جامد تأثیر می گذارد. منطقه همگرا ناپدید می شود و موقعیت محوری نقاط ترکیبی با عدد رینولدز افزایش می یابد. تکامل تقریباً خطی با افزایش عدد رینولدز است. اثر شدت تلاطم در خروجی نازل نیز مورد بررسی قرار می گیرد. برای یک عدد رینولدز ثابت، موقعیت ترکیبی محوری تقریباً به صورت خطی با شدت تلاطم افزایش می‌یابد.

International Journal of Engineering

Journal Homepage: www.ije.ir

Friction and Wear Performance of Brake Pad and Optimization of Manufacturing Parameters using Grey Relational Analysis

U. V. Saindane*, S. Soni, J. V. Menghani

Mechanical Engineering Department, Sardar Vallabhbhai National Institute of Technology, Surat, India

PAPER INFO

Paper history:
Received 17 October 2021
Received in revised form 02 December 2021
Accepted 15 December 2021

Keywords:
Brake Pad
Friction
Wear
Grey Relational Analysis
Optimization
Characterization

ABSTRACT

Brake pads play very important role in the safety of automobiles as they control the speed of the vehicle. Therefore manufacturing aspects of the brake pads and improvement in their performance were studied in this paper. Experiments are designed based on Taguchi's L9 orthogonal array. Manufacturing pressure, temperature and time are taken into consideration as process variables. Nine sets of experiments were conducted. Each experiment consisted of distinct combination process variables. Thus Brake pads with Kevlar and Lapinus fibers as a reinforcement and Epoxy resin as a binder, Barium sulfate as a filler and Aluminium oxide as a friction modifier were manufactured using the hot compression method during each experiment. Friction and Wear performance was accessed by the measurement of the coefficient of friction and weight loss during the trial on the pin on disc apparatus. Specific wear rate was obtained by measuring the differences in density and weight values before and after the trial run.The required values of process parameters i.e. pressure (500 psi), time (8 min.) and temperature (180 °C) which give optimum values of coefficient of friction and Wears were determined using Grey relational analysis.

***doi**: 10.5829/ije.2022.35.03c.07*

NOMENCLATURE

COF	Coefficient of friction	CBP	Commercial brake pad sample
SWR	Wear rate	GRA	Grey relational analysis

1. INTRODUCTION

The performance assessment of brake pads is required on regularly because the brake pad is mainly responsible for maintaining the vehicle's safety and control. The performance of the brake pad is assessed by the comparison method. In this comparison, friction and wear characteristics of newly developed brake pads were compared with the same characteristics of commercial brake pads available in the market. The friction and wear characteristics for both the brake pads are obtained by conduction of trial using pin on disc apparatus or dynamometers. The dry sliding behavior of friction composite predicts the accurate friction performance for the automobile brake pads [1]. The comparison of dry sliding behavior and wear mechanism of low metallic and copper-free brake pads was performed to select the optimum friction composite [2]. Two commercial pads 1) high metallic fiber material, includes 7% copper fibers, 2) low metallic friction material contains thermal graphite (TG), and cellulose fibers as copper substitutes were investigated. The thermal behavior of the two friction materials was nearly identical. Cu-based friction material, on the other hand, was more thermally stable. This work is related to the work discussed in this paper as both compares newly developed brake pads with commercial brake pad used in practice. Pin-on-disc testing was performed to investigate the sliding behavior

*Corresponding Author Institutional Email: ds17me002@med.svnit.ac.in (U. V. Saindane)

Please cite this article as: U. V. Saindane, Sandeep Soni, J. V. Menghani, Friction and Wear Performance of Brake Pad and Optimization of Manufacturing Parameters using Grey Relational Analysis, ***International Journal of Engineering, Transactions C: Aspects*** Vol. 35, No. 03, (2022) 552-559

and wear products of a low-steel friction material against a cast iron disc at varied applied loads to study the influence of the temperature rise produced by frictional heating [3]. Dry sliding test runs were performed on the composite specimens prepared during the current work in an exactly similar way which was presented by Wahlström et al.[4] The pin on disc test is performed on the brake pad. The wear and coefficient of friction are the two characteristics that vary depending on the load and speed conditions. The wear formation mechanism is affected by the load and speed of the rotor disc and pin. i.e. at low speed less iron oxide is formed in between the disc and pin; as a result collected wear debris shows equiaxed morphology during low load and lower temperature wherein plate-like wear particles can be seen during high load and higher temperature test conditions [5]. The pin on disc test parameters is selected to study their effect on the morphology of wear debris [6].

The quality of the brake pad mainly depends on material selection, mold design and process parameters. Because mould design and material selection are done at the product development stage, process parameter selection becomes critical for decreasing the faults and enhancing the quality. Process parameters are selected using optimization techniques such as Taguchi approach and the grey relational analysis approach. The study of process parameters that contributes to the mechanical stability of epoxy-based composites is effectively carried out using Taguchi optimization-based grey relational approach [7]. The use of Taguchi L9 orthogonal array was made to design the number of experiments. It was found that a set of nine experiments results in an adequate combination of process parameters that determines the performance of the brake pad [8, 9]. However, the use of grey relational analysis on the experiments obtained by Taguchi L9 orthogonal array was rarely attempted in the previous literature for optimizing the performance of synthetic fibers reinforced polymer composite.

An attempt was made in this paper to manufacture the Kevlar / Aramid fiber reinforced epoxy composite for use as a brake pad in the automobile. Nine combinations of three process parameters namely pressure, temperature and time were selected to manufacture nine sets of brake pads using Taguchi L9 orthogonal array. Friction and wear performance of brake pads were evaluated using the trials conducted on the pin on disc test apparatus. The required combination of process parameters that gives optimum tribological performance was obtained using grey relational grades. Finally, the comparison of newly developed brake pad with commercial brake pad is carried out considering the COF, wear and wear rate.

2. EXPERIMENTAL

The brake pads utilized in this investigation were mostly non-asbestos organic friction materials with five major components (see Table 1). Brake pad prototypes were made utilizing the traditional compression molding method. i.e. Dry mixing, compaction, hot molding and heat treatment (post-curing) [10]. To achieve homogenous mixing of ingredients, a dry mix was made using ball milling for 30 minutes. A hot press with a capacity of 150 tonnes was used to compress the material. The punch was hydraulically powered, and the die was a 14-cavity steel plate. The mold was heated by 1500 W heaters, and the machine's electrical controls and safety switches were situated on a separate panel. Two heaters were placed above the die plate and two heaters were placed below it, for a total of four heaters (Figure 1). Brake samples were produced in the set of nine experiments under consideration of distinct values of time, pressure and temperature. Time, pressure, and temperature, which are all manufacturing characteristics, are used as control variables at three distinct levels (see Table 2).

2. 1. Design of Experiments L9 orthogonal array was used to investigate the influence of factors [8]. and nine distinct combinations of process parameters were obtained designing the nine experiments (see Table 3).

TABLE 1. Formulation of friction composite

Sr. No	Ingredients	Weight %
1	Phenolic resin	15.00
2	Barium Sulfate	50.00
3	Kevlar fiber	3.00
4	Lapinus fiber	27.00
5	Aluminium oxide	5.00

Figure 1. Hot press machine

Each experiment yields a separate set of samples, thus nine experiments give nine samples.

2. 2. Pin on Disc Test Tribological testing on kevlar and lapinus fiber reinforced friction composite materials was conducted in dry conditions using a pin-on-disc test setup (DUCOM product) in line with ASTM: G 99V [11]. The machine comprises a stationary loaded test specimen that slides against a spinning disc with its axis in the normal direction to the disc (see Figure 2) [12]. The test was conducted on a grey cast iron disc (0.61 Ra surface roughness, hardness 72 HRC) with a 60 mm diameter track to simulate the speed-load limits of genuine brake systems. Before starting a new test, the disc surface was cleaned with acetone-soaked paper and dried with a hot air blower for two minutes. During the test, COF was calculated automatically by taking into account the normal load and frictional force. The frictional force was measured using a transducer mounted on the loading arm. DUCOM's WINDCOM software was used to continuously monitor the COF and record the individual readings. The difference in weight before and after the intended test was determined using a precision electronic scale with an accuracy of 60.01 mg to estimate the weight loss of the specimen.

TABLE 2. Levels of process parameters

	Factors	Levels		
	Process parameters	1	2	3
Moulding parameters	Time (minutes) (A)	4	6	8
	Pressure (psi) (B)	500	600	700
	Temperature (°C) (C)	140	160	180

TABLE 3. Design of experiments using L9 orthogonal matrix

Exp. No.	Time (A) (minutes)	Pressure (B) (psi)	Temperature (C) (°C)
1	4	500	140
2	4	600	160
3	4	700	180
4	6	500	160
5	6	600	180
6	6	700	140
7	8	500	180
8	8	600	140
9	8	700	160

The specific wear rate (WR, cm^3/N-m) was then computed as follows [13].

$$SWR = \frac{\Delta M}{(\rho \times F \times L)} \quad (1)$$

where, ΔM (g) is the weight loss after the ending of the whole test, ρ (g/cm^3) is the friction samples density, F (N) is the average friction force and L (m) is the sliding distance.

The experimental trials were performed thrice for each test, average values of the results were reported.

3. RESULTS AND DISCUSSION

To select the superior specimen, higher is the better criteria were adopted for COF and lower is the better criteria were adopted for the values of wear and wear rate of the samples [14]. The maximum value of COF (0.486) was obtained for experiment 7 which is carried out at extreme conditions of temperature and time i.e. at 180 °C, 8 minutes and moderate pressure 500 psi. The minimum value of the coefficient of friction was obtained at 180 °C, 700 psi and 4 minutes. Specific wear rate was a maximum of 7.312 at experiment 8 which is performed at 140 °C, 600 psi and 8 min. The minimum value of specific wear rate (1.283) is observed for experiment 7 which is performed at 180 °C, 500 psi and 8 minutes. The value of wear in terms of weight loss is maximum for experiment 6 which is performed at 140 °C, 700 psi and 6 minutes. Minimum wear in terms of weight loss is observed in experiment 7. Also the wear rate is found lower (1.283×10^{-6} cm^3 / Nm) for experiment 7 which yields sample 7. However there was no exact trend found for values of COF, specific wear rate and wear in terms of weight loss corresponding to individual process

Figure 2. (a) Pin on Disc test set up (b) Pins

TABLE 4. Experimental values for manufactured samples

Properties	Exp. 1 (Sample 1)	Exp.2 (Sample 2)	Exp.3 (Sample 3)	Exp. 4 (Sample 4)	Exp. 5 (Sample 5)	Exp.7 (Sample 7)	Exp. 6 (Sample 6)	Exp. 8 (Sample 8)	Exp. 9 (Sample 9)
COF	0.389	0.316	0.252	0.400	0.29	0.486	0.391	0.283	0.329
SWR (10^{-6} cc / Nm)	1.301	2.999	4.31	2.158	2.807	1.283	5.441	7.312	3.951
Wear (gm)	0.009	0.011	0.01	0.011	0.009	0.005	0.024	0.022	0.011

parameters. But when the combination of process parameters is considered then corresponding values of COF, SWR and wear (gm) follows a particular trend (see Table 4).

The performance characteristics such as wear, COF are assessed under the same load, speed, time and sliding distance conditions for all nine samples. Careful examination of graphs of COF and wear of best three samples from all nine samples revealed the drastic variation because all samples were manufactured by varying the process parameters as per Table 3 [15] (see Figures 3-5). The maximum value of COF was obtained by sample 7. Also, Minimumun wear in terms of weight loss was observed for Expiment 7 i.e. sample 7. Wear rate (1.283 10^{-6}cm^3 / N.m) was also observed for sample 7.

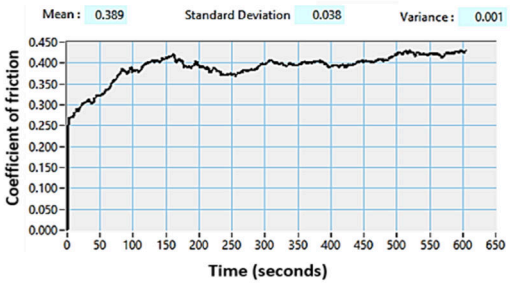

Figure 3. Friction graph (Sample 1)

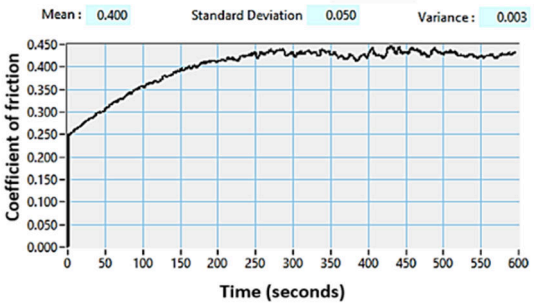

Figure 4. Friction graph (Sample 4)

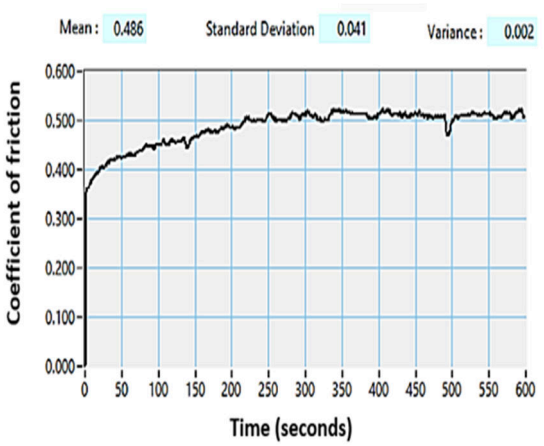

Figure 5. Friction graph (Sample 7)

However minimum wear in micrometer was observed by comparing the wear trend through the DUCOM software interface (Figures 6-9). All nine samples were compared in groups of three at a time, with the superior sample resulting in the least amount of wear. As a result, sample 3 has shown smaller wear compared to samples 1 and 2 (see Figure 6). Sample 4 showed minimum wear when compared to samples 5 and 6 (see Figure 7). Also sample 9 showed minimum wear as compared to samples 7 and 8 (see Figure 8).Thus, sample 7 had a larger COF (0.486) and the same sample exhibited the smaller wear (0.005 gm). However, when the Wear value was retrieved in a micrometers using a software interface, sample 4 was found to be superior, as it showed the least amount of wear among samples 3, 9 and 4 during the 10-minute test (see Figure 9) [16]. This situation has resulted in the Multi response optimization problem.

3. 1. Grey Relational Analysis GRA was performed to arrive at an optimum combination of process parameters which results in optimum COF, wear and wear rate. A response such as COF should be maximized while wear rate, wear must be minimized

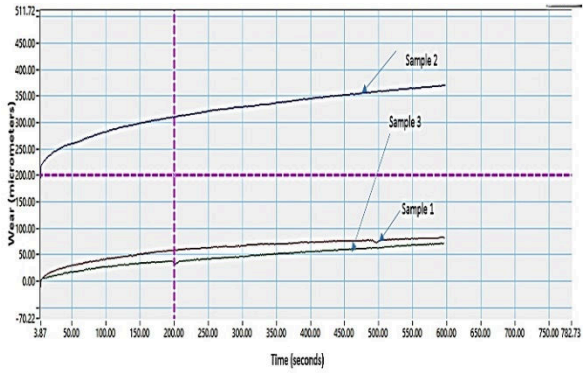

Figure 6. Wear Graph (Sample 1, 2, 3)

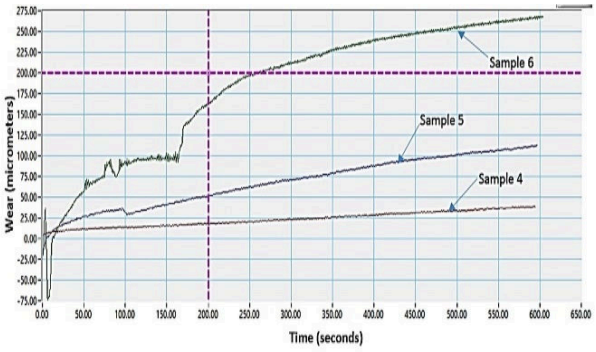

Figure 7. Wear graph (Sample 4, 5 and 6)

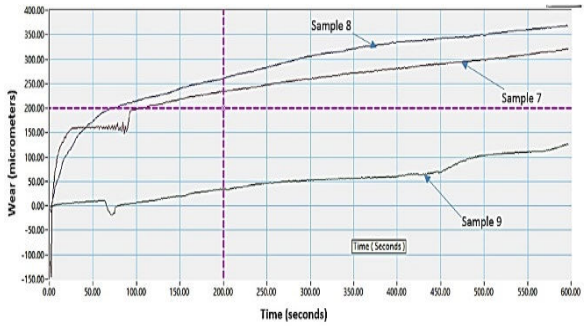

Figure 8. Wear Graph (Sample 7, 8 and 9)

[17]. Therefore the COF response was assigned with higher-the-better and wear and wear rate were assigned lower-the-better respectively to process the data in GRA. All of the sequences were analyzed using Equations (2), (3) and the outcomes were represented in Tables 5 and 6. means reference and comparability sequence. the distinguishing coefficient ϵ can be put into Equation (5) to obtain the Grey relational coefficient (Table 7). Using Equations (5-8) thus Grey relational grade and rank of each experiment are evaluated (Table 8) [18].

$$a^*(k) = \frac{\max a^i - a^i(k)}{\max a^i(k) - \min a^i(k)} \quad (2)$$

$$a^*(k) = \frac{a^i(k) - \min a^i(k)}{\max a^i(k) - \min a^i(k)} \quad (3)$$

$$\varepsilon(k) = \frac{\Delta_{min} + \gamma\ \Delta_{max}}{\Delta_{oi}(k) + \gamma\ \Delta_{max}} \quad (4)$$

$$\Delta_i(k) = [x_o(l) - x_i(l)] \quad (5)$$

$$\Delta_{max} = \max_i \max_k [x_o(l) - x_i(l)] \quad (6)$$

$$\Delta_{min} = \min_i \min_k [x_o(l) - x_i(l)] \quad (7)$$

$$\gamma_i = \frac{1}{n} \sum_{k=1}^{n} \epsilon_i(k) \quad (8)$$

where $x_o(l)$ is the reference sequence and $x_i(l)$ is the comparability sequence. $\epsilon_i = 0.5$ is well-known, and the lower value of ϵ_i pointed at higher distinguished ability.

TABLE 5. Normalized Value

Exp. No	COF	Wear	SWR
1	0	0.211	0.003
2	0.556	0.316	0.285
3	1	0.263	0.502
4	0.366	0.316	0.145
5	0.838	0.211	0.253
6	0.369	1	0.69
7	0.866	0.895	1
8	0.084	0	0
9	0.812	0.316	0.443

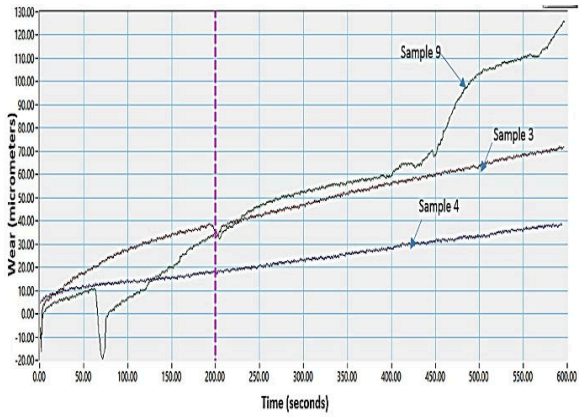

Figure 9. Wear Graph (Sample 3, 4, 9)

Experiment 7 which yields sample 7 showed rank 1 since it has higher grade value (Table 9). Thus experiment 7 can be chosen as an experiment that gives optimum performance among all nine experiments according to Grey relational analysis. Thus the optimum combination of process parameters are 8 minutes, Pressure at 500 Psi and Temperature of 180 ^{o}C .

TABLE 6. Deviation sequence responses

Exp No.	COF	Wear	SWR
1	1	0.789	0.997
2	0.444	0.684	0.715
3	0	0.737	0.498
4	0.634	0.684	0.855
5	0.162	0.789	0.747
6	0.631	0	0.31
7	0.134	0.105	0
8	0.916	1	1
9	0.188	0.684	0.557

TABLE 7. Grey relational coefficients

Exp No.	COF	Wear	SwR
1	0.333	0.388	0.334
2	0.53	0.422	0.411
3	1	0.404	0.501
4	0.441	0.422	0.369
5	0.755	0.388	0.401
6	0.442	1	0.617
7	0.789	0.826	1
8	0.353	0.333	0.333
9	0.727	0.422	0.473

TABLE 8. Rank using GRA

Exp. No.	Grade	Rank
1	0.35	8
2	0.45	6
3	0.64	3
4	0.41	7
5	0.51	5
6	0.69	2
7	0.87	1
8	0.34	9
9	0.54	4

TABLE 9. comparison of developed brake pad with commercial brake pad

Properties	CBP	Sample 7
COF	0.403	0.5666
Wear rate	0.163	1.283
Wear (gm)	0.006	0.005

Figure 10. Brake pads (a) Commercial (b) Newly developed

4. CONCLUSIONS

In this study, friction composites consisting of Kevlar and Lapinus fibers are manufactured and tested for tribological properties utilizing a hot compression process. Taguchi design of experiments was used to create the experimental design, which was then followed by Grey relational analysis to find the optimal combination of process parameters to increase the COF and decrease the wear and wear rate.

The following are some of the study's key findings:

1. The number of experiments obtained by using the Taguchi L9 orthogonal array technique has resulted in nine sets of results which proved to be adequate to reveal the improvement in tribological properties of brake pads
2. The COF, Wear and Wear rate values did not follow the specific trend in response to the change in individual process parameters.
3. The COF, wear and wear rate values follow a particular declining or increasing trend in response to change in values of a combination of process parameters.
4. The highest COF value (0.566), lowest wear (0.005 gm) and wear rate (1.283) value was determined for experiment 7, which was conducted at extreme

temperatures and times, namely 180°C for 8 minutes and moderate pressure 500 psi.

5. The wear values in micrometers during the pin on disc test were obtained as the lowest value for experiment 9 which yield sample 9.
6. GRA gives an optimum combination of process parameters in conditions where multiple superior values (samples 7 and 9) for multiple responses (COF, wear) are available. Experiment 7 which yields sample 7 showed the highest grade (0.87) and rank one.
7. When the newly developed brake pad was compared with the commercial brake pad, COF showed a 14.46 % rise where wear had decreased by 16.67 % and wear rate showed a 87.29 % rise in its value.
8. The optimum combination which gives optimum tribological performance for brake pad is obtained at 8 minutes, Pressure at 500 Psi and Temperature 180 ^{o}C.

Thus Kevlar / Lapinus fibers reinforced epoxy composite proved to be effective against the commercial brake pad samples and could be a possible replacement.

5. REFERENCES

1. Saindane. U , Soni. S and Menghani. J, "Dry sliding behavior of carbon-based brake pad materials," ***International Journal of Engineering, Transactions B Applications***, Vol. 34, No. 11, (2021), doi: 10.5829/IJE.2021.34.11B.14
2. Tavangar. H, Moghadam. A, Khavandi and S, B., "Comparison of dry sliding behavior and wear mechanism of low metallic and copper-free brake pads", ***Tribology International***, Vol. 151, No. 2, (2020), doi: 10.1016/j.triboint.2020.106416
3. Alemani, M., Gialanella, S., Straffelini, G., Ciudin, R., Olofsson, U., Perricone, G. and Metinoz, I.J.W., "Dry sliding of a low steel friction material against cast iron at different loads: Characterization of the friction layer and wear debris", ***Wear***, Vol. 376, (2017), 1450-1459, doi: 10.1016/j.wear.2017.01.040
4. Wahlström, J., Lyu, Y., Matjeka, V. and Söderberg, A.J.W., "A pin-on-disc tribometer study of disc brake contact pairs with respect to wear and airborne particle emissions", ***Wear***, Vol. 384, (2017), 124-130, doi: 10.1016/j.wear.2017.05.011
5. Federici, M., Gialanella, S., Leonardi, M., Perricone, G. and Straffelini, G.J.W., "A preliminary investigation on the use of the pin-on-disc test to simulate off-brake friction and wear characteristics of friction materials", ***Wear***, Vol. 410, (2018), 202-209, doi: 10.1016/j.wear.2018.07.011
6. Menapace, C., Leonardi, M., Matějka, V., Gialanella, S. and Straffelini, G.J.W., "Dry sliding behavior and friction layer formation in copper-free barite containing friction materials", ***Wear***, Vol. 398, (2018), 191-200, doi: 10.1016/j.wear.2017.12.008
7. Sumesh, K. and Kanthavel, K.J.J.o.I.T., "Grey relational optimization for factors influencing tensile, flexural, and impact properties of hybrid sisal banana fiber epoxy composites", ***Journal of Industrial Textiles***, (2020), 1528083720928501, doi: 10.1177/1528083720928501
8. Koksal, S., Ficici, F., Kayikci, R., Savas, O.J.M. and Design, "Experimental optimization of dry sliding wear behavior of in situ alb2/al composite based on taguchi's method", ***Materials & Design***, Vol. 42, (2012), 124-130, doi: 10.1016/j.matdes.2012.05.048
9. Wang, Y., Cui, G., Shao, Z., Bao, Y. and Gao, H.J.M.E.S., "Optimization of the hot pressing process for preparing flax fiber/pe thermoplastic composite", ***Mechanical Engineering Science***, Vol. 1, No. 1, (2019), doi: 10.33142/me.v1i1.660
10. Singh, T.J.J.o.M.R. and Technology, "Optimum design based on fabricated natural fiber reinforced automotive brake friction composites using hybrid critic-mew approach", ***Journal of Materials Research and Technology***, (2021), doi: 10.1016/j.jmrt.2021.06.051
11. Leonardi, M., Menapace, C., Matějka, V., Gialanella, S. and Straffelini, G.J.T.I., "Pin-on-disc investigation on copper-free friction materials dry sliding against cast iron", ***Tribology International***, Vol. 119, (2018), 73-81, doi: 10.1016/j.triboint.2017.10.037
12. Saindane. U, S, S. and J, M., "Studies on mechanical properties of brake friction materials derived from carbon fibres reinforced polymer composite", ***Materials Today Proceedings,***, Vol. 2021, No. 5760–5765, doi: 10.1016/j.matpr.2021.04.079
13. Ahmadijokani, F., Shojaei, A., Arjmand, M., Alaei, Y. and Yan, N.J.C.P.B.E., "Effect of short carbon fiber on thermal, mechanical and tribological behavior of phenolic-based brake friction materials", ***Composites Part B Engineering***, Vol. 168, (2019), 98-105, doi: 10.1016/j.compositesb.2018.12.038
14. Singh, T., Chauhan, R., Patnaik, A., Gangil, B., Nain, R. and Kumar, A.J.P.C., "Parametric study and optimization of multiwalled carbon nanotube filled friction composite materials using taguchi method", ***Polymer Composites***, Vol. 39, No. S2, (2018), E1109-E1117, doi: 10.1002/pc.24576
15. El-Tayeb, N. and Liew, K.J.W., "On the dry and wet sliding performance of potentially new frictional brake pad materials for automotive industry", ***Wear***, Vol. 266, No. 1-2, (2009), 275-287, doi: 10.1016/j.wear.2008.07.003
16. Kwabena Gyimah, G., Huang, P. and Chen, D.J.J.o.T., "Dry sliding wear studies of copper-based powder metallurgy brake materials", ***Journal of Tribology***, Vol. 136, No. 4, (2014), 041601, doi: 10.1115/1.4027477
17. Subbaya, K., Suresha, B., Rajendra, N., Varadarajan, Y.J.M. and Design, "Grey-based taguchi approach for wear assessment of sic filled carbon–epoxy composites", ***Materials & Design***, Vol. 41, (2012), 124-130, doi: 10.1016/j.matdes.2012.04.051
18. Singh, T., Patnaik, A., Chauhan, R.J.M. and Design, "Optimization of tribological properties of cement kiln dust-filled brake pad using grey relation analysis", ***Materials & Design***, Vol. 89, (2016), 1335-1342, doi: 10.1016/j.matdes.2015.10.045
19. Liew, K., Nirmal, U.J.M. and Design, "Frictional performance evaluation of newly designed brake pad materials", ***Materials & Design***, Vol. 48, (2013), 25-33, doi: 10.1016/j.matdes.2012.07.055
20. Mahale, V., Bijwe, J. and Sinha, S.J.W., "A step towards replacing copper in brake-pads by using stainless steel swarf", ***Wear***, Vol. 424, (2019), 133-142, doi: 10.1016/j.wear.2019.02.019
21. Pincheira, G., Canales, C., Medina, C., Fernández, E., Flores, P.J.P.o.t.I.o.M.E., Part L: Journal of Materials: Design and Applications, "Influence of aramid fibers on the mechanical behavior of a hybrid carbon–aramid–reinforced epoxy composite", ***Proceedings of the Institution of Mechanical Engineers, Part L: Journal of Materials: Design and Applications***, Vol. 232, No. 1, (2018), 58-66, doi: 10.1177/1464420715612827
22. Akhondizadeh. M, Fooladi Mahani. M, M, R. and S, M., "A new procedure of impact wearevaluation of mill liner", ***International Journal of Engineering, Transactions A: Basics***, Vol. 28, No. 4, (2015), 610–619, doi: 10.5829/idosi.ije.2015.28.04a.13

Persian Abstract

چکیده

لنت های ترمز نقش بسیار مهمی در ایمنی خودرو دارند زیرا سرعت خودرو را کنترل می کنند. بنابراین جنبه های تولید لنت ترمز و بهبود عملکرد آنها در این مقاله مورد مطالعه قرار گرفته است. آزمایشات بر اساس آرایه متعامد Taguchy L9 طراحی شده است. فشار تولید ، دما و زمان به عنوان متغیرهای فرآیند در نظر گرفته می شوند. نه مجموعه آزمایش انجام شد. هر آزمایش متغیرهای فرآیند ترکیبی متمایزی را شامل می شد. بنابراین لنت های ترمز با الیاف کولار و لاپینوس به عنوان تقویت کننده و رزین اپوکسی به عنوان چسب ، سولفات باریم به عنوان پرکننده و اکسید آلومینیوم به عنوان اصلاح کننده اصطکاک با استفاده از روش فشرده سازی گرم در طول هر آزمایش تولید شدند. عملکرد اصطکاک و سایش با اندازه گیری ضریب اصطکاک و کاهش وزن در طول آزمایش روی پین بر روی دستگاه دیسک قابل دسترسی بود. میزان سایش خاص با اندازه گیری تفاوت در چگالی و مقادیر وزن قبل و بعد از اجرای آزمایشی به دست آمد. مقادیر مورد نیاز پارامترهای فرآیند یعنی فشار، زمان و دما که مقادیر بهینه ضریب اصطکاک و سایش را ارائه می دهد با استفاده از تجزیه و تحلیل رابطه خاکستری تعیین گردید.

International Journal of Engineering

Journal Homepage: www.ije.ir

Experimental Formability Study of Ti6Al4V Sheet Metal using Friction Stir Heat Assisted Single Point Incremental Forming Process

V. D. Golakiya*[a], M. K. Chudasama[b]

[a] *Mechanical Engineering Department, Dr S& S S Ghandhy Government Engineering College Surat, Gujarat Technology University, Gujarat, India*
[b] *Mechanical Engineering Department, Government Engineering College Surat, Gujarat Technology University-395001, Gujarat, India*

P A P E R I N F O

Paper history:
Received 20 October 2021
Received in revised form 27 November 2021
Accepted 14 December 2021

Keywords:
Single Point Incremental Forming
Friction Stir Incremental Forming
Ti6Al4V
Formability

A B S T R A C T

Single Point Incremental Forming (SPIF) process is a novel approach of flexible sheet metal forming method in which 3D component can be allowed to form. The process is characterized by die less flexible, lower lead time and higher formability as compare to conventional stamping process. The present work involves set of experiments of 1 mm thick Ti6Al4V sheet using the friction stir SPIF process at room temperature and investigating the effect of wall angle, speed, feed and step size on formability of the sheet. The results revealed that, the maximum formability of frustum cone specimen was obtained at wall angle of 45° and wall angle is the most significant parameter. With an increase in wall angle and feed, the formability of sheet blank decreases while increases in tool rotational speed, the formability found to increase. In addition, it is also observed that, there was no significant influence of step size on formability of sheet.

doi: *10.5829/ije.2022.35.03c.08*

1. INTRODUCTION

Single point incremental forming (SPIF) process is a novel sheet metal forming process. SPIF process is characterized with higher flexibility, lower tooling cost and reduces lead time due to die-less sheet metal forming process [1]. It is more suitable for rapid prototypes and small - medium scale production of sheet metal parts, which needs no special type of tooling and has low initial cost as compared to conventional stamping forming process [2]. The blank sheets metals are localized incrementally deformed using a simple hemispherical end forming tool, whose path is specified in a CNC machining center or robot. SPIF process has higher formability because of mode of deformation of sheet under stretching and shearing action [3]. Due to great formability at room temperature, the SPIF method is extensively used for the aluminum and steel alloy sheet material. However, the process has limited to industrialize because of lower surface quality, uniform thickness, geometrical accuracy and higher forming time of formed parts [4].

The uses of lightweight material such as titanium alloy components have continuously increased in the important fields such as aeronautical, automotive and biomedical field due to economic, environmental and biomedical compatible in nature. These alloy materials have good mechanical properties such as high strength to weight ratio, toughness, wear resistance fatigue behavior and corrosion resistance compared to other materials such as aluminum and steel alloys [5]. Among the titanium alloys, the Ti6Al4V is used 80 % of total titanium alloy in the USA [6]. However, the Ti6Al4V titanium sheet is difficult to form at room temperature because of they possess low uniform elongation, resistance to deformation, high springback and yield to tensile ratio (high hardness and poor formability). So, they are commonly formed with low-speed forming at elevated temperature of 750~950 °C [7]. Lightweight materials such as AA2024-T3, AZ31 B-O, AA6061-T6,

*Corresponding Author Institutional Email: vdgolakiya.gec@gmail.com
(V. D. Golakiya)

Please cite this article as: V. D. Golakiya, M. K. Chudasama, Experimental Formability Study of Ti6Al4V Sheet Metal using Friction Stir Heat Assisted Single Point Incremental Forming Process, ***International Journal of Engineering, Transactions C: Aspects*** Vol. 35, No. 03, (2022) 560-566

AA6063 and titanium alloys and high strength alloy such as MnB5, DP 980 and DC04 steel alloy have possessed a poor formability at room temperature. In order to form these alloys, heat assisted incremental sheet forming (ISF) techniques are more suitable with minimum tooling cost and lower lead time at higher temperature such as laser heat assisted, electrical heat assisted, induction heat assisted friction stir heat assisted processes [8].

In the past two decades, many researchers and academicians have carried out experiments to analyze the forming of lightweight sheet materials using different types of the heat assisted ISF techniques. Duflou et al. [9] have formed cone shape specimens of Ti6Al4V with laser heat assisted technique of ISF with local dynamic heating. The results showed that cone shape specimens were formed with lower forming force and higher dimension accuracy. Ambrogio et al. [10] studied the influence of process parameters such as tool diameter, step size, feed rate and lubrication on the formability of magnesium alloy AZ31B at the room temperature and in warm condition. The formability of AZ31B was observed higher in warm conditions as compared to room temperature. Further, complex design of heating equipment is creating difficulties while carried out the forming of sheet. Fan et al. [11] developed a new technique to heat the sheet metal based on electric current. In this technique, the localized heat is generated at tool-sheet interference by DC power supply. They investigated maximum formable angle and part accuracy on the TiAl2Mn1.5 titanium and the AZ31 magnesium alloys. In 2010, Fan et al. [12] were formed sheet metal of the Ti6Al4V alloy by using electrical heat assisted technique and observed that this technique is more suitable to form a desired shape in the range of temperature 500–600 °C with a minor oxidation. Later on, Ambrogio et al. [5] used electrical heat assisted incremental forming technique to form difficult to form-alloy such as AZ31B-O, AA2024-T3, Ti-6Al-4V. They investigated the influence of different operating parameters on formability and surface quality of formed parts. Rahmani et al. [13] have investigated the process of incremental forming on AA6063 material using warm heating. They have reported that, axial feed and temperature most significant parameter on formability and surface roughness.

The heat assisted techniques of SPIF process have been classified for global heating and local heating of blank sheet by Xu et al. [14]. These heat assisted techniques showed the substantial enhancements in the formability of hard to form materials but there is a significantly increase in both the process complexity and tooling cost. However, friction stir heat assisted SPIF is the most suitable as direct heating method with higher flexibility and lower cost [15, 16]. In friction stir heat assisted technique, sheet metal is formed with tool spinning at very high relative speed, which generates frictional heating of the sheet. The use of this technique are mainly found in technical literature that focuses on steel and aluminum sheets. Ambrogio et al. [17] investigated the influence of the step size and the tool feed rate on temperature deviations at the tool interface, during the SPIF of aluminum alloy (AA5754) and titanium Ti6Al4V sheets. They have reported that optimized feed of the tool and step size give better formability along with process productivity and quality of formed part without any external heating equipment. Chausov et al. [18] suggested that a range of deformation rates of high- strength titanium alloys pass into a state of increased ductility without loss of strength properties by using additional force impulse loading, and the implementation of dynamic non-equilibrium processes. Grün et al. [19] investigated the behavior of Ti6Al4V sheet formability with friction stir SPIF process technique. The result showed that medium tool rotation of 2000 rpm speed lead to lower the rate of tool wear, improved the formability and reduce the forming forces.

To the best of author's knowledge, experimental investigation of process parameters on forming of Ti6Al4V sheet metal without use of heating equipment in single point incremental process is not reported so far. Because of wide use of Ti6Al4V titanium alloy in the field of biomedical, aeronautics and automotive, friction stir heat assisted single point incremental forming of Ti6Al4V sheet has been investigated in this study. In order to evaluate the formability of sheet metal part in SPIF process, the parameters like speed, feed, step size and wall angle were selected.

2. PRINCIPLE AND EQUIPMENT OF EXPERIMENTAL SETUP

Figure 1 shows the principle experimental set up employed in present work. The experimental set up consist of basic elements such as sheet blank, forming tool, vice, fixture and a CNC vertical machining center. The 3-axis CNC Machine (Jyoti PX20 with Siemens controller) with a maximum working space of 510 x 510 x 510 mm^3 and 400 kg_f load capacity of table is used for experimental work.

The tool is made of tungsten carbide (WC) material with a 10 mm diameter hemispherical-end; it is selected due to its high hardness, heat resistance and wear resistance. The blank sheet is firmly clamped with clamping screws in the fixture. A tool with hemispherical shape is forming the blank sheet incrementally in to desired shape. The Ti6Al4V alloy, a hard-to-form lightweight alloy sheets has been selected for experimental tests. Its chemical constituents (as–received condition) are Ti- 87.49 % Al–6.8 %, V– 4.8,

H–0.015 %, Fe–0.3, O-0.2%, Si-0.15%, C-0.1 %, N-0.05 and others-0.4 % in mass percentage. Titanium is an allotropic substance consisting of a cubic structure (α-Ti) and a compact hexagonal structure up to a temperature of 882°C (β-Ti). The truncated cone-specimens were formed from 98 x 98 mm^2 blank size sheets having a thickness of 1 mm. All test samples of sheet have been cut from annealed 1-mm-thick Ti6Al4V alloy sheets by water jet machining process. Before each experiment, OKS200 MoS2 paste lubricant was applied on top surface of blank sheet, which prevent the oxidation of the specimen surface at higher temperature during forming process (Figure 2).

The truncated cone geometries with constant angle is formed with 46 mm top base diameter and vertical depth of 18 mm. The truncated con was employed to determine the SPIF formability of Ti6Al4V. The desired tool path to form the truncated cone specimen was generated using Microsoft Excel Software. All truncated specimens with constant angle have been formed using Z-level tool path. In Z-level tool path, first tool moves in XY- plane, reaches its starting point, then tool takes a step in the vertically (z-axis) downward with specified step size. This motion of tool continues till the complete specimen is formed. Figure 3 shows the CAD truncated cone specimen model with tool path.

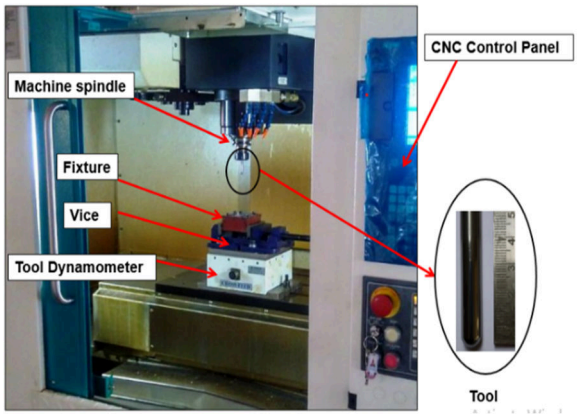

Figure 1. Experimental set for SPIF process with Jyoti PX20 CNC milling machine

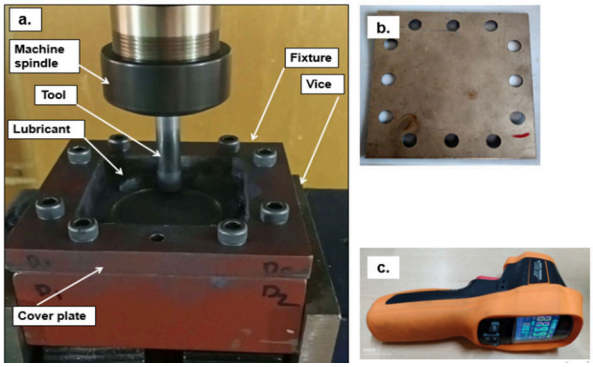

Figure 2. (a) The sheet during processing with OKS MoS2 Paste Lubricant (b) The sheet provided with desired dimension (c) Infrared non-contact temperature measurement gun

3. EXPERIMENTAL RESULTS AND DISCUSSIONS

The plan of experiments with process parameters are summarized in Table 1. In present study, there are four variables parameters such as speed, feed, step size and wall angle. The formability is one of the important response parameter of sheet metal forming process. Formability of sheet material in SPIF process is represented in different approach such as fracture forming limit, maximum formable angle and maximum forming depth.

In present work, maximum forming depth of specimen is measured as a formability of Ti6Al4V sheet material, which can be measured just before specimen part fractured during forming process. All specimens are formed till either design depth of 18 mm or the fractured of specimen during forming process. After the fractured the specimens are unloaded from the fixture and depth of fractured specimens are reported as the Z-axis co-ordinate on computer screen of the machine. The experimentation was carried out to investigate influence of various parameters such as speed, feed, step size and wall angle on formability.

3. 1. Influence of Wall Angle The conical frustums specimens with diameter of 46 mm at the top and wall angle of 55°, 50°, and 45° are selected to evaluate the formability in the friction stir heat assisted SPIF process of Ti-6Al-4V alloy. The plan of experiments and the experiment results are shown in Table 1.

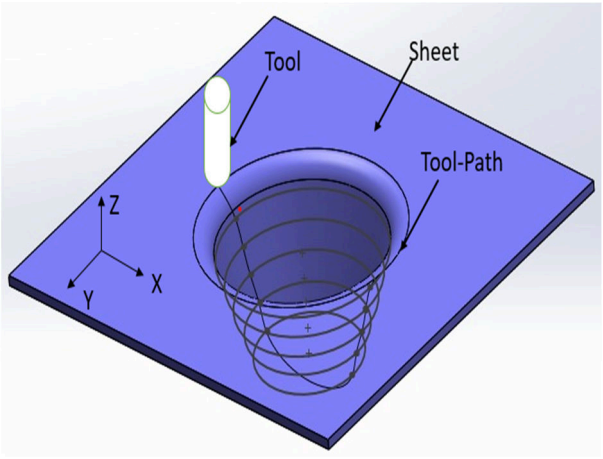

Figure 3. CAD model of truncated cone with Tool path

TABLE 1. Plan of experimental work and result

(a) Formability test results by varying the speed and step size with constant wall angle

Exp. No.	Wall angle (α)-degree	Speed (s)-rpm	Feed (f)-mm/min	step-size (z)-mm	Depth of formed part (d)-mm
1	55	700	1000	0.25	6
2	55	1000	1000	0.1	5.5
3	55	1400	800	0.25	6.25

(b) Formability test results of wall angle

Exp. No.	Wall angle(α)-degree	Depth of formed part (d)-mm	Constant parameters
3	55	6.25	speed 1400 rpm, feed 800 m/min, tool diameter 10 mm and step size 0.25mm.
4	50	7.25	
5	45	18	

(c) Formability test results of speed

Exp. No.	Speed(s)-rpm	Depth of formed part (d)-mm	Constant parameters
6	700	7.50	wall angle 45°, feed 800 mm/min, tool diameter 10mm and step size 0.25mm.
7	1000	10.25	
5	1400	18	

(d) Formability test results of feed

Exp. No.	Feed (f)-mm/min	Depth of formed part (d)- mm	Constant parameters
5	800	18	wall angle 45°, speed 1400 rpm, tool diameter 10mm and step size 0.25mm.
8	1000	6.25	
9	1200	5.5	

(f) Formability test results of step size with varying wall angle

Exp. No.	Step size (z)-mm	Wall angle (α)-degree	Depth of formed part (d)-mm	Constant parameters
4	0.25	50°	7.25	speed 1400 rpm and tool diameter 10mm.
10	0.1	50°	7.25	
5	0.25	45°	18)	
11	0.1	45°	18	

In the first set of three specimens as shown in Table 1(a) with wall angle of 55° was formed with varying the speed and step size. All three specimens had early failed with poor surface finish as shown in Figure 4. It shows that wall angle is the most significant parameter for formability. In the second set of three specimens as shown in Table 1(b) with wall angle of 55°, 50° and 45° have been formed with considering other parameters as constant. As can be seen from the results and as shown in Figure 5, the specimen with wall angle of 45° has successfully formed at a depth of 18 mm and wall angle with 50° and 55° had early failed at a depth of 7.52 and 5.25 mm, respectively. The result showed that forming depth decreases with an increase in the wall angle as shown in Figure 6(a). The sheet metal had more stretching at higher wall angle, hence thinning of sheet metal increases with an increase in the value of wall angle based on cosine law.

3. 2. Influence of Speed In the third set of three experiments plan with varying the speed as shown in Table 1(c), the specimens have formed with varying the speed and keep other parameters constant.

The specimen formed successfully at forming depth of 18 mm with speed of 1400 rpm but specimens are failed at depth of 7.5 mm and 10.25 mm at lower

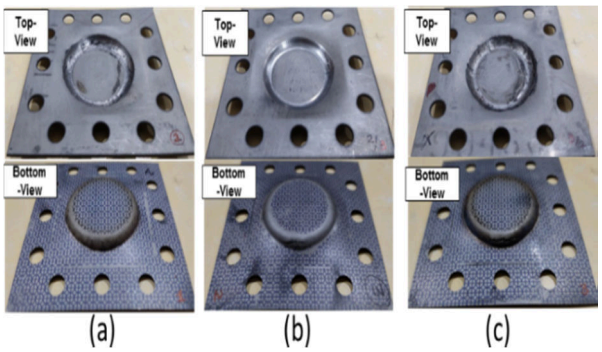

Figure 4. Specimens formed by varying the speed and step size with constant wall angle (a) exp no.1 (b) exp no.1 (c) exp no.3

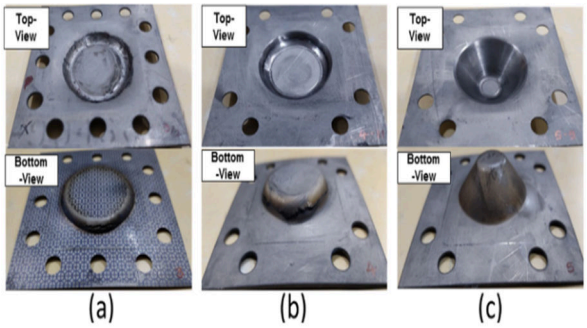

Figure 5. Specimens formed with varying the wall angle of (a) 55° (b) 50° (c) 45°

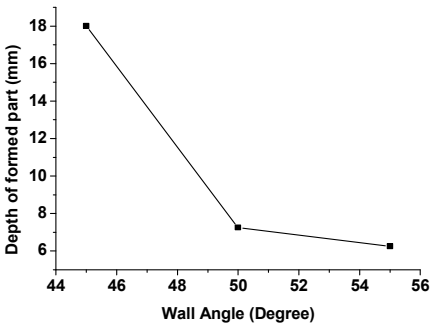

(a)

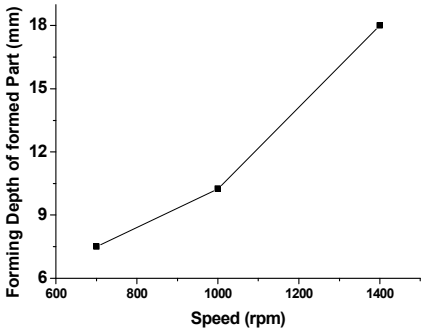

(b)

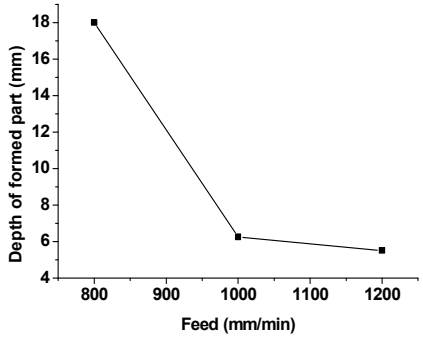

(c)

Figure 6. Effect of (a). Wall angle, (b). Speed, and (c). Feed-parameters on depth of formed part

speed of 700 and 1000 rpm, respectively as shown in Figure 7. It seems that forming depth is increases with an increase in tool rotation speed as shown in Figure 6 (b) because of thermal softening effect at tool-sheet interface. At the low rotations speed of 700 and 1000 rpm, the range of temperatures were lower at tool interface 60 to 90 °C observed by Infrared non-contact temperature measurement gun, as shown in Figure 2(a). At such low temperature, insufficient heat generated in the forming zone resulted in reduced formability of the part. In SPIF process, friction heat generation at tool-sheet interface is directly proportional to tool rotation speed [20].

3. 3. Influence of Feed In the fourth set of three experiments plan with varying the feed as shown in Table 1(d), the specimens have been formed with varying the feed of 800, 1000 1200 mm/min with keeping other parameters constant. Figure 8 (a) shows that specimen with feed of 800 mm/min was successfully formed but the specimens with feed of 1000 and 1200 mm/min had failed at depth of 6.25 and 5.5 mm, respectively as shown in Figure 8 (b, c). Further, as shown in Figure 6 (c) depth of forming specimens had increased with decreased in the value of feed.

At the lower feed, the more heat generated at interface between tool and work-piece due to slower rolling of the tooltip over the contact surface and rate of the heat dissipated is very slow. The metal is becoming ductile in nature and more straining occurred because of increasing the temperature at forming zone. Hence, the formability of sheet metal is increased. For higher feed, the formability decreased due to lower heat generation at tool interface, faster the tool tip rolls over the contact surface.

3. 4. Influence of Step Size In the fifth set of three experiments plan, the influence of step size with varying wall angle as shown in Table 1(f). As can be seen from results, the specimens had formed without any crack at the 45° wall angle in two 0.1 and 0.25 step sizes as shown in Figure 9 (c, d).

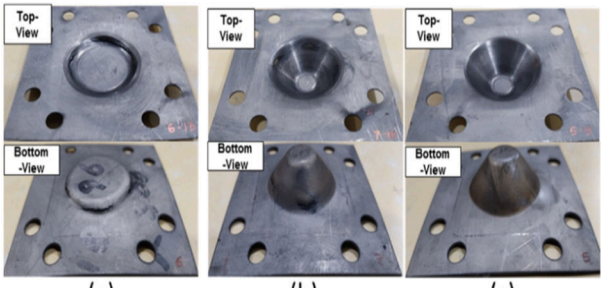

Figure 7. Specimens formed with varying the speed (rpm) of (a) 700 (b) 1000 (c) 1400

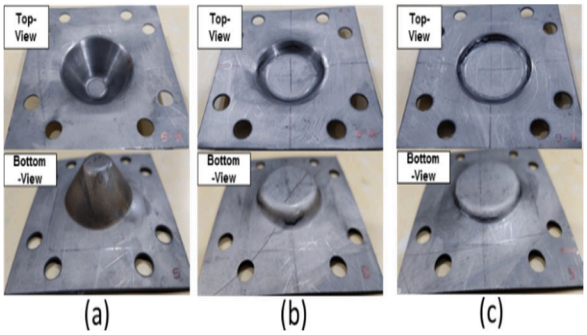

Figure 8. Specimens formed with varying the feed (mm/min) of (a) 800 (b) 1000 (c) 1200

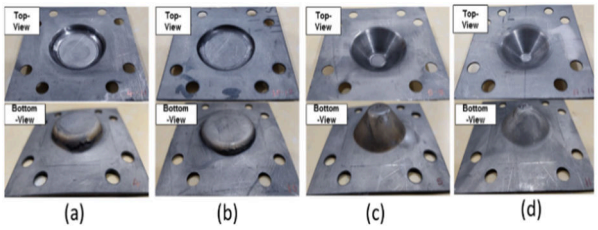

Figure 9. Specimens with varying the step size (mm) with wall angle (a) 0.25, 50° (b) 0.1, 50° (c) 0.25, 45° (d) 0.1, 45°

On the other hand, the specimens with wall angle of 55° early failed at depth of 7.25 mm as shown in Figure 9 (a, b).This shows that wall angle is more significant parameter than step size and, there is no significant effect is found on formability with varying the step size of 0.1 mm and 0.25 mm.

4. CONCLUSIONS

In this study, experimental investigation of single point friction stir incremental forming process of Ti-6Al-4V is performed. The results of the study can be summarized as follows:

- Process parameters, such as wall angle, speed and feed have influence on the formability of sheet metal blank. Formability is increased with a decrease in the wall angle from 55° to 45° and the highest formability is obtained in term of maximum forming depth of 18 mm at wall angle of 45° due to lower the stretching of material. It has been found that the wall angle has significant influence on the formability of sheet metal.
- With an increase in the speed from 700 to 1400 rpm, the formability of sheet metal is increasing of 7.5 mm to 18 mm in term of maximum forming depth. The sheet metal shows higher formability at higher temperature cause of higher rubbing action at contact surface due to increases speed. While formability decreases from 18 mm to 5.5 mm in term of forming depth as the feed increasing from 800 to 1200 mm/min. At higher feed rate, formability is lower due to poor accumulation of heat at contact surface, causes more rate of heat dissipated.
- Furthermore, step size of 0.1 and 0.25 mm did not have any significant effect on formability.
- The most influencing parameters in this process are wall angle followed by tool rotation speed and feed. So with correct combination of these parameters, it can come up to safe forming of the Ti6Al4V blank sheet without additional heat assisted equipment.

In this approach, the present study helps to user to get recommendations about, parameters with their range should be select to form the hard to form material of Ti-6Al-4V by friction stir SPIF process at room temperature.

5. REFERENCES

1. Arfa, H., Bahloul, R. and BelHadjSalah, H.J.I.j.o.m.f., "Finite element modelling and experimental investigation of single point incremental forming process of aluminum sheets: Influence of process parameters on punch force monitoring and on mechanical and geometrical quality of parts", ***International Journal of Material Forming***, Vol. 6, No. 4, (2013), 483-510, doi: 10.1007/s12289-012-1101-z
2. Vahdani, M., Mirnia, M.J., Bakhshi-Jooybari, M. and Gorji, H.J.T.I.J.o.A.M.T., "Electric hot incremental sheet forming of ti-6al-4v titanium, aa6061 aluminum, and dc01 steel sheets", ***International Journal of Advanced Manufacturing Technology***, Vol. 103, No. 1-4, (2019), 1199-1209, doi: 10.1007/s00170-019-03624-2
3. Jackson, K. and Allwood, J.J.J.o.m.p.t., "The mechanics of incremental sheet forming", ***Journal of Materials Processing Technology***, Vol. 209, No. 3, (2009), 1158-1174, doi: 10.1016/j.jmatprotec.2008.03.025
4. Mohanraj, R. and Elangovan, S.J.T.o.t.C.S.f.M.E., "Incremental sheet metal forming of ti–6alٜ–v alloy for aerospace application", ***Transactions of the Canadian Society for Mechanical Engineering***, Vol. 44, No. 1, (2019), 56-64, doi: 10.1139/tcsme-2018-0276
5. Ambrogio, G., Filice, L., Gagliardi, F.J.M. and Design, "Formability of lightweight alloys by hot incremental sheet forming", ***Materials & Design***, Vol. 34, (2012), 501-508, doi: 10.1016/J.MATDES.2011.08.024
6. Eylon, D. and Seagle, S.J.S.P., "Titanium'99: Science and technology", Vol., No., (2000), 866-875.
7. Lee, H.-S., Yoon, J-.H., Park, C.H., Ko, Y.G., Shin, D.H. and Lee, C.S.J.J.o.M.P.T., "A study on diffusion bonding of superplastic ti–6al–4v eli grade", ***Journal of Materials Processing Technology***, Vol. 187,(2007), 526-529, doi: 10.1016/j.jmatprotec.2006.11.215
8. Liu ,Z.J.T.I.J.o.A.M.T., "Heat-assisted incremental sheet forming: A state-of-the-art review", ***The International Journal of Advanced Manufacturing Technology***, Vol. 98, No. 9, (2018), 2987-3003, doi: 10.1007/s00170-018-2470-3
9. Duflou, J., Callebaut, B., Verbert, J. and De Baerdemaeker, H.J.C.a., "Laser assisted incremental forming: Formability and accuracy improvement", ***CIRP Annals***, Vol. 56, No. 1, (2007), 273-276, doi: 10.1016/j.cirp.2007.05.063
10. Ambrogio, G., Filice, L. and Manco, G.J.C.a., "Warm incremental forming of magnesium alloy az31", ***CIRP Annals***, Vol. 57, No. 1, (2008), 257-260, doi: 10.1016/j.cirp.2008.03.066
11. Fan, G., Gao, L., Hussain, G., Wu, Z.J.I.J.o.M.T. and Manufacture, "Electric hot incremental forming: A novel technique", ***International Journal of Machine Tools and Manufacture***, Vol. 48, No. 15, (2008), 1688-1692, doi: 10.1016/j.ijmachtools.2008.07.010
12. Fan, G., Fengtao Sun, Meng, X., Lin Gao and Tong, G., "Electric hot incremental forming of ti-6al-4v titanium sheet", ***The International Journal of Advanced Manufacturing Technology***, Vol. 49, No. 9-12, (2010), 941-947, doi: 10.1007/s00170-009-2472-2
13. Rahmani, F., Seyedkashi, S. and Hashemi, S.J.I.J.o.E., "Experimental study on warm incremental tube forming of aa6063 aluminum tubes", ***International Journal of Engineering, Transactions C: Aspects***, Vol. 33, No. 9, (2020), 1773-1779, doi: 10.5829/ije.2020.33.09c.11
14. Xu, D., Lu, B., Cao, T., Zhang, H., Chen, J., Long, H., Cao, J.J.M. and Design, "Enhancement of process capabilities in electrically-assisted double sided incremental forming", ***Materials & Design***, Vol. 92, (2016), 268-280, doi: 10.1016/j.matdes.2015.12.009

15. Buffa, G., Campanella, D. and Fratini, L.J.T.I.J.o.A.M.T., "On the improvement of material formability in spif operation through tool stirring action", ***The International Journal of Advanced Manufacturing Technology***, Vol. 66, No. 9-12, (2013), 1343-1351, doi: 10.1007/s00170-012-4412-9
16. Otsu, M., Katayama, Y. and Muranaka, T., "Effect of difference of tool rotation direction on forming limit in friction stir incremental forming", in Key Engineering Materials, Trans Tech Publ. Vol. 622, (2014), 390-397.
17. Ambrogio, G. and Gagliardi, F.J.T.I.J.o.A.M.T., "Temperature variation during high speed incremental forming on different lightweight alloys", ***The International Journal of Advanced Manufacturing Technology***, Vol. 76, No. 9-12, (2015), 1819-1825, doi: 10.1007/s00170-014-6398-y
18. Chausov, M., Pylypenko, A., Berezin, V., Volyanska, K., Maruschak ,P., Hutsaylyuk, V., Markashova, L., Nedoseka, S. and Menou, A.J.T., "Influence of dynamic non-equilibrium processes on strength and plasticity of materials of transportation systems", ***Transport***, Vol. 33, No. 1, (2018), 231-241, doi: 10.3846/16484142.2017.1301571301549.
19. Grün, P., Uheida, E., Lachmann, L., Dimitrov, D. and Oosthuizen, G.J.T.I.J.o.A.M.T., "Formability of titanium alloy sheets by friction stir incremental forming", ***The International Journal of Advanced Manufacturing Technology***, Vol. 99, No. 5 ,(2018) 1993-2003 ,doi: 10.1007/s00170-018-2541

Persian Abstract

چکیده

فرآیند شکل دهی افزایشی تک نقطه ای (SPIF) یک رویکرد جدید از روش شکل دهی فلزی انعطاف پذیر است که در آن می توان به اجزای سه بعدی اجازه شکل گیری داد. این فرآیند با قالب کمتر انعطاف‌پذیر، زمان هدایت کمتر و شکل‌پذیری بالاتر در مقایسه با فرآیند مهر زنی معمولی مشخص می‌شود. کار حاضر شامل مجموعه ای از آزمایشات ورق Ti6Al4V به ضخامت ۱ میلی متر با استفاده از فرآیند SPIF اصطکاکی در دمای اتاق و بررسی تأثیر زاویه دیوار، سرعت، تغذیه و اندازه پله بر شکل پذیری ورق است. نتایج نشان داد که حداکثر شکل‌پذیری نمونه مخروط فروستوم در زاویه دیواره ٤٥ درجه به دست آمد و زاویه دیوار مهم‌ترین پارامتر است. با افزایش زاویه دیوار و تغذیه، شکل پذیری ورق خالی کاهش می یابد در حالی که با افزایش سرعت چرخش ابزار، شکل پذیری افزایش می یابد. علاوه بر این، همچنین مشاهده شد که اندازه پله تأثیر معنی‌داری بر شکل‌پذیری ورق نداشت.

IJE TRANSACTIONS C: Aspects Vol. 35, No. 03, (March 2022) 567-571

International Journal of Engineering

Journal Homepage: www.ije.ir

Investigation of Microstructure and Mechanical Properties of Newly Developed Advanced High Strength TRIP Steel

A. Abbasian*[a], A. Ravangard[b], I. Hajian Nia[a], S. Mirzamohammadi[a]

[a] *Department of Materials and Metallurgical Engineering, Technical and Vocational University (TVU), Tehran, Iran*
[b] *Department of Mechanical Engineering, Technical and Vocational University (TVU), Tehran, Iran*

PAPER INFO

Paper history:
Received 18 October 2021
Received in revised form 20 December 2021
Accepted 23 December 2021

Keywords:
TRIP1100 Steel
Mechanical Properties
Microstructure
EBSD
Fracture Behavior

ABSTRACT

In this research, the heat treatment and production of high-strength advanced TRIP1100 steel were investigated and then the mechanical properties of the welds of this steel were evaluated by spot welding. For this purpose, the effect of rolling process and heat treatment of alloy steel sheets to achieve the ultra-high strength TRIP1100 steel microstructure was discussed. Microstructural examinations by Scanning Electron Microscopy (SEM) identified ferrite with bainite phases and martensite in matrix. The microstructural characteristics were examined using SEM microscopy with Electron Backscatter Diffraction (EBSD) analysis. The EBSD results showed that the type and orientation of the grains changed and the fraction of high-angle to low-angle boundaries in the present steel varied due to the presence of different phases. The EBSD results showed the acceptable rate of primary austenite in the structure according to the phaseology of this method. Having desirable mechanical properties was one of the most important results of this study, which at the same time maintained impact resistance and mechanical strength.

doi: *10.5829/ije.2022.35.03c.09*

1. INTRODUCTION

In recent years, advanced high-strength steels have been widely developed due to the need to increase the safety of car occupants and save fuel, and this is due to the ability to withstand static and dynamic forces, especially in accidents. This advantage of steels makes it possible to make parts with complex shapes and enhanced designs with forming processes. In recent years, advanced high strength steels have been evolving and their applications are developing especially in the automotive industry. These steels are now being used in vehicles to improve their efficiency and safety. TRIP steel are a class of high-strength steel alloys typically used in naval and marine applications and in the automotive industry. TRIP stands for "Transformation induced plasticity," which implies a phase transformation in the material, typically when a stress is applied. These alloys are known to possess an outstanding combination of strength and ductility [1]. Currently, TRIP (transformation plasticity) steels with low alloying elements are known so that the total amount of alloying elements in these steels does not reach more than 3.5%. In these steels, due to the application of thermomechanical processes, austenite to martensite transforms at room temperature. TRIP steels offer an extraordinary combination of strength and flexibility. As a result, it is suitable for making reinforced parts with complex shapes [2-5]. The microstructure of high-strength steels makes it possible to achieve greater elongation and a combination of excellent strength and flexibility for these steels. TRIP steels have a multi-phase microstructure with a complex shape, which includes a ferrite field with hard phases within it. This alloy contains varying amounts of residual austenite, ranging from 5 to 18% in some cases. Carbide-free bainite phases in soft ferrite field are present in this alloy. The austenite of

*Corresponding Author Email: abbasian_phd@yahoo.com (A Abbasian)

Please cite this article as: A. Abbasian, A. Ravangard, I. Hajian Nia, S. Mirzamohammadi, Investigation of Nicrostructure and Mechanical Properties of Newly Developed Advanced High strength TRIP steel, ***International Journal of Engineering, Transactions C: Aspects*** Vol. 35, No. 03, (2022) 567-571

these steels is transformed into martensite during plastic deformation. Therefore, today, the use of these steels in the automotive industry is a hot topic and is under research and development [6]. Applications of this steel in the upper pillar B include roof columns, engine support chassis, front and rear rails and seat frame [7] .The microstructure of TRIP steels consists of ferrite, bainite, martensite and greater than 5% of retained austenite. The latter is the most important phase constituent of TRIP steels, because its stress induced transformation to martensite results in work hardening of steel during deformation, and hence delays the onset of necking, eventually leading to a higher ductility [7, 8]. The bainite is formed by isothermal holding at a temperature below the bainite start transformation temperature (Bs) during cooling from intercritical annealing temperature.

TRIP steels have less volume fraction of hard phases such as martensite and bainite, therefore their initial yield stress is usually lower than that of DP steels. However, due to the progressive transformation of austenite to martensite, TRIP steels can reach ultimate tensile strength (UTS) values even higher than those for DP steels [9]. In this research, the process of production and manufacture of new TRIP1100 steel from a special alloy was investigated. The aim of this study was to achieve the best microstructural quality with suitable primary austenite and optimal mechanical properties.

2. MATERIALS AND METHODS

In this study, the test steel was cast by an induction furnace under the control of basic parameters, Materials that were melted and then cast. Among the wastes were steel sheets that had been calculated and carefully adjusted before chemical analysis. the chemical composition of this steels of which was analyzed by spectroscopy, is presented in Table 1. Cast ingots weighing 30 kg with dimensions of 100 × 100 × 30 cm after homogenization in the furnace for 1 hour at a temperature of 1000 ° C by hot rolling process and in 3 passes reached a thickness of 3.2 mm [8]. The heated rolling sheets were then cooled in an oven at 1000 ° C for 1 hour after annealing and then cooled rolling to a thickness of 1 mm in hydrochloric acid solution after mechanical deoxidation and acid washing. In order to achieve the desired microstructures (TRIP1100), the heat treatment cycle was designed using dilatometry at 950 ° C with sample dimensions in terms of 10 × 5 × 5 cm. By calculating from the dilatometry data, the intercritical temperatures and the starting temperature of the binetic and martensitic transformations were obtained, which are presented in Table 2 [9].

Figure 1 shows a schematic of the heat treatment cycle designed and performed on the test steel to achieve the desired structure. In order to achieve the microstructure of TRIP1100 steel, the sheets were subjected to intercritical annealing operation at 780 ° C for 360 s in a two-phase area and immediately immersed in a furnace containing molten salt bath at a temperature of 350 ° C for 600 s.

The tensile test of the samples was performed with a length of 5 cm and according to ASTM A370 standard with a speed of 1 mm/min. Then by wire cut from the middle of the fracture sample was cut to examine the cross-sectional microstructure of the sample [10].

To observe the microstructure of TRIP1100 steel, the samples were sanded and polished. Also, 2% Nital solution was used to prepare the SEM image [11]. To investigate the microstructure of TRIP steel, a JSM7001F type field emission microscope equipped with an EBSD return electron diffraction detector with TSL OIM ANALYSIS 8 analysis software was used. The samples were prepared and in the final stage, their cross section was polished with one micron diamond paste. In order to achieve a suitable surface quality for imaging, the final polishing of the samples was performed with 0.04 micron colloidal silica slurry, then a step size of 100 nm was selected for the studies. After tensile test, after failure of samples, their failure surface was examined using stereograph OLYMPUS and SEM PHILIPS XL3.

3. RESULTS AND DISCUSSION

Properties and advantages of advanced high strength steels the most important features and advantages of this type of steels can be mentioned as follows: These steels have a more complex microstructure compared to traditional steels and are mainly multi-phase to be able to have Provide a suitable and improved combination of strength and flexibility. In engineering alloys, flexibility

TABLE 1. Weight percentage of chemical composition of TRIP1100 steel used (wt%)

C%	Mn%	Si%	S%	P%	Cr%	V%	Ni%	Cu%	Al%	Fe%
0.18	2.45	1.1	0.036	0.048	0.058	0.02	0.04	0.08	0.01	Base

TABLE 2. Temperatures calculated by dilatometry

A_{C1} (°C)	A_{C3} (°C)	Calculation method
718	810	Dilatometry

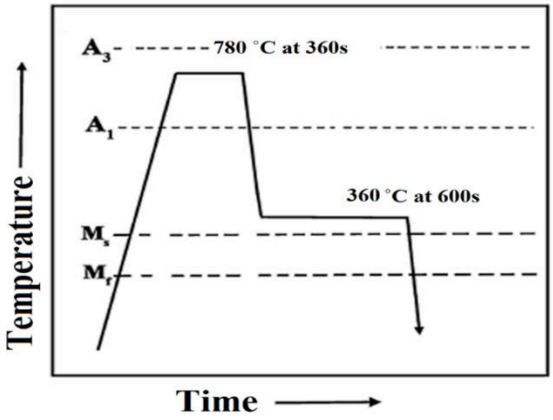

Figure 1. Schematic of TRIP steel heat treatment cycle

usually decreases with increasing strength. In other words, increasing strength is associated with decreasing toughness. We know that in high strength alloys the failure behavior tends to semi-brittle and brittle behaviors, but in steels (AHSS) the flexibility is high and as a result the probability of their failure decreases. Their high ductility makes it possible to produce specimens with complex shapes. Due to the use of different strength mechanisms and their ability to Work hardening, at the same time the strength and toughness of these alloys has been improved. Reduce the weight of the car by increasing the use of thinner and high strength steel sheets, which leads to reduced fuel consumption and reduced emissions.

Regarding advanced steels, it should be noted that a large amount of research by reputable companies has been spent annually to improve the design and use of these steels. For example, a comprehensive assessment and identification of applicable technology advances for AHSS steels was conducted in 2009. To complete the first phase in 2011, optimization of the steel structure of these steels was developed. Also, the future steel car has high hopes for the production of high-volume cars in the period 2015-2020 in phase 2 of this project. One of the attractions of this project is that for electric hybrid vehicles (PHEV), which do not discuss pollution and will soon replace current vehicles with fossil fuels, strength, vehicle speed and weight loss are of particular importance [8]. Figure 2 is a comparison of the percentage increase in the use of new steels. The key achievements of this project with regard to achieving a combination of strength and flexibility can be presented as follows:

•Achieve 29% body weight reduction
•Use of 97% HSS and AHSS steels
•Use of nearly 50% steels with a strength above 1000MPa
•Earn 5 crash safety stars
•Reduce greenhouse gas emissions

As shown in Figure 3, the microstructure of TRIP1100 steels in all directions tested includes polygonal ferrite, bainite, residual austenite (RA) and martensite/austenite (M/A) islands [12]. Due to the microstructure, residual austenite can be obtained in the bainite regions that formed during the isothermal transformation at 350 °C. Also, some residual block austenite is observed in polygonal ferrite grains [8]. In this alloy, the amount of silicon is higher than ordinary steels because the presence of silicon inhibits the formation of cementite and helps to retain all the carbon in the remaining austenite [4]. It has been shown that addition of silicon can prevent the deposition of cementite because silicon has very little solubility in cementite [13]. As austenite is further enriched by carbon in the isothermal transformation step, the onset of martensite is lower than room temperature. Therefore, part of the austenite does not convert to martensite after quenching at room temperature. This stable residual austenite is converted to martensite due to the TRIP phenomenon in the mechanically loaded steel [14].

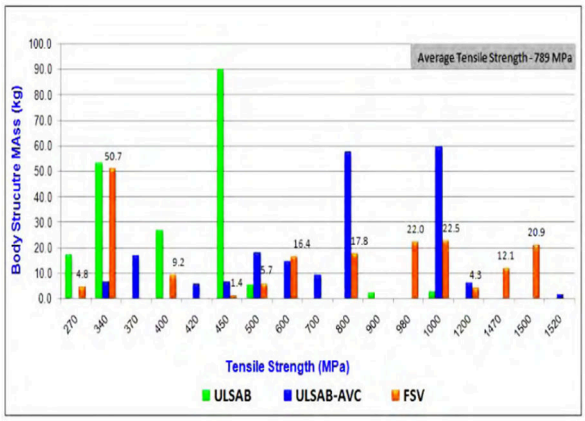

Figure 2. A comparison of the percentage increase in the use of new steels due to the increase in strength [7]

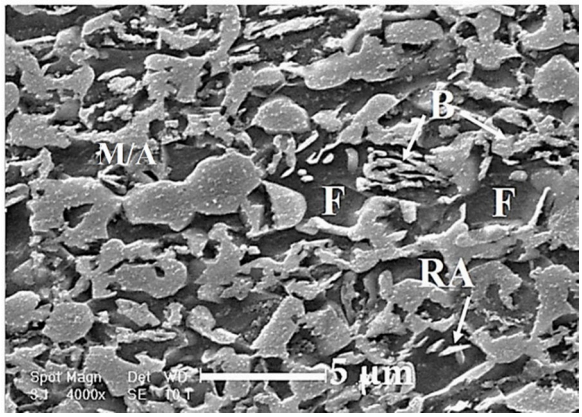

Figure 3. SEM image of TRIP steel

A more accurate knowledge of the properties is necessary to characterize the microstructure and the existing phases. For this purpose, electron diffraction analysis of EBSD return electrons was used to investigate the phase fraction. Figure 4a and b show the image of the crystal directions together with the IPF + IQ map image quality and phase fraction for TRIP1100 steel from EBSD analysis, respectively. According to Figure 4a, the size of polygonal ferrite grains was obtained between 0.5 to 4 µm and M/A phase islands between 1 and 2 µm.

The presence of residual austenite in the microstructure was determined by phase map in the range of Figure 4b, about 6.5% at the level of 50 µm. The images obtained from the phase map show the uniform distribution of the austenite remaining in the microstructure. It can be said that the remaining austenite has two block morphologies and very fine grains. The block remaining austenite forms within the M/A, while the residual austenite appears between the bainite masses as very fine grains [4]. Figure 4a shows a series of black and dark areas that have a lower IQ than the background, These areas are martensite. Martensites are darker due to lower image quality.

The stress diagram in terms of strain in the rolling direction and the average of the test results are shown in Figure 5 and Table 3, respectively. Examination of sources shows that the ratio of tensile strength (TS) to yield strength (YS) for high strength steels should not be less than 1.25 because flexibility is affected [8]. The TS/YS rate for TRIP1100 steel is more than 2.2, which indicates the steel's ability to work harder and more flexibly [5]. Table 3 shows the mechanical properties of TRIP steel.

To investigate the type of fracture of TRIP1100 steel, failure analysis was performed after tensile test. In

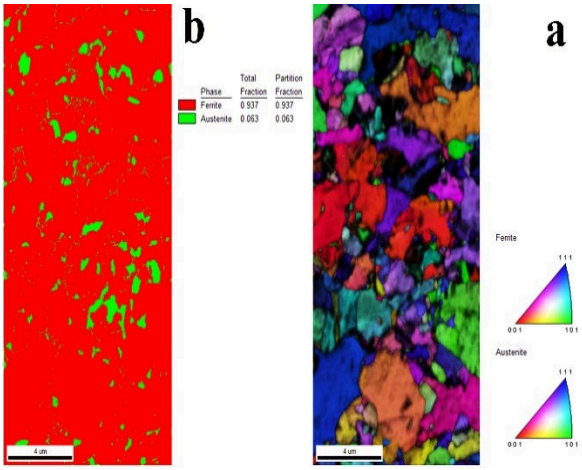

Figure 4. (a) Crystal image and IPF image quality map + IQ MAP, b) Fuzzy fraction of steel in the direction of TRIP rolling from EBSD results

TABLE 3. Mechanical properties of TRIP steel.

Yield strength (MPa)	Ultimate tensile strength (MPa)	Elongation (%)	Hardness (HV)
501 ± 12	1150 ± 13	23 ± 1	336 ±12

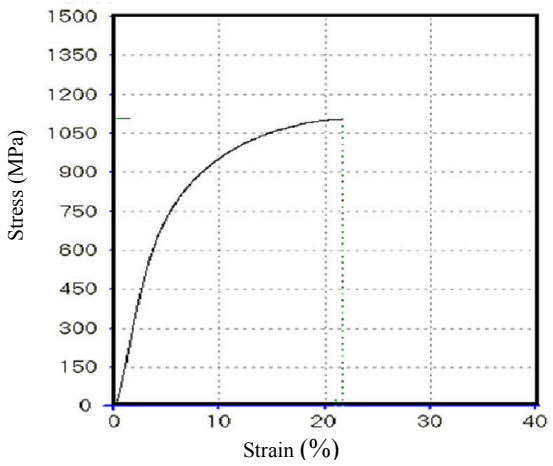

Figure 5. Stress diagram in terms of TRIP steel engineering strain in the rolling direction

TRIP1100 steel, fractures were detected with almost coaxial dimples and the bruises contained impurities that caused fracture and spread the crack during plastic deformation [14]. Figure 6 shows the SEM image of the TRIP1100 steel fracture surface. The present steel contains brittle and soft phases next to each other, therefore at the fracture surface, soft breakage and brittle failure are observed [15]. Cleavage failure, which had a lower percentage of failure surface than existing dimples, is indicated in Figure 6 by the arrow.

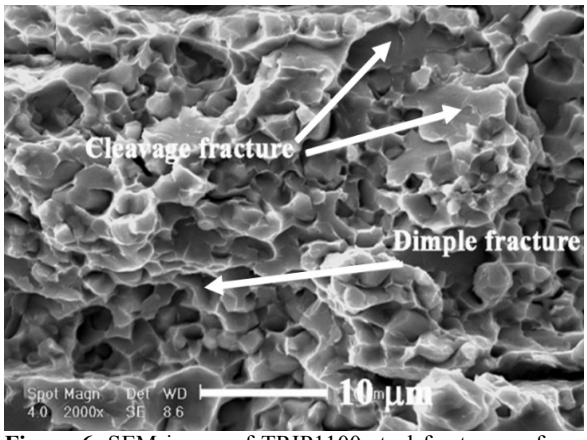

Figure 6. SEM image of TRIP1100 steel fracture surface, arrows represent dimples and cleavage failure

4. CONCLUSION

The microstructure of TRIP1100 steels in all directions tested includes polygonal ferrite, bainite, residual austenite (RA) and martensite/austenite (M/A) islands. According to the microstructure, residual austenite can be obtained in the bainite regions that formed during the isothermal transformation at 350 °C.

1. The presence of residual austenite in the microstructure was determined by phase map in the range of Figure 5b, about 6.5% at the surface of 50 µm. The images obtained from the phase map show the uniform distribution of the austenite remaining in the microstructure. It can be said that the remaining austenite has two block morphologies and very fine grains. The block remaining austenite forms within the M/A, while the residual austenite appears between the bainite masses as very fine grains.
2. The SEM image shows the failure surface of TRIP1100 steel. The present steel contains brittle and soft phases next to each other, due to at the fracture surface, soft failure and brittle failure are observed. Cleavage failure had a lower percentage of failure surface than existing dimples.
3. The TS/YS rate for TRIP1100 steel is more than 2.2, which indicates the steel's ability to work harder and more flexibly.

5. REFERENCES

1. "Specification for automotive weld quality- resistance spot welding of steel", AWS, (2007).
2. M. Pouranvari, S. P. H. Marashi and Safanama, D.S., "Failure mode transition in ahss resistance spot welds. Part ii: Experimental investigation and model validation", ***Materials Science and Engineering A***, Vol. 528, No. 29–30, doi: 10.1016/j.msea.2011.08.016
3. Jung, G., Lee, K., Lee, J., Bhadeshia, H., Suh, D.J.S., Welding, T.o. and Joining, "Spot weldability of trip assisted steels with high carbon and aluminium contents", ***Science and Technology of Welding and Joining***, Vol. 17, No. 2, (2012), 92-98, doi: 10.1179/1362171811Y.0000000081
4. Amirthalingam, M., "Microstructural development during welding of trip steels", (2010).
5. Zum Mallen, R., Tarr, S. and Dykeman, J., "Recent applications of high strength steels in north american honda production", in Great Designs in Steel Conference. (2008).
6. Pan, J., Sripichai, K., Lin, P., Wang, D. and Lin, S., Mechanics modeling of spot welds under general loading conditions and applications to fatigue life predictions, in Failure mechanisms of advanced welding processes. (2010), Elsevier.1-23.
7. Matsushita, M., Ikeda, R. and Oi, K.J.W.i.t.W., "Development of a new program control setting of welding current and electrode force for single-side resistance spot welding", ***Welding in the World***, Vol. 59, No. 4, (2015), 533-543, doi: 10.1007/s40194-015-0228-1
8. Pouranvari, M., Marashi, S.J.M.S. and A, E., "Failure mode transition in ahss resistance spot welds. Part i. Controlling factors", ***Materials Science and Engineering A***, Vol. 528, No. 29-30, (2011), 8337-8343, doi: 10.1016/j.msea.2011.08.017
9. Pouranvari, M., Marashi, S.J.S., welding, T.o. and joining, "Critical review of automotive steels spot welding: Process, structure and properties", ***Welding and Joining***, Vol. 18, No. 5, (2013), 361-403, doi: 10.1179/1362171813Y.0000000120
10. Tamarelli, C.M.J.S.M.D.I., Michigan, "The evolving use of advanced high-strength steels for automotive applications", Steel Market Development Institute, (2011).
11. Mikno, Z., Stepien, M. and Grzesik, B.J.W.i.t.W., "Optimization of resistance welding by using electric servo actuator", ***Welding in the World***, Vol. 61, No. 3, (2017), 453-462, doi: 10.1007/s40194-017-0437-x.
12. Hajiannia, I., Ashiri, R., Pakmanesh, M., Shamanian, M. and Atapour, M.J.J.o.E.F.M., "Evaluation of performance of resistance spot welded joints with different parameters in advanced high strength trip steel", ***Journal of Environmental Friendly Materials***, Vol. 3, No. 1, (2019), 9-16, doi:
13. Pouranvari, M., Mousavizadeh, S., Marashi, S., Goodarzi, M., Ghorbani, M.J.M. and Design, "Influence of fusion zone size and failure mode on mechanical performance of dissimilar resistance spot welds of aisi 1008 low carbon steel and dp600 advanced high strength steel", ***Materials & Design***, Vol. 32, No. 3, (2011), 1390-1398, doi: 10.1016/j.matdes.2010.09.010
14. Emre, H.E. and Kaçar, R., "Development of weld lobe for resistance spot-welded trip800 steel and evaluation of fracture mode of its weldment", ***The International Journal of Advanced Manufacturing Technology***, Vol. 83, No. 9-12, (2016), doi: 10.1007/s00170-015-7605-1
15. Kim, C.-H., Choi, J.-K., Kang, M.-J., Park, Y.-D.J.J.o.A.i.M. and Engineering, M., "A study on the co2 laser welding characteristics of high strength steel up to 1500 mpa for automotive application", ***Journal of Achievements***, Vol. 39, No. 1, (2010), 79-86.

Persian Abstract

چکیده

در این پژوهش به بررسی عملیات حرارتی و تولید فولاد فوق استحکام بالای پیشرفته TRIP1100 پرداخته شد و سپس به ارزیابی خواص مکانیکی جوش های این فولاد که توسط نقطه‌ای انجام شده بود پرداخته شده است. برای این منظور تأثیر فرآیند نورد و عملیات حرارتی ورق های فولادی آلیاژ سازی شده جهت دستیابی به ریزساختار فولاد TRIP1100 فوق استحکام بالای پیشرفته پرداخته شد. بررسی های ریزساختاری توسط میکروسکوپ الکترونی روبشی زمینه فریت با فازهای بینیت، مارتنزیت را مشخص کرد. مشخصات میکروساختاری با استفاده از میکروسکوپ SEM با آنالیز EBSD، بررسی شدند. نتایج EBSD نشان داد، نوع و جهت‌گیری دانه ها تغییر کرده و کسر مرزهای با زاویه زیاد به زاویه کم در فولاد حاضر به دلیل وجود فاز های مختلف متغیر و فراوانی دارد، نتایج EBSD میزان مورد قبولی آستنیت اولیه را در ساختار با توجه به فاز شناسی این روش نمایش داد. دارا بودن خواص مکانیکی مطلوب از مهم ترین نتایج این پژوهش بود که همزمان ضربه پذیری و استحکام مکانیکی حفظ شد.

International Journal of Engineering

Journal Homepage: www.ije.ir

Experimental Investigation and Numerical Simulation of Air Circulation in a Non-AC Bus Coach System

S. J. Niranjana[a]*, S. S. Kubsad[b], S. Manjunatha[c], Y. Nagaraj[d], I. Bhavi[e], B. M. Angadi[e], A. J. Chamkha[f], M. B. Vanarotti[g]

[a] *Department of Mechanical Engineering, School of Engineering and Technology, CHRIST (Deemed to be University), Bengaluru- 560076, Karnataka, India*
[b] *Department of Mechanical Engineering, Atria Institute of Technology, Bengaluru- 560024, Karnataka, India*
[c] *Department of Mathematics, School of Engineering and Technology, CHRIST (Deemed to be University), Bengaluru- 560076, Karnataka, India*
[d] *Department of Mechanical Engineering, SJM Institute Technology, Chitradurga-577502, Karnataka, India*
[e] *BLDEA's V.P. Dr. P.G. Halakatti College of Engineering and Technology, Vijayapur-586103, Karnataka, India*
[f] *Faculty of Engineering, Kuwait College of Science and Technology, Doha District, 7th Ring Road, 35004, Kuwait*
[g] *Sanjeevan Engineering & Technology Institute, Sanjeevan Knowledge City, Panhala, Kolhapur, Maharastra, India*

PAPER INFO

Paper history:
Received 29 November 2021
Received in revised form 21 December 2021
Accepted 23 December 2021

Keywords:
Air Circulation
CFD Analysis
Non-AC Bus
Wind Tunnel Test

ABSTRACT

Air circulation plays a vital role in the comfort of passengers in a bus, being a non-AC bus without any aid from the air conditioning system. The circulation of air is utterly dependent on the design of the bus and the natural flow of air. However, optimize the flow of air inside the bus, a study on the design of the bus is needed. In this regard, experimental work was carried out to achieve uniform airflow by redesigning the coach into an aerodynamic shape. The openings are provided at the leading edge of the bus to evaluate the best possibility for air to circulate in the bus. Three openings were provided at the leading edge of the bus, the first and second openings were mere openings, and the third opening was fitted with a roof vent providing three different geometric patterns to airflow. The initial boundary conditions were developed by considering that all windows and doors of the bus are closed. The scaling ratio of 1:20 was considered for modeling the bus. The experiments were conducted in the wind tunnel test rig. It was observed from the experimentation that the velocity of the air was considered to be the most influential parameter for the optimal air circulation. The velocities of 21.96 m/s and 22.68 m/s were obtained inside bus. The obtained experimental velocities were validated with results obtained by the Computational Fluid Dynamics (CFD). It was observed that a deviation of 5% for the given velocity of 20 m/s.

***doi**: 10.5829/ije.2022.35.03c.10*

NOMENCLATURE

v	Velocity of air (m/s)	g	Acceleration due to gravity (m/s^2)
ρ	Density (kg/m^3)	ρ_{air}	Density of air (kg/m^3)
Δh	Manometer height (m) (Final – Initial)		

1. INTRODUCTION

The non-AC bus is a major mode of transport in developing countries. During the journey passengers, comfort plays a vital role by Niranjan et al. [1]. The uneven airflow inside a non-AC bus may cause discomfort on the passenger. Kanekar et al. [2] stated the passenger's comfort will be improved by redesigning the existing structure of a bus. Drag force is the resistance offered by air against a moving object and which can be reduced with a small modification in the external geometry. Patidar et al. [3] experimented on an existing and modified bus model and proved a low drag coefficient. Norwazan et al. [4] states that reduction in

*Corresponding Author Institutional Email: *niranjana.s@christuniversity.in* (S. J. Niranjana)

Please cite this article as: S. J. Niranjana, S. S. Kubsad, S. Manjunatha, Y. Nagaraj, I. Bhavi, B. M. Angadi, A. J. Chamkha, M. B. Vanarotti, Experimental Investigation and Numerical Simulation of Air Circulation in a Non-AC Bus Coach System, ***International Journal of Engineering, Transactions C: Aspects*** Vol. 35, No. 03, (2022) 572-579

the fuel consumption and efficiency of the vehicle is determined by aerodynamic drag and coefficient of lift. Petzalla et al. [5] experimented on sedan-type vehicles with different vehicle geometrical features such as hood angle, rear angle, screen angle, and corner radius. They conclude the use of rear screen angle can reduce that drag. The crashes are happening due to the crosswind effect, a severe problem in some countries. The body's ideal shape suggests that a rounded front face, rounded. topsides, and sharp rear corners improve directional stability. Vollaro [6] stated the use of air screen doors and windows will improve the ventilation in non-AC buses during traffic signals and bus stops. During hot sunny days, the airflow inside a coach is an important aspect. Aliahmadipour et al. [7] explored the temperature and velocity distribution inside the coach. Heated manikins were used to study the temperature distribution with the passenger sitting and sleeping positions.

Shen et al. [8] found that the slight modification in the existing coach results in better passenger comfort. Rodrigues et al. [9] conducted an aerodynamic study and explored that changing small dimensions in the geometry reduces the drag and fuel consumption up to 20% and 10%, respectively.

The CFD analysis for a three-dimensional bus coach was carried out using ANSYS software, and the results are within the acceptable limit [10, 11]. Niranjana et al. [12] numerically analysed Ashok Leyland MTX Micra 28-seater on different types of boundary conditions and estimated the drag force would reduce to 0.67 by redesigning the bus structure.

Kale et al. [13] experimented on a non-AC bus, during the journey, the air enters from a rare window and moves towards the driver in a, and the velocity of air is almost one-tenth of the bus speed. They were opening the alternative window found to improve the air circulation in a non-AC-bus, increasing the passenger comfort [14, 15]. An experimental investigation was conducted on a scaled bus model in a wind tunnel test by placing the bus model exactly in the centre. The readings of drag and velocities were measured inside the bus [16, 17]. Niranjan et al. [18] provided a proper duct system that enhances passengers' comfort by the uniform airflow inside a non-AC bus. The amount of air required to cool the non-AC bus is the algebraic sum of heat generated from the glass, roof, passenger and engine loads are considered while designing a proper duct system and the cross-section of the duct by Fayazbakhsh and Bahrami [19]. Mathematical modelling of flow over surfaces was studied using CFD [20, 21]. Rahate et al. [22] designed an air distribution system for operation theatre using flow visualization techniques to improve flow characteristics. Kumar et al. [23] carried out an experimental study on flow characteristics around twin wind blades.

This work aims to create a uniform airflow in non-AC buses by providing adequate inlets near the front and top of the bus. The main issue in the existing public transportation system in developing and underdeveloped countries is achieving uniform airflow inside a non-AC bus. The bus will generally be completely filled during peak travel hours, with no available seats. The person in the window seat will experience a high flow of air and close the window to avoid it, causing the person standing in the aisle to suffocate.

The main objective of this work is to reach uniform airflow inside a non-AC bus system by redesigning the bus structure, modelling and fabricating a scaled bus model, and experimenting with and numerically simulating the scaled bus model.

2. MATERIALS AND METHODOLOGY

This work attempts to achieve uniform airflow inside the non-AC bus coach by providing proper openings at three levels, like two openings in the front and one in the bus's rooftop. 3-D model of passenger vehicle (bus) was developed by SOLIDWORK software as shown in Figure 1 with the dimensions of 350 mm in length and 105 mm in width and height, respectively. The topology of the fluid flow zone of interest was defined with the help of Computer-Aided Design (CAD) software. It was an essential aspect of the design and optimization process.

2. 1. Experimentation A scaled MiTR non-AC bus model of 1:20 for experimental analysis is fabricated using a transparent acrylic sheet of thickness 6mm, as shown in Figure 2. Acrylic is a translucent synthetic material with excellent strength, stiffness and optical clarity. In contrast to many other transparent plastics, they possess superior weathering properties. Table 1 shows material property of acrylic sheet used to construct the bus model.

A scaled bus model is placed at the centre of the wind tunnel to measure the velocity. The provision is provided to measure the bus's velocity at three different positions, one is at the front of the first seat, the second in the middle

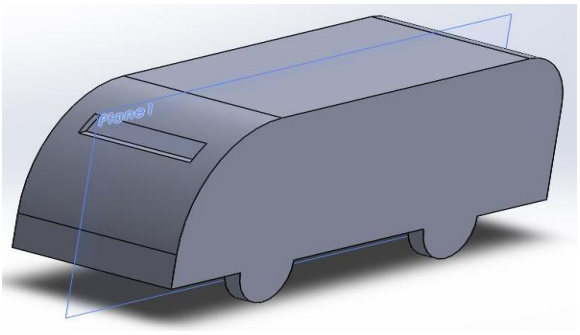

Figure 1. 1:20 Scaled model of non-AC bus

(a) Side view

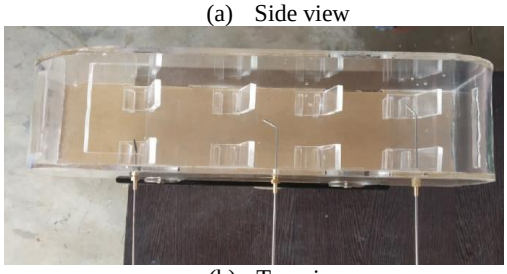

(b) Top view

Figure 2. The scaled model of bus

TABLE 1. Material properties of acrylic sheet

Tensile Strength (MPa)	Flexural Modulus (MPa)	Light Transmission	Water Absorption	Density (g/cm^3)
75	115	>92%	0.2%	1.19

of the bus, and the last is provided in front of the last seat. The velocity port can be adjusted between the seats as shown in Figure 2b.

Wind tunnel test facility (600 x 600 x 2000) mm. is used for measuring the airflow inside a non-AC bus. The wind tunnel capacity of airflow is up to 45 m/s, and the setup has a facility for drag, lift, smoke and velocity tests, as shown in Figure 3. After repeated initial readings, the maximum error was noticed around 0.5%.

Recalibration and testing of wind gauges is done in wind tunnels. It usually contains a variety of settings for testing objects or recalibrating wind gauges in various wind speeds. The object or wind gauge will not be destroyed while in use, and the wind gauge will be able to measure the wind precisely and correctly both outdoors and indoors. This investigation concentrates on velocity distribution inside a non-AC bus. The test wind velocity can be set by adjusting the Pitot tube at the centre of the test area by using a lever mechanism. Initial readings in the static manometer are to be noted and then successive readings are noted to set the machine's RPM to conduct the experiment. The difference between initial and final readings will give a height. From Equation (1), the velocity at the inlet of the test chamber is calculated.

Figure 3. Wind tunnel test rig with scaled bus model

Once the required velocity of the machine is attained, and the machine's initial setup is done. The scaled bus model is placed exactly at the centre of the test chamber in a wind tunnel. The machine is run at 850 and 1015 RPM, respectively, to achieve the required velocity of 20m/s and 25m/s (considering the Indian driving cycle for ergonomic study for heavy passenger vehicles). Further, the manometer readings before starting the machine and later the successive readings at three different positions are noted. The initial and final reading difference gives the required height, and substituting in Equation (1), the velocity is calculated at the three different levels.

$$V = \sqrt{\frac{2\rho g \Delta h}{\rho_{air}}} \quad (1)$$

Initial readings in the multibank manometer are measured, and it found to be 19.4cm. The final readings at three different positions are measured and tabulated in Table 2.

2. 2. Boundary Conditions

The experimental analysis is carried for two different velocities through the inlet region for 20m/s and 25m/s, respectively. The Numerical analysis is carried out with a velocity of 20m/s. Only the inlets ports are kept open and all other openings (windows, doors) of the bus are kept closed.

TABLE 2. Multibank manometer readings for the five different cases

Case	RPM	Position 1 in cm	Position 2 in cm	Position 3 in cm
1	850	21.5	21.3	21.3
	1015	22.5	22.5	22.3
2	850	22.2	22.4	22.4
	1015	23.5	24	24
3	850	20.5	23.5	23.6
	1015	22	25	25.5
4	850	23.3	23.6	23.4
	1015	25	25.4	25.2
5	850	21.5	21.7	21.8
	1015	24.6	24.9	24.8

The computational domain surrounds the Inflow and outflow borders. Aside from symmetry and solid walls, it is assumed that the velocity distribution is uniform at the inflow and pressure is assumed to be zero-gradient at the outflow. Table 3 indicates the assumed conditions and equations for the numerical analysis. There are four parameters for the convergence pressure, temperature, momentum and turbulence. 10-6 for K- ε and 10-4 for pressure, velocity and temperature.

3. RESULTS AND DISCUSSION

3. 1. Experimental Investigation This section discusses the detailed results of a successful trial of wind tunnel test for airflow in the non-AC bus. In the first trial, the machine is kept at the height of 7.9 cm and run at 700rpm speed, and later machine ends with the same speed with a height of 9.5 cm. Substituting these readings in Equation (1), we noticed that velocity is 16 m/s. But the required velocity to conduct a test on the scaled bus model is 20m/s and 25m/s. To achieve the target, the speed of the machine is increased from 700 to 800rpm. Thus, obtained velocity is found to be 19.2 m/s. After several successive trials, it is noticed that if the machine runs at 850rpm and 1015rpm, the velocity is found to be 20m/s and 25m/s, respectively.

After setting the standard experimental set up the specimen is placed at the chamber's centre. Figure 4 represents the position of slots at three different test cases, respectively. In case 1, the openings are provided only in the first slot of the front end. And all other regions are closed. In case 2, the openings provided only on the roof vent outside, and all other slots are closed. In case 3, the openings provided only in the top slot and all other slots are closed. Case 4 illustrates the outlets provided only inside the roof vent and all other slots closed. In case 5, the openings are provided only in the second slot of the frontend and all other slots are closed. The value of the velocity of the air flow in the bus for all five different cases is tabulated in Table 4.

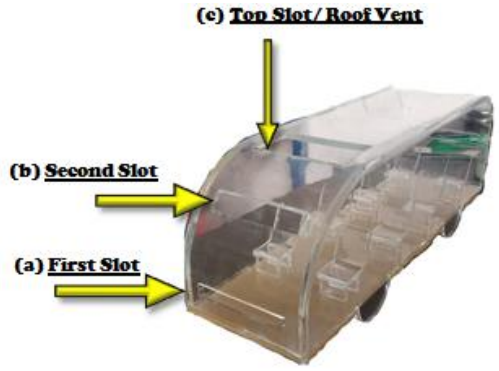

Figure 4. Scaled bus model with different test cases

It is found that out of all five cases result, the case five results show that the air's velocity is uniform in the non-AC bus coach.

Based on the experimental results, Figures 5a to 5e are plotted to explain the input and output velocity at three different positions.

From Figures 5a and 5b, it is observed that velocity is not uniform. Since air entered in Figure 5a is hitting the passenger's foot, air will be diverted non-uniformly, and from Figures 5b and 5c, it is observed that the air entered from the roof vent will not pass to the driver and few passengers sitting next to the driver. Hence the uniform air circulation is not found. Figures 5d and 5e explore that air velocity is found to be uniform in all three positions, which is due to air entering from the front end and in the

TABLE 3. Appendix

Type	Explanation
Governing Equation	Navier stoke equation • Pressure-momentum • Mass conservation • Continuity viscosity • K- ε equation $\rho\frac{Du}{Dt} = \rho\left(\frac{\partial u}{\partial t} + u.\nabla u\right) =$ $\nabla p + \nabla\left\{\mu\left(\nabla u + (\nabla u)^T - \frac{2}{3}(\nabla.u)I\right) + \xi(\nabla.u)I\right\} + \rho g$
Initial Condition	It is running at atmospheric pressure condition ie normal temperature and pressure (NTP).
Boundary Condition	At inlet velocity, outlet- zero pressure and walls – Adiabatic
Assumptions	The velocity near the entire setup remains constant. There is no variation in the property of fluid and temperature.

TABLE 4. Velocity of air at different position

Cases	RPM	Input Velocity in m/s	Velocity at Position 1 in m/s	Velocity at Position 2 in m/s	Velocity at Position 3 in m/s
Case 1	850	20	18.37	17.48	17.48
	1015	25	22.32	22.32	21.59
Case 2	850	20	15	26.6	26.9
	1015	25	21.59	30.8	32.08
Case 3	850	20	25.98	26.9	26.29
	1015	25	30.8	31.83	31.32
Case 4	850	20	19.64	20.44	20.83
	1015	25	29.74	30.54	30.27
Case 5	850	20	21.96	22.68	22.68
	1015	25	26.3	27.78	27.78

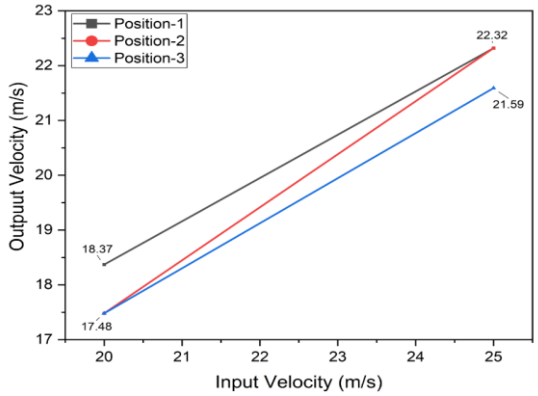

(a)

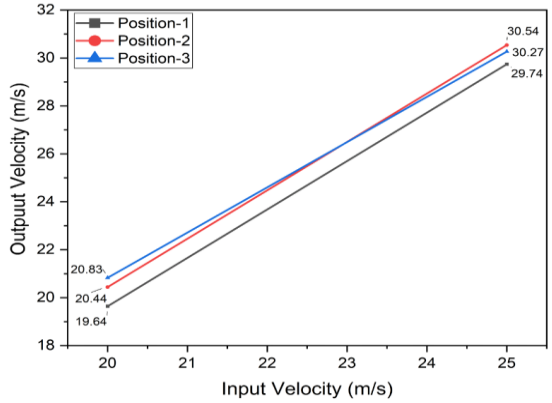

(b)

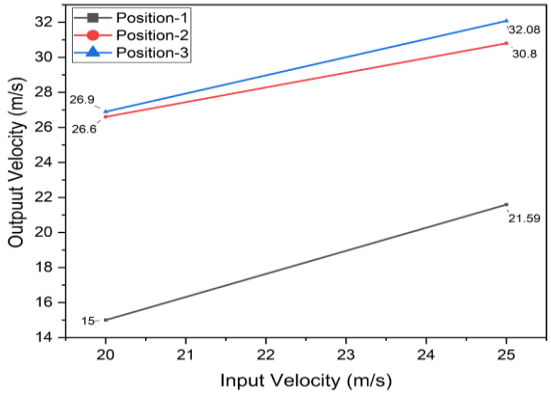

(c)

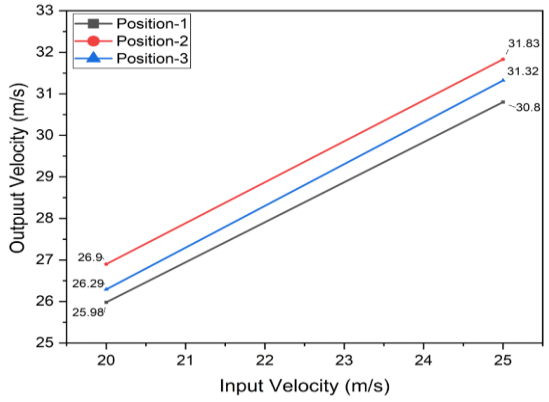

(d)

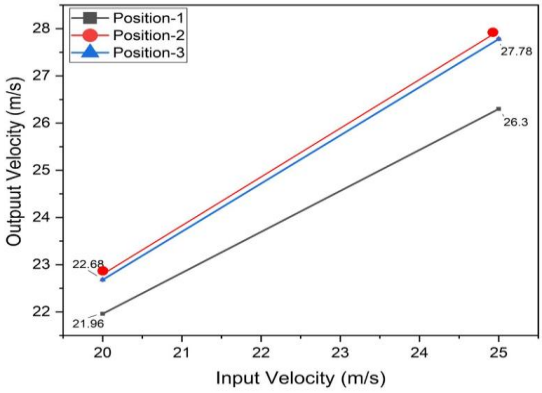

(e)

Figure 5. Velocity distribution curve

appropriate height of the sitting position of passengers. Hence, we can conclude that obstacles for airflow are comparatively less in case of Figure 5e.

3. 2. CFD Analysis The CFD analysis for case 5 (opening in the front and all other regions are closed) is considered, as this case results are better among the different test cases. The discretization of a scaled non-AC bus model is as shown in Figure 6.

The three-dimensional tetra mesh and 779151 elements are used for the analysis. The quality parameters like aspect ratio, Jacobian, minimum and maximum angle, skew angle and warpage are maintained during the discretization process. Assign an inlet, outlet, body, side and top as different layers in the bus, and these files are imported on a three-dimensional layout with the ANSYS Fluent CFD code in a staggered grid system.

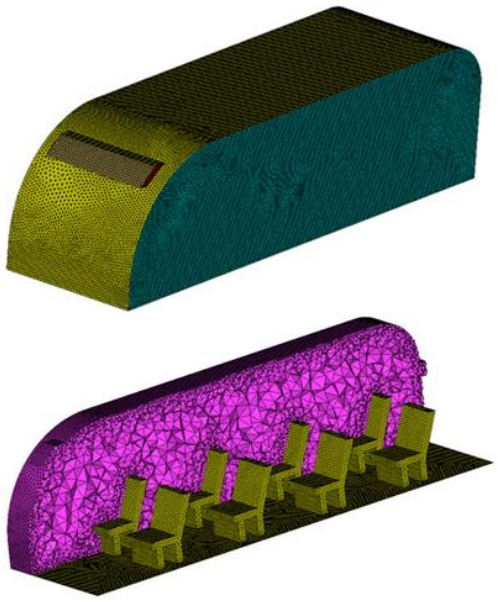

Figure 6. Meshed model of the bus

The governing equations are solved using the finite-volume approach, and the turbulence effect is analyzed with an equation k-ε model.

The CFD analysis is carried out using ANSYS Fluent 16.0 software, and velocity is measured at different regions. The input velocity of 20m/s is assigned in the front slot of the bus, as shown in Figure 7a. Figure 7b explores that air velocity is 21m/s in front of first row chairs of the bus, and the velocity is 15m/s in the middle of the aisle, as shown in Figure 7c. Finally, it is found that the outlet velocity is measured to be 22m/s, as depicted in Figure 7d. The recirculation of air near the inlet and outlet results in vertex formation, which increases the velocity slightly, as shown in Figures 7b and 7d.

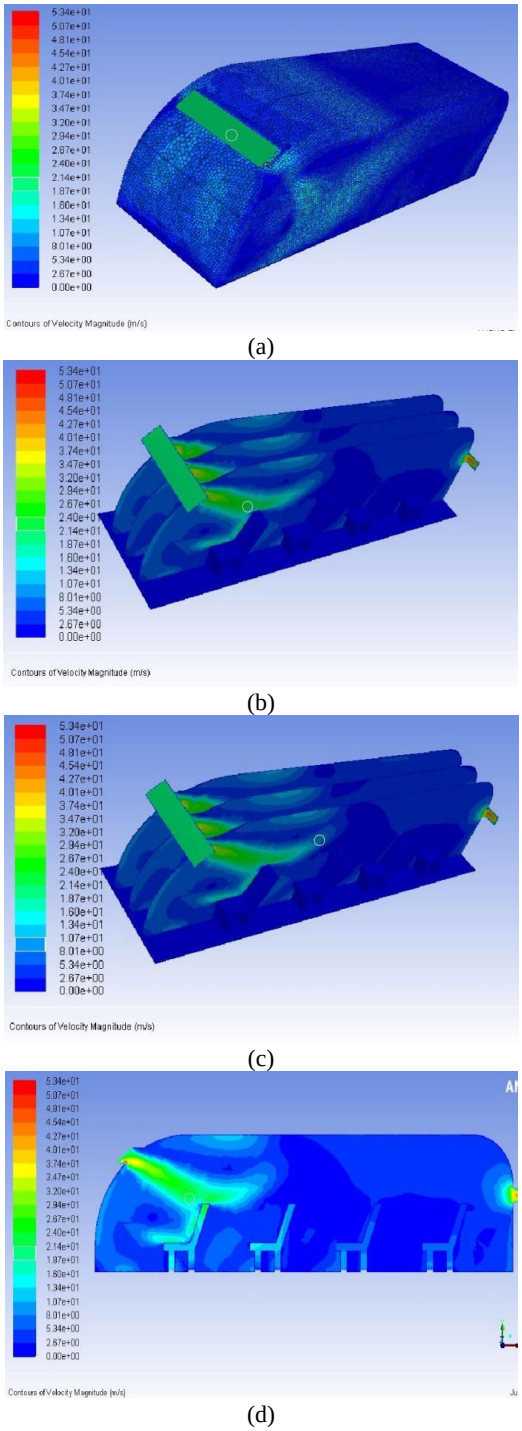

Figure 7. CFD results using ANSYS fluent software

Table 5 represents the comparison results of experimental and CFD analysis. It is found that the velocity at the front and rear end match with CFD analysis results, and velocity at the middle of the aisle is comparatively less, which is due to obstacles in the bus.

Figure 8 represents the experimental and numerical method results. The velocity at three different positions is shown.

Table 6 represents the number of iterations conducted for the CFD analysis. As the number of elements is increased, the velocity at position one inside the bus is decreased, and at some iterations, the value of velocity is closely matching hence convergence is achieved. The values are plotted in Figure 9. In order to reduce the computational time for the numerical analysis 779151 elements were considered for the study.

TABLE 5. Comparison results between experimental and numerical methods

Input Velocity of 20 m/s	Experimental Results in m/s	Numerical Results in m/s
In front of first seat	21.96	21
Middle of aisle	22.68	15
Near last seat	22.68	22

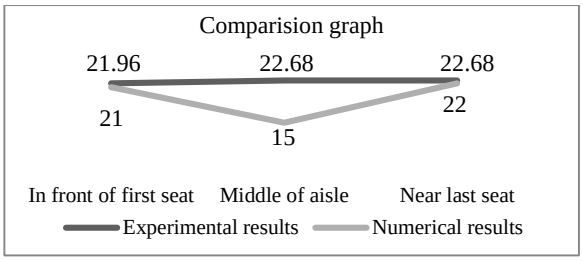

Figure 8. CFD and experimental results comparison

TABLE 6: Analysis iteration

Sl No	Number of Elements	Velocity at Position 1 in m/s
1	10000	41.6
2	100000	35.2
3	300000	29.4
4	500000	24.6
5	790000	21
6	900000	20.8
7	110000	21.04

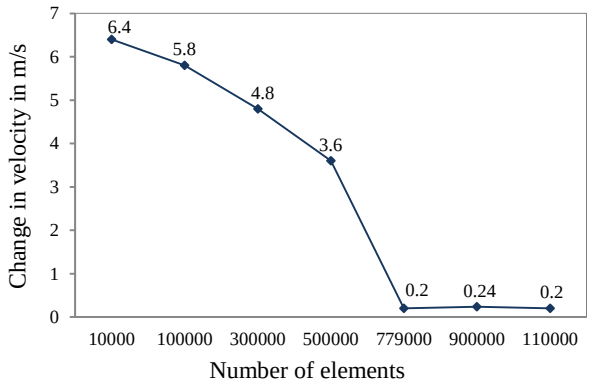

Figure 9. Mesh independency (Convergence criteria)

4. CONCLUSION

An experimental investigation of uniform airflow for a scaled MiTR non-AC bus model of 1:20 has been conducted. The bus model is fabricated using transparent acrylic sheet of thickness 6mm. The numerical simulation of uniform airflow for the test model is performed using CFD. The major outcome of the study reveals that the velocity distribution curve is uniform in the case 5 test condition and the numerical and experimental results are in close agreement with a deviation of less than 5%.

5. REFERENCES

1. Niranjana, S. J., Kubsad, S. S., Ravichandran, G., and Santhosh, N. "A Comprehensive Understanding of Airflow in Non Air conditioned Bus Coaching System." ***International Journal of Engineering and Advanced Technology***, Vol. 9, No. 3, (2020), 1222–1225. https://doi.org/10.35940/ijeat.C5317.029320
2. Kanekar, S., Thakre, P., and Rajkumar, E. "Aerodynamic study of state transport bus using computational fluid dynamics." ***IOP Conference Series: Materials Science and Engineering***, Vol. 263, (2017), 062052. https://doi.org/10.1088/1757-899X/263/6/062052
3. Patidar, A., Gupta, U., and Bansal, A. "Fuel Efficiency Improvement of Commercial Vehicle by Investigating Drag Resistance." In SAE International, 2015. https://doi.org/10.4271/2015-01-2893
4. Norwazan, A. R., Khalid, A. J., Zulkiffli, A. K., Nadia, O., and Fuad, M. N. "Experimental and Numerical Analysis of Lift and Drag Force of Sedan Car Spoiler." ***Applied Mechanics and Materials***, Vol. 165, (2012), 43–47. https://doi.org/10.4028/www.scientific.net/AMM.165.43
5. Petzäll, J., Torlund, P. Å., Falkmer, T., Albertsson, P., and Björnstig, U. "Aerodynamic design of high-sided coaches to reduce cross-wind sensitivity, based on wind tunnel tests." ***International Journal of Crashworthiness***, Vol. 13, No. 2, (2008), 185–194. https://doi.org/10.1080/13588260701788476
6. Vollaro, R. de L. "Indoor Climate Analysis for Urban Mobility Buses: a CFD Model for the Evaluation of thermal Comfort." ***International Journal of Environmental Protection and Policy***, Vol. 1, No. 1, (2013), 1. https://doi.org/10.11648/j.ijepp.20130101.11
7. Aliahmadipour, M., Abdolzadeh, M., and Lari, K. "Air flow simulation of HVAC system in compartment of a passenger coach." ***Applied Thermal Engineering***, Vol. 123, (2017), 973–990. https://doi.org/10.1016/j.applthermaleng.2017.05.086
8. Shen, K., Li, F., and Ni, J. "1D/3D Coupling Calculation Analysis on Bus Cooling System." ***Energy and Power Engineering***, Vol. 06, No. 14, (2014), 550–556. https://doi.org/10.4236/epe.2014.614048
9. Rodrigues, A. F. A., Gertz, L. C., Cervieri, A., and Telh, M. A. "Aerodynamic Analysis of a Vehicle Minibus." In SAE Technical Paper Series, 23rd SAE Brasil International Congress and Display, 2014. https://doi.org/10.4271/2014-36-0327
10. Shafie, N. E. A., Kamar, H. M., and Kamsah, N. "Effects of air supply diffusers and air return grilles layout on contaminants concentration in bus passenger compartment." ***International Journal of Automotive Technology***, Vol. 17, No. 5, (2016), 751–762. https://doi.org/10.1007/s12239-016-0074-1
11. Thabet, S., and Thabit, T. H. "CFD Simulation of the Air Flow around a Car Model (Ahmed Body)." ***International Journal of Scientific and Research Publications (IJSRP)***, Vol. 8, No. 7, (2018), 2250–3153. https://doi.org/10.29322/IJSRP.8.7.2018.p7979
12. Shravanabelagola Jinachandra, N., Sadashivappa Kubsad, S., Sarpabhushana, M., Siddaramaiah, S., and Rajashekaraiah, T. "Modeling and computational fluid dynamic analysis on a non-AC bus coach system." ***Heat Transfer***, Vol. 49, No. 8, (2020), 4870–4877. https://doi.org/10.1002/htj.21857
13. Kale, S. R., Veeravalli, S. V., Punekar, H. D., and Yelmule, M. M. "Air flow through a non-airconditioned bus with open windows." ***Sadhana***, Vol. 32, No. 4, (2007), 347–363. https://doi.org/10.1007/s12046-007-0029-3
14. John, P., Sriram, B., R, S. K., Kumar, S. V., Ramasamy, P., and Vijay Ram, C. "Ventilation Improvement in a Non-AC Bus." In SAE International, 2013. https://doi.org/10.4271/2013-01-2457
15. S, V., C, V. R., and P, S. "Evaluation of Bus Ventilation Methods Using CFD." In ***SAE International***. https://doi.org/10.4271/2013-26-0043
16. Ünal, Ş. "An Experimental Study on a Bus Air Conditioner to Determine its Conformity to Design and Comfort Conditions." ***Journal of Thermal Engineering***, Vol. 3, No. 1, (2016), 1089–1089. https://doi.org/10.18186/thermal.277288
17. Moureh, J., Menia, N., and Flick, D. "Numerical and experimental study of airflow in a typical refrigerated truck configuration loaded with pallets." ***Computers and Electronics in Agriculture***, Vol. 34, No. 1–3, (2002), 25–42. https://doi.org/10.1016/S0168-1699(01)00178-8
18. Niranjana, S., Kubsad, S. S., Nagaraj, Y., Manjunath, S., and Shivakumar, S. "Experimental Investigation of Air Circulation Using Duct System in a Non-AC Bus Coach." ***IOP Conference Series: Materials Science and Engineering***, Vol. 1065, No. 1, (2021), 012006. https://doi.org/10.1088/1757-899X/1065/1/012006
19. Fayazbakhsh, M. A., and Bahrami, M. "Comprehensive Modeling of Vehicle Air Conditioning Loads Using Heat Balance Method." In SAE International, 2013. https://doi.org/10.4271/2013-01-1507
20. Askari, S., and Shojaeefard, M. H. "Mathematical Modeling of Potential Flow over a Rotating Cylinder." ***International Journal of Engineering, Transactions A: Basics***, Vol. 24, No. 1, (2011), 55–63. Retrieved from https://www.sid.ir/en/Journal/ViewPaper.aspx?ID=194565
21. Sharifipour, M., Bonakdari, H., and Zaji, A. H. "Impact of the Confluence Angle on Flow Field and Flowmeter Accuracy in Open Channel Junctions." ***International Journal of Engineering, Transactions B: Applications***, Vol. 28, No. 8, (2015), 1145–1153. Retrieved from

https://www.ije.ir/article_72560.html

22. Rahate, S. D., and Sarode, A. D. "Design of Air Distribution System for Operation Theatre Using Flow Visualization Techniques to Improve Flow Characteristics." ***International Journal of Engineering, Transactions A: Basics***, Vol. 33, No. 1, (2020), 164–169. https://doi.org/10.5829/IJE.2020.33.01A.19

23. Kumar, R., and Saranprabhu, M. K. "Experimental Study on Flow Characteristics Around Twin Wind Blades (RESEARCH NOTE)." ***International Journal of Engineering, Transactions B: Applications***, Vol. 31, No. 5, (2018), 820–825. https://doi.org/10.5829/ije.2018.31.05b.18

Persian Abstract

چکیده

گردش هوا نقشی حیاتی در راحتی مسافران اتوبوس ایفا می‌کند، زیرا یک اتوبوس بدون AC بدون هیچ کمکی از سیستم تهویه مطبوع بهره‌مند است. گردش هوا کاملاً به طراحی اتوبوس و جریان طبیعی هوا بستگی دارد. با این حال، برای بهینه‌سازی جریان هوا در داخل اتوبوس، مطالعه در مورد طراحی اتوبوس مورد نیاز است. در این راستا، کار آزمایشی برای دستیابی به جریان هوای یکنواخت با طراحی مجدد اتوبوس به شکل آیرودینامیکی انجام شد. دهانه‌ها در لبه جلویی اتوبوس برای ارزیابی بهترین امکان برای گردش هوا در اتوبوس فراهم شده است. سه دهانه در لبه جلویی اتوبوس تعبیه شده بود، دهانه اول و دوم بازشونده بودند و دهانه سوم با یک دریچه سقفی تعبیه شده بود که سه الگوی هندسی مختلف را برای جریان هوا فراهم می‌کرد. شرایط مرزی اولیه با در نظر گرفتن بسته بودن تمام پنجره‌ها و درهای اتوبوس ایجاد شد. نسبت مقیاس ۱:۲۰ برای مدل سازی اتوبوس در نظر گرفته شد. آزمایش‌ها در دکل آزمایشی تونل باد انجام شد. از آزمایش مشاهده شد که سرعت هوا به عنوان تأثیرگذارترین پارامتر برای گردش بهینه هوا در نظر گرفته شد. سرعت های ۲۱/۹۶ متر بر ثانیه و ۲۲/۶۸ متر بر ثانیه در داخل اتوبوس به دست آمد. سرعت‌های تجربی به‌دست‌آمده با نتایج به‌دست‌آمده توسط دینامیک سیالات محاسباتی (CFD) تأیید شد. انحراف ۵ درصد برای سرعت داده شده ۲۰ متر بر ثانیه مشاهده گردید.

International Journal of Engineering

Journal Homepage: www.ije.ir

Role of Mixing Method and Solid Content on Printability of Alumina Inks for Stereolithography 3D Printing Process

A. Khecho[a], S. A. Ghaffari[a]*, M. Behzadnasab[b], M. Rahmat[b]

[a] *School of Metallurgy and Materials Engineering, Iran University of Science and Technology, Tehran, Iran*
[b] *Faculty of Polymer Processing, Iran Polymer and Petrochemical Institute, Tehran, Iran*

PAPER INFO

Paper history:
Received 03 November 2021
Received in revised form 16 December 2021
Accepted 16 December 2021

Keywords:
Additive Manufacturing
Alumina
Digital Light Processing
Rheology

ABSTRACT

Additive manufacturing of ceramics via stereolithography method is a promising way to fabricate high-resolution ceramic parts with complex geometry, which is hard to obtain with traditional ceramic shaping methods. In order to shape the ceramics with the Digital Light Processing (DLP), a mixture of photocurable resin and ceramic powders, called ink, must be prepared. In this paper, the printability of the Alumina-glass inks, with different solid contents were prepared by two mixing methods, having long and short mixing durations. In order to evaluate the printability of inks, the rheological behavior of suspensions was investigated, and printing parameters such as curing time and layer thickness were changed. The ceramic-resin suspensions were prepared via 24-hour ball-milling and 10,000 rpm mechanical homogenizing. The suspension containing 60 wt% solid content and prepared by mechanical homogenizing showed the best stability with 8% sedimentation within 4 days and the lowest viscosity of 1.37 Pa·s at shear rates of 30 s^{-1}, exhibiting a suitable viscosity for DLP printing. Therefore, a mechanical homogenizer can be a promising and quick method for mixing by providing simultaneously appropriate rheology and printability.

doi: *10.5829/ije.2022.35.03c.11*

1. INTRODUCTION

Conventional shaping methods of advanced ceramics, especially for fabricating complex shaped components, have always been challenging. The development of Additive Manufacturing as a layered fabricating technique has overcome some of the difficulties and now is recommending an alternative way of shaping ceramics by providing both unique structures and acceptable dimensional accuracy [1–3].

In Ceramic Stereolithography, which is a photopolymerization-based technique, ceramic particles are dispersed in the photosensitive resin, and the ceramic part is manufactured layer by layer by the exposure of UV light (either laser or projector) [4–6].

In preparing a printable ink for the stereolithography process, loading a photocurable resin with high ceramic solid content is essential to lower the shrinkage in sintering and provide a high density with desirable mechanical properties. Meanwhile, increasing the solid content in resin makes the suspension thicker by losing its auto-leveling property and increasing the light scattering effect due to refractive index contrast between the resin and the ceramic powder. As a result, the printing procedure becomes more difficult. This property is one of the pivotal points required in Stereolithography, especially in bottom-up Digital Light Processing (DLP) to spread thin layers. Therefore, preparing a highly ceramic-loaded resin with eligible rheological properties is essential [5, 7–11].

Besides the auto-leveling property, it is necessary to create sufficient adhesion between the newly cured layer and the build plate to dominate the vacuum force and prevent the sample from being removed in bottom-up

*Corresponding Author Institutional Email: amirghaffari@iust.ac.ir (S.A. Ghaffari)

Please cite this article as: A. Khecho, S. A. Ghaffari, M. Behzadnasab, M. Rahmat, Role of Mixing Method and Solid Content on Printability of Alumina Inks for Stereolithography 3D Printing Process, ***International Journal of Engineering, Transactions C: Aspects*** Vol. 35, No. 03, (2022) 580-586

DLP. Instead, there is no vacuum force in the top-down DLP approach, which makes the printing process smoother; nevertheless, the bottom-up approach is more common due to its higher resolution, faster printing process, and less material waste [12]. Also, the mentioned problems can be minimized by careful selection of the resin components and dispersants or by changing the particle size distribution of the ceramic powder and the suitable mixing method to control the light scattering effect [13, 14]. Besides selecting the proper mixing method, the preparation time can also be an essential factor to distinguish the 3D printing technique from the conventional shaping methods.

For manufacturing dense ceramic parts, printing ceramic-resin inks with a high amount of ceramic powder might develop a better sintering quality. The desirable amount of ceramic powder in resin should be at least 40 vol% to obtain a fully dense ceramic part after debinding and sintering [10, 15]. However, the viscosity is highly affected by the ceramic particles. Resins with higher solid content would increase the viscosity and deteriorate the self-leveling property [16]. As reported, for ceramic-resin photocurable suspensions, shear-thinning behavior and viscosity of 3-5 Pa·s at 30 s^{-1} shear rate are preferable [14, 15].

This study presents the Alumina-resin inks' preparation for bottom-up DLP printing by employing two mixing methods having a significant difference in preparation time. The effect of mixing methods and solid contents on rheological properties, stability to sedimentation and accordingly printability was investigated.

2. MATERIALS AND METHODS

2. 1. Raw Materials and Ink Preparation Ceramic-loaded photocurable resins were prepared using α-Alumina powder (d90=5 µm and 99.99% purity), soda-lime glass frit, etc., methacrylate-based photosensitive resin, containing certain amounts of defoamer, dispersant, and photoinitiator (Maan Polymer). Firstly, the Alumina powder and the glass frit were fast milled for 10 minutes at a weight ratio of 7 to 3 and sieved through a 270 mesh screen. Then, according to Table 1, the powder mixture was added to the resin monomer in a stepwise manner and two different mixing methods were applied for the suspensions; i.e. high-speed mechanical homogenizer (total time of 10 minutes in 10,000 rpm speed) and ball-milling (24 hours using Alumina balls).

2. 2. DLP 3D Printing In stereolithography, there is a vat containing photocurable resin which is exposed to UV light. Then it is polymerized layer by layer according to a computer-aided design (CAD) file, which is sliced into 2D layers. The 3D part is fabricated on a build plate moving along the Z-axis and solidifying the photocurable liquid in each layer. There are two types of light sources used in stereolithography, i.e., laser beam and projection. In projection-based stereolithography or Digital Light Processing (DLP), the layer is polymerized by the exposure of the UV projection light at once. The light source can be positioned either at the top or bottom of the vat [17]. In this work, the samples were printed by a bottom-up approach. The stereolithography process was performed via Parsa 3D bottom-up DLP Printer, using Vivitek 4000 Lumen projector. The models were printed according to the optimized parameteres of layer thickness, curing time, and amount of the photoinitiator, as shown in Table 2. The schematic of DLP printing is shown in Figure 1.

TABLE 1. Alumina-resin inks characteristics

Label	Powder		Mixing method
	wt%	vol%	
B50	50	23	Ball-mill
H50	50	23	Mechanical homogenizer
B60	60	31	Ball-mill
H60	60	31	Mechanical homogenizer

2. 3. Sintering Sintering of the samples was carried out at a temperature of 1400 °C. First, for resin burn-out, samples were heated at rate of 5 °C/min up to 400 °C maintained for 1 hour, and then heated up to sintering temperature at rate of 10 °C/min, with 1.5 hours soaking time.

TABLE 2. DLP printing parameters

Sample	Curing time	Layer thickness	Photoinitiator
H50	2.3 s	30 µm	3.33%
B50			
H60	2.3 s	30 µm	4%
B60			

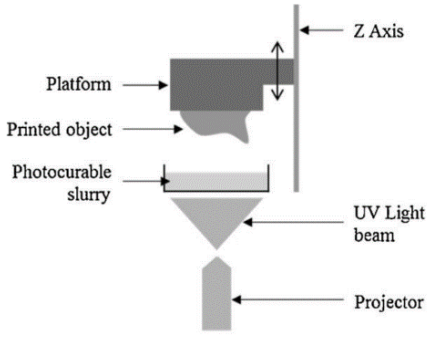

Figure 1. Schematic of bottom-up DLP printing [18]

2. 4. Characterization The rheological properties were tested at room temperature using a rotational rheometer (MCR301, Anton Parr, Austria), varying the shear rate from 0.1 to 1000 s^{-1}. For measuring the stability of the suspensions at room temperature, the prepared inks were kept 4 days in the dark place, considering the total initial suspension height as H and the settled suspension as H_0.

3. RESULTS AND DISCUSSION

3. 1. Ink Properties The rheological behavior and stability of the printable inks with 50 and 60 wt% solid contents are shown in Figure 2. The viscosity of resins increased by introducing ceramic powder, from 0.15 Pa·s in pure resin to of 0.57 and 1.75 Pa·s in the shear rate of 30 s^{-1} for 50% and 60 wt%, respectively. All samples' viscosity was within the accepted range for pouring in a 3D printer tank [19].

The Alumina-glass inks' viscosity is reduced with the shear rate increase, exhibiting a non-Newtonian, shear-thinning behavior, a desirable rheological property for the stereolithography process [14, 20, 21].

In stereolithography 3D printing, the resin is cleaned up from the VAT surface by a moving paddle between the layer printing intervals. The resin's shear-thinning behavior is directly related to self-leveling properties, where the resin must rapidly fill the empty spaces after paddle sweep [22, 23].

As shown in Figure 2, all the samples had a high viscosity in low shear rates, and the samples with more ceramic powders (B60 and H60), showing higher viscosity. The viscosity of the samples decreases by increasing the shear rate and reaching a plateau, significantly for the lower powder samples (B50 and H50), as previously seen in other reports. The more stable viscosity at a higher shear rate, the better is self-leveling properties and, consequently, the better printing process. It can be concluded that high solid content resins show less stable viscosity at high shear rates [24].

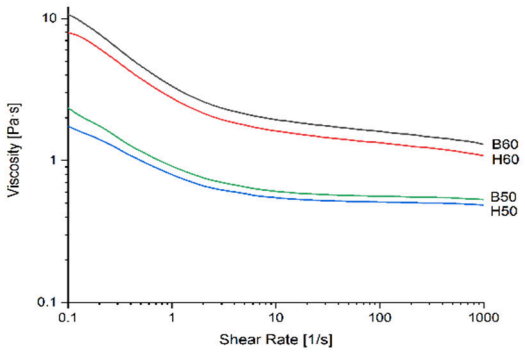

Figure 2. Viscosity variations of the suspensions

Despite the two different preparing methods, it is observed that the inks indicate relatively similar rheological behaviors and viscosity values of the same orders. In other words, mixing processes have not significantly affected the rheological behavior. The ball-milled samples have relatively higher viscosities (in all shear rates) compared to mechanically homogenized samples. In general, DLP ceramic slurries' viscosity needs to be less than 20 Pa·s within the shear rate of 10-100 s^{-1} [25]. B60 ink, as the most viscose ink, exhibits a viscosity of about 1.75 Pa·s at 30 s^{-1} shear rate, which, as reported, is still suitable for the stereolithography process [14, 15, 24].

The lower viscosity in mechanical homogenized inks and increase in flowability can be attributed to the agglomerates' break up and more dispersion of the particles in the resin [15]. As a result, H60 ink has a viscosity of 1.37 Pa·s at shear rates 30 s^{-1} which is lower than B60 ink. On the other hand, although ball-milling is well-known as an effective method in preparing ceramic slurries, there is a time limitation to use it for slurry preparation. Even though ball-milling duration is not investigated as a parameter in this research, it was believed that long-time milling and overmixing of ceramic loaded resins could interrupt dispersion by damaging the structure of resin and dispersants. In other words, overmixing has increased the viscosity by reducing particle size. Particle size plays a vital role in viscosity. When the particles become finer, and the surface area is increased, more dispersant may be needed to cover all the particles' surface. So, the viscosity of the suspension will increase, as reported previously [26, 27]. Moreover, it can be said that damaging the dispersant within the resin and losing its functionality would be another possible reason for viscosity-increasing [28].

The stability and viscosity have the same critical role in the performance of ceramics slurries for the DLP process. As it is mentioned previously, low viscosity slurries were obtained by using lower solid load and larger particle sizes [22]. However, this results in sedimentation enhancement. Sedimentation of slurries during the printing process leads to discontinuity and inhomogeneity [5, 28, 29]. The sedimentation rate test is normally used to evaluate the stability of suspensions. Figure 3 shows the sedimentation of the suspensions within 3 days. As shown in Figure 3 and discussed earlier, the suspensions containing 60 wt% solid (B60 and H60), were significantly more stable than the suspensions with lower solid content. Also, it was observed that the sedimentation rate of the inks having 50 wt% solid had increased considerably after 36 hours. Generally, H60 is the most stable suspension with 8% sedimentation over 4 days. Therefore, as expected, in a 2-hour printing duration or more, the ink stayed homogeneous, and settlement was negligible.

The mixing method effect on slurries' stability is quite different in low and high ceramic loading samples. As shown in Figure 3, in lower solid content samples, the ball-milled sample (B50) is more stable than H50. As discussed, ball-milling has resulted in finer particles and relatively higher viscosity, making the settlement rate of the particles lower, according to Stock's law [26, 27]. Therefore, the B50 sample has settled slower than the H50 sample. Whereas in the samples with higher solid inks, the effect of the mixing method was less significant. By increasing the mixing or sedimentation test time, this difference would be more effective, which was not investigated in this study. Therefore, by comparing the two mixing methods and considering that for ceramic manufacturing, high-solid content suspensions are required. It seems that high-speed mechanical homogenizing is a better mixing option.

3. 2. 3D Printing In the bottom-up method, the cured layer must be detached from the VAT in each step of layer printing, following by recoating fresh ceramic slurry to be prepared for the next layer printing [12]. However, in printing the suspensions, the main issue was to make the first layer stick to the build plate. Besides the detachment force that is induced for each cured layer, the layer adhesion can be enhanced by adjusting the curing time, layer thickness, and the amount of the photoinitiator [30]. These parameters influence the curing depth, a crucial parameter determining the accuracy of the printing [31].

In Figure 4, an example of a sample printed from a suspension containing 20 wt% solid and prepared by mechanical homogenizing is shown. It can be seen that

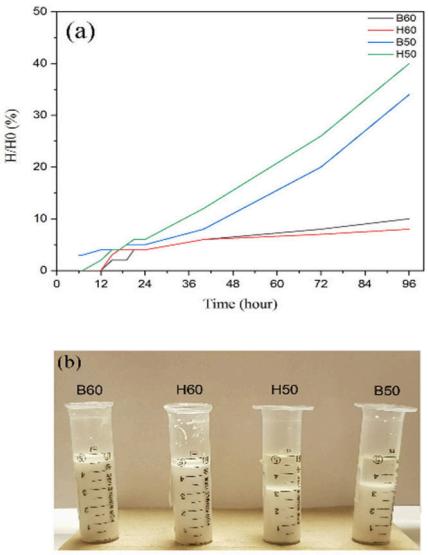

Figure 3. Stability of Alumina-glass suspensions prepared by two different mixing methods: a)Stability test after 4 days b)Sedimentation over time (showing H/H_0 value vs time)

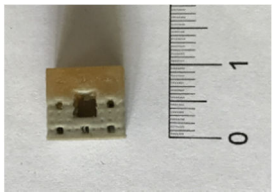

Figure 4. Two-phased printed sample from suspension containing 20 wt% solid content

the suspension instability has resulted in phase separation in suspension and a two-phased sample. The ceramic particles have settled too quickly before the sample is printed entirely, which highlights the significant effect of the solid loading on the suspension stability.

H50 was successfully printed by adjusting the printing condition as curing time of 2.3 s, layer thickness of 30 µm, and 3.33% of photoinitiator. Eventually, as the viscosity of H50 and B50 was quite the same, both were printable with a similar condition. But the switching in mixing method of 50 wt% inks from mechanical homogenizing to ball-milling resulted in drastic changes in the quality and accuracy of printing, as is shown in Figure 5. Small holes of the printing model did not form, the size of larger holes decreased, and the sample's edges were extended. This could be attributed to light scattering, which is intensified as a result of ball-milling, delivering more radiation to the sideways. Previously, the sedimentation and viscosity results showed that ball-milling was more effective in deagglomeration and production of finer particles in ceramic slurry.

By increasing the ceramic content to 60 wt%, as expected, the curing energy was not enough for the previous set of 50 wt% inks. The low adhesion was assumed to be a result of the high curing time, causing the first layer to stick to the silicon vat instead of the build plate. However, decreasing the curing time and then the layer thickness to 15 µm showed that the penetration depth was not high enough to cure a single layer completely. In other words, in curing each layer, the resin monomers did not get the necessary activation energy for polymerization due to the high light scattering effect, which caused the resin to be more stable to light exposure [8, 32]. Although a sample containing ~60 wt% ceramic powder was printable with 15 µm layer thickness, however; considering the long printing duration, this condition was not reasonably practical.

Therefore, for modifying the reactivity and reducing the activation energy needed for polymerization in 60 wt% suspensions, the photoinitiator amount in resin was doubled, reaching the ratio of 4 to 100 per weight [33]. Adding more photoinitiator helped increase the layer thickness up to 30 µm, without any sensible changes in the viscosity. According to Hinczewski et al. [9], the photoinitiator does not influence the viscosity of the resin monomer. On the contrary, increasing the photoinitiator

amount led to new problems related to the light stability of the resin. The resin got highly sensitive to the environmental light during the preparation and printing so that the prepared ink was used to polymerize quickly overnight, even though it was kept in the dark place.

As shown in Figure 5, suspension propagated around the printed samples (both 50 and 60 wt%), and the printing accuracy has declined drastically. Propagation might happen due to high light scattering, which causes the reduction of the cure depth. In other words, ball-milling has intensified the scattering, delivering more radiation to the sideways [17, 31]. Probably, ball-milling produced finer particles or broke up agglomerates, resulting in more light scattering. Additionally, long ball-milling time damaged the dispersant in the resin, affecting the inter-particle spaces. Both finer particles and damaged dispersants declined the photopolymerization process [28, 33].

Eventually, it was found that for the bottom-up approach, H60 suspension is the most convenient ink to print Alumina-glass ceramic parts. By considering the properties resulted for ball-milling, it is prepared quickly, the viscosity is low enough, and no sedimentation occurs during the printing process. Moreover, using Maan polymer resin, it was not possible to increase the solid ceramic content by more than 60 wt% due to high light scattering and difficulties in first layer adhesion to the build plate.

In order to consolidate printed parts, sintering was carried out in 1400 ˚C. By increasing the solid content, the shrinkage and relative density of samples changed. Typically, Alumina ceramics is reaching maximum density in the range of 1500 to 1700 ˚C [34, 35], but by adding the glass as a sintering aid, the full dense alumina-glass bodies fabricated at 1400 ˚C.

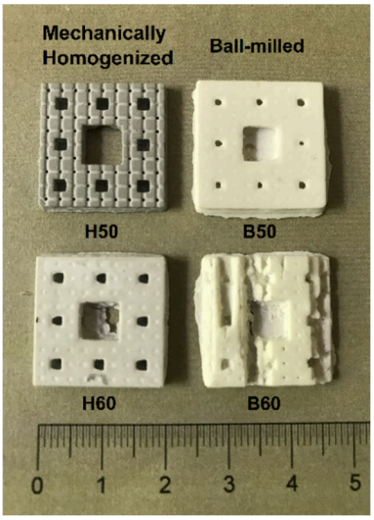

Figure 5. Printed samples via bottom-up approach; samples printed from suspensions H50, B50, H60 and B60

4. CONCLUSIONS

In this work, employing two different mixing methods for the DLP 3D printing showed that the effectiveness of mixing techniques mainly varies when the amount of the solid loading is changed. Ball-milling created higher viscosities and stability for the suspensions containing 50 wt% solid content. In comparison, high-speed mechanical homogenizing was found to be more suitable for preparing the suspensions with 60 wt% solid content. However, the suspensions have shown shear-thinning behavior and viscosities in the accepted range for DLP printing for both mixing methods.

5. ACKNOWLEDGMENTS

The authors are acknowledged colleagues from Iran Polymer and Petrochemical Institute, Additive Manufacturing laboratory, who provided insight and expertise that greatly assisted this research.

6. REFERENCES

1. Wu, Z., Liu, W., Wu, H., Huang, R., He, R., Jiang, Q., Chen, Y., Ji, X., Tian, Z., Wu, S., "Research into the mechanical properties, sintering mechanism and microstructure evolution of Al2O3-ZrO2 composites fabricated by a stereolithography-based 3D printing method", ***Materials Chemistry and Physics***, Vol. 207, (2018), 1–10. https://doi.org/10.1016/j.matchemphys.2017.12.021
2. He, R., Liu, W., Wu, Z., An, D., Huang, M., Wu, H., Jiang, Q., Ji, X., Wu, S. Xie, Z., "Fabrication of complex-shaped zirconia ceramic parts via a DLP- stereolithography-based 3D printing method", ***Ceramics International***, Vol. 44, No. 3, (2018), 3412–3416. https://doi.org/10.1016/j.ceramint.2017.11.135
3. Borlaf, M., Serra-Capdevila, A., Colominas, C., Graule, T., "Development of UV-curable ZrO2 slurries for additive manufacturing (LCM-DLP) technology", ***Journal of the European Ceramic Society***, Vol. 39, (2019), 3797–3803. https://doi.org/10.1016/j.jeurceramsoc.2019.05.023
4. Wu, H., Liu, W., He, R., Wu, Z., Jiang, Q., Song, X., Chen, Y., Cheng, L., Wu, S., "Fabrication of dense zirconia-toughened alumina ceramics through a stereolithography-based additive manufacturing", ***Ceramics International***, Vol. 43, No. 1, (2017), 968–972. https://doi.org/10.1016/j.ceramint.2016.10.027
5. Xing, H., Zou, B., Lai, Q., Huang, C., Chen, Q., Fu, X. and Shi, Z., "Preparation and characterization of UV curable Al2O3 suspensions applying for stereolithography 3D printing ceramic microcomponent", ***Powder Technology***, Vol. 338, (2018), 153–161. https://doi.org/10.1016/j.jeurceramsoc.2019.05.023
6. Schmidt, J., Elsayed, H., Bernardo, E., Colombo, P., "Digital light processing of wollastonite-diopside glass-ceramic complex structures", ***Journal of the European Ceramic Society***, Vol. 38, (2018),4580–4584. https://doi.org/10.1016/j.jeurceramsoc.2018.06.004
7. Hu, K., Wei, Y., Lu, Z., Wan, L., and Li, P., "Design of a Shaping System for Stereolithography with High Solid Loading Ceramic Suspensions", ***3D Printing and Additive. Manufacturing***, Vol. 5, No. 4, (2018), 311–318. https://doi.org/10.1089/3dp.2017.0065

8. da Silva Bartolo, P.J., Jorge, M.A., da Conceicao Batista, F., Almeida, H.A., Matias, J.M., Vasco, J.C., Gaspar, J.B., Correia, M.A., Andre, N.C., Alves, N.F. and Novo, P.P., Virtual and rapid manufacturing: advanced research in virtual and rapid prototyping, CRC Press, 2007.
9. Hinczewski, C., Corbel, S., Chartier, T., "Ceramic suspensions suitable for stereolithography." ***Journal of the European Ceramic Society***, Vol. 18, (1998), 583–590. https://doi.org/10.1016/S0955-2219(97)00186-6
10. Schmidt, J., Altun, A., Schwentenwein, M., Colombo, P., " Complex mullite structures fabricated via digital light processing of a preceramic polysiloxane with active alumina fillers ", ***Journal of the European Ceramic Society***, Vol. 39, (2019), 1336-1343. https://doi.org/10.1016/j.jeurceramsoc.2018.11.038.
11. Johansson, E., Lidström, O., Johansson, J., Lyckfeldt, O., Adolfsson, E., "Influence of resin composition on the defect formation in alumina manufactured by stereolithography", ***Materials***, Vol. 10, No. 2, (2017), 138. https://doi.org/10.10.3390/ma10020138
12. Liravi, F., Das, S., Zhou, C., "Separation force analysis and prediction based on cohesive element model for constrained-surface Stereolithography processes", ***Computer Aided Design***, Vol. 69, (2015), 134-142. https://doi.org/10.1016/j.cad.2015.05.002
13. Chartier, T., Dupas, C., Lasgorceix, M., Brie, J., Delhote, N., Chaput, C., "Additive manufacturing to produce complex 3D ceramic parts", ***Journal of Ceramic Science and Technology***, Vol. 6, No. 2, (2015), 95–104. https://doi.org/10.4416/JCST2014-00040
14. Zhang, S., Sha, N., Zhao, Z., "Surface modification of α-Al2O3 with dicarboxylic acids for the preparation of UV-curable ceramic suspensions", ***Journal of the European Ceramic Society***, Vol. 37, No. 4, (2017), 1607–1616. https://doi.org/10.1016/j.jeurceramsoc.2016.12.013
15. Li, K., Zhao, Z., "The effect of the surfactants on the formulation of UV-curable SLA alumina suspension", ***Ceramics International***, Vol. 43, No. 6, (2017), 4761–4767. https://doi.org/10.1016/j.ceramint.2016.11.143
16. Dehurtevent, M., Robberecht, L., Hornez, J.-C., Thuault, A., Deveaux, E., Behin, P., "Stereolithography: A new method for processing dental ceramics by additive computer-aided manufacturing", ***Dental Material***, Vol. 33, No. 5, (2017), 477–485. https://doi.org/10.1016/J.DENTAL.2017.01.018
17. Zakeri, S., Vippola, M., Levänen, E., "A comprehensive review of the photopolymerization of ceramic resins used in stereolithography", ***Additive Manufacturing***, Vol. 35, (2020), 101177. https://doi.org/10.1016/j.addma.2020.101177
18. Santoliquido, O., Colombo, P., Ortona, A., "Additive Manufacturing of ceramic components by Digital Light Processing: A comparison between the "bottom-up" and the "top-down" approaches", ***Journal of the European Ceramic Society***, Vol. 39, No. 6, (2019), 2140–2148. https://doi.org/10.1016/j.jeurceramsoc.2019.01.04
19. Griffith, M.L., Halloran, J.W., "Free form fabrication of ceramics via stereolithography", ***Journal of the American Ceramic Society***, Vol. 79, No. 10, (1996), 2601–2608. https://doi.org/10.1111/j.1151-2916.1996.tb09022.x
20. Appiagyei, K.A., Messing, G.L., Dumm, J.Q., "Aqueous slip casting of transparent yttrium aluminum garnet (YAG) ceramics", ***Ceramics International***, Vol. 34, (2008), 1309–1313. https://doi.org/10.1016/j.ceramint.2007.03.010
21. Liu, W., Lv, L., Li, Y., Wang, Y., Wang, J., Xue, C., Dong, Y., Yang, J., "Effects of slurry composition on the properties of 3-1 type porous PZT ceramics prepared by ionotropic gelation", ***Ceramics International***, Vol. 43, (2017), 6542–6547. https://doi.org/10.1016/j.ceramint.2017.02.079
22. Gao, Y., Ding, J., "Low solid loading, low viscosity, high uniform shrinkage ceramic resin for stereolithography based additive manufacturing", ***Procedia Manufacturing***, Vol. 48, (2020), 749–754. https://doi.org/10.1016/j.promfg.2020.05.109
23. Camargo, I., Morais, M., Fortulan, C., Branciforti, M., "A review on the rheological behavior and formulations of ceramic suspensions for vat photopolymerization", ***Ceramics International,*** Vol. 47, (2021), 11906-11921. https://doi.org/10.1016/j.ceramint.2021.01.03
24. Zhang, K., Xie, C., Wang, G., He, R., Ding, G., Wang, M., Dai, D., Fang, D., "High solid loading, low viscosity photosensitive Al2O3 slurry for stereolithography based additive manufacturing", ***Ceramics International***, Vol. 45, No. 1, (2019), 203–208. https://doi.org/10.1016/j.ceramint.2018.09.152
25. Chen, Z., Li, J., Liu, C., Liu, Y., Zhu, J., Lao, C., "Preparation of high solid loading and low viscosity ceramic slurries for photopolymerization-based 3D printing", ***Ceramics International***, Vol. 45, No. 9, (2019), 11549–11557. https://doi.org/10.1016/j.ceramint.2019.03.024
26. Hu, C., Chen, Y., Liu, H., Huang, X., Huo, Y., Yang, T., Jia, Z. and Wang, H., "Effect of SiC powder on the properties of SiC Slurry for Stereolithography", ***Ceramics International***, Vol. 47, No. 9, (2021), 12442–12449. https://doi.org/10.1016/j.ceramint.2021.01.101
27. Liu, Y., Zhan, L., Wen, L., Cheng, L., He, Y., Xu, B., Wu, Q. and Liu, S., "Effects of particle size and color on photocuring performance of Si3N4 ceramic slurry by stereolithography", ***Journal of the European Ceramic Society***, Vol. 41, (2021), 2386–2394. https://doi.org/10.1016/j.jeurceramsoc.2020.11.032
28. Ding, G., He, R., Zhang, K., Xia, M., Feng, C. and Fang, D., He, Y., Xu, B., Wu, Q. and Liu, S., "Dispersion and stability of SiC ceramic slurry for stereolithography", ***Ceramics International***, Vol. 46, (2020), 4720–4729. https://doi.org/10.1016/j.ceramint.2019.10.203
29. Wu, X., Xu, C., Zhang, Z., "Preparation and optimization of Si3N4 ceramic slurry for low-cost LCD mask stereolithography", ***Ceramics International***, Vol. 47, (2020), 9400–9408. https://doi.org/10.1016/j.ceramint.2020.12.072
30. Sataloff, R.T., Johns, M.M., Kost, K.M., Stereolithography: Materials, Processes and Applications, Springer Science & Business Media, 2011.
31. Wu, H., Cheng, Y., Liu, W., He, R., Zhou, M., Wu, S., Song, X., Chen, Y., "Effect of the particle size and the debinding process on the density of alumina ceramics fabricated by 3D printing based on stereolithography", ***Ceramics International***, Vol. 42, No. 15, (2016), 17290–17294. https://doi.org/10.1016/j.ceramint.2016.08.024
32. Gebhardt, A., Hötter, J.-S., Additive manufacturing: 3D printing for prototyping and manufacturing, Carl Hanser Verlag GmbH Co KG, 2016.
33. Chartier, T., Badev, A., Abouliatim, Y., Lebaudy, P., Lecamp, L., "Stereolithography process: Influence of the rheology of silica suspensions and of the medium on polymerization kinetics - Cured depth and width.", ***Journal of the European Ceramic Society***, Vol. 32, (2012), 1625–1634. https://doi.org/10.1016/j.jeurceramsoc.2012.01.010
34. Xue, L.A., Chen, I., "Low□Temperature Sintering of Alumina with Liquid□Forming Additives", ***Journal of the American Ceramic Society***, Vol. 74, (1991) 2011–2013. https://doi.org/10.1111/j.1151-2916.1991.tb07825.x
35. Kamarudin, N. H., Harun, Z., Othman, M. H. D., Hubadillah, S. K., Jamaluddin, M. R., Yusof, K. N., "Preliminary Characterization of Corn Cob Ash as an Alternative Material for Ceramic Hollow Fiber Membrane (CHFM/CCA)", ***International Journal of Engineering, Transactions B: Applications***, Vol. 31, No. 8, (2018), 1389–1397. https://doi.org/10.5829/ije.2018.31.08b.30

Persian Abstract

چکیده

ساخت افزایشی سرامیک‌ها با استفاده از استریولیتوگرافی را می‌توان به عنوان روشی مطمئن برای ساخت قطعات با شکل‌های پیچیده در نظر گرفت، چرا که اغلب ساخت برخی از قطعات خاص با روش‌های شکل‌دهی متداول سرامیک‌ها مشکل است. در روش استریولیتوگرافی، قطعات سرامیکی با استفاده از یک سوسپانسیون رزین حساس به نور و ذرات سرامیکی چاپ می‌شوند. در این پژوهش، قابلیت چاپ جوهرهای آلومینا–شیشه در درصدهای مختلف ماده جامد و با استفاده از دو روش اختلاط مورد بررسی قرار گرفته است. جهت بررسی قابلیت چاپ، خواص رئولوژیکی سوسپانسیون‌ها و همچنین شرایط چاپ مانند زمان تابش نور و ضخامت لایه به عنوان متغیر در نظر گرفته شدند. سوسپانسیون‌های رزین– آلومینا، توسط بالمیل به مدت ۲٤ ساعت و هموژنایزر مکانیکی با سرعت ۱۰۰۰۰ دور بر دقیقه تهیه شدند. سوسپانسیون حاوی ٦۰ درصد وزنی پودر و آماده شده توسط هموژنایزر مکانیکی، بهترین پایداری با حدود ۸ درصد ته‌نشینی در طی ٤ روز از خود نشان داد. بعلاوه، گرانروی سوسپانسیون‌های تهیه شده با هموژنایزر مکانیکی در مقایسه با بالمیل، کمترین و با مقدار ۱/۳۷ Pa·s در نرخ برشی $30\ s^{-1}$ اندازه‌گیری شدند که مطابق تحقیقات انجام شده برای روش استریولیتوگرافی گرانروی مناسبی تلقی می‌شود. درنتیجه، هموژنایزر مکانیکی، به عنوان یک روش اختلاط سریع برای تهیه سوسپانسیون‌های فرایند چاپ سه‌بعدی استریولیتوگرافی می‌تواند به کار رود.

International Journal of Engineering

Journal Homepage: www.ije.ir

Study on Attapulgite as Drilling Fluid Clay Additive in Persian Gulf Seawater

M. A. Choupani, S. S. Tabatabaee Moradi*, S. A. Tabatabaei Nejad

Faculty of Petroleum and Natural Gas Engineering, Sahand University of Technology, Tabriz, Iran

PAPER INFO

Paper history:
Received 8 November 2021
Received in revised form 20 December 2021
Accepted 23 December 2021

Keywords:
Clay Mineral
Drilling Fluid
Filtration
Herschel-bulkley Model

ABSTRACT

Drilling fluids are a vital part of every successful well construction operation. Water based fluids are used commonly due to better environmental compatibility, lower cost and easier preparation. In offshore drilling, seawater can be used as the basis of water based fluids. Salinity of seawater restricts application of some additives. For example, bentonite settles in saline environments. In this study, a synthetic water is prepared based on Persian Gulf seawater. Bentonite, pre-hydrated bentonite and attapulgite suspensions were developed based on fresh water and prepared synthetic water. Rheological and filtration properties of fluids were tested to check their performance in synthetic seawater. Results of filtration measurements showed a thick mud cake and high filtration volume in pre-hydrated bentonite fluids. In the case of attapulgite, filtration volume of suspensions in synthetic water increased comparing to suspensions in fresh water. However, filtration properties were acceptable. Study on rheological properties revealed that Herschel-Bulkley model can predict rheological properties with a good accuracy. This is the case for suspensions in both fresh and seawaters. Also it was seen that all suspension had a flow behavior index less than 1, showing their shear thinning character. By increasing clay concentrations, higher consistency index, yield stress and gel strength values were reported. At higher clay concentration a stronger three-dimensional network of clay particles in aqueous environment and consequently a stronger gel structure were formed. Overall, it can be concluded that attapulgite can be used in the saline environment of Persian Gulf seawater.

***doi**: 10.5829/ije.2022.35.06c.12*

NOMENCLATURE

N	rotational speed (rpm)	τ	shear stress ($\frac{lb_f}{100ft^2}$)
n	flow behavior index (dimensionless)	τ_y	yield stress ($\frac{lb_f}{100ft^2}$)
k	consistency index (cp)	γ	shear rate ($\frac{1}{s}$)
WBM	water based mud	θ_N	dial reading at rotational speed of N
OBM	Oil based mud	μ	fluid viscosity
FW	fresh water	μ_p	plastic viscosity (cp)
SSW	synthetic seawater		

1. INTRODUCTION

Success in the drilling of oil and gas wells significantly depends on the drilling fluid performance. Drilling fluids are used in the well construction process for various purposes, including but not limited to cutting transport, bit cooling and lubrication, formation damage reduction, control of formation fluid pressure, transmission of formation information and providing wellbore stability [1-4].

There are three main types of drilling fluids: water based mud (WBM), Oil based mud (OBM) and pneumatic fluids. Due to the lower cost, better environmental compatibility and easy preparation procedures, water based muds are the most commonly used drilling fluid in the industry. In practice, various compositions of WBMs have been developed based on

*Corresponding Author Email: s.sh.tabatabaee@gmail.com (S. S. Tabatabaee Moradi)

Please cite this article as: M. A. Choupani, S. S. Tabatabaee Moradi, S. A. Tabatabaei Nejad, Study on Attapulgite as Drilling Fluid Clay Additive in Persian Gulf Seawater, ***International Journal of Engineering, Transactions C: Aspects*** Vol. 35, No. 03, (2022) 587-595

environmental considerations, geological and technical conditions of the well being drilled.

In the simplest form, a water based fluid is prepared by hydration of bentonite in water. Water as the basis is usually provided from local sources, like rivers, lakes, etc. to exclude additional cost of transportation. In the case of offshore drilling, seawater is preferred for preparation of WBMs. Bentonite, formed by weathering of volcanic ash, is a clay mineral of smectite group, mostly composed of montmorillonite mineral ($(Al,Mg)_2(OH)_2(Si,Al)_4O_{10}(Ca)_x$ on H_2O). It is accepted as a common drilling fluid additive with a good hydration ability to decrease mud filtration volume, increase cutting transport ability and enhance rheological properties [5-9].

Attraction of positive ions by the negatively charged layers of bentonite attributes to the clay swelling, which in turn leads to the enhancement of drilling fluid rheological properties. However, in saline environment where seawater is preferred, high concentration of metal cations, such as Ca^{2+}, Mg^{2+}, Na^{+} etc. are present, which create an electrostatic charge imbalance in the layers of bentonite. This hinders the effective hydration and swelling of bentonite particles and even may lead to their flocculation and settling [10-12].

Researchers studied the behavior of bentonite WBM in the saline environments. Kelessidis et al. [13] investigated rheological behavior of Wyoming bentonite suspensions in different electrolyte concentration. Authors showed that salt addition to bentonite suspensions leads to decrease of parameters in the Herschel–Bulkley model i.e. yield stress, flow consistency index and flow behavior index.

Duman and Tunc [14] investigated the electro-kinetic and rheological properties of sodium bentonite in different electrolyte solutions. Based on experimental results, authors showed viscosity decrease with increase in salt concentration and concluded that divalent and trivalent cations significantly affect the properties of bentonite suspension.

Abu-Jdayil [15] studied the rheological properties of bentonites with different sodium to calcium ratios. It was found that salt addition decreased the viscosity and yield stress of bentonite suspensions and changed it's rheological behavior from shear-thinning to Newtonian and shear-thickening

Ren et al. 16] used a modified thixotropic loop to study the effect of salinity on rheological properties of bentonite suspensions. They reported that in saline environments, formation of gel structure between clay particles is hindered.

To reduce the adverse effect of seawater salinity on the performance of bentonite, one may suggest the use of desalination facilities to remove ions, especially divalent cations, from seawater. However, this process is costly, time consuming and not feasible due to the restricted capacity of desalination equipment [11].

To overcome this issue, researchers suggested use of salt-tolerant polymers, water-insoluble fiber materials, salt-tolerant clay minerals and pre-hydrated bentonite [11, 17]. Attapulgite and sepiolite are two type of non-swelling salt-tolerant clays. Sepiolite ($Si_{12}Mg_8O_{32}.nH_2O$) is a fibrous mineral of magnesium silicate group with acceptable rheological properties at high temperature and saline environments [18, 19]. Attapulgite or Palygorskite ($Si_8O_{20}(Mg,Al, Fe)_5(OH)_2(OH_2)_4.4H_2O$)) is a needle like crystalline hydrated magnesium aluminum silicate with good rheological properties in saline environments [20]. Pre-hydrated bentonite, which is suggested as drilling fluid additive for saline environments, is prepared by hydration of the bentonite in fresh water for a specific time and then mixing the prepared suspension with salt water.

In this work, suspensions of bentonite, pre-hydrated bentonite and attapulgite in the synthetic Persian Gulf seawater were prepared and their rheological and filtration properties were investigated to check the feasibility of Persian Gulf seawater application as the basis of drilling fluids.

2. MATERIALS AND METHODS

Different drilling fluid compositions were prepared based on standard API procedures and tested for density, pH, rheological and filtration properties [21]. Fluids were developed based on fresh water (FW) and synthetic Persian Gulf seawater (SSW). SSW was prepared to be used instead of real seawater to exclude the effect of different compositions in samples on the experimental results. To prepare synthetic water, the result of Ion Chromatography analysis of seawater samples was used to calculate the type and mass of each salt, which should be dissolved in the fresh water. Table 1 present the amount of each salt in 1 liter of fresh water.

Additives, i.e. bentonite, attapulgite and soda ash, were provided by local producers. Soda ash was used to adjust the fluid pH. For preparation of bentonite and

TABLE 1. Amount of salts required for perpetration of SSW

Salts	Salt mass per liter of fresh water, g/L
NaCl	28
KCl	0.8
$MgCl_2\,2H_2O$	13.75
$CaCl_2\,6H_2O$	1.82
Na_2SO_4	4.99
$NaHCO_3$	0.1

attapulgite suspensions, additives were weighted based on chosen concentration and then mixed with water (fresh or seawater) for 20 minutes at 2000 rpm of the mixer (Figure 1). Pre-hydrated bentonite suspension was prepared by pre-mixing of 87.5 mL of fresh water and chosen amount of bentonite for 15 minutes at 2000 rpm. The mixture was left in the laboratory for 24 hours to achieve full bentonite hydration. The bentonite suspension in fresh water was then added to 262.5 mL of SSW.

Compositions of the developed drilling fluids are presented in Table 2.

As presented in Table 2, suspensions of 10% by the weight of bentonite and attapulgite were so viscous that could not be used in the tests. Also suspensions of 8% and 10% pre-hydrated bentonite could not be used in the experiments due to high viscosity of pre-mixed FW and bentonite. Settling of bentonite was observed, preparing 6%, 8% and 10% suspensions of bentonite in SSW, which hindered their use in experimental study (Figure 2).

2. 1. Filtration Measurement Filtration properties, i.e. filtration volume and filter cake thickness, are of great importance in a successful drilling operation. Filtration of drilling fluid into the permeable subsurface formations reduce formation permeability and may lead to misinterpretation of well logging and well testing measurements. Presence of the filter cake, which forms on the borehole wall, helps to decrease filtration volume and promotes borehole stability. Filter cake should be thin and have low permeability. Thicker cakes with high permeability reduce diameter of the hole and leads to higher possibility of stuck pipes, increased torque and drag and poor primary cementing job [22-24].

Therefore, the goal in drilling fluid design is to reduce filtration volume and decrease mud cake permeability and thickness. In this work, to measure filtration properties, i.e. filtration volume and filter cake thickness, filter press was used (Figure 3).

Figure 1. High speed drilling fluid mixer

TABLE 2. Composition of drilling fluids based on fresh water and synthetic seawater

Sample	Name	FW, mL	SSW, mL	Soda ash, g	Bentonite, g	Attapulgite, g	Density, pcf	pH	Comments
1	6% Ben. FW	350	-	0.5	21	-	63	10.6	
2	8% Ben. FW	350	-	0.5	28	-	65	10.65	
3	10% Ben. FW	350	-	0.5	35	-	-	10.7	High viscosity, could not be tested
4	6% Att. FW	350	-	0.5	-	21	64	10.57	
5	8% Att. FW	350	-	0.5	-	28	67	10.68	
6	10% Att. FW	350	-	0.5	-	35	-	10.7	High viscosity, could not be tested
7	6% Ben. SSW	-	350	0.5	21	-	-	-	Settling of bentonite
8	8% Ben. SSW	-	350	0.5	28	-	-	-	Settling of bentonite
9	10% Ben. SSW	-	350	0.5	35	-	-	-	Settling of bentonite
10	6% Att. SSW	-	350	0.5	-	21	77	9..35	
11	8% Att. SSW	-	350	0.5	-	28	80	9.3	
12	10% Att. SSW	-	350	0.5	-	35	83	9.27	
13	6% Ben. Pre H.	87.5	262.5	0.5	21	-	73	10.2	
14	8% Ben. Pre H.	87.5	262.5	0.5	28	-	-	-	High viscosity of pre-mixture
15	10% Ben. Pre H.	87.5	262.5	0.5	35	-	-	-	High viscosity of pre-mixture

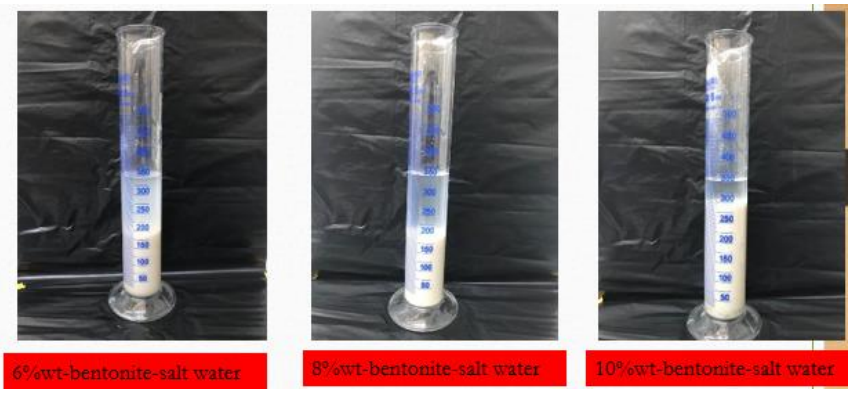

Figure 2. Settling of bentonite in SSW

Figure 3. Filter press

Filtration measurements involves placing the fluid in filter press cup and applying a 100 psi pressure on the fluid. The volume of filtered fluid through a filter paper is reported as the filtration volume (cm^3/30 min). Also, thickness of the cake, formed on the filter paper is reported.

2. 2. Rheological Measurements Many drilling parameters such as Rate of Penetration (ROP), rock cutting transport to the surface, mud hydraulics, filter cake formation, filtration volume etc. are significantly dependent on the fluid rheological properties [25, 26].

In this work, rheological properties were measured using a Fann viscometer at different rotational speeds. To fit the exact rheological model to measured data, below steps were followed [27]:

1. Dial readings of the viscometer at 3, 6, 100, 200, 300 and 600 rpm for each fluids were recorded.

2. Rotational speed and dial reading at each speed were converted to shear stress and shear rate using following formulas:

$$\tau = 1.067\ \theta_N \quad (1)$$

$$\gamma = 1.703\ N \quad (2)$$

where τ is shear stress ($\frac{lb_f}{100ft^2}$), γ is shear rate ($\frac{1}{s}$), N is rotational speed (rpm) and θ_N is dial reading at rotational speed of N.

3. Recorded values of N and θ_N were used to calculate the parameters of Newtonian, Bingham Plastic and Herschel-Bulkley models. For Newtonian model, shear stress is related to the shear rate as:

$$\tau = \mu\,\gamma \quad (3)$$

where

$$\mu = \frac{300}{N}\theta_N \quad (4)$$

In Equations (3) and (4), μ is the fluid viscosity.

For Bingham Plastic model, the relation between shear stress and shear rate is described as:

$$\tau = \mu_p\,\gamma + \tau_y \quad (5)$$

where

$$\mu_p = \theta_{600} - \theta_{300} \quad (6)$$

$$\tau_y = \theta_{300} - \mu_p \quad (7)$$

μ_p is plastic viscosity (cp) and τ_y is yield stress ($\frac{lb_f}{100ft^2}$).

Herschel-Bulkley model relates shear stress and shear rate as:

$$\tau = \tau_y + k\,\gamma^n \quad (8)$$

where

$$\tau_y = 2\theta_3 - \theta_6 \quad (9)$$

$$n = 3.32\log(\frac{R_{600}}{R_{300}}) \quad (10)$$

$$k = 510\ \frac{\theta_{600}}{511^n} \quad (11)$$

In Equations (8-11), n is flow behavior index (dimensionless) and k is consistency index (cp).

4. Knowing parameters of each model, shear stress values at different shear rates are calculated using models.

5. Measured values of shear stress and shear rate (step 2) are plotted against calculated shear stress and shear rate (step 4).

6. Error of each rheological model at each shear rate point is calculated. The model with least average absolute error is selected as the best fitted rheological model to describe the behavior of drilling fluids.

Gel strength of drilling fluid determines its ability to suspend cuttings and solid additives when fluid circulation is stopped in the annular space. The magnitude of yield stress and gel strength depend on attractive forces between particles in the fluid. Gel strength is measured under static condition, while dynamic condition is applied for yield stress measurement. To measure gel strength, fluid was kept static for 10 seconds and 10 minutes and then the viscometer was started at the rate of 3 RPM. The maximum dial indicator deflections were reported as the initial gel strength and 10 minutes' gel strength respectively [21, 28]. It should be noted that all experiments were conducted at laboratory temperature (23 ˚C).

3. RESULTS AND DISCUSSION

Results of filtration and theological experiments are explained and discussed in this section.

3. 1. Results of Filtration Measurements Results of filtration test on different drilling fluid compositions are shown in Table 3.

According to Table 3, increase in additive concentration, i.e. solid concentration, leads to less filtration volume and thicker mud cakes. It is also evident that filtration properties of attapulgite suspension in SSW is acceptable. However, comparing to attapulgite suspension in FW, filtration volume increased. This is due to the negative effect of ions in the SSW on the attapulgite performance. In the case of pre-hydrated bentonite, a thick cake and high filtration volume confirm the weak performance of the bentonite in saline environment, even in the pre-hydrated form. Therefore, this suspension was not tested for rheological properties.

TABLE 3. Filtration properties of drilling fluid

No.	Name	Filtration volume, cm^3/30 min	Thickness of mud cake, mm
1	6% Ben. FW	27.5	3.6
2	8% Ben. FW	22.5	4.1
3	6% Att. FW	10	2.8
4	8% Att. FW	8	3.5
5	6% Att. SSW	17.5	1.8
6	8% Att. SSW	14.5	1.9
7	10% Att. SSW	13	2.7
8	6% Ben. Pre H.	86	7.1

3. 2. Results of Rheological Measurements

3. 2. 1. Determination of Rheological Models Results of rheological measurement were firstly used to determine the best fitted model. As an example, measured and calculated rheological properties for suspensions of 8% and 10% attapulgite in SSW are shown in Figures 4 and 5.

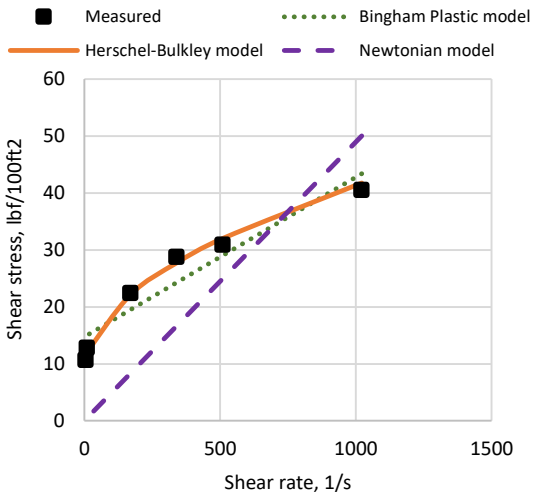

Figure 4. Determination of rheological model for 8% attapulgite suspension in SSW

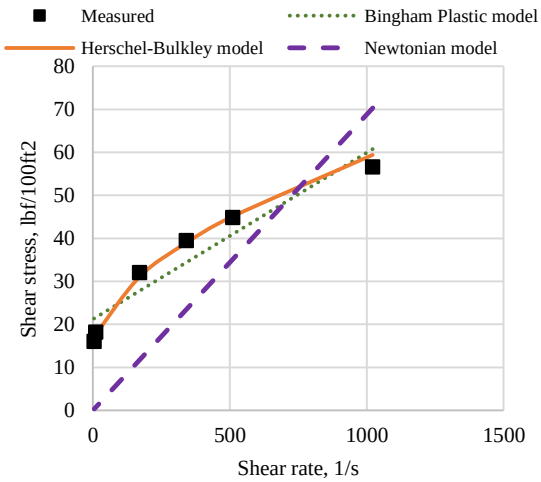

Figure 5. Determination of rheological model for 10% attapulgite suspension in SSW

Figures 4 and 5 represents real viscometer data versus rheological models. Its obvious that Herschel-Bulkley model gives better fit to data than others. Procedure of fitting rheological model to measured data was repeated for all drilling fluids and average absolute error for each rheological model was calculated. Details are presented in Table 4.

As it can be seen from the Table 4, for all bentonite and attapulgite suspensions, Herschel-Bulkley model fits the rheological data with a better accuracy.

3. 2. 2. Rheological Properties of Suspensions in FW Rheological parameters (n, k and τ_y and gel strength) of the bentonite and attapulgite suspensions in FW are presented in Figures 6 and 7. As it can be seen from these figures that flow behavior index (n) has a value less than 1 for all suspensions in fresh water. The index (n) shows the degree of non-Newtonian rheological behavior. For n values less than 1, a shear-thinning behavior, happened, i.e. showing decrease of effective viscosity with shear rate increase, as is expected [29, 30].

Also it is evident that an increase in clay (bentonite and attapulgite) concentration results in higher k, yield stress and gel strength values. This is due to the fact that at higher clay concentration a stronger three dimensional network and gel structure is formed between clay particles and water molecules [31].

However, despite of consistency index, yield stress and gel strength, an increase in clay concentration resulted in a slight decrease in n value. Experimental studies in the literature show that a lower n value in turbulent fluid flow contributes to a less pressure drop of drilling fluid in the circulation path [32, 33].

TABLE 4. Average absolute error in rheological models

No.	Name	Average absolute error in rheological model, %		
		Newtonian	Bingham Plastic	Herschel-Bulkley
1	6% Ben. FW	57.8	11.8	2.7
2	8% Ben. FW	58	7.3	3.1
3	6% Att. FW	58.7	10.3	1.6
4	8% Att. FW	59.8	12.1	2.6
5	6% Att. SSW	53.8	17.7	5
6	8% Att. SSW	56.8	16.3	3.5
7	10% Att. SSW	57.3	15.8	2.6

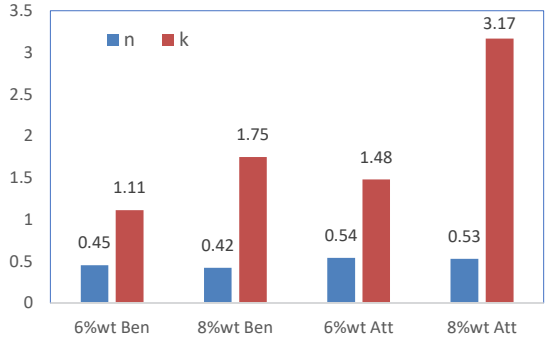

Figure 6. Comparison of rheological properties (n, k) for attapulgite and bentonite suspension in FW

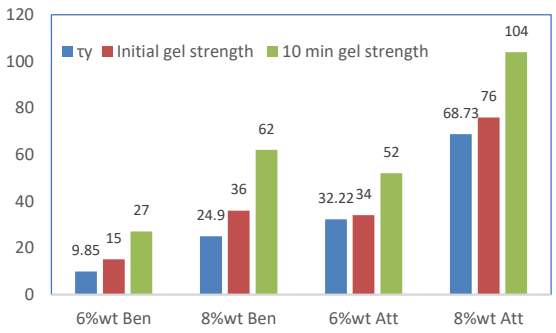

Figure 7. Comparison of rheological properties (τ_y and gel strength) for attapulgite and bentonite suspension in FW

3. 2. 3. Rheological Properties of Suspensions in SSW Bentonite particle settled down in the SSW and pre-hydrated bentonite suspension showed weak filtration properties. Therefore, only rheological properties of attapulgite suspensions in SSW were investigated. Rheological curves of 6%, 8% and 10% attapulgite in SSW are shown in Figure 8. As data implies, increase in attapulgite concentration reduces the adverse effect of salt on the rheological properties of the suspensions.

In Figure 9, consistency index and flow behavior index for attapulgite suspension in FW and SSW are compared.

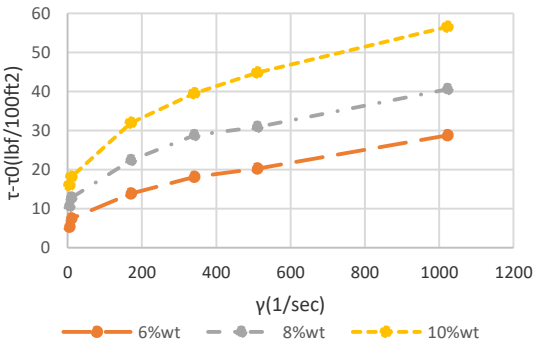

Figure 8. Rheological properties of the attapulgite suspensions in SSW

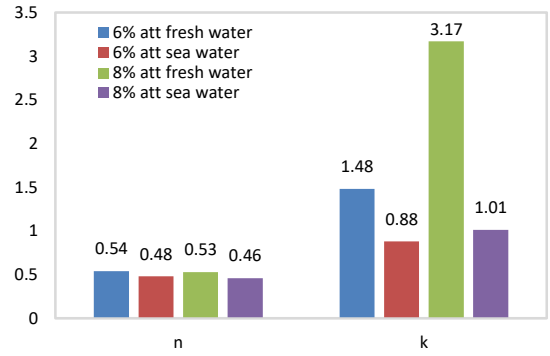

Figure 9 Rheological properties of attapulgite suspension in FW and SSW

Figure 9 shows that values of *n* and *k* decrease in SSW. Salt prevents water penetration into the attapulgite, which leads to a weaker three-dimensional structure, and further decrease of consistency.

4. CONCLUSION

Performance of drilling fluids depend on the combination of fluid flow parameters, fluid filtration characteristics, well geometry, operational conditions etc. In this work, rheological and filtration properties of bentonite, pre-hydrated bentonite and attapulgite suspensions in FW and SSW were investigated.

Results of filtration measurements showed that because of salt negative effect on attapulgite performance, filtration volume of suspensions in SSW increased comparing to attapulgite suspensions in FW. In the case of pre-hydrated bentonite, a thick cake and high filtration volume were observed, which confirms the weak performance of the bentonite in saline environment, even in the pre-hydrated form.

Fitness of Newtonian, Bingham Plastic and Herschel-Bulkley models to the measured rheological data were examined. Results showed that Herschel-Bulkley model can be used for prediction of rheological properties with a good accuracy. This is the case for suspensions in both FW and SSW.

All suspension had a flow behavior index less than 1, showing their shear thinning character. A slight decrease of *n* value is observed by increase in clay concentration. However, a lower n value is desirable for turbulent fluid flow, as it contributes to a less fluid pressure drop.

By increasing bentonite and attapulgite concentrations, higher *k*, yield stress and gel strength values were reported. At higher clay concentration a stronger three-dimensional network of clay particles in aqueous environment and consequently a stronger gel structure are formed.

Based on experimental results, performance of the attapulgite suspensions in the SSW confirmed its application in saline environemnts. The SSW, in this study, was prepared in the laboratory based on the Persian Gulf sea water. Results show that developed composition can be adjusted further and be used in drilling of offshore wells in Persian Gulf.

5. REFERENCES

1. Vipulanandan, C., Mohammed, A., "Effect of drilling mud bentonite contents on the fluid loss and filter cake formation on a field clay soil formation compared to the API fluid loss method and characterized using Vipulanandan models", ***Journal of Petroleum Science and Engineering,*** 189, (2020), 107029. doi: https://doi.org/10.1016/j.petrol.2020.107029
2. Dvoynikov, M.V., Nutskova, M.V., Blinov, P.A., "Developments Made in the Field of Drilling Fluids by Saint Petersburg Mining University", ***International Journal of Engineering, Transactions A: Basics***, 33, (2020), 702-711. doi: 10.5829/ije.2020.33.04a.22
3. Lijuan, P., Xiaoping, L., Wu, L., Fuhao, Z., Tongliang, W., Huang, W., Fuwei, W., "Study on Rheological Property Control Method of "Three High" Water Based Drilling Fluid", ***International Journal of Engineering, Transactions B: Applications***, 33, (2020), 1687-1695. doi: 10.5829/ije.2020.33.08b.28
4. Leusheva, E, Morenov, V., Tabatabaee Moradi, S.Sh., "Effect of Carbonate Additives on Dynamic Filtration Index of Drilling Mud", ***International Journal of Engineering, Transactions B: Applications***, 33, (2020), 934-939. doi: 10.5829/ije.2020.33.05b.26
5. Willson, S.M., Driscoll, P., Judzis, A, Black, A., Martin, W., Ehgartner, B., Hinkebein, T., "Drilling Salt Formations Offshore With Seawater Can Significantly Reduce Well Costs", ***SPE Drilling & Completion***, 19, (2004), 147–155. doi: https://doi.org/10.2118/87216-PA
6. Liu, J., Cheng, Y., Zhou, F., Amutenya Evelina, L.M., Long. W., Chen, S., He, L., Yi, X., Yang, X., "Evaluation method of thermal stability of bentonite for water-based drilling fluids", ***Journal of Petroleum Science and Engineering,*** (2021), 109239. doi: https://doi.org/10.1016/j.petrol.2021.109239
7. Temraz, M.G., Hassanien, I., "Mineralogy and rheological properties of some Egyptian bentonite for drilling fluids", ***Journal of Natural Gas Science and Engineering***, 31, (2016), 791-799. doi: http://dx.doi.org/10.1016/j.jngse.2016.03.072
8. Gautam, S., Guria, Ch., Rajak, D.K., Pathak, A.K., "Functionalization of fly ash for the substitution of bentonite in drilling fluid", ***Journal of Petroleum Science and Engineering,*** 166, (2018), 63-72. doi: https://doi.org/10.1016/j.petrol.2018.02.065
9. Karagüzel, C., Çetinel, T., Boylu, F., Çinku, K., Çelik, M.S., "Activation of (Na, Ca)-bentonites with soda and MgO and their utilization as drilling mud", ***Applied Clay Science,*** 48, (2010), 398-404. doi: 10.1016/j.clay.2010.01.013
10. Scheid, C.M., de Carvalho, R.V., de Oliveira, B.R., de Oliveira Borges, R.F., Calçada, L.A., "Evaluation of the dissolution kinetics of NaCl particles in aqueous drilling fluids viscosified with bentonite", ***Journal of Petroleum Science and Engineering,*** 174, (2019), 563-571. doi: https://doi.org/10.1016/j.petrol.2018.11.017
11. Zou, Z., Zhou, F., Wang, Q., Zhao, Q., Tian, Y., Liu, W., Chen, L., "Enhanced dispersive stability of bentonite suspension in

saline water-based mud", ***Colloids and Surfaces A,*** 579, (2019), 123589. doi: https://doi.org/10.1016/j.colsurfa.2019.123589

12. Li, M., Wu, Q., Han, J., Mei, Ch., Lei, T., Lee, S., Gwon, J., "Overcoming Salt Contamination of Bentonite Water-Based Drilling Fluids with Blended Dual-Functionalized Cellulose Nanocrystals", ***ACS Sustainable Chemistry & Engineering*** 8, (2008), 11569-11578. doi: https://dx.doi.org/10.1021/acssuschemeng.0c02774
13. Kelessidis, V.C., Tsamantaki, C., Dalamarinis, P., "Effect of pH and electrolyte on the rheology of aqueous Wyoming bentonite dispersions", ***Applied Clay Science,*** 38, (2007), 86-96. doi: 10.1016/j.clay.2007.01.011
14. Duman, O., Tunç, S., "Electrokinetic and rheological properties of Na-bentonite in some electrolyte solutions", ***Microporous and Mesoporous Materials,*** 117, (2009), 331-338. doi: 10.1016/j.micromeso.2008.07.007
15. Abu-Jdayil, B., "Rheology of sodium and calcium bentonite–water dispersions: Effect of electrolytes and aging time", ***International Journal of Mineral Processing***, 98, (2011), 208-213. doi: 10.1016/j.minpro.2011.01.001
16. Ren, J., Deshun, Y., Zhai, R., "Rheological behavior of bentonite-water suspension at various temperatures: Effect of solution salinity", ***Engineering Geology***, 295, (2021), 106435. doi: https://doi.org/10.1016/j.enggeo.2021.106435
17. Mirarab Razi, M., Mirarab Razi, F., "An Experimental Study of Influence of Salt Concentration, Mixing Time, and pH on the Rheological Properties of Pre-Hydrated Bentonite Slurries Treated by Polymers", ***Journal of Dispersion Science and Technology,*** 34, (2013), 764-770. doi: https://doi.org/10.1080/01932691.2012.695942
18. Altun, G., Ettehadi Osgouei, A., "Investigation and remediation of active-clay contaminated sepiolite drilling muds", ***Applied Clay Science***, 102, (2014), 238-245. doi: http://dx.doi.org/10.1016/j.clay.2014.10.002
19. Ettehadi, A., Ulker, C., Altun, G., "Nonlinear viscoelastic rheological behavior of bentonite and sepiolite drilling fluids under large amplitude oscillatory shear", ***Journal of Petroleum Science and Engineering***, 208, (2022), 109210, doi: https://doi.org/10.1016/j.petrol.2021.109210
20. Asghari, I., Esmaeilzadeh, F., "Manipulation of key parameters in RESS process for attapulgite particles utilizing in drilling mud and investigation on its rheological characteristics", ***Journal of Petroleum Science and Engineering***, 112, (2013), 359-369. doi: http://dx.doi.org/10.1016/j.petrol.2013.09.013
21. American Petroleum Institute Specifications 13I, "Recommended Practice Standard Procedure for Laboratory Testing of Drilling Fluids", (2009).
22. Rabbani, A., Salehi, S., "Dynamic modeling of the formation damage and mud cake deposition using filtration theories coupled with SEM image processing", ***Journal of Natural Gas Science and Engineering***, 42, (2017), 157-168. doi: http://dx.doi.org/10.1016/j.jngse.2017.02.047
23. Fattah, K.A., Lashin A., "Investigation of mud density and weighting materials effect on drilling fluid filter cake properties and formation damage", ***Journal of African Earth Sciences***, 117, (2016), 345-357. doi: http://dx.doi.org/10.1016/j.jafrearsci.2016.02.003
24. Tran, M.H., Abousleiman, Y.N., Vinh, X.N., "The Effects of Low-Permeability Mud cake on Time-Dependent Wellbore Failure Analyses", in IADC/SPE Asia Pacific Drilling Technology Conference and Exhibition, (2010). doi: https://doi.org/10.2118/135893-MS
25. Gudarzifar, H., Sabbaghi, S., Rezvani, A., Saboori, R., "Experimental investigation of rheological & filtration properties and thermal conductivity of water-based drilling fluid enhanced", ***Powder Technology***, 368, (2020), 323-341. doi: https://doi.org/10.1016/j.powtec.2020.04.049
26. Mohamed, A., Salehi, S., Ahmed, R., "Significance and complications of drilling fluid rheology in geothermal drilling: A review", ***Geothermics***, 93, (2021), 102066. doi: https://doi.org/10.1016/j.geothermics.2021.102066
27. Ochoa, M.V., "Analysis of drilling fluid rheology and tool joint effect to reduce errors in hydraulics calculations", PhD Dissertation, Texas A&M University, (2006).
28. Ramsey, M.S., "Practical Wellbore Hydraulics and Hole Cleaning", Gulf Professional Publishing, (2019). doi: https://doi.org/10.1016/B978-0-12-817088-5.00006-X.
29. Kamali, F., Saboori, R., Sabbaghi, S., "Fe_3O_4-CMC nanocomposite performance evaluation as rheology modifier and fluid loss control characteristic additives in water-based drilling fluid", ***Journal of Petroleum Science and Engineering***, 205, (2021), 108912. doi: https://doi.org/10.1016/j.petrol.2021.108912
30. Nabati, A., Bahrainian, S.S., Haji Dolu, E., "Improved Rheological Model of Oil-Based Drilling Fluid for Southwestern Iranian Oilfields", ***Journal of Petroleum Science and Technology***, 8, (2018), 53-71. doi: 10.22078/jpst.2017.2706.1459
31. Ouaer. H., Gareche, M., Rooki, R., "Rheological studies and optimization of Herschel–Bulkley parameters of an environmentally friendly drilling fluid using genetic algorithm", ***Rheologica Acta***, 57, (2018), 693-704. doi: https://doi.org/10.1007/s00397-018-1110-z
32. Kelessidis, V.C., Dalamarinis, P., Maglione, R., "Experimental study and predictions of pressure losses of fluids modeled as Herschel–Bulkley in concentric and eccentric annuli in laminar, transitional and turbulent flows", ***Journal of Petroleum Science and Engineering***, 77, (2011), 305-312. doi: https://doi.org/10.1016/j.petrol.2011.04.004
33. Kelessidis, V.C., Maglione, R., Tsamantaki, C., Aspirtakis, Y., "Optimal determination of rheological parameters for Herschel–Bulkley drilling fluids and impact on pressure drop, velocity profiles and penetration rates during drilling", ***Journal of Petroleum Science and Engineering***, 53, (2006), 203-224. doi: https://doi.org/10.1016/j.petrol.2006.06.004

Persian Abstract

چکیده

سیالات حفاری جز ضروری هر عملیات موفقیت آمیز ساخت چاه هستند. سیالات پایه آبی به دلیل تطابق بهتر با محیط زیست، هزینه کمتر و آماده سازی ساده تر به طور رایج استفاده می شوند. در حفاری فراساحلی، آب دریا می تواند به عنوان پایه سیالات پایه آبی استفاده شود. شوری آب دریا، کاربرد برخی از افزودنی ها را محدود می کند. به عنوان مثال، بنتونیت در محیط های شور ته نشین می شود. در این مطالعه، یک آب مصنوعی بر اساس آب دریای خلیج فارس آماده شد. مخلوط های بنتونیت، بنتونیت پیش هیدراته و آتاپولجیت در آب شیرین و آب مصنوعی ساخته شده، توسعه داده شدند. به منظور ارزیابی عملکرد این سیالات در آب مصنوعی، ویژگی های رئولوژیکی و فیلتراسیون آن ها آزمایش شدند. نتایج اندازه گیری فیلتراسیون نشان دهنده تشکیل کیک گل ضخیم و حجم بالای فیلتراسیون در سیال بنتونیت پیش هیدراته بود. در مورد اتاپولجیت، حجم فلتراسیون در آب مصنوعی در مقایسه با سیال اتاپولجیت در آب شیرین بیشتر بود. اما ویژگی های فیلتراسیون قابل قبول بودند. مطالعه ویژگی های رئولوژیکی نشان داد که مدل هرشل بالکلی می تواند با دقت خوبی جهت پیش بینی خواص رئولوژیکی سیالات به کار رود. این مورد درباره سیالات در آب دریا و آب شیرین صادق بود. همچنین مشاهده شد که شاخص رفتار سیال در همه سیالات کمتر از ۱ بود که نشان دهنده رفتار کاهش گرانروی با افزایش نرخ برش در سیالات می باشد. با افزایش غلظت رس، مقادیر بیشتری از شاخص یکپارچگی، تنش تسلیم و استحکام ژل گزارش شد. در غلظت های بالاتر رس، شبکه سه بعدی قوی تر و در نتیجه سختار ژل قوی تری در محیط های آبی تشکیل می شود. به طور کلی، می توان نتیجه گرفت که اتاپولجیت در محیط شور آب دریای خلیج فارس قابل استفاده است.

International Journal of Engineering

Journal Homepage: www.ije.ir

Exploration of *Eucheuma* Seaweed Algae Extract as a Novel Green Corrosion Inhibitor for API 5L Carbon Steel in Hydrochlorid Acid Medium

A. Nikitasari*, G. Priyotomo, A. Royani, S. Sundjono

Research Center for Metallurgy and Material, National Research and Innovation Agency, Indonesia

P A P E R I N F O

Paper history:
Received 28 September 2021
Received in revised form 03 December 2021
Accepted 23 December 2021

Keywords:
Eucheuma Extract
Corrosion Inhibitor
API 5L
Electrochemical Measurement
Hydrochloric Acid

A B S T R A C T

Regarding the issue of green chemistry and the vision of human sustainability, a novel corrosion inhibitor for API 5L carbon steel was explored from *Eucheuma* seaweed algae. The inhibiting performance of *Eucheuma* extract was studied by electrochemical measurements such as potentiodynamic polarization and electrochemical impedance spectroscopy (EIS). In this work, the Fourier Transform Infra-Red (FTIR) was also employed to confirm the main phenolic compounds of *Eucheuma* extract. The electrochemical measurement result indicated that the *Eucheuma* extract was an efficient corrosion inhibitor in reducing corrosion attacks of API 5L carbon steel in hydrochloric acid medium. The improved corrosion resistance is attributed to the complicated items, including extract concentration and holding time. *Eucheuma* inhibitor efficiency up to 90% (96.4%) with concentration 500ppm and 30min holding time indicated that *Eucheuma* could be used as a green inhibitor. It was found that the *Eucheuma* extract was a mixed-type corrosion inhibitor that inhibit both the cathodic and anodic corrosion reaction. This study was helpful to discover the seaweed algae that was abundant in Indonesia's marine for inhibiting corrosion of API 5L carbon steel in an aggressive environment.

doi:*10.5829/ije.2022.35.06c.13*

NOMENCLATURE

CR	Corrosion rate, mils per year (mpy)	R_{ct}	Charge transfer resistance (Ω)
EIS	Electrochemical Impedance Spectroscopy	R_s	Solution resistance (Ω)
FTIR	Fourier Transform Infra Red	I_{corr}	Corrosion current density (A/m^2)
OCP	Open Circuit Potential	E_{corr}	Corrosion potential (V)

1. INTRODUCTION

Low carbon steel such as API 5L is one of the most widely materials used and extensively applied for oil and gas exploration, drilling, and production [1]. These steels are important due to their low cost, easily fabrication, excellent welding, and forming abilities. However, they are vulnerable to corrosion attack when exposed to corrosive agents [2].

Hydrochloric acid (HCl) is one of the corrosive agents commonly used in industries for acid cleaning, descaling, and pickling. Corrosion inhibitors can be useful for avoiding the corrosion caused by hydrochloric acid [3].

In the last few years, the use of natural and organic extract as green corrosion inhibitors has attracted many researchers' attention. The green corrosion inhibitors have many advantages such as biodegradable, non-toxic, environmentally friendly and ecologically acceptable, inexpensive, readily available, renewable and safe to use compared to the chemical ones [4].

There are several previous works about environmentally-friendly corrosion inhibitors in a hydrochloric acid medium, such as reviewed by Yang ang Yang [5] and research conducted by Jiddawi et

*Corresponding Author Email: arininikitasari89@gmail.com (A. Nikitasari)

Please cite this article as: A. Nikitasari, G. Priyotomo, A. Royani, S. Sundjono, Exploration of *Eucheuma* Seaweed Algae Extract as a Novel Green Corrosion Inhibitor for API 5L Carbon Steel in Hydrochlorid Acid Medium, ***International Journal of Engineering, Transactions C: Aspects*** Vol. 35, No. 03, (2022) 596-603

al. [6] that used organic compound aniline and phenol. Besides that, some researchers used natural sources Rosmarinus officinalis plant [7], Hyalomma insect [8], and the waste from sunflower seedhull [3] as corrosion inhibitors. In contribution to the research on the natural compound for effective corrosion inhibition in HCl medium, this present work uses *Eucheuma* seaweed algae as the new resource.

Eucheuma is a group of red seaweed algae usually found in Indonesia [5]. *Eucheuma* extract has potential to be used as a green corrosion inhibitor due to the exhibits high growth rates and contains high polyphenol [6]. However, this algae has never been studied before as corrosion inhibitors. Due to the purposes below, this research aims to explore of *Eucheuma* seaweed algae extracts to inhibit the corrosive impact on API 5L carbon steel in hydrochloric acid (0.1 M HCl). Potentiodynamic polarization, electrochemical impedance spectroscopy (EIS) and FTIR were used to assess this work.

2. MATERIALS AND METHODS

2. 1. Materials Carbon steel API 5L specimens having a chemical composition in wt % (C, 0.05; Si, 0.13; Mn, 0.73; P, 0.02; S, 0.004; Fe remainder) were used. Carbon steel was cut with a size of 1 cm x 1 cm x 1 cm, connected with cable wire, and mounted with an exposed area of 1 cm^2. Prior the experiment, the specimens were mechanically abraded using different grades (120 – 1200) of silicon carbide emery paper and subsequently cleaned with acetone, then rinsed with distilled water.

2. 2. *Eucheuma* Extract and Medium For the *Eucheuma* seaweed algae extract process, at first, seaweed was cleaned with tap water and dried at room temperature for five days. The dried *Eucheuma* was chopped and collected in 70% of ethanol (maceration) for 72h. The ratio between dried *Eucheuma* and ethanol for the maceration process was 1:3, respectively. The maceration result was filtrated and evaporated to obtain the extract. To investigate the chemical composition of the *Eucheuma* extract, FTIR was employed.

The hydrochloric acid medium that used in this experiment was 0.1 M HCl. *Eucheuma* extract with various concentration i.e. 0, 50, 100, 200, 400, and 500 ppm was mixed into 0.1 M HCl. All specimens were immersed in the medium without and with 30 min of holding time before electrochemical measurement. The temperature of the medium also varied (room temperature, 40°C, and 50°C) to evaluate the influence of temperature on the corrosion rate.

2. 3. Electrochemical Measurement Electrochemical measurements were performed using GAMRY Series G-750 Corrosion Measurement System. For measurement, the three-electrode corrosion cell was used [7]. API 5L specimens with an exposed area of 1 cm^2 were utilized as a working electrode. A platinum and SCE (saturated calomel electrode) electrode were acted as counter and reference electrodes, respectively.

Potentiodynamic polarization was carried out in the potential range of ±250 mV from the OCP potential. The scanning rate of the polarization curve was about 1 mV/s. The electrochemical impedance spectroscopy (EIS) measurements were conducted with the frequency range of 100 kHz and 10 mHz. The measurements were done with a signal of 10 mV peak to peak. In addition, the impedance results were fitted to obtain the charge transfer resistance (R_{ct}). All the electrochemical measurements were recorded in triplicate.

3. RESULT AND DISCUSSION

3. 1. Polarization Test Result Figure 1 illustrates the cathodic and anodic polarization curves for API 5L carbon steel immersed in 0.1 M HCl containing various concentrations of *Eucheuma* green inhibitor at different temperatures without holding time. In addition, potentiodynamic polarization curves for API 5L in 0.1 M HCl solution at various temperatures and concentrations of *Eucheuma* extract with 30 min of holding time are represented in Figure 2. It is observed that by adding inhibitor, the potential tends to be a similar value but current shifts toward less current. Hence, it is indicated that *Eucheuma* extract was a mixed-type corrosion inhibitor and improved the corrosion resistance of API 5L in the hydrochloric acid medium [8]. From Figures 1 and 2, the polarization curve of the specimen without inhibitor at 50°C has the lowest potential value and the highest current. Therefore, the greatest corrosion rate is specimen without inhibitor at 50°C.

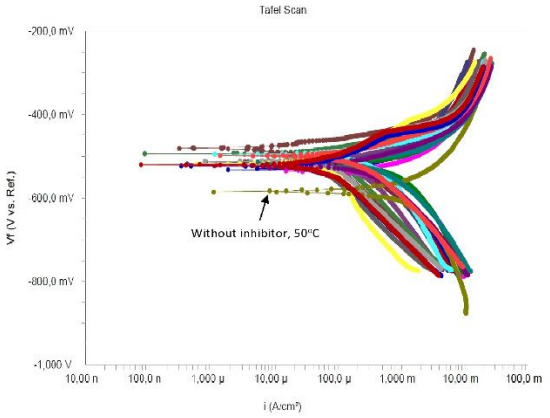

Figure 1. Polarization curves of API 5L in 0.1 M HCl and various *Eucheuma* inhibitor at different temperatures without holding time

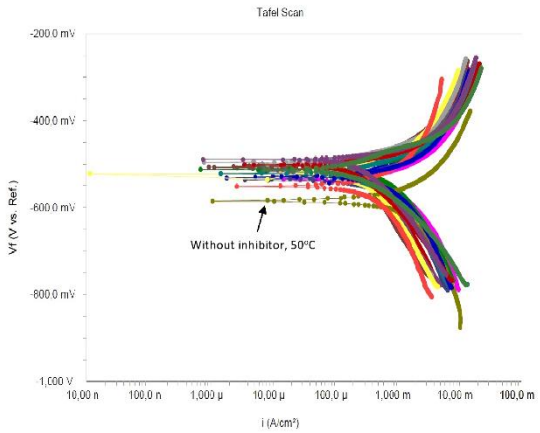

Figure 2. Polarization curves of API 5L in 0.1 M HCl and various *Eucheuma* inhibitor at different temperatures with 30 minute of holding time

In this study, the electrochemical corrosion parameters such as corrosion potential (Ecorr) and corrosion current densities (Icorr) were automatically calculated based on Butler–Volmer and Tafel equations [9]. Tafel slope analysis and fitting of the polarization curves were performed using Echem analyst software to obtain the corrosion rate of API 5L carbon steel. Table 1 listed the parameters of API 5L in 0.1 M HCl and various inhibitor concentrations at room temperature with 30 min of holding time that resulted from polarization test.

According to Table 1, corrosion current density (Icorr) and corrosion rate decrease significantly with increasing inhibitor concentration. Figure 3 summarizes the corrosion rate of API 5L in 0.1 M HCl with various concentrations of *Eucheuma* inhibitor at different temperatures. All specimens with a low inhibitor concentration have a higher corrosion rate than specimens with higher inhibitor concentration. When "30 min holding time" was used, the corrosion rate was lower than "no holding time" specimens. This behavior could justify the adsorption process of inhibitors on the steel surface. The holding time gives a chance to the inhibitor for covering the steel surface. Corrosion rate also boosts with the increasing of temperature based on Figure 3.

TABLE 1. Parameters obtained from polarization test

Concentration (ppm)	Ecorr (mV)	Icorr (mA/cm^2)	Corrosion rate (mpy)
0	-532	6.65E-4	304
50	-523	4.65E-4	212.9
100	-513	2.22E-4	101.5
200	-494	9.58E-5	43.88
400	-481	5.63E-5	25.77
500	-514	5.28E-5	24.17

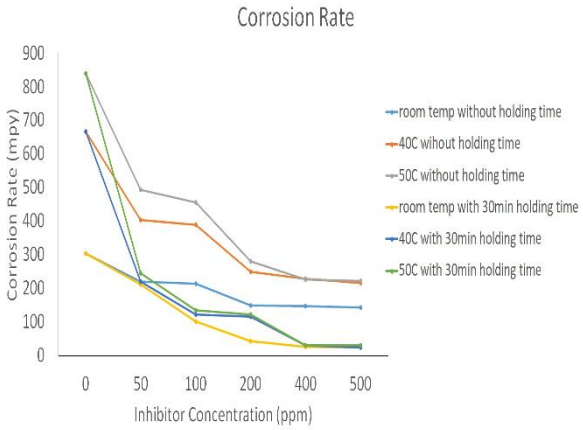

Figure 3. Corrosion rate of API 5L in 0.1 M HCl and various *Eucheuma* inhibitor at different temperatures

Inhibition efficiency (η) can be formulated by Equation (1):

$$\eta = \frac{CR - CR(in)}{CR} x100\% \quad (1)$$

where CR and CR(in) are corrosion rate without and with the presence of inhibitor, respectively. Figure 4 showed the inhibitor efficiency of all specimens. Compared to ''no holding time", specimens with holding time presented a more pronounced inhibition effect.

Inhibitor efficiency increase with ane increas in inhibitor concentration and temperature. The highest inhibition efficiency (96.4%) was specimen containing a *Eucheuma* inhibitor with a concentration of 500ppm with 30 min holding time at 50°C. It is seen that the corrosion rate decreases by adding inhibitor so that it is reduced by 28 times at 500 ppm concentration of the inhibitor. Therefore, it is obvious that the *Eucheuma* extract inhibitor is useful [13].

3. 2. EIS Test Results The inhibition performance of *Eucehuma* extract on API 5L carbon steel was further

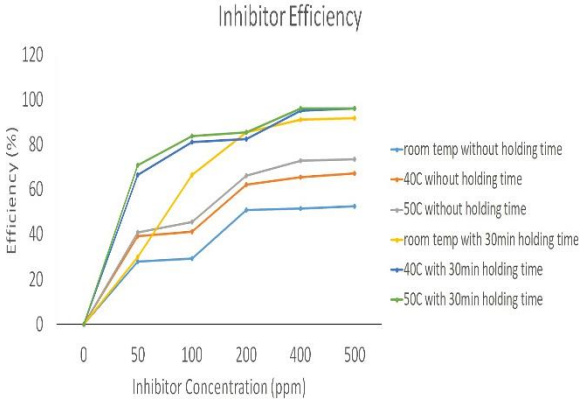

Figure 4. Inhibitor efficiency of API 5L in 0.1 M HCl and various *Eucheuma* inhibitor at different temperatures

analyzed by means of electrochemical impedance spectroscopy (EIS) measurements under different experimental conditions.

Figure 5 showed a Bode plot for API 5L in 0.1 M HCl environment with and without inhibitor at different temperatures. The peak in the Bode plot indicated the existence of the relaxation time. The higher impedance was obtained for API 5L with the highest concentration of inhibitor in each temperature. Furthermore, the corrosion resistance of steel substrate increased when the concentration of *Eucheuma* extract increased, as the total impedance obviously increased due to the results in Figure 5. According to Figure 5 (a), the phase angles increased from -40 to -60°. The increasing of phase angle with the increasing of inhibitor concentration indicated that the *Eucheuma* inhibitor was physically adsorbed on the surface [14].

Nyquist plot for API 5L carbon steel in 0.1 M HCl and various inhibitor concentrations with and without holding time at different temperatures presented in Figure 6 Based on Figure 6, all impedance spectra implied a single depressed capacitive semicircle, indicating that the steel dissolution is related to the charge transfer process [15]. In addition, the diameter of the Nyquist plot's semicircle increases with the increasing concentration of *Eucheuma* extract. This phenomenon revealed that *Eucheuma* extract inhibits the corrosion process due to the electronegative charge of the heteroatoms contained in the extracts and the electropositive charge on the steel surface [16].

Electrical circuit model used to interpret EIS data. The suggested electrical circuit model for API 5L in 0.1M HCl and *Eucheuma* inhibitor is shown in Figure 7. The electrical circuit model in Figure 7 includes R_S as solution resistance, R_{ct} as charge transfer resistance, and CPE as constant phase element. In this study, CPE was used instead of capacitance (C) for the circuit model due to all angles of phases are less than 90° based on Figure 5 [10]. CPE was introduced as "capacitance dispersion" that related to capacity of the material surface area of complex surface roughness and inhomogeneous reaction [17]. The CPE element has a fixed phase shift angle and its impedance describes the expression: $ZCPE= 1/Y_0(j\omega)n$, where Y_0 and 'a' are the parameters related to the shift phase angle [18].

Figure 8 depicts the charge transfer resistance value obtained using the fitting of the electrical circuit model. Charge transfer resistance (R_{ct}) value increase with the increase of inhibitor concentration, as shown in Figure 8. Holding time also increases the R_{ct} value. The increasing R_{ct} value indicates that charge transfer from solution to the steel surface and vice versa inhibited by more inhibitor concentration [17].

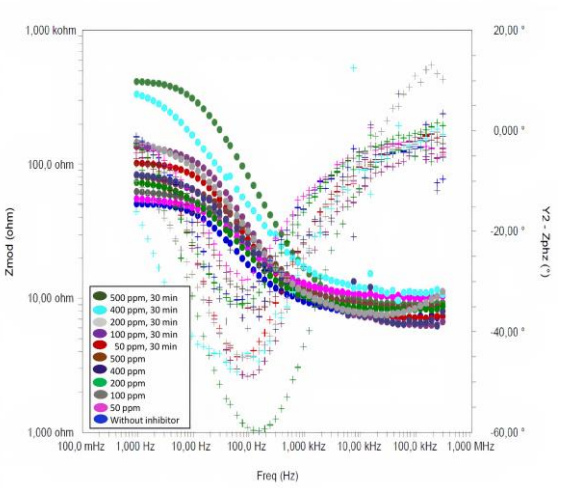

(a) Bode plot at room temperature

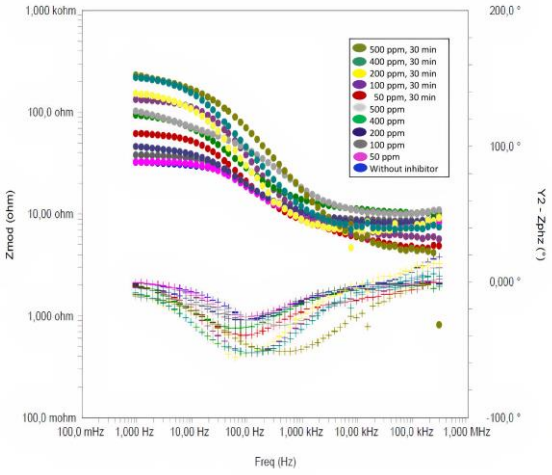

(b) Bode plot at 40ºC

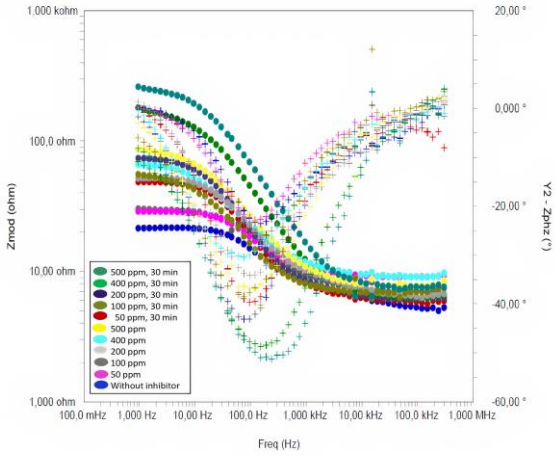

(c) Bode plot at 50ºC

Figure 5. Bode plot of API 5L in 0.1 M HCl and various *Eucheuma* inhibitor concentration

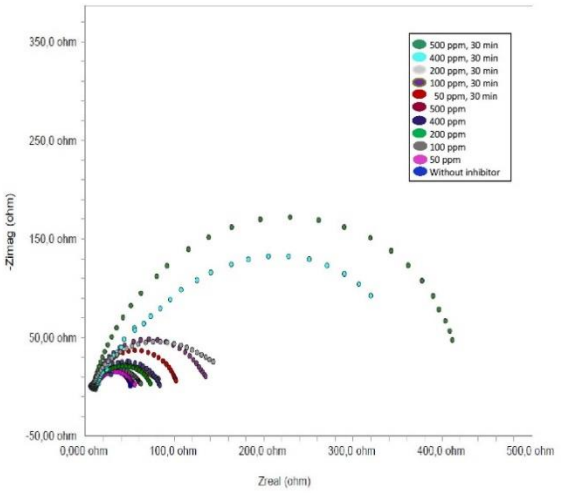

(a) Nyquist plot at room temperature

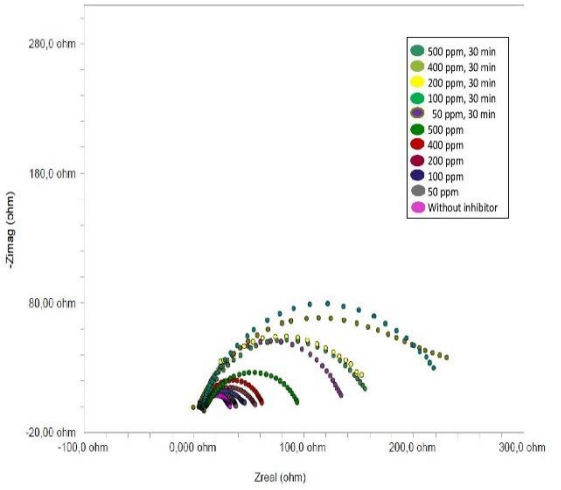

(b) Nyquist plot at 40°C

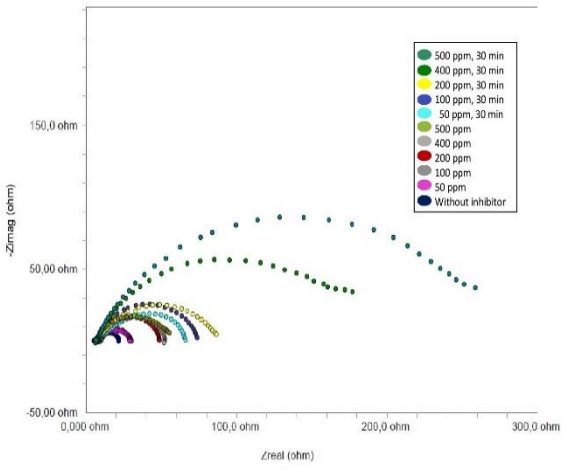

(c) Nyquist plot at 50°C

Figure 6. Nyquist plot of API 5L in 0.1 M HCl and various *Eucheuma* inhibitor concentration

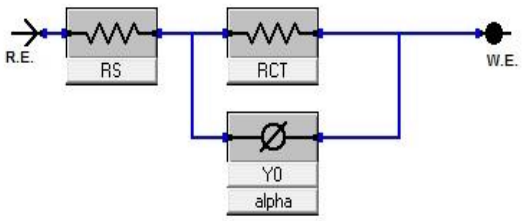

Figure 7. Electrical circuit model

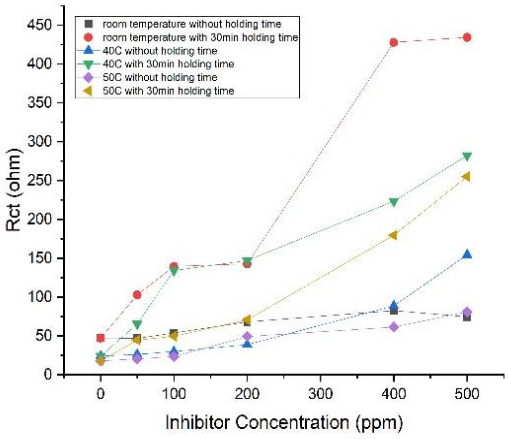

Figure 8. R_{ct} value

3. 3. Thermodynamics of the Electrochemical Process The thermodynamics result of the electrochemical process at various temperature and concentration are listed on the Table 2. The 500 ppm *Eucheuma* inhibitor at 50°C shows superior inhibition as it has the greatest surface coverage area (0.964).

It has been reported that organic inhibitors are absorbed on the metal surface and adsorption are fitted with Langmuir adsorption isotherms and prevents corrosion. The fundamental details of *Eucheuma* inhibitor also were explored using Langmuir adsorption isotherm, according to the following equation:

$$\frac{C_{inh}}{\theta} = \frac{1}{K_{ads}} + C_{inh} \quad (2)$$

where θ equals to η/100, K_{ads} is the equilibrium constant of the adsorption process, and C_{inh} represents to the inhibitor concentration. Figure 9 depicts plot C_{inh} vs C_{inh}/θ based on Equation (2). The intercept of this plot represents the K_{ads} value. Figure 9 reveals that *Eucheuma* inhibitor follows the Langmuir adsorption inhibitor because the high value of R^2. Therefore, it can be described that the molecules of *Eucheuma* inhibitor are absorbed in a single-layer on the metal surface.

TABLE 2. Thermodynamic parameters

T (K)	Cinh (ppm)	θ	Kads (L/mol)	ΔG (kJ/mol)	ΔH (kJ/mol)	ΔS (J/mol)
298	100	0.666	0.023	-24.84		
	200	0.856				
	400	0.915				
	500	0.920				
313	100	0.815	0.029	-26.74	14.82	133
	200	0.827				
	400	0.954				
	500	0.962				
323	100	0.839	0.036	-28.19		
	200	0.855				
	400	0.963				
	500	0.964				

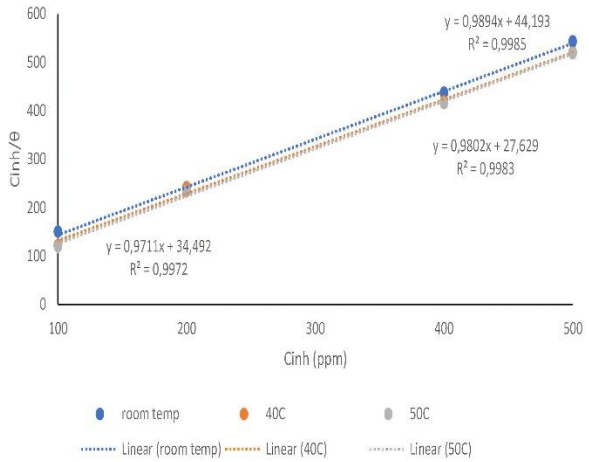

Figure 9. Langmuir adsorption isotherm plot of *Eucheuma* inhibitor at various temperature

Based on Table 2, the maximum value of K_{ads} at temperature 50ºC. It indicates the greater adsorbed inhibitors on the metal surface when the temperature increased. Furthermore, the type of adsorption can be acquired with the calculation of adsorption free energy (ΔG). Equation (3) shows the relationship between ΔG and K_{ads}. The value of R is 8.314 J/K. mole and T is absolute temperature in K. Clarifying the calculated result of ΔG, the range of ΔG is -25 kJ/mol and -28 kJ/mol. The negative value of ΔG confirms the feasibility of adsorption process. Moreover, it concluded that inhibition mechanism of the *Eucheuma* inhibitor is mainly physical adsorption on the metal surface and *Eucheuma* inhibitor is chemical adsorption at higer temperature [19].

$$\Delta G = - R.T \ln (10^6 . K_{ads}) \quad (3)$$

Equation (4) is used to determine the value of the heat of adsorption (ΔH) and the entropy (ΔS).

$$\ln K_{ads} = ln\frac{1}{C_{solvent}} - \frac{\Delta H}{R.T} + \frac{\Delta S}{R} \quad (4)$$

ΔH and ΔS are slope and intercept of ln K_{ads} vs T^{-1} curve respectively. These two parameters are presented in Table 2. The positive value of ΔH indicates an increase in irregularities due to desorption of H_2O molecules from surface and adsorption of the inhibitors molecules in each site [3]. The The positive amount of entropy elicits that the thermal stability of the film increases at elevated temperature and their irreversibility process [20].

3. 4. FTIR Test Results The FTIR of the *Eucheuma* extract is represented in Figure 10. A broad peak with the wavenumber value of 3372.68 cm^{-1} has corresponded to OH bonds. Besides, the strong peak of 2922.28 and 2856.7 cm^{-1} are related to the binding of C-H group. It is also clear that the peaks at 1729.26 and 1631.85 cm^{-1} are related to the vibrational mode of the bindings of C=O and C=C, respectively. The wavenumber values of 1452.46 and 1412.92 cm^{-1} are depicted the bond of O-H. The peak at 1167.95 and 1049.32 cm^{-1} belonged to C-O.

Consequently, it can be concluded that *Eucheuma* extract contained elements of O, H, and C with a cyclic group of carbon or polyphenol compound which attracted the steel substrates according to have free electrons. This behavior could justify the decrease in the corrosion rate of API 5L substrate in HCl solution in the presence of *Eucheuma* extract as a green inhibitor.

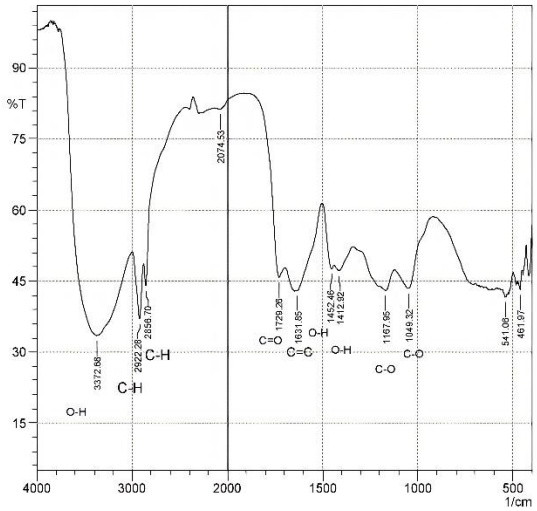

Figure 10. FTIR result of *Eucheuma* extract

4. CONCLUSION

Eucheuma seaweed algae was successfully used for the first time as a green corrosion inhibitor for API 5L carbon steel in the hydrochloric acid medium. Corrosion resistance of API 5L boosts with the concentration of *Eucheuma* inhibitor and holding time. Temperature also improves efficiency of inhibitor. In the presence of 500 ppm inhibitor with 30 min holding time at 50ºC, the inhibition efficiency reaches about 96.4%. The corrosion rate at this concentration of inhibitor was also reduced by about 28 times.

The charge and ion transfer on the steel surface decrease because of the complex formation between the inhibitor and the ions of the steel surface. Therefore, the charge transfer resistance will improve and the corrosion rate will reduce with the existance of *Eucheuma* inhibitor. The inhibiton mechanism of *Eucheuma* inhibitor follows Langmuir adsorption isotherm. *Eucheuma* inhibitor is adsorbed on the metal surface forming a passive layer that can prevent corrosion process. These results confirm that the introduction of aromatic rings and OH to organic compounds is suitable as a corrosion inhibitor in the hydrochloric acid medium.

5. REFERENCES

1. Villavicencio, J., Ulloa, N., Lozada, L., Moreno, M., Castro, L. "The Role of Non-Metallic Al2O3 Inclusions, Heat treatments and Microstructure on The Corrosion Resistance of an API 5L X42 Steel" ***Journal of Materials Research and Technology,*** Vol. 9, No. 3, (2020), 5894-5911. DOI: 10.1016/j.jmrt.2020.03.116.
2. Loto, R.T., Olukeye, T., Okorie, E. "Synergistic Combination Effect of Clove Essential Oil Extract with Basil and Atlas Cedar Oil on The Corrosion Inhibition of Low Carbon Steel" ***South African Journal of Chemical Engineering,*** Vol. 30, (2019), 28-41, DOI: 10.1016/j.sajce.2019.08.001.
3. Hassannejad, H., Nouri, A. "Sunflower Seed Hull Extract as a Novel Green Corrosion Inhibitor for Mild Steel in HCl Solution" ***Journal of Molecular Liquids,*** Vol. 254, (2018), 377-382, DOI: 10.1016/j.molliq.2018.01.142.
4. Al-Akhras, N and Mashaqbeh, Y. "Potential Use of Eucalyptus Leaves as Green Corrosion Inhibitor of Steel Reinforcement" ***Journal of Building Engineering,*** Vol. 35, (2020), 101848, DOI: 10.1016/j.jobe.2020.101848.
5. Yang, D and Yang, H. "The Temperature Dependent Extraction of Polysaccharides from *Eucheuma* and The Rheological Synergistic Effect in Their Mixtures with Kappa Carrageenan." ***LWT-Food Science Technology,*** Vol. 129, (2020), 109515, DOI: 10.1016/j.lwt.2020.109515.
6. Jiddawi, N., Kautsky, N., Halling, C. "Herbivory and Substrate Type Influence Growth of The Macroalgae *Eucheuma* Denticulatum (N. L. Burman) Collins & Hervey, 1917 on a Tropical Coral Reef" ***Journal of Experimental Marine Biology and Ecology Coral-macroalgal interactions,*** Vol. 543, No. 1 (2021), 542-543, DOI: 10.1016/j.jembe.2021.151606.
7. Khavasfar, A., Moayed, M.H., Jafari, A.H. "An Investigation on The Performance of an Imidazoline Based Commercial Corrosion Inhibitor on CO_2 Corrosion of Mild Steel" ***International Journal of Engineering, Transactions A: Basics,*** Vol. 20, No. 1, (2007), 35-44.
8. Liu, Y., Song, Z., Wang, W., Jiang, L., Zhang, Y., Guo, M., Song, F. and Xu, N."Effect of Ginger Extract as Green Inhibitor on Chloride-Induced Corrosion of Carbon Steel in Simulated Concrete Pore Solutions" ***Journal of Cleaner Production,*** Vol. 214, (2019), 298-307, DOI: 10.1016/j.jclepro.2018.12.299.
9. Hu, J., Zhu, Y., Hang, J., Zhang, Z., Ma, Y., Huang, H., Yu, Q. and Wei, J., "The Effect of Organic Core–Shell Corrosion Inhibitors on Corrosion Performance of The Reinforcement in Simulated Concrete Pore Solution" ***Construction and Building Materials,*** Vol. 267, (2020), 121011, DOI: 10.1016/j.conbuildmat.2020.121011.
10. Bidi, M.A., Azadi, M., Rassouli, M. "A New Green Inhibitor for Lowering the Corrosion Rate of Carbon Steel in 1 M HCl Solution: Hyalomma tick extract" ***Materials Today Communications,*** Vol. 24, (2020), DOI: 10.1016/j.mtcomm.2020.100996.
11. Hanini, K., Merzoug, B., Boudiba, S., Selatnia, I., Laouer, H., Akkal, S. "Influence of Different Polyphenol Extracts of Taxus Baccata on The Corrosion Process and Their Effect as Additives in Electrodeposition" ***Sustainable Chemistry and Pharmacy,*** Vol. 14, (2019), DOI: 10.1016/j.scp.2019.100189.
12. Shahrabi, T., Hosseini, M., Ghorbani, M., Arshadi, M. "Synergistic Influence of Benzoate Ions on Inhibition of Corrosion of Mild Steel in 0.5M Sulfuric Acid by Benzotriazole" ***International Journal of Engineering, Transactions B: Applications,*** Vol. 16, No. 3, (2003), 255–264.
13. Belakhdar, A., et al., "Computational and Experimental Studies on The Efficiency of Rosmarinus Officinalis Polyphenols as Green Corrosion Inhibitors for XC48 Steel in Acidic Medium." ***Colloids Surfaces A,*** Vol. 606, (2020), 125458, DOI: 10.1016/j.colsurfa.2020.125458.
14. Eddy, N.O., Odoemelam, S.A., Ama, I.N., "Ethanol Extract of Ocimum Gratissimum as A Green Corrosion Inhibitor for The Corrsion of Mild Steel in H2SO4" ***Green Chemistry Letters and Reviews,*** Vol. 3, No. 3, (2010), 165–172, DOI: 10.1080/17518251003636428.
15. Singh, A., Ansari, K.R., Chauhan, D.S., Quraishi, M.A., Kaya, S. "Anti-Corrosion Investigation of Pyrimidine Derivatives as Green and Sustainable Corrosion Inhibitor for N80 Steel in Highly Corrosive Environment: Experimental and AFM/XPS Study" ***Sustainable Chemistry and Pharmacy,*** Vol. 16, (2020), DOI: 10.1016/j.scp.2020.100257.
16. El-Askalany, A.H., Mostafa, S.I., Shalabi, K., Eid, A.M., Shaaban, S. "Novel Tetrazole-Based Symmetrical Diselenides as Corrosion Inhibitors for N80 Carbon Steel in 1 M HCl Solutions: Experimental and Theoretical Studies" ***Journal of Molecular Liquids,*** Vol. 223, (2016), 497-508, DOI: 10.1016/j.molliq.2016.08.088
17. Nikitasari, A., Mabruri, E., Riastuti, R. "Corrosion Behavior of CA6NM in Simulated Geothermal Brine Highlighted by Electrochemical Impedance Spectroscopy" ***Engineering and Applied Science Research,*** Vol. 48, No. 4, (2021), 359-367, DOI: 10.14456/easr.2021.38.
18. Brytan, Z., Niagaj, J., Reiman, Ł. "Corrosion Studies using Potentiodynamic and EIS Electrochemical Techniques of Welded Lean Duplex Stainless Steel UNS S82441" ***Applied Surface Science,*** Vol. 388, (2016), 160-168, DOI: 10.1016/j.apsusc.2016.01.260.
19. Deyab, M.A. " Corrosion inhibition of heat exchanger tubing material (titanium) in MSF desalination plants in acid cleaning solution using aromatic nitro compounds" ***Desalination,*** Vol. 439, (2018), 73-79, DOI: 10.1016/j.desal.2018.04.005.
20. Pramana, R.I., Kusumastuti, R., Soedarsono, J.W., Rustandi, A. "Corrosion Inhibition of Low Carbon Steel by Pluchea Indica Less. in 3.5% NaCL Solution" ***Advanced Materials Research,*** Vol. 785-786, (2013), 20-24, DOI: 10.4028/www.scientific.net/amr.785-786.20.

Persian Abstract

چکیده

با توجه به موضوع شیمی سبز و چشم انداز پایداری انسان، یک بازدارنده خوردگی جدید برای فولاد کربنی API 5L از جلبک جلبک دریایی ***Eucheuma*** مورد بررسی قرار گرفت. عملکرد بازدارندگی عصاره ***Eucheuma*** با اندازه‌گیری‌های الکتروشیمیایی مانند قطبش پتانسیودینامیک و طیف‌سنجی امپدانس الکتروشیمیایی (EIS) مورد بررسی قرار گرفت. در این کار، تبدیل فوریه مادون قرمز (FTIR) نیز برای تایید ترکیبات فنلی اصلی عصاره ی ***Eucheuma*** به کار گرفته شد. نتایج اندازه گیری الکتروشیمیایی نشان داد که عصاره ***Eucheuma*** یک بازدارنده خوردگی کارآمد در کاهش حملات خوردگی فولاد کربنی API 5L در محیط اسید هیدروکلریک است. مقاومت در برابر خوردگی بهبود یافته به موارد پیچیده، از جمله غلظت عصاره و زمان نگهداری نسبت داده می شود. راندمان بازدارنده Eucheuma تا ۹۰٪ (۹۶/٤٪) با غلظت ppm ۵۰۰ و زمان نگهداری ۳۰ دقیقه نشان داد که عصاره ***Eucheuma*** می‌تواند به عنوان یک مهارکننده سبز مورد استفاده قرار گیرد. مشخص شد که عصاره ***Eucheuma*** یک بازدارنده خوردگی نوع مخلوط است که هم واکنش خوردگی کاتدی و هم آندی را مهار می کند. این مطالعه برای کشف جلبک دریایی که در دریای اندونزی برای مهار خوردگی فولاد کربنی API 5L در یک محیط تهاجمی فراوان بود، مفید بود.

International Journal of Engineering

Journal Homepage: www.ije.ir

An Optimal Boolean Approach for Computational Modeling of Gene Regulatory Networks from Temporal Gene Expression Profile

F. Razmi[a], A. Rowhanimanesh*[b], A. Dideban[a]

[a] *Department of Electrical Engineering, Semnan University, Semnan, Iran*
[b] *Department of Electrical Engineering, University of Neyshabur, Neyshabur, Iran*

PAPER INFO

Paper history:
Received 18 June 2021
Received in revised form 31 July 2021
Accepted 25 December 2021

Keywords:
Computational Modeling
Gene Regulatory Network
Temporal Gene Expression Profile
Optimization
Genetic Algorithm
Yeast

ABSTRACT

Deciphering the crucial interactions among genes is one of the key issues in understanding the fundamental molecular and intracellular mechanisms of cell. Computational modeling of gene regulatory networks can be used as a powerful tool in various fields of molecular biomedicine such as identification of metabolic, regulator, and signal transduction pathways, analysis of complex genetic diseases, and drug discovery. In this paper, an optimal Boolean approach was proposed for computational modeling of gene regulatory networks from temporal gene expression profile. In this method, the optimal values of the Boolean thresholds of gene expression signals and the parameters of the interaction patterns between target and regulator genes are all designed as a mixed-integer nonlinear programming solved by Genetic Algorithm. To evaluate the performance of the proposed scheme, it has been applied to a well-known time course microarray data and gene regulatory network of *Saccharomyces cerevisiae* from the literature. The reference network has 11 genes, 9 targets, and 61 regulatory interactions, and the original transcriptional dataset includes 18 time points for each gene expression signal. In this case study, the proposed computational model contains 142 unknown parameters that are optimally determined through optimization. The results demonstrate the efficiency of the proposed approach.

***doi**: 10.5829/ije.2022.35.03c.14*

1. INTRODUCTION

In recent years, many researches have used the converging technologies of the industrial revolution 4.0 era to significantly affect future medicine [1, 2]. With the aid of gene expression profiling technology such as DNA microarray, it is possible to study the behavior and interactions of thousands of genes simultaneously [3, 4]. This technology is one of the most influential tools for discovering the transcriptional and translational dynamics of genes that leads to computational modeling and analysis of the interactions between genes as Gene Regulatory Networks (GRNs) [5-7]. Due to the nature of gene regulation, important mechanisms are involved in this process such as DNA, RNA, and protein interactions. Usually, the proteins that are translated from genes or produced from chemical reaction networks can play the role of transcription factors to activate or inhibit the transcription of some genes. The purpose of inferring gene regulatory networks is to decipher the interaction patterns among target and regulator genes from the spatial and temporal profiles of gene expression data. Additionally, this paradigm can lead to the identification of genes that play key roles in metabolic and signal transduction pathways. Computational modeling and analysis of GRNs demonstrate how some genes affect other genes in a complex manner. This information can be widely used in various areas of biological and medical researches such as molecular medicine, drug discovery, P4 medicine, and cell/tissue engineering [8, 9].

Different methods have been proposed in the literature for computational modeling of GRNs. Some

*Corresponding Author Institutional Email: rowhanimanesh@neyshabur.ac.ir (A. Rowhanimanesh)

Please cite this article as: F. Razmi, A. Rowhanimanesh, A. Dideban, An Optimal Boolean Approach for Computational Modeling of Gene Regulatory Networks from Temporal Gene Expression Profile, ***International Journal of Engineering, Transactions C: Aspects*** Vol. 35, No. 03, (2022) 604-612

of them are reviewed here. Ren and Jinde [10] described a robust analysis scheme based on Lyapunov stability theory and linear matrix inequality (LMI) for asymptotic stability of delayed GRNs with time-varying delays. Xiao et al. [11] proposed a reduced-order approach to consider the stability analysis in GRNs with discrete time delays. Zañudo et al. [12] used the notion of discrete dynamic networks to investigate how computational modeling of oncogenic signaling can help personalized treatment of cancer. Chen et al. [13] proposed a Markovian method for controlling the dynamics of GRNs. Barbuti et al. [14] reviewed various techniques used in mathematical modeling of GRNs including ordinary differential equations (ODE), Boolean networks, Petri nets, P systems, and reaction systems.

Mandon et al. [15] considered attractor-based sequential reprogramming of GRNs based on Boolean network models. Dai and Liu [16] proposed a computational approach for inferring gene-gene interactions from time-series data based on Bayesian network modeling, estimation of distribution algorithms, and depth-first search. Hajiramezanali et al. [17] presented optimal classification of cellular trajectories under regulatory model uncertainty based on partially-observed Boolean dynamical systems and noisy gene expression data. In recent years, special attention has been focused on computational modeling and analysis of GRNs based on time-course gene expression data, as reported inliterature [18-20], that is the main topic of this study.

In this paper, we propose an optimal Boolean approach for computational modeling of GRNs from temporal gene expression profile. Both fundamental steps of systems identification including Model Structure Design and Parameter Optimization are described. The proposed model structure is a general and computationally efficient model which contains four set of parameters including expression threshold, regulator weight, regulator delay, and activation limit. The parameter optimization is formulated as a mixed-integer nonlinear programming. In order to solve this optimization problem in a general manner, Genetic Algorithm (GA) is used. Furthermore, a general preprocessing method is introduced for normalization and smooth interpolation of gene expression time series. To evaluate the performance of the proposed model, it is applied to a benchmark time course microarray data and reference gene regulatory network of *Saccharomyces cerevisiae* from the literature. The results demonstrate that the proposed approach could accurately model the benchmark GRN with more simplicity and understandability.

This paper is organized as follows: In the next section, the reference gene regulatory network and the time-course transcriptional dataset of the case study of this paper are described. Then, a general preprocessing method is introduced for normalization and interpolation of gene expression time series. In section 3, an optimal Boolean approach is proposed for computational modeling of GRNs from temporal gene expression profile. The results of evaluation are demonstrated in section 4. Finally, section 5 concludes the paper.

2. TEMPORAL GENE EXPRESSION PROFILE

2. 1. The Reference GRN Gene regulation is one of the key mechanisms in cell cycle control, when proper functioning of the cell cycle is vital for the survival of an organism. Functional abnormalities in cell cycle process may lead to noteworthy alterations in the phenotypical aspects of the cell and even, programmed cell death. Yeasts, the eukaryotic single-celled microorganisms as members of the fungus kingdom, have been widely used in systems biology for studying cell cycle control especially from genomic perspective [21]. Many remarkable investigations have been performed in the literature on the cell cycle of *Saccharomyces cerevisiae* as a well-known species of yeast. Most of these researches have been focused on the gene regulatory networks and the spatial and temporal profiles of gene expression which are incorporated in the mechanisms of cell cycle control. In general, these studies on yeast microorganisms are valuable because some results can be generalized to complex organisms.

In the case study of this paper, a commonly-used reference GRN [22], which play a significant role in the cell cycle control of *Saccharomyces cere*visiae, have been considered. This reference GRN have been frequently used by the previous works in the literature [23, 24]. As shown in Figure 1, the reference network has 11 genes including *cln1*, *cln2*, *cln3*, *clb1*, *clb2*, *clb5*, *clb6*, *cdc14*, *cdc20*, *mcm1*, and *swi5*. There are 9 target

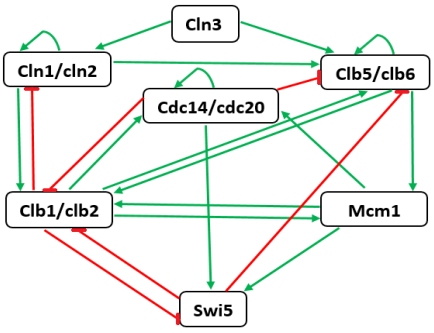

Figure 1. The reference gene regulatory network [22-24]

genes which are totally regulated by 61 regulatory interactions. The green arrow lines indicate which

regulator genes play the role of activator and which target genes are affected by them in the form of upregulation. Similarly, the inhibitors that lead to the down-regulation of their targets are illustrated by red blocking lines. More details about this reference GRN are available in literature [22-24].

2. 2. The Time-Course Gene Expression Data The time-course gene expression data, measured by transcriptional profiling technologies such as DNA microarray, has been frequently exploited as training dataset for computational modeling of GRNs. In this paper, we use the well-known temporal gene expression profile of the yeast Saccharomyces cerevisiae. This dataset has been introduced by Spellman et al. [25] and it is available on Gene Expression Omnibus (GEO) with accession number of GSE22[1]. In the mentioned dataset, the expression levels of genes have been measured over 2 hours with sampling period of 7 minutes. Thus, the training dataset includes the time series with 18 time points for each gene.

2. 3. Preprocessing Procedure In this paper, a general preprocessing method is introduced for normalization and interpolation of gene expression time series. In order to consider the effect of down-regulation and up-regulation of genes accurately, normalization of the magnitude of gene expression levels is required. Also, in most of the transcriptional profiling procedures, the value of sampling period is large. But most of the computational models of GRN need more number of samples to increase the identification accuracy. For this reason, interpolation can be an effective approach to provide smooth approximated signals from original time course gene expression dataset. Here, we use shape-preserving piece-wise cubic Hermite interpolation technique that is an appropriate scheme from the aspects of computational efficiency and smoothness [26]. Particularly in the continuous-time models of GRN such as ODE models, in which precise approximation of the derivatives of expression signals are required, the above-mentioned interpolation procedure can be highly helpful. Figure 2 depicts the temporal gene expression profile of the case study after preprocessing.

3. THE PROPOSED MODELING APPROACH

3. 1. Boolean Model Structure A system identification problem consists of two fundamental steps: a) Model Structure Selection, and b) Parameter Optimization. In this paper, a general but computationally simple Boolean model structure is proposed for computational modeling of GRNs. Transparency and understandability of model structure are important desirable characteristics. The proposed Boolean model structure is shown in Figure 3. This model contains four set of parameters: 1) Expression Threshold, 2) Regulator Weight, 3) Regulator Delay, and 4) Activation Limit.

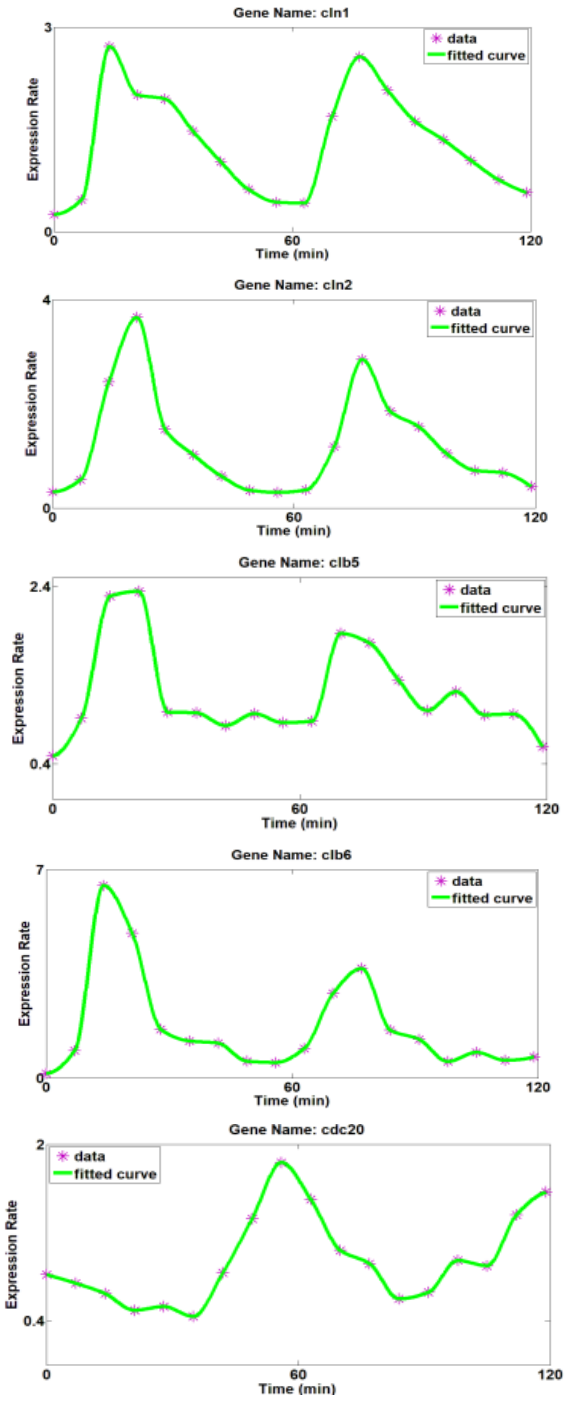

[1] https://www.ncbi.nlm.nih.gov/geo/query/acc.cgi?acc=GSE22

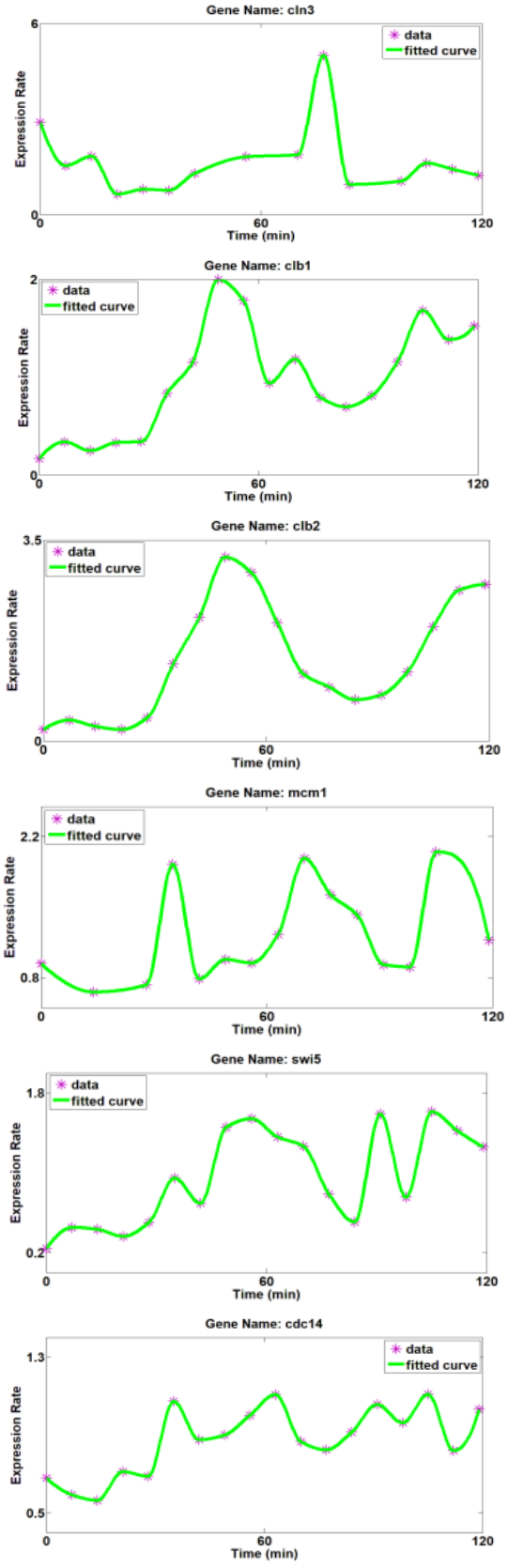

Figure 2. The temporal gene expression profile after preprocessing

In Boolean models of GRNs, genes are considered to be On or Off. Since the gene expression level is a real-valued variable, a threshold is required to convert this continuous signal to a binary one. As the dynamics and molecular function of genes are different, due to the generality, an independent expression threshold parameter is defined for each gene. Also, the effects of regulators on their target gene are not generally the same. To address this issue, we define independent Weight and Delay parameters for each regulator-target interaction link. Weight illustrates the intensity of regulation between a regulator and its target, and Delay represents how late this regulation is affected. Finally, in order to aggregate the regulatory effects of activators and inhibitors on a target gene, an activation limit is defined for each target.

As shown in Figure 3, for the case study of this paper, the proposed Boolean model structure has totally 142 parameters including 11 parameters for expression threshold, 61 for regulator weight, 61 for regulator delay, and 9 for activation limit. The governing equations of this model are as follows:

$$G_{cln1}(k+1) = H((A_{cln1}(k) - I_{cln1}(k) - B_{cln1}(k)) \quad (1)$$

$$A_{cln1}(k) = W_{cln1}^{cln1} * G_{cln1}\left(k - d_{cln1}^{cln1}\right) + W_{cln1}^{cln2} * G_{cln2}\left(k - d_{cln1}^{cln2}\right) + W_{cln1}^{cln3} * G_{cln3}\left(k - d_{cln1}^{cln3}\right)$$

$$I_{cln1}(k) = W_{cln1}^{clb1} * G_{clb1}\left(k - d_{cln1}^{clb1}\right) + W_{cln1}^{clb2} * G_{clb2}\left(k - d_{cln1}^{clb2}\right) \quad (2)$$

$$G_{cln2}(k+1) = H((A_{cln2}(k) - I_{cln2}(k) - B_{cln2}(k))$$

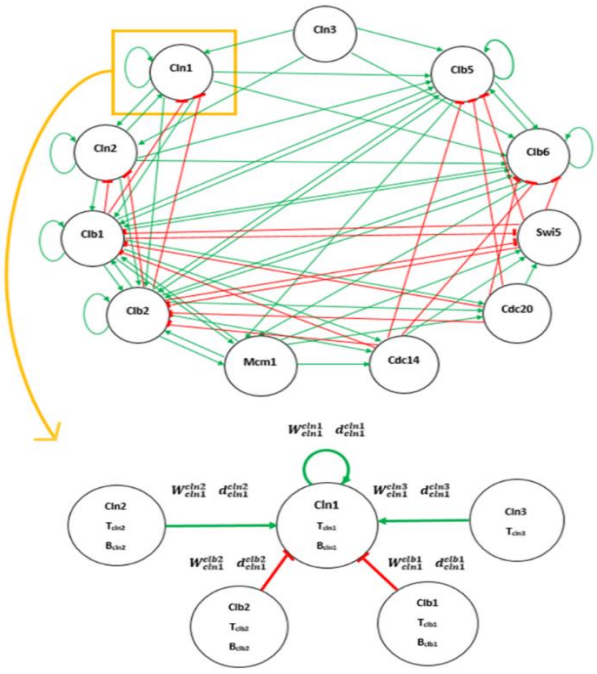

Figure 3. The proposed model structure

$$A_{cln2}(k) = W_{cln2}^{cln2} * G_{cln2}\left(k - d_{cln2}^{cln2}\right)) + W_{cln2}^{cln1} * G_{cln1}\left(k - d_{cln2}^{cln1}\right) + W_{cln2}^{cln3} * G_{cln3}\left(k - d_{cln2}^{cln3}\right)$$

$$I_{cln2}(k) = W_{cln2}^{clb1} * G_{clb1}\left(k - d_{cln2}^{clb1}\right) + W_{cln2}^{clb2} * G_{clb2}\left(k - d_{cln2}^{clb2}\right) \quad (3)$$

$$G_{clb5}(k+1) = H((A_{clb5}(k) - I_{clb5}(k) - B_{clb5}(k))$$

$$A_{clb5}(k) = W_{clb5}^{clb5} * G_{clb5}\left(k - d_{clb5}^{clb5}\right) + W_{cln5}^{cln1} * G_{cln1}\left(k - d_{clb5}^{cln1}\right) + W_{clb5}^{cln2} * G_{cln2}\left(k - d_{clb5}^{cln2}\right) + W_{clb5}^{cln3} * G_{cln3}\left(k - d_{clb5}^{cln3}\right) + W_{clb5}^{clb1} * G_{clb1}\left(k - d_{clb5}^{clb1}\right) + W_{clb5}^{clb2} * G_{clb2}\left(k - d_{clb5}^{clb2}\right) + W_{clb5}^{clb6} * G_{clb6}\left(k - d_{clb5}^{clb6}\right) \quad (4)$$

$$I_{clb5}(k) = W_{clb5}^{swi5} * G_{swi5}\left(k - d_{clb5}^{swi5}\right) + W_{clb5}^{cdc20} * G_{cdc20}\left(k - d_{clb5}^{cdc20}\right) + W_{clb5}^{cdc14} * G_{cdc14}\left(k - d_{clb5}^{cdc14}\right)$$

$$G_{clb6}(k+1) = H((A_{clb6}(k) - I_{clb6}(k) - B_{clb6}(k))$$

$$A_{clb6}(k) = (W_{clb6}^{clb6} * G_{clb6}\left(k - d_{clb6}^{clb6}\right) + W_{cln6}^{cln1} * G_{cln1}\left(k - d_{clb6}^{cln1}\right) + W_{clb6}^{cln2} * G_{cln2}\left(k - d_{clb6}^{cln2}\right) + W_{clb6}^{cln3} * G_{cln3}\left(k - d_{clb6}^{cln3}\right) + W_{clb6}^{clb1} * G_{clb1}\left(k - d_{clb6}^{clb1}\right) + W_{clb6}^{clb2} * G_{clb6}\left(k - d_{clb6}^{clb2}\right) + W_{clb6}^{clb5} * G_{clb5}\left(k - d_{clb6}^{clb5}\right))$$

$$I_{clb6}(k) = \left(W_{clb6}^{swi5} * G_{swi5}\left(k - d_{clb6}^{swi5}\right) + W_{clb6}^{cdc20} * G_{cdc20}\left(k - d_{clb6}^{cdc20}\right) + W_{clb6}^{cdc14} * G_{cdc14}\left(k - d_{clb6}^{cdc14}\right)\right) \quad (5)$$

$$G_{cdc20}(k+1) = H((A_{cdc20}(k) - I_{cdc20}(k) - B_{cdc20}(k))$$

$$A_{cdc20}(k) = (W_{cdc20}^{clb1} * G_{clb1}\left(k - d_{cdc20}^{clb1}\right) + W_{cdc20}^{clb2} * G_{clb2}\left(k - d_{cdc20}^{clb2}\right) + W_{cdc20}^{mcm1} * G_{mcm1}\left(k - d_{cdc20}^{mcm1}\right)) \quad (6)$$

$$I_{cdc20}(k) = 0$$

$$G_{clb1}(k+1) = H((A_{clb1}(k) - I_{clb1}(k) - B_{clb1}(k))$$

$$A_{clb1}(k) = (W_{clb1}^{clb1} * G_{clb1}\left(k - d_{clb1}^{clb1}\right) + W_{clb1}^{clb2} * G_{clb2}\left(k - d_{clb1}^{clb2}\right) + W_{clb1}^{clb5} * G_{clb5}\left(k - d_{clb1}^{clb5}\right) + W_{clb1}^{clb6} * G_{clb6}\left(k - d_{clb1}^{clb6}\right) + W_{clb1}^{cln1} * G_{cln1}\left(k - d_{clb1}^{cln1}\right) + W_{clb1}^{cln2} * G_{cln2}\left(k - d_{clb1}^{cln2}\right) + W_{clb1}^{mcm1} * G_{mcm1}\left(k - d_{clb1}^{mcm1}\right)) \quad (7)$$

$$I_{clb1}(k) = W_{clb1}^{swi5} * G_{swi5}\left(k - d_{clb1}^{swi5}\right) + W_{clb1}^{cdc20} * G_{cdc20}\left(k - d_{clb1}^{cdc20}\right) + W_{clb1}^{cdc14} * G_{cdc14}\left(k - d_{clb1}^{cdc14}\right)$$

$$G_{clb2}(k+1) = H((A_{clb2}(k) - I_{clb2}(k) - B_{clb2}(k))$$

$$A_{clb2}(k) = (W_{clb2}^{clb2} * G_{clb2}\left(k - d_{clb2}^{clb2}\right) + W_{clb2}^{clb1} * G_{clb1}\left(k - d_{clb2}^{clb1}\right) + W_{clb2}^{clb5} * G_{clb5}\left(k - d_{clb2}^{clb5}\right) + W_{clb2}^{clb6} * G_{clb6}\left(k - d_{clb2}^{clb6}\right) + W_{clb2}^{cln1} * G_{cln1}\left(k - d_{clb2}^{cln1}\right) + W_{clb2}^{cln2} * G_{cln2}\left(k - d_{clb2}^{cln2}\right) + W_{clb2}^{mcm1} * G_{mcm1}\left(k - d_{clb2}^{mcm1}\right)) \quad (8)$$

$$I_{clb2}(k) = W_{clb2}^{swi5} * G_{swi5}\left(k - d_{clb2}^{swi5}\right) + W_{clb2}^{cdc20} * G_{cdc20}\left(k - d_{clb2}^{cdc20}\right) + W_{clb2}^{cdc14} * G_{cdc14}\left(k - d_{clb2}^{cdc14}\right)$$

$$G_{mcm1}(k+1) = H((A_{mcm1}(k) - I_{mcm1}(k) - B_{mcm1}(k))$$

$$A_{mcm1}(k) = (W_{mcm1}^{clb1} * G_{clb1}\left(k - d_{mcm1}^{clb1}\right) + W_{mcm1}^{clb2} * G_{clb2}\left(k - d_{mcm1}^{clb2}\right) + W_{mcm1}^{clb5} * G_{clb5}\left(k - d_{mcm1}^{clb5}\right) + W_{mcm1}^{clb6} * G_{clb6}\left(k - d_{mcm1}^{clb6}\right))$$

$$I_{mcm1}(k) = 0 \quad (9)$$

$$G_{swi5}(k+1) = H((A_{siw5}(k) - I_{siw5}(k) - B_{siw5}(k))$$

$$A_{siw5}(k) = (W_{swi5}^{cdc14} * G_{cdc14}\left(k - d_{siw5}^{cdc14}\right) + W_{swi5}^{mcm1} * G_{mcm1}\left(k - d_{siw5}^{mcm1}\right))$$

$$I_{siw5}(k) = \left(W_{swi5}^{clb1} * G_{clb1}\left(k - d_{siw5}^{clb1}\right) + W_{swi5}^{clb2} * G_{clb2}\left(k - d_{siw5}^{clb2}\right)\right) \quad (10)$$

where G_X is the normalized expression level of gene X, A_T is the activation term which leads to the upregulation of target gene T, I_T is the inhibition term which leads to the downregulation of target gene T, B_T is the activation limit for target gene T, H is the Hard-limit function, W_T^R and d_T^R are respectively the weight and delay of the regulatory effect of regulator R on target T, and k is the number of timepoint in the interpolated temporal profile.

3. 2. Parameter Optimization by GA In order to find the optimal values of the unknown parameters of the proposed Boolean model structure of the previous section, the time-course gene expression data described in section 2 is used. The parameters of Expression Threshold, Regulator Weight, and Activation Limit are real-valued, but the parameters of Regulator Delay are integer. According to this point, and with respect to the nonlinearity available in model equations and error metric, the parameter optimization problem is a mixed-integer nonlinear programming. Solving constrained nonlinear optimization problems, especially with mixed-integer decision variables, is generally difficult and conventional optimization methods may not solve these problems effectively, and consequently the exact optimal solutions cannot be found easily. Therefore, as an alternative, various metaheuristic algorithms have been proposed in the literature to efficiently find the near-optimal solutions for complex optimization problems [27-29].

One of the most powerful and general-purpose metaheuristic algorithms is GA that is recognized as derivative-free population-based global optimizer. Different versions of GA have been proposed in the literature and it has been combined with other artificial intelligence methods to improve its computational efficiency, accuracy, and convergence speed for diverse

types of optimization problems including constrained, multi-objective, nonlinear, nonconvex, mixed-integer, and largescale problems [30-32]. More importantly, GA has been widely used in different domains of applications such as food science [33], control engineering [34], medicine [35], nanotechnology [36], machine learning [37], and civil engineering [39, 39]. As shown in Figure 4, GA is applied to solve the mixed-integer nonlinear programming of this study.

4. RESULTS

In this section, GA is used for parameter optimization of the proposed Boolean model structure of section 3.1. As the training dataset, the preprocessing procedure introduced in section 3.3 was applied to the benchmark temporal gene expression profile of section 3.2, and the interpolated time series were sampled at a period of 5 minutes. We used the genetic algorithm solver of Global Optimization Toolbox in MATLAB. Figure 5 represents the relative values of Expression Threshold for each gene. As displayed in this figure, the expression threshold has a distinguishing value for each gene. Figure 6 demonstrates the output of the proposed optimal Boolean model in comparison with the temporal gene expression profile in a Boolean manner. The blue dots are the actual values and the red circles are the values identified by the proposed method. The identification error is 17.59% in terms of mean absolute error.

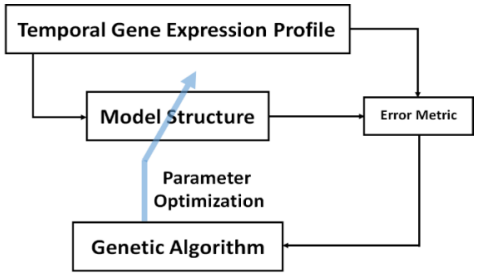

Figure 4. Parameter optimization by Genetic Algorithm

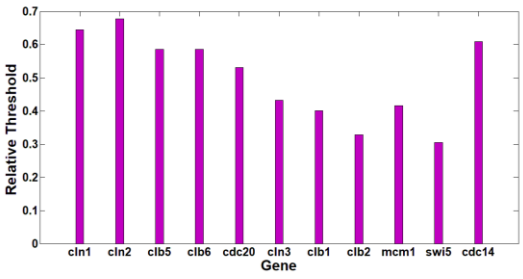

Figure 5. The relative values of Expression Threshold for each gene

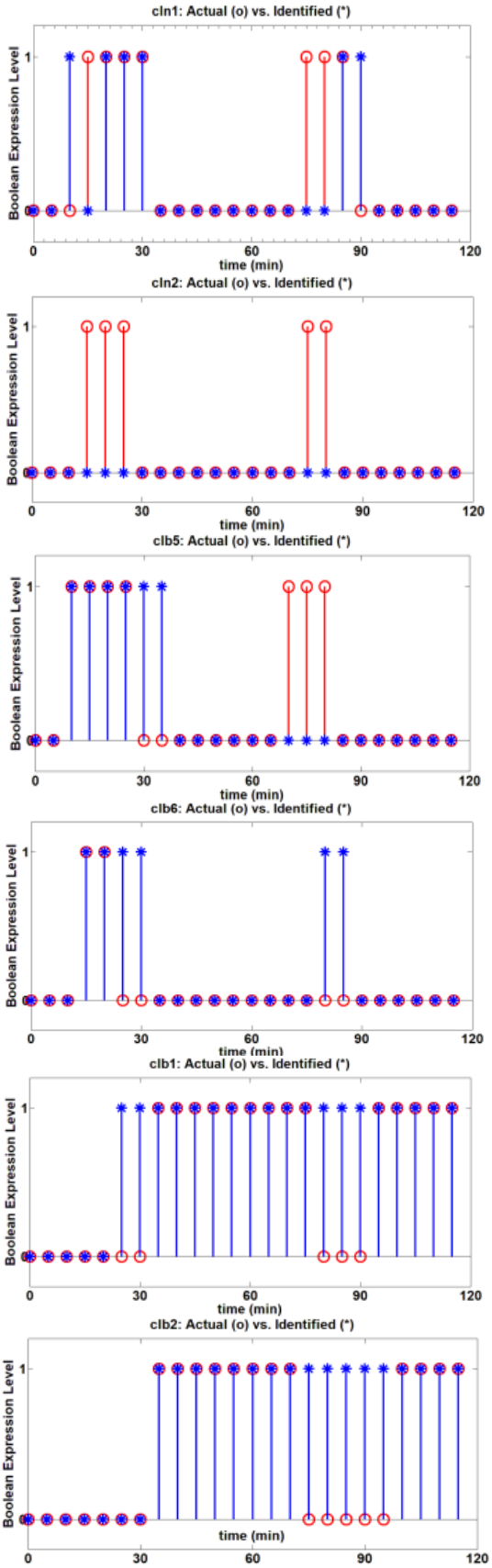

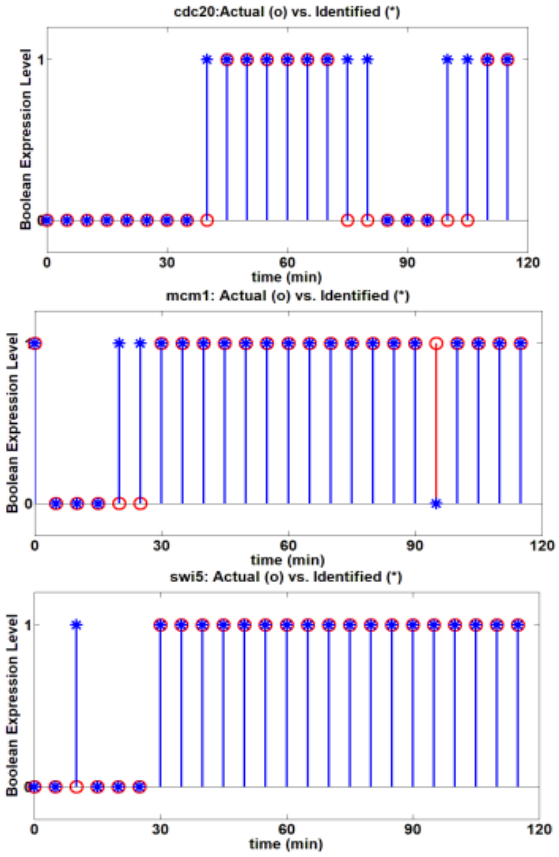

Figure 6. The output of the proposed model (identified) vs. the temporal gene expression profile (actual)

5. CONCLUSION

This paper proposed an optimal Boolean approach for computational modeling of gene regulatory networks from the temporal transcriptional data. The model structure is a flexible and computationally efficient model which contains four sets of parameters including expression threshold, regulator weight, regulator delay, and activation limit. The parameter optimization was formulated as a mixed-integer nonlinear programming and solved by genetic algorithm. Also, a general preprocessing method was introduced for normalization and interpolation of gene expression time series. To evaluate the performance of the proposed approach, it has been applied to a well-known time-course microarray data and reference gene regulatory network of *Saccharomyces cerevisiae* from the literature. The reference network has 11 genes, 9 targets, and 61 regulatory interactions, and the original transcriptional dataset includes 18 timepoints for each gene expression signal. The proposed model contains 142 unknown parameters. The results demonstrated that the proposed model could successfully identify the gene regulatory network with the identification error of 17.59% in terms of mean absolute error.

6. REFERENCES

1. Khezri, R., Hosseini, R., and Mazinani, M. "A Fuzzy Rule-based Expert System for the Prognosis of the Risk of Development of the Breast Cancer." ***International Journal of Engineering, Transactions A: Basics,*** Vol. 27, No. 10 (2014), 1557-1564. DOI: 10.5829/idosi.ije.2014.27.10a.09
2. Rowhanimanesh, A., and Akbarzadeh-T, M. R., "Stigmergic cooperation of nanoparticles for swarm fuzzy control of low-density lipoprotein concentration in the arterial wall." Applied ***Soft Computing*** 34 (2015), 799-812. DOI: 10.1016/j.asoc.2015.05.013
3. Shaeiri, Z., and Ghaderi, R., "Modification of the fast global k-means using a fuzzy relation with application in microarray data analysis." ***International Journal of Engineering, Transactions C: Aspects,*** Vol. 25, No. 4 (2012), 283-292. DOI: 10.5829/idosi.ije.2012.25.04c.03
4. Nachtigall, P., Bovolenta, L., James, P., Bastian, F., Ney, L., Danillo, P., "A comparative analysis of heart microRNAs in vertebrates brings novel insights into the evolution of genetic regulatory networks." ***BMC Genomics*** 22.1 (2021), 1-20. DOI: 10.1186/s12864-021-07441-4
5. Xiang, C., Min, Li., Ruiqing, Z., Siyu, Z., Fang-X, Wu., Yaohang, Li., and Jianxin, W., "A novel method of gene regulatory network structure inference from gene knock-out expression data." ***Tsinghua Science and Technology*** 24.4 (2019), 446-455. DOI: 1 0. 2 6 5 9 9/T ST. 2 0 1 8. 9 0 1 0 0 9 7
6. Delgado, F. M., and Francisco, G., "Computational methods for Gene Regulatory Networks reconstruction and analysis: A review." ***Artificial Intelligence in Medicine*** 95 (2019), 133-145. DOI: 10.1016/j.artmed.2018.10.006
7. Sanguinetti, G. "Gene regulatory network inference: an introductory survey." Gene Regulatory Networks. ***Humana Press***, New York, NY, (2019), 1-23. Doi: 10.1007/978-1-4939-8882-2_1
8. Sun, X., Ji, Z., and Q. Nie., "Inferring latent temporal progression and regulatory networks from cross-sectional transcriptomic data of cancer samples." ***PLoS Computational Biology*** 17.3 (2021), e1008379. DOI: 10.1371/journal.pcbi.1008379
9. Zou, C., and Xingyuan W., "Robust stability of delayed Markovian switching genetic regulatory networks with reaction–diffusion terms." ***Computers & Mathematics with Applications*** 79.4 (2020), 1150-1164. DOI: 10.1016/j.camwa.2019.08.024
10. Ren, F., and Jinde C., "Asymptotic and robust stability of genetic regulatory networks with time-varying delays." ***Neurocomputing*** 71.4-6 (2008), 834-842, DOI: 10.1016/j.neucom.2007.03.011
11. Xiao, S., Xian, Z., Xin, W., and Yantao, W., "A reduced-order approach to analyze stability of genetic regulatory networks with discrete time delays." ***Neurocomputing*** 323, (2019), 311-318. doi.org/10.1016/j.neucom.2018.10.005
12. Zañudo, J., GT., Steven, N., Steinway, and Réka, A., "Discrete dynamic network modeling of oncogenic signaling: Mechanistic insights for personalized treatment of cancer." ***Current Opinion in Systems Biology*** 9 (2018), 1-10. DOI: 10.1016/j.coisb.2018.02.002
13. Chen, P.CY., and Jeremy W.C., "A Markovian approach to the control of genetic regulatory networks." ***Biosystems*** 90.2, (2007), 535-545. DOI: 10.1016/j.biosystems.2006.12.005
14. Barbuti, R., Gori, R., Milazzo, P., and Nasti, L., "A survey of gene regulatory networks modelling methods: from differential equations, to Boolean and qualitative bioinspired models." ***Journal of Membrane Computing*** (2020), 1-20. DOI: 10.1007/s41965-020-00046

15. Hugues, M., Cui, S., Stefan, H., Jun, P. and loic, P., "Sequential reprogramming of Boolean networks made practical." International Conference on Computational Methods in Systems Biology, (2019). DOI: 10.1007/978-3-030-31304-3_1
16. Dai, C., and Juan, L., "Inducing pairwise gene interactions from time-series data by EDA based bayesian network." IEEE Engineering in Medicine and Biology 27th Annual Conference. IEEE, (2006). DOI: 10.1109/IEMBS.2005.1616308
17. Hajiramezanali, E., Imani, M., Barga-N, U., Qian, X., and Dougherty, E.R., "Scalable optimal Bayesian classification of single-cell trajectories under regulatory model uncertainty." ***BMC Genomics*** 20.6 (2019), 1-11. DOI: 10.1186/s12864-019-5720-3
18. Maróti, Z., Tombácz, D., Prazsák, I., Moldován, N., Csabai, Z., Torma, G., Balázs, Z., Kalmár, T., Dénes, B., Snyder, M. and Boldogkői, Z., "Time-course transcriptome analysis of host cell response to poxvirus infection using a dual long-read sequencing approach." ***BMC Research Notes*** 14.1 (2021), 1-7. DOI: 10.1186/s13104-021-05657-x
19. Rowhanimanesh, A., "A Novel Approach for the Analysis of Time-course Gene Expression Data Based on Computing with Words." Journal of Biomedical Informatics 120 (2021), 103868. DOI: 10.1016/j.jbi.2021.103868
20. Jose, M., Alvarez, M., Brooks, D., Swift, J., and Coruzzi, G.M., "Time-Based Systems Biology Approaches to Capture and Model Dynamic Gene Regulatory Networks." ***Annual Review of Plant Biology*** 72, (2021), 105-131. DOI: 10.1146/annurev-arplant-081320-090914
21. Bähler, J., "Cell-cycle control of gene expression in budding and fission yeast." Annu. Rev. Genet. 39 (2005), 69-94. DOI: 10.1146/annurev.genet.39.110304.095808
22. Kaderali, L., and Radde, N., "Inferring gene regulatory networks from expression data." C***omputational Intelligence in Bioinformatics***. Springer, Berlin, Heidelberg, (2008), 33-74. DOI: 10.1007/978-3-540-76803-6_2
23. Radde, N., and Kaderali, L., "Bayesian inference of gene regulatory networks using gene expression time series data." International Conference on Bioinformatics Research and Development. Springer, Berlin, Heidelberg, 2007. DOI: 10.1007/978-3-540-71233-6_1
24. Fangting, Li., Tao, L., Ying, Lu., Ouyang, Qi., and Tang, C., "The yeast cell-cycle network is robustly designed." ***Proceedings of the National Academy of Sciences*** 101.14 (2004), 4781-4786. DOI: 10.1073/pnas.0305937101
25. Spellman, P.T., Shelock, G., Zhang, M.Q., Q.Z., Lyer, V.R., Anders, K., A., Eisen, M.B., Brown, P.O., Botstein, D., Futcher, B., "Comprehensive identification of cell cycle–regulated genes of the yeast Saccharomyces cerevisiae by microarray hybridization." ***Molecular Biology of the Cell*** 9.12, (1998), 3273-3297. DOI: 10.1091/mbc.9.12.3273
26. De Boor, C., "A practical guide to splines". Vol. 27. New York: Springer-verlag, (1978).
27. Yang, X.S., Engineering optimization: an introduction with metaheuristic applications. John ***Wiley & Sons***, 2010.
28. Rowhanimanesh, A., and Akbarzadeh-T, M.R., "Perception-based heuristic granular search: Exploiting uncertainty for analysis of certain functions." ***Scientia Iranica*** 18, No. 3 (2011): 617-626. DOI: 10.1016/j.scient.2011.04.015
29. Zarepor-A, A., and Mosalman-Y, H., "Location Allocation of Earthquake Relief Centers in Yazd City Based on Whale Optimization Algorithm." ***International Journal of Engineering, Transactions B: Applications,*** *Vol.* 34, No. 5 (2021), 1184-1194. DOI: 10.5829/ije.2021.34.05b.12
30. Rowhanimanesh, A., and Efati, S., "A novel approach to improve the performance of evolutionary methods for nonlinear constrained optimization." ***Advances in Artificial Intelligence***, (2012). DOI: 10.1155/2012/540861
31. Mohammadi, S., and Babagoli, M., "A Hybrid Modified Grasshopper Optimization Algorithm and Genetic Algorithm to Detect and Prevent DDoS Attacks." ***International Journal of Engineering***, ***Transactions A: Basics,*** Vol. 34, No. 4 (2021), 811-824. DOI: 10.5829/ije.2021.34.04a.07
32. Rowhanimanesh, A., and Akbarzadeh-T, M.R., "Perception-based evolutionary optimization: Outline of a novel approach to optimization and problem solving." In Proceedings of IEEE International Conference on Systems, Man and Cybernetics (2010), 4270-4275. DOI: 10.1109/ICSMC.2010.5642481
33. Mohebbi, M., Barouei, J., AkbarzadehT, M.R., Rowhanimanesh, A., Habibi-N, M.B., Yavarmanesh, M., "Modeling and optimization of viscosity in enzyme-modified cheese by fuzzy logic and genetic algorithm." ***Computers and Electronics in Agriculture*** 62.2, (2008), 260-265. DOI: 10.1016/j.compag.2008.01.010
34. Rowhanimanesh, A., Karimpour, A., Pariz, N., "Optimal path planning for controllability of switched linear systems using multi-level constrained GA." ***Applications of Soft Computing*** (2009): 399-408. DOI: 10.1007/978-3-540-89619-7_39
35. Aalaei, S., Shahraki, H., Rowhanimanesh, A., Eslam, S., "Feature selection using genetic algorithm for breast cancer diagnosis: experiment on three different datasets." ***Iranian Journal of Basic Medical Sciences*** 19.5, (2016), DOI: 10.22038/ijbms.2016.6931
36. Parvane, M., Rahimi, E., Jafarinejad, F., "Optimization of quantum cellular automata circuits by genetic algorithm." ***International Journal of Engineering, Transactions B: Applications,*** Vol. 33, No. 2, (2020), 229-236. DOI: 10.5829/ije.2020.33.02b.07
37. Yazdi, H.S., Rowhanimanesh, A., Modares, H., "A general insight into the effect of neuron structure on classification." ***Knowledge & Information Systems*** 30.1, (2012), 135-154. DOI: 10.1007/s10115-011-0392-6
38. Rowhanimanesh, A., Khajekaramoin, A., Akbarzadeh-T, M.R. "Evolutionary constrained design of seismically excited buildings: sensor placement." ***Applications of Soft Computing*** (2009): 159-169. DOI: 10.1007/978-3-540-89619-7_16
39. Davani Motlagh, A., Sadeghian, M.S., Javid, A.H., Asgari, M.S., "Optimization of Dam Reservoir Operation Using Grey Wolf Optimization and Genetic Algorithms (A Case Study of Taleghan Dam)." ***International Journal of Engineering***, ***Transactions A: Basics,*** Vol. 34, No. 7 (2021), 1644-1652. DOI: 10.5829/ije.2021.34.07a.09

Persian Abstract

چکیده

رمزگشایی از فعل و انفعالات حیاتی بین ژن ها یکی از موضوعات اصلی در درک مکانیسم های بنیادی مولکولی و درون سلول است. مدل سازی محاسباتی شبکه های تنظیم کننده ژن می تواند به عنوان ابزاری قدرتمند در زمینه های مختلف زیست پزشکی مولکولی مانند شناسایی مسیرهای متابولیکی، تنظیم کننده و سیگنالینگ، همچنین تجزیه و تحلیل بیماری های پیچیده و کشف دارو استفاده شود. در این مقاله، یک روش بولین بهینه برای مدل سازی محاسباتی شبکه های تنظیم کننده ژن مبتنی بر پروفایل زمانی داده های بیان ژن پیشنهاد شده است. در این روش، مقادیر بهینه آستانه بولین سیگنال های بیان ژن و پارامترهای الگوی برهم کنش بین ژن های هدف و ژن های تنظیم کننده همگی در قالب یک برنامه ریزی غیرخطی مختلط طراحی شده که توسط الگوریتم ژنتیک حل می‌شود. جهت ارزیابی روش پیشنهادی، از آن برای مدلسازی شبکه تنظیم کننده ژن *ساکارومایسس سرویزیه* مبتنی بر پروفایل زمانی داده های بیان ژن استفاده شده است. شبکه مرجع دارای ۱۱ ژن است که ۹ ژن هدف و ٦١ برهم کنش تنظیمی را شامل می شود. در دیتاست اصلی مربوط به پروفایل زمانی داده های ترانسکریپتومیکس، هر سیگنال بیان ژن شامل ۱۸ نمونه زمانی است. در این مطالعه موردی، مدل محاسباتی پیشنهادی شامل ١٤٢ پارامتر ناشناخته است که از طریق بهینه سازی توسط الگوریتم ژنتیک تعیین می شوند. نتایج بدست آمده کارایی روش پیشنهادی را نشان می دهند.

AIMS AND SCOPE

The objective of the International Journal of Engineering is to provide a forum for communication of information among the world's scientific and technological community and Iranian scientists and engineers. This journal intends to be of interest and utility to researchers and practitioners in the academic, industrial and governmental sectors. All original research contributions of significant value focused on basics, applications and aspects areas of engineering discipline are welcome.

This journal is published in three quarterly transactions: Transactions A (Basics) deal with the engineering fundamentals, Transactions B (Applications) are concerned with the application of the engineering knowledge in the daily life of the human being and Transactions C (Aspects) - starting from January 2012 - emphasize on the main engineering aspects whose elaboration can yield knowledge and expertise that can equally serve all branches of engineering discipline.

This journal will publish authoritative papers on theoretical and experimental researches and advanced applications embodying the results of extensive field, plant, laboratory or theoretical investigation or new interpretations of existing problems. It may also feature - when appropriate - research notes, technical notes, state-of-the-art survey type papers, short communications, letters to the editor, meeting schedules and conference announcements. The language of publication is English. Each paper should contain an abstract both in English and in Persian. However, for the authors who are not familiar with Persian, the publisher will prepare the latter. The abstracts should not exceed 250 words.

All manuscripts will be peer-reviewed by qualified reviewers. The material should be presented clearly and concisely:

- *Full papers* must be based on completed original works of significant novelty. The papers are not strictly limited in length. However, lengthy contributions may be delayed due to limited space. It is advised to keep papers limited to 7500 words.
- *Research* notes are considered as short items that include theoretical or experimental results of immediate current interest.
- *Technical notes* are also considered as short items of enough technical acceptability with more rapid publication appeal. The length of a research or technical note is recommended not to exceed 2500 words or 4 journal pages (including figures and tables).

Review papers are only considered from highly qualified well-known authors generally assigned by the editorial board or editor in chief. Short communications and letters to the editor should contain a text of about 1000 words and whatever figures and tables that may be required to support the text. They include discussion of full papers and short items and should contribute to the original article by providing confirmation or additional interpretation. Discussion of papers will be referred to author(s) for reply and will concurrently be published with reply of author(s).

INSTRUCTIONS FOR AUTHORS

Submission of a manuscript represents that it has neither been published nor submitted for publication elsewhere and is result of research carried out by author(s). Presentation in a conference and appearance in a symposium proceeding is not considered prior publication.

Authors are required to include a list describing all the symbols and abbreviations in the paper. Use of the international system of measurement units is mandatory.

- On-line submission of manuscripts results in faster publication process and is recommended. Instructions are given in the IJE web sites: www.ije.ir-www.ijeir.info
- Hardcopy submissions must include MS Word and jpg files.
- Manuscripts should be typewritten on one side of A4 paper, double-spaced, with adequate margins.
- References should be numbered in brackets and appear in sequence through the text. List of references should be given at the end of the paper.
- Figure captions are to be indicated under the illustrations. They should sufficiently explain the figures.
- Illustrations should appear in their appropriate places in the text.
- Tables and diagrams should be submitted in a form suitable for reproduction.
- Photographs should be of high quality saved as jpg files.
- Tables, Illustrations, Figures and Diagrams will be normally printed in single column width (8cm). Exceptionally large ones may be printed across two columns (17cm).

PAGE CHARGES AND REPRINTS

The papers are strictly limited in length, maximum 6 journal pages (including figures and tables). For the additional to 6 journal pages, there will be page charges. It is advised to keep papers limited to 3500 words.

Page Charges for Papers More Than 6 Pages (Including Abstract)	
For International Author ***	**$55 / per page**
For Local Author	**100,000 Toman / per page**

AUTHOR CHECKLIST

- Author(s), bio-data including affiliation(s) and mail and e-mail addresses).
- Manuscript including abstracts, key words, illustrations, tables, figures with figure captions and list of references.
- MS Word files of the paper.

International **J**ournal of **E**ngineering, P.O. Box 13145-1659, Tehran, I.R. Iran
Materials and Energy Research Center, 5 Ahuramazda St., Alvand Ave., Argentina Sq., Tehran, Islamic Republic of Iran
www.merc.ac.ir - www.emerc.ac.ir

THOMSON REUTERS

WEB OF SCIENCE

Scopus®

CAS®
A DIVISION OF THE
AMERICAN CHEMICAL SOCIETY

Google
Scholar